Development of InGaAsN solar cells and characterization of their degradation in space radiative environment

Maxime Levillayer

Université Fédérale
Toulouse Midi-Pyrénées

THÈSE

En vue de l'obtention du

DOCTORAT DE L'UNIVERSITÉ DE TOULOUSE

Délivré par l'Institut Supérieur de l'Aéronautique et de l'Espace

---

Présentée et soutenue par

Maxime LEVILLAYER

Le 26 novembre 2021

Development of InGaAsN solar cells and characterization of their degradation in space radiative environment

---

Ecole doctorale : **GEETS - Génie Electrique Electronique,Télécommunications et Santé : du système au nanosystème**

Spécialité : **Photonique et Systèmes Optoélectronique**

Unité de recherche :
LAAS - Laboratoire d'Analyse et d'Architecture des Systèmes

Thèse dirigée par
Guilhem ALMUNEAU et LAURENT ARTOLA

Jury

Mme Karine COULIé, Rapporteure
M. Mircea GUINA, Rapporteur
M. Romain CARIOU, Examinateur
M. Guilhem ALMUNEAU, Directeur de thèse
M. Laurent ARTOLA, Co-directeur de thèse
M. Stéphane COLLIN, Président

Development of InGaAsN solar cells and characterization of their degradation in space radiative environment

Abstract

The current development of artificial satellites used for telecommunication, scientific and military applications, requires the conception of powerful and reliable electrical sources that can be used in a space environment. On-board systems rely predominantly on photovoltaic conversion and more specifically on multi-junction solar cell (MJSC) technology.

The standard MJSC structure used in space applications is the triple junction GaInP/(In)GaAs/Ge. In order to increase further the efficiency of this MJSC, it is necessary to optimize photon harvesting in the near infrared region. This can be achieved by replacing the germanium subcell by a subcell with a 1 eV bandgap energy. Even higher efficiencies can be obtained if the 1 eV subcell is integrated within a four-junction architecture. For its integration to be possible, this 1 eV subcell needs to be based on a material with the same lattice parameter as GaAs or Ge. It also needs to photogenerate more than 15 mA/cm^2 under integration condition and it should exhibit high radiation hardness to enable long lifespan space missions.

In the framework of this thesis, we have developed solar cells based on the InGaAsN quaternary to fulfil all these requirements. We have grown solar cell structures and InGaAsN bulk layers by molecular beam epitaxy (MBE). Through multiple material characterizations, we have studied the impact of the growth conditions on the optoelectronic properties of InGaAsN.

InGaAsN solar cells were fabricated through clean room technological processing steps (lithography, metallisation, etching). These solar cells were then characterized with current-voltage and quantum efficiency measurements. In MJSC integration conditions, our device could generate current densities as high as 8 mA/cm^2. Increasing the nitrogen content and the thickness of the absorber would lead to higher photocurrents enabling current-matching in the MJSC. The integration of an InGaAsN subcell within a GaAs/InGaAsN tandem structure was also demonstrated.

InGaAsN solar cells and samples dedicated to photoluminescence (PL) and deep level transient spectroscopy (DLTS) analysis were then irradiated with 1 MeV electrons and protons. Comparing the InGaAsN material properties and the solar cell characteristics before and after irradiation allowed us to evaluate the degradation rate of InGaAsN cells. These solar cells exhibit a radiation hardness towards electrons and protons greater than their GaAs counterparts.

Développement de cellules solaires InGaAsN et caractérisation de leur dégradation en environnement radiatif spatial

Résumé

L'essor des satellites artificiels couvrant des applications de télécommunication et d'observation scientifique, ainsi que des besoins miliaires, requiert le développement de puissants systèmes d'alimentation électrique en milieu spatial. Ces systèmes reposent très majoritairement sur la conversion photovoltaïque et la technologie des cellules solaires à multi-jonction (MJSC).

La structure standard de MJSC utilisée pour les applications spatiales est la tri-jonction GaInP/(In)GaAs/Ge. Afin d'augmenter le rendement de cette MJSC, il est nécessaire de mieux exploiter le proche infrarouge en remplaçant la sous-cellule de germanium ou en introduisant une 4e sous-cellule dont l'énergie de bande interdite est égale à 1 eV. Cette cellule doit avoir le même paramètre de maille que Ge ou GaAs et doit être capable de générer environ 15 mA/cm^2 en condition d'intégration. De plus, il est indispensable que cette cellule soit résistante aux radiations spatiales afin de garantir une longue durée de vie de la structure MJSC.

Dans le cadre de cette thèse, nous avons étudié le quaternaire InGaAsN pour répondre à ces exigences d'intégration MJSC et de tenue en milieu spatial. Nous avons commencé par faire croître des couches cellules solaires et des couches bulk d'InGaAsN par épitaxie par jets moléculaires (EJM). De nombreuses caractérisations matériaux nous ont permis de comprendre l'impact des conditions de croissance épitaxiale sur les propriétés opto-électroniques de l'InGaAsN et ainsi d'optimiser notre procédé de fabrication.

Des cellules solaires ont par ailleurs été fabriquées en salle blanche (lithographie, métallisation, gravure) avant d'être caractérisées par mesure courant-tension et réponse spectrale. En conditions d'intégration MJSC, nos cellules pourraient générer des densités de courant environ égales à 8 mA/cm^2. L'intégration de ces cellules au sein d'une structure tandem GaAs/InGaAsN a par ailleurs été démontrée.

Des cellules solaires InGaAsN ainsi que des échantillons pour la photoluminescence (PL) et la spectroscopie de défauts profonds (DLTS) ont par la suite été irradiés sous électrons et protons 1 MeV. La comparaison des caractéristiques matériaux et cellules avant et après irradiation nous a permis d'analyser les mécanismes de dégradation ayant lieu dans l'InGaAsN. Globalement, les cellules solaires d'InGaAsN apparaissent plus résistantes aux irradiations électroniques et protoniques que les cellules de GaAs.

International peer reviewed journal

- M. Levillayer et al., "As-grown InGaAsN subcells for multijunction solar cells by molecular beam epitaxy," *IEEE Journal of Photovoltaics*, 2021, *10.1109/JPHOTOV.2021.3093048*.
- M. Levillayer et al., "Degradation study of InGaAsN PIN solar cell under 1 MeV electrons irradiation," *IEEE Transactions on Nuclear Science*, 2021, *10.1109/TNS.2021.3068044*.

International conferences

- Oral presentation at the *Next-PV* workshop, *Nov.* 2020.
- Oral presentation at the *RADECS Conference*, *Oct.* 2020.
- Poster presentation at the 47th *IEEE Photovoltaic Specialists Conference (PVSC)*, 2020. Proceeding: "Development of 1 eV InGaAsN PIN subcell for MJSC integration and space application," pp. 0473-0475, *10.1109/PVSC45281.2020.9300570*.

National conferences

- Oral presentation at the *GEETS* Congress, *Apr.* 2021. Award of the best presentation in the Photonic and Optoelectronic systems Session.
- Oral presentation at the *CNES COMET* workshop "Optique et Optoélectronique", *Mar.* 2021
- Poster presentation at the *Ecole des Houches, Physics of Solar Cells*, Les Houches, *Mar.* 2020
- Oral presentation at the *Journées Nationales du Photovoltaïque (JNPV)* conference, Dourdan, *Dec.* 2019
- Oral presentation at the *CNES COMET* workshop "Générateurs Solaires", Toulouse, *Mar.* 2019

Remerciements

Que serait un manuscrit de thèse sans une section Remerciements croustillante et non-exhaustive ? Probablement ennuyeux et impersonnel. Plus concrètement, je pense que remercier en début d'ouvrage illustre un aspect essentiel de la Recherche avec un grand "R" : le collectif. L'époque n'est plus aux grands polymathes mais aux équipes qui mettent en commun des savoirs complémentaires. Je commencerai donc tout naturellement par remercier mes encadrant·e·s avec lesquel·le·s j'ai pu construire et mener ce projet de recherche. Merci donc à mes directeurs de thèse Guilhem et Laurent pour avoir su trouver ce subtil équilibre encadrement/autonomie. Merci également à Christophe, Sophie et Thierry *i.e.* les expert·e·s irradiation de l'ONERA et à Chantal et Alex *i.e.* les virtuoses de la croissance épitaxiale du LAAS. Une pensée également pour Corinne et toutes les personnes avec qui j'ai pu interagir au CNES. Enfin, un merci tout particulier à Inès qui cumule trois casquettes : encadrante + camarade écologie + amie !

Je suis également très reconnaissant de l'aide apportée en salle banche par l'équipe TEAM du LAAS qui mérite amplement son Cristal collectif. Merci aussi aux ingénieurs des plateformes de caractérisation optiques et électriques et merci à Richard et François de m'avoir initié aux secrets de la DLTS. Il me semble également important de remercier les permanents de l'équipe PHOTO du LAAS, à la fois pour leur assistance technico-scientifique (ou scientifico-technique ?) et pour leur bonne humeur inébranlable (mais si, mais si). J'ai aussi eu le plaisir de croiser de nombreuses âmes non-permanentes durant ces trois courtes années. Je pense notamment aux aïeux Clara, Oleks, Lizzie et Jean-Baptiste, aux co-disciples de la photonique François, Lucas, Nathan, Sébastien et Romain, et à Moana et Sylvain avec qui j'ai aimé travailler. Mention spéciale à Antoine (aka Tonio la malice) et Ivan (SIFE), les compagnons du Dubliners et de la discussion politique enivrée.

Je n'oublie pas non plus mes amis de l'ONERA avec qui j'ai pu échanger maintes fois à la machine à café. Je pense à tous les doctorants et notamment à mes acolytes Abdess et Loanne mais aussi à Nour, Hector et Pablo. Un grand merci aux gens qui m'ont aidé au DPHY : Romain, Claude, Sabine et bien d'autres.

Cette thèse n'aurait pas pu se faire sans l'aide de collègues de labos partenaires tels que Stéphanie à l'IES, Hélène au LPCNO, Jean et Nicolas au III-V Lab. J'en profite également pour remercier les membres de mon jury de thèse pour l'intérêt qu'ils ont porté pour mes travaux : merci Mircea, Karine, Stéphane et Romain.

Je tiens particulièrement à remercier ma famille et notamment mes parents bretons et mon frère islandais. Et bien entendu merci à la reine de la pizza, des guirlandes et de la LSF sans qui ces trois années auraient été moins heureuses. Enfin je voudrais saluer tous ceux et celles qui, aujourd'hui comme demain, choisiront le vélo plutôt que la voiture, cuisineront des lentilles plutôt que du bœuf, visiteront la Bretagne plutôt que les Maldives.

List of Acronyms

ARC	Anti-Reflection Coating
BGCC	Background Carrier Concentration
BOL	Beginning Of Life
BSF	Back Surface Field
DDD	Displacement Damage Dose
DLTS	Deep Level Transient Spectroscopy
ECV	Electrochemical Capacitance-Voltage
EOL	End Of Life
EQE	External Quantum Efficiency
FF	Fill Factor
IQE	Internal Quantum Efficiency
MJSC	Multi-Junction Solar Cell
MBE	Molecular Beam Epitaxy
NIEL	Non-Ionizing Energy Loss
PL	Photoluminescence
PV	Photovoltaic
RHEED	Reflection High-Energy Electron Diffraction
RTP	Rapid Thermal Processing
SCR	Space Charge Region
SIMS	Secondary Ion Mass Spectroscopy
SRH	Shockley-Read-Hall
SEM	Scanning Electron Microscopy
TLM	Transfer Length Method
TRPL	Time-Resolved Photoluminescence
XRD	X-Ray Diffraction

Contents

General Introduction

Context and Motivations

The rise of the solar photovoltaic (PV) technologies is intimately related to the Space Race between the United States and the Soviet Union. As both superpowers were developing artificial satellites and exploration rovers, the need for in-board electrical power became a key technological challenge. Silicon and later on GaAs solar cells were then developed in order to take advantage of the most obvious energy source available in space: the Sun. From the first solar cells used in Vanguard 1 in 1958 to the solar array wings equipping the international space station, the power conversion efficiency of the cells has considerably increased. Unlike for most PV terrestrial applications where the W/$ ratio is regarded as the most important factor, the key parameter for the space solar modules is the W/kg ratio also called power-to-weight ratio.

Advanced architectures relying on *III-V* semiconductors were then developed to achieve higher photovoltaic efficiencies. These structures are called multi-junction solar cells (MJSC) and are composed of multiple subcells stacked and connected with tunnel junctions in a vertical configuration. The most standard MJSC structure currently used for space applications is the monolithic GaInP/(In)GaAs/Ge triple junction epitaxially grown on a germanium substrate, as represented in Figure 1.

MJSC architectures lead to higher efficiencies because they allow for a better utilization of the solar spectrum. Each subcell harvests a specific part of the incident solar spectrum, which minimizes the thermalisation and transmission losses. However, most of the MJSC architectures rely on series connected subcells, which constraints the electrical current to be the same in every part of the device. The standard triple junction presented above is then found to be unoptimized, as its germanium bottom cell delivers significantly more photocurrent than the top and middle cells.

In order to improve further their efficiency, the architecture of the MJSCs should be redesigned to ensure a better management of the near infrared light. Such a thing could be achieved by replacing the germanium in the bottom cell by a material with a 1 eV bandgap energy. Even higher efficiencies could be obtained with a four-junction architecture, introducing a 1 eV subcell between the GaAs middle-cell and the Ge bottom-cell. Either way, this solar cell must be based

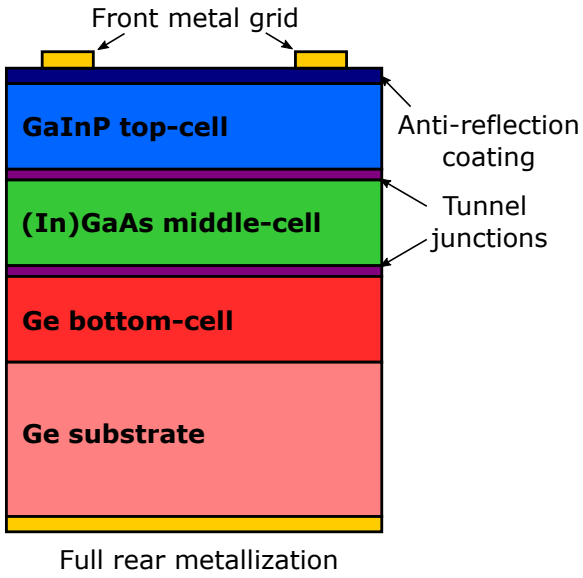

Figure 1: Architecture of the standard 3J solar cells used in space applications.

on a 1 eV material that can be grown lattice-matched to a GaAs or a Ge substrate.

The InGaAsN quaternary alloy has been proposed as a candidate for this application as both the bandgap energy and the lattice parameter of this semiconductor can be tuned with varying its indium and nitrogen contents. In addition to the already-mentioned requirements, the 1 eV dilute nitride solar cells should exhibit high radiation hardness if they are to be used in a space environment. Indeed, the outer space is a radiative and hostile medium, which implies that space solar cells constantly operate under high energy particles irradiation (electrons, protons, ions).

The study of the radiation resistance of InGaAsN solar cells has been very limited so far. This PhD thesis aims to strengthen the understanding of the degradation mechanisms occuring in InGaAsN solar cells subjected to space-representative irradiation.

Thesis outline

The **first chapter** of this thesis introduces the basic physical principles of the solar cells with a focus made on the MJSC technology. The space radiative environment is also presented along with the radiation/matter interactions.

Chapter 2 is dedicated to the InGaAsN material. A literature review is conducted to present both the optoelectronic properties of InGaAsN and the reported photovoltaic performances of 1 eV dilute nitrides solar cells.

The **third chapter** covers the InGaAsN growth study that was conducted during this thesis. The impact of the molecular beam epitaxy growth conditions on

the structural, optical and electrical properties of InGaAsN is assessed through multiple characterizations performed on solar cell epitaxial stacks and on bulk layers. Overall, this chapter provides an insight on the material properties of the InGaAsN absorber of the solar cells.

Chapter 4 describes the technological process that was used to fabricate single junction InGaAsN solar cells and GaAs/InGaAsN tandem solar cells. Current-voltage and spectral response characterization results are then presented. The photovoltaic performances of the cells are analysed using the material properties obtained in the previous chapter.

The **last chapter** is a degradation study of the InGaAsN solar cells subjected to 1 MeV electron and 1 MeV proton irradiation. The radiation response of single junction InGaAsN cells and GaAs/InGaAsN tandem solar cells is analysed by comparing the materials properties and the photovoltaic performances before and after irradiation.

Chapter 1

Space photovoltaics technologies and irradiation-induced degradations

In this first chapter, we describe the solar cell technology used for space application and we introduce the effect of space radiations on semiconductors.

The first part of this chapter is dedicated to the fundamentals of semiconductors and solar cells physics. The history of the space solar cells is then introduced before describing the state of the art technology used for space application: the multi-junction solar cells.

In the second part, we introduce the space radiation environment and we detail particle/matter interactions. We then show how the introduction of defects through irradiation leads to the degradation of the solar cells. Finally, we describe the methods used to model solar cell degradation and we present the particle accelerator technologies used to simulate space environment. A literature review on solar cell irradiation-induced degradation is then conducted.

Contents

1.1 High efficiency solar cells for space application

1.1.1 Photovoltaic effect and theory of solar cells

The photovoltaic effect was discovered in 1839 by Edmond Becquerel when he observed the apparition of an electrical voltage on two metal blades connected together under sunlight [1]. The tension that was observed is called the photovoltage and can be explained by the photoelectric effect and the difference between the Fermi levels of the materials.

Since the first demonstration of a silicon solar cell at Bell Labs in 1954 [2], most of the solar cell technologies that have been developed are based on semiconductors. Semiconductors are materials in which the electrons can be either in the valence band (occupying electron orbitals) or in the conduction band (moving freely in the lattice). Those two bands are separated by a so-called *band gap* in which there are no energy state to occupy.

Contrary to insulator materials, the band gap energy of semiconductors is narrow enough to allow electron transition from the valence to the conduction band. This transition can typically happen under optical excitation when light is shone upon the semiconductor and constitutes the first step of the photovoltaic effect. A photon that hits a semiconductor material can be absorbed if its energy is larger than the semiconductor band gap. An electron from the valence band is then excited towards the conduction band which ultimately leads to the creation of a free electron/hole pair. The electron and the hole are called photocarriers and can move freely within the lattice through diffusion and drift transport. However, photocarriers can also relax and return to their initial energy level through radiative and non-radiative recombination. To avoid this, the photocarriers need to be spatially separated and *pn* junctions are generally used to achieve this role.

In a *pn* junction[1], a *p*-doped layer with holes as majority carriers is put in contact with a *n*-doped layer with electrons as majority carriers. As the Fermi level of the two layers line up, the electrons (respectively the holes) diffuse to the *p*-doped layer (respectively *n*-doped layer). Since electrons are flowing out of the *n*-layer and holes out of the *p*-layer, and as fixed charges (dopant ions) remain on each side of the junction, a built-in potential starts to appear. This built-in potential is associated with an electric field ξ that extends across the so-called depletion region or space charge region (SCR), as depicted in Figure 1.1. This electric field leads in turn to a drift current that flows in the reverse direction compared to the diffusion current. An equilibrium is then reached and results in the following band diagram:

At equilibrium conditions, *i.e.* without light illumination and when no external bias is applied, the diffusion and the drift currents cancel each other out and there is no net carrier flow in the device. However, when a direct (positive)

[1] In this chapter, we only describe *pn* junctions although the same mechanisms and equations apply to *np* junctions.

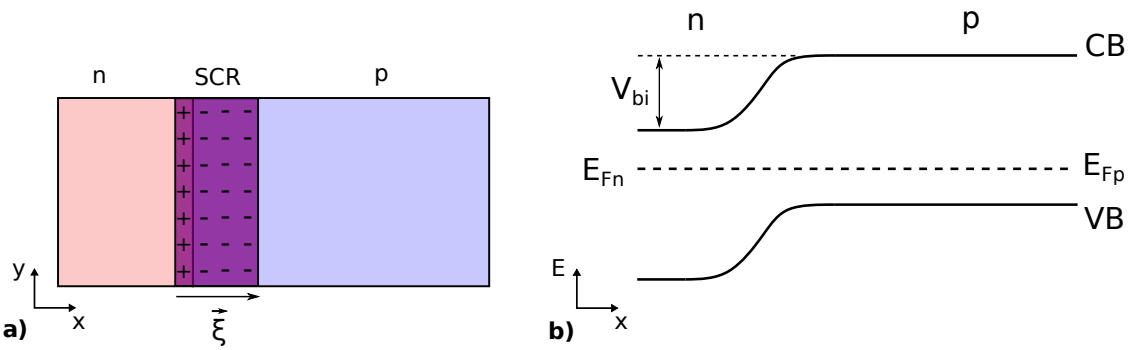

Figure 1.1: a) *pn* junction with space charge region and electric field b) band diagram of the *pn* junction.

bias is applied to the junction, the built-in potential and the space charge region start to decrease until the point they no longer exist. Then, there is no more potential barrier to prevent the majority carriers to diffuse and the current starts to increase exponentially: the diode is said to be 'ON'.

On the other hand, when an indirect (negative) bias is applied, the space charge region becomes wider and no current is able to flow in the ideal diode conditions. A dark current can yet be measured in real devices, resulting from generation and recombination mechanisms caused by thermal excitation. The dark *I-V* characteristics of a *pn*-junction can be described with the following diode equation, where I_0 is the dark saturation current, q is the elementary charge, n is the diode ideality factor, k is the Boltzmann constant and T the temperature:

$$I = I_0.(exp(\frac{qV}{nkT}) - 1) \tag{1.1}$$

Under light, the system moves to a non-equilibrium state where free carriers are photogenerated in the semiconductor. The photocarriers can undergo different mechanisms as depicted in Figure 1.2 and part of these carriers will be separated by the *pn*-junction.

Depending on the external bias condition, different scenarios can take place:

- If the junction operates in short-circuit conditions (p and n side externally connected with no load), the separation of charges leads to the formation of a net electrical current flow: the short-circuit current I_{sc}.
- If the junction operates under open-circuit conditions (no carriers can be extracted from the device), the concentration of majority carriers in p and n-type region increases. This increase leads to the splitting of the quasi Fermi levels which results in the creation of a tension at the terminals of the diode: the open-circuit voltage V_{oc}.

Overall, the *I-V* characteristic of a *pn*-junction under illumination can be de-

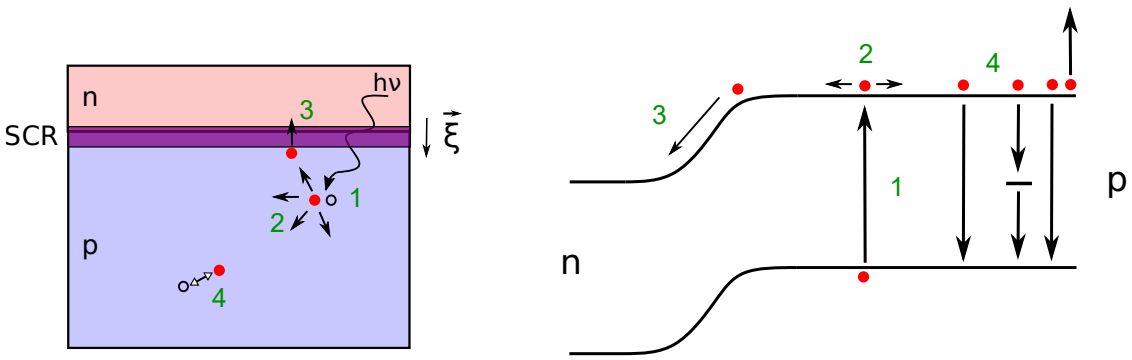

Figure 1.2: Basic mechanisms taking place in a *pn* junction under illumination: 1) free carriers photogeneration, 2) electron diffusion, 3) electron drift collection, 4) Radiative, SRH (Shockley-Read-Hall) and Auger recombination. The same mechanisms apply to hole carriers.

scribed as its dark *I-V* characteristic shifted by the photogenerated current I_{ph}:

$$I = [I_0.(exp(\frac{qV}{nkT}) - 1)] - I_{ph} \tag{1.2}$$

As a convention and for clarity sake, the photovoltaic characteristic (*i.e.* the evolution of current with voltage) is often plotted in the first quadrant as -*I* vs *V*. Furthermore, real devices are usually subject to series and shunt resistances which can be accounted for by introducing R_s and R_{sh} in the light *I-V* equation. The equivalent electrical circuit is given in Figure 1.3, where R_{load} corresponds to the resistance of the electrical load connected to the cell.

$$I = I_{ph} - [I_0.(exp(\frac{q(V + IR_s)}{nkT}) - 1)] - \frac{V + IR_s}{R_{sh}} \tag{1.3}$$

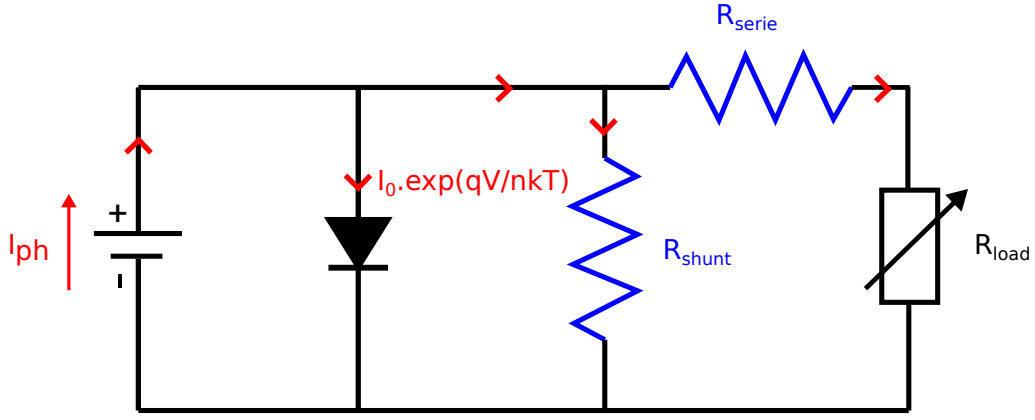

Figure 1.3: Equivalent circuit of the *pn*-junction under illumination

Figure 1.4 presents a typical *I-V* curve along with its corresponding *P-V* characteristic. The power delivered by the cell *P* is simply calculated as the product of the voltage and the current.

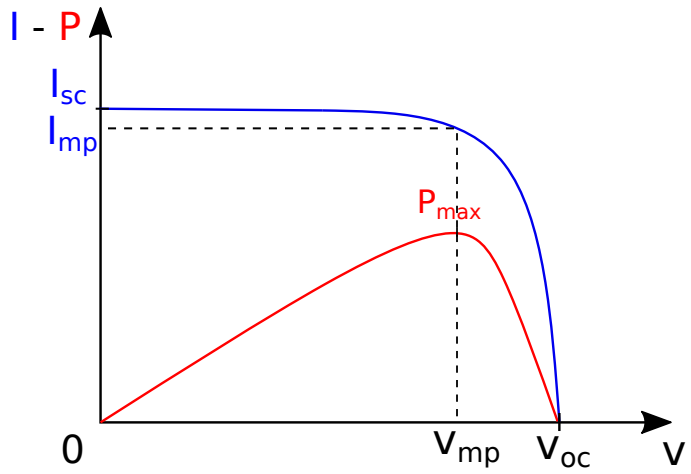

Figure 1.4: *I-V* and *P-V* characteristics with maximum power point

In addition to the already mentioned V_{oc} and I_{sc}, a cell is characterized by its maximum power point. This maximum power P_{max} is equal to the product of V_{mp} and I_{mp} and allows us to introduce another important parameter: the fill factor FF. It corresponds to the "squareness" of the *I-V* curve and is equal to:

$$FF = \frac{V_{mp}.I_{mp}}{V_{oc}.I_{sc}} = \frac{P_{max}}{V_{oc}.I_{sc}} \tag{1.4}$$

For a given I_{sc} and V_{oc}, having a fill factor close to the unity is then really important to obtain a large output power. In order to ensure that, parasitic resistances (R_{series} and R_{shunt}) should be minimized. High series and low shunt resistances can arise from the *pn*-junction, the edges of the cells and the metal contacts required to extract carriers from the cell. Finally, we can calculate the efficiency η of the cell by dividing its output power by the solar irradiance it receives at standard conditions:

$$\eta = \frac{P_{max}}{P_{inc}} = \frac{P_{max}}{H_0.A_{cell}} \tag{1.5}$$

P_{inc} is the incoming light power, A_{cell} is the area of the cell and H_0 is the solar irradiance which depends on the solar cell environment. The efficiency of a solar cell is sometimes also designated as the power conversion efficiency PCE.

The Sun has an effective temperature of 5780 K and is a source of radiation that closely follows the black body model. Figure 1.5 represents the solar spectra that corresponds to the light that the Earth receives outside its atmosphere (AM0) and as received at our latitudes, after it is filtered by the atmosphere (AM1.5G).

For terrestrial applications, the standard solar irradiance AM1.5G is taken as 1000 W/m^2 (ASTM G-173-03). Today, the typical efficiency of crystalline-Si modules (95 % of the solar PV market) is slightly over 17 % [3]. On the other hand, the solar irradiance corresponding to space applications is equal to 1366.1 W/m^2 (ASTM E-490). The efficiency of the standard III-V multijunction solar cells typically used for space applications ranges from 28 to 30 % [4].

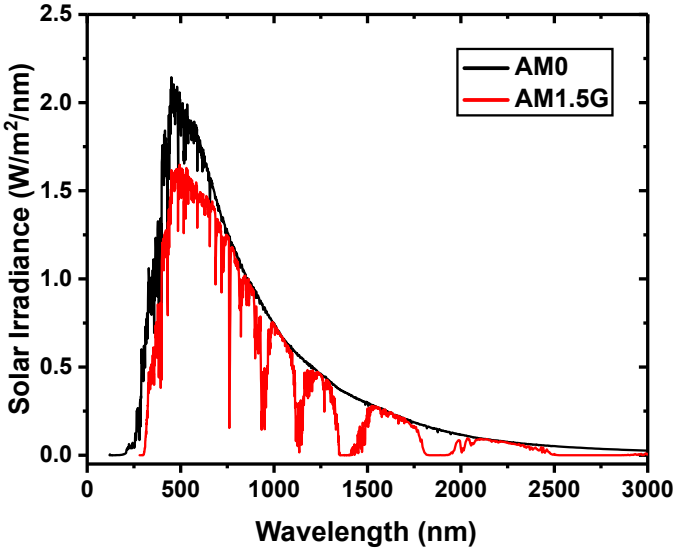

Figure 1.5: AM0 (*ASTM E-490*) and AM1.5G (*ASTM G173-03*) spectra

1.1.2 Retrospective of space photovoltaic technologies

Even though the first solar cells developed in Bell laboratories were designed for terrestrial applications, their prohibitive cost ($/W) kept them out of the electrical power market. However, this technology brought a lot of interest from the U.S. Army who was by the time developing Earth orbiting satellites. The history of space photovoltaics is indeed intimately connected with the Space Race and begins when the United States launched Vanguard 1 in 1958, which was the first artificial satellite to take advantage of solar energy conversion. It was equipped with six square Si solar cells with 10 % efficiency (under AM0) that were supposed to power its beacon transmitter [5]. Two months later, the Soviets launched Sputnik 3 which also relied on Si solar cells.

While the efficiency and most importantly the power to mass ratio of Si cells kept on increasing, the Russian decided to develop GaAs solar cells for their better temperature stability and their higher radiation resistance [6]. As space missions became longer, this latter parameter became predominant and it drove the transition from Si to GaAs-based solar cells in space applications [7]. 11 % efficient GaAs solar arrays were then used for Venus observation mission on Venera-2 and Venera-3 in 1966 and on the Moon rovers Lunokhod-1 (1970) and Lunokhod-2 (1972).

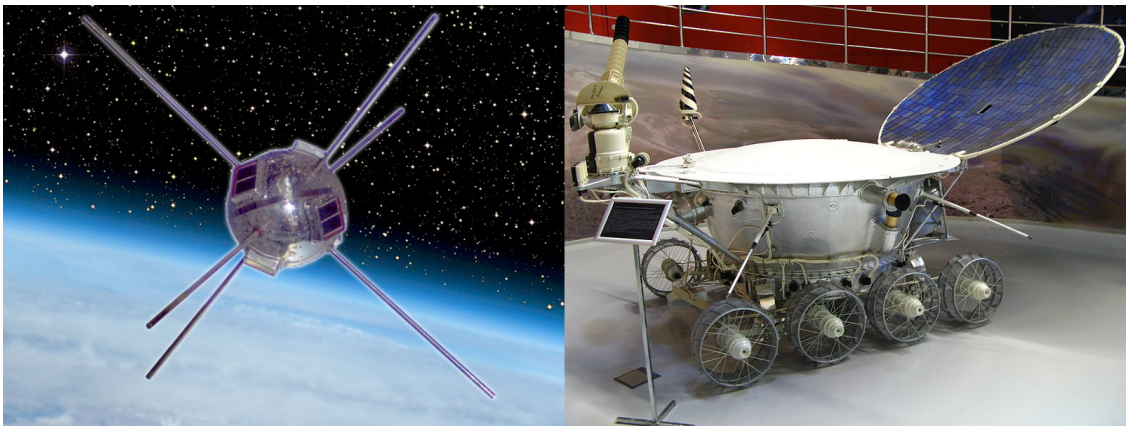

Figure 1.6: On the left, the satellite Vanguard 1 designed by the USA (*CC BY-SA* NASA). On the right, a moon rover Lunokhod engineered by the USSR (*CC BY-SA* Petar Milošević).

To further increase the power to mass ratio, AlGaAs/GaAs tandem cells were developed by the USSR in the Ioffe Institute and a 19 % efficiency cell was reported in 1983 [8]. This technology was then used to make the 70 m^2 solar arrays of the MIR space station in 1986 [6, 9]. On the other side, the International Space Station (ISS), whose first module was launched in 1998, uses Si bifacial cells distributed into eight 34 m×12 m solar array wings (SAW), accounting for a 120 kW power capacity [10, 11].

In the 90s, the booming of satellite communications led to a growth of the space solar cell market. In 1996, Spectrolab demonstrated a 25.7 % BOL (beginning of life) efficient GaInP/GaAs/Ge triple junction cell marking the advent of the III-V multijunction cell technology [12].

In 2008, the American company announced that they had reached a 30 % cell that was production-ready [13]. Today, the space photovoltaics market is dominated by the standard GaInP/GaAs/Ge cells [4], which are being manufactured in the U.S. by Spectrolab and SolAero and in Europe by AZUR SPACE and CESI.

Table 1.1: Main 3J models commercially available

Manufacturer	Model	BOL Efficiency under AM0 (%)
Spectrolab [14]	UTJ	28.3
	XTJ prime	30.7
SolAero [15]	ZTJ	29.5
AZUR SPACE [16]	3G28C	28
	3G30C	30
CESI [17]	CTJ30	29.5

1.1.3 Multi-junction solar cells

Multi-junction solar cell is today the technology that provides the most efficient cells. It consists in the stacking of several subcells on top of each other in order to optimize light harvesting. It then acts as a workaround for one of the major compromise there is for mono-junction solar cells: the band gap energy of the active material. Indeed, a narrow band gap semiconductor absorbs a large part of the solar spectrum - giving rise to a high electrical current density - but can only provide a low voltage. Most of the energy is then lost through thermalization when hot carriers relax by releasing phonons in the lattice. In addition to this energy loss, thermalization causes the device to heat, which in turns leads to the degradation of the solar cell efficiency. Oppositely, a wide band gap material cell results in a low current / high voltage characteristic, where most of the energy is lost through light transmission (non-absorption). The main types of energy losses and the corresponding *I-V* characteristics are shown in Figure 1.7.

Using architectures that include more than one junction allows to reduce these losses. In order to do that, the subcells with the highest band gap energy should be placed at the top of the structure to convert high energy photons while transmitting the others to the subsequent junctions. The resulting structure can be considered as several solar cells connected in series[2] that would receive different solar spectra, as shown in Figure 1.8.

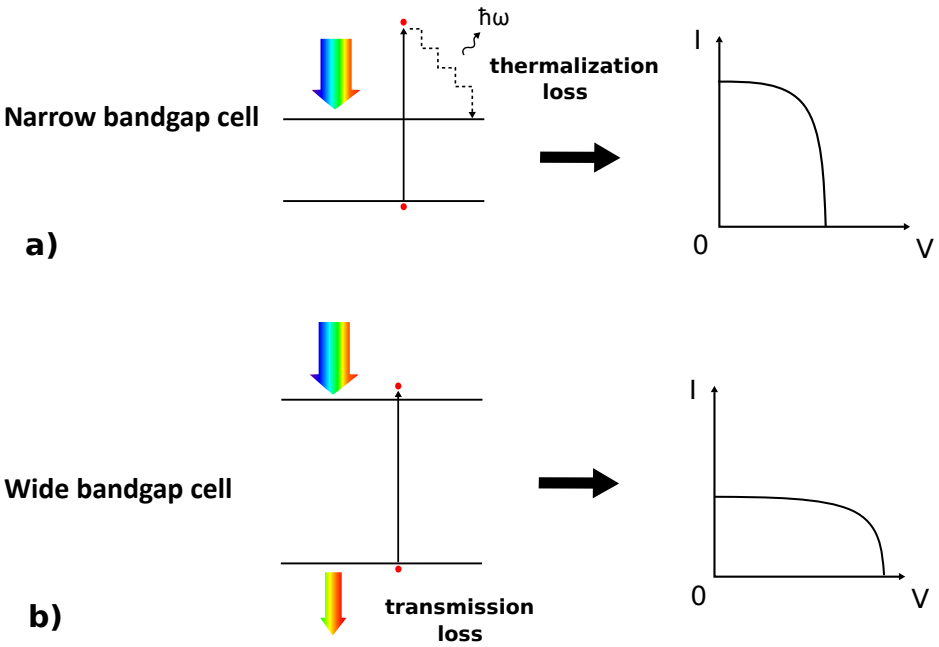

Figure 1.7: Light management and associated *I-V* characteristics of a) low band gap and b) high band gap solar cells under illumination.

[2]We only consider here 2-terminal devices since it is the most common approach for MJSC.

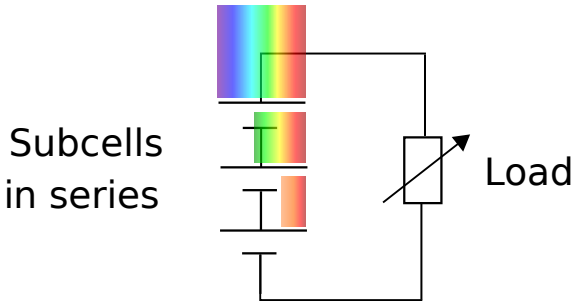

Figure 1.8: Electrical equivalent circuit of MJSC with corresponding incident light on each cell.

As for any device connected in series, the electrical current needs to be the same in all parts of the circuit, meaning that the subcells are "forced" to generate the same intensity. On the other side, the voltage of series-connected subcells adds up. This results in enhanced voltage characteristics and in higher conversion efficiencies as it can be seen on the NREL (National Renewable Energy Laboratory) efficiency chart in Figure 1.9.

The highest efficiencies shown on this graph correspond to MJSC with up to six subcells. They rely on the III-V semiconductor family which offers a wide range of materials with different band gap and lattice parameter. However, the high efficiencies provided by MJSC come at the price of high engineering complexity. As already mentioned, the subcells need to generate the same current, which is called satisfying the current-matching condition. To do this, each subcell must be engineered in terms of material and architecture. First, the *pn* junction materials should be chosen according to their band gap energy in such a way that every subcells can absorb the same amount of photons. Nonetheless, the collection efficiency is generally different from one subcell to the other. Absorbing the same photon quantity is then not a sufficient condition to ensure that the photocurrent is the same in all the cells. Hence, their thickness also needs to be tailored. Thinning the top cells increases transmittance and allows more light to reach the bottom cells, which can, as a result, equilibrate the photocurrents.

Another important feature of the MJSC is the tunnel junction. This component is of utmost importance as it allows electrons to go from one cell to another tunneling from an n^+-doped region to a p^+-doped one without losing energy. This mechanism is called the tunnel effect and emerges from the quantum nature of electrons whose wave functions can spread across potential barriers. As depicted in Figure 1.10, a tunnel junction is made of two very thin and highly doped n and p layers presenting an overlapping of the n-layer conduction band with the p-layer valence band.

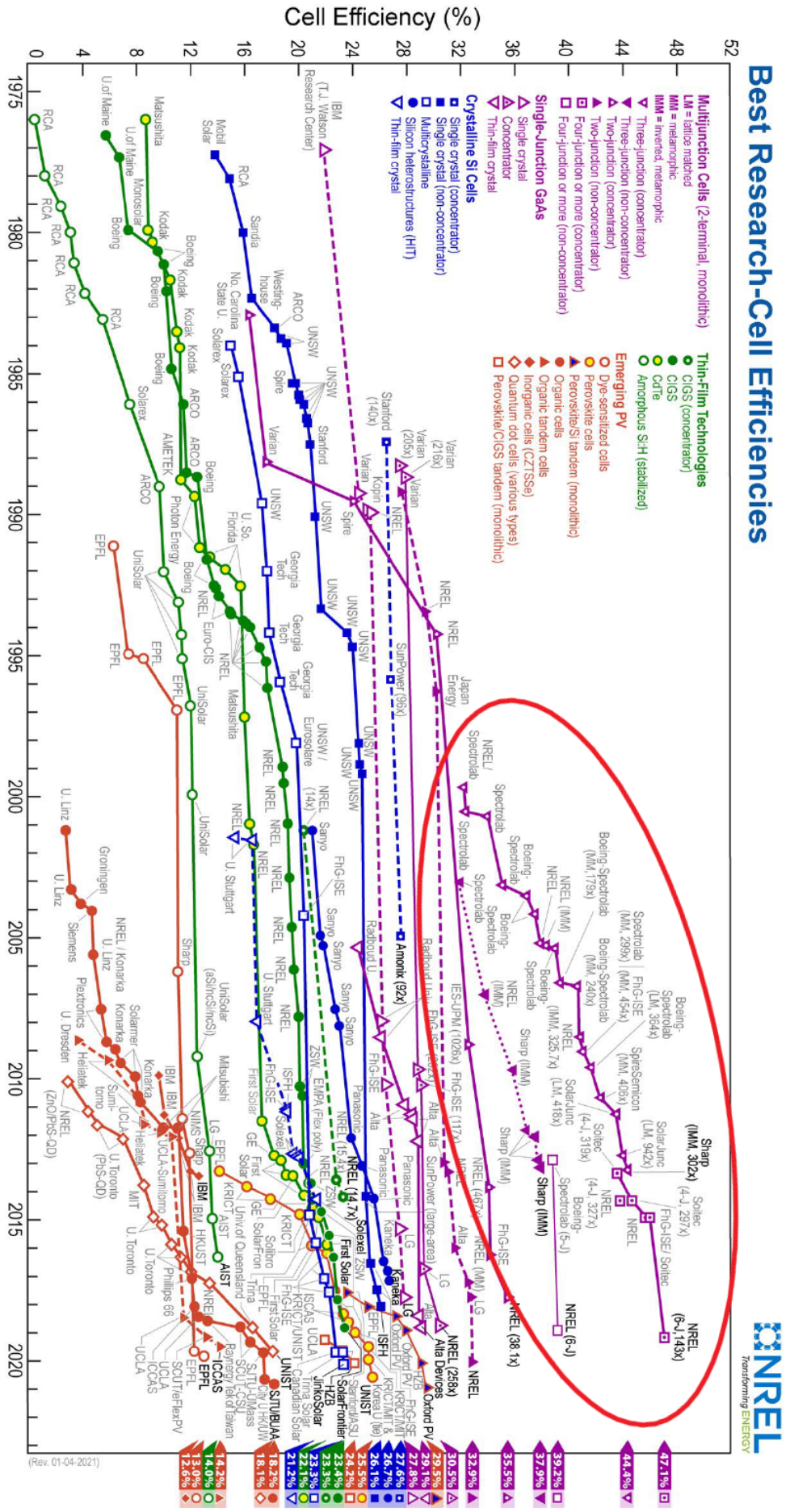

Figure 1.9: 2020 NREL efficiency chart with MJSC technologies circled in red [18]

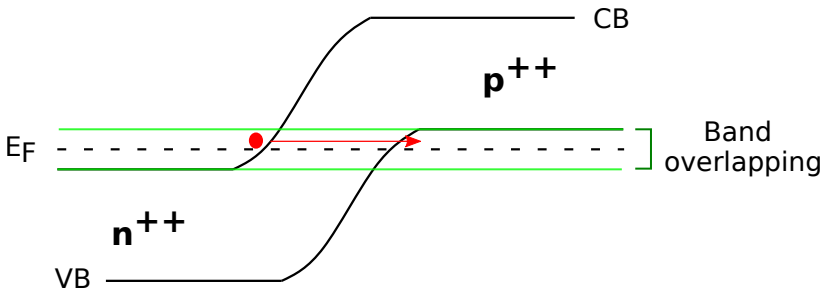

Figure 1.10: Band structure of a tunnel junction. The band overlapping allows electrons to tunnel through the potential barrier.

Last technological challenge but not least is the stacking of the cells itself. There are currently 3 main strategies to fabricate MJSC:

Monolithic growth of lattice-matched subcells is the most common technique. It requires all the materials constituting the subcells to have the same lattice parameter as the substrate on which they are grown. *pn* junctions are then grown on top of each other starting from the bottom to the top cells. The major constraint with this technique is that the lattice-matching condition drastically reduces the list of material candidates for making subcells. Today, most of the lattice-matched MJSC are based on Ge and GaAs substrates, whose lattice constants are conveniently very close. The record efficiency for a lattice-matched MJSC is 43.5 % under concentration ($418 \times AM1.5D$) and was reported by Solar Junction [19] in 2012. Research is also being carried out on Si, GaSb [20] and InP substrates [21]. Figure 1.11 shows the band gap energy against the lattice parameter for typical III-V semiconductors.

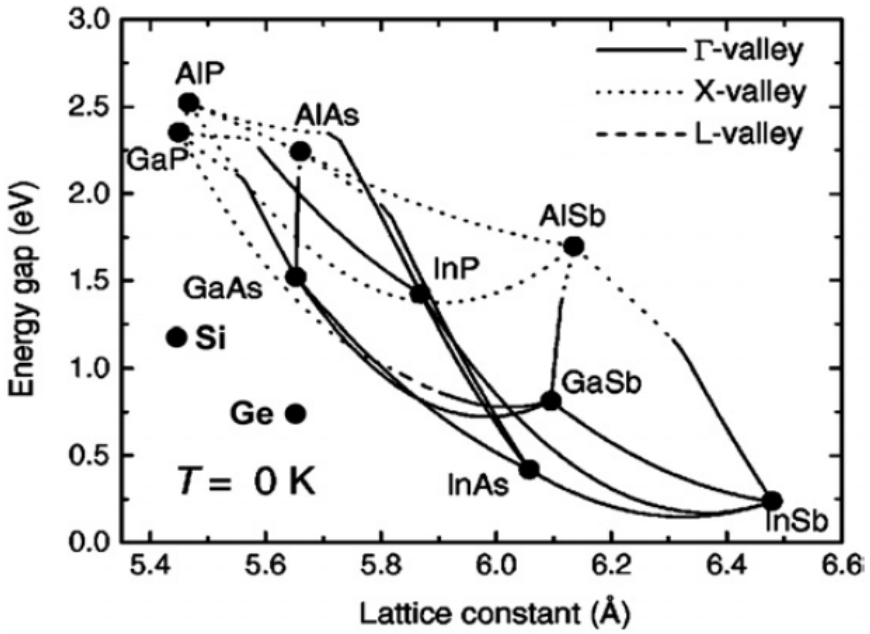

Figure 1.11: Energy band gap vs lattice parameter for common III-V semiconductors [22].

The wafer-bonding approach was developed between the Fraunhofer ISE, Soitec and the CEA-LETI. It consists in bonding cells with different lattice parameters that were grown separately and on different substrates. This technological process includes a mechanical polishing and a Ar sputtering of the wafers surface in order to decrease their roughness, followed by the surface-activated bonding that is triggered when the wafers are put under pressure. Using this technology, a cell with 46.1 % efficiency under concentrated sunlight ($312 \times AM1.5D$) was reported in 2016 [23].

The inverted metamorphic (IMM) growth method was invented by the NREL and relies both on lattice-matched and lattice-mismatched (metamorphic) junctions. Subcells are grown in the inverted way meaning that large band gap cells are grown first while the lowest band gap ones are grown at the end. In order to manage the difference in lattice parameters, compositionally graded buffers are grown, which prevents the threading dislocations to spread into the metamorphic subcells. Once the epitaxial growth is finished, the structure is flipped and mounted on a silicon handle. Its growth substrate is then removed by chemical etching to reveal the first grown / top cell. The NREL reported on a 47.1 % efficient MJSC under concentration ($143 \times AM1.5D$) in 2020, which remains today the world record for photovoltaic conversion efficiency [24].

We can see that wafer bonding and IMM growth techniques lead to higher efficiencies. This can be explained by the absence of the lattice-matching condition enabling the use of a wider panel of semiconductors. The architectures that can be obtained are thus closer to the optimal band gap combination. However, and despite their somewhat lower efficiencies, monolithic growth of lattice-matched structures remains the only approach used in the industry. Indeed, it doesn't require processing steps as critical as substrate transfer can be, and benefits from decades of epitaxial growth optimization. It is then industrially scalable and provides cheaper and more reliable cells compared to IMM and wafer-bonded devices.

1.2 Effect of space irradiation on solar cells

1.2.1 Space radiation environment

Generally speaking, space is a radiative and hostile environment. However, it cannot be considered as a homogeneous medium. Indeed, radiation is a general term that can refer to different energetic particles such as photons, electrons, protons or ions (alpha particles and heavier ions). These particles come from different radiation sources (see Figure 1.12) and travel through space with a kinetic energy that ranges from few eV to hundreds of GeV.

At the solar system scale, the Sun is the most important primary source of radiation as it constantly emits solar wind and produces solar flares. Besides, its activity is periodical and follows a nearly 11 years cycle alternating minimum

and maximum solar activities. On the one hand, the solar wind is a plasma originating from the Sun's corona and composed of low energy electrons, protons and alpha particles. On the other hand, solar flares are observable and punctual events that lead to the emission of high energy particles. They originate from the reorganization of magnetic field lines near sunspots, which releases a huge amount of magnetic stored energy.

Very high-energy particles can also come from outside the solar system: they are called galactic cosmic rays (GCR) and result from supernova explosions [25]. The most famous cosmic ray is the so-called "Oh my God" particle that was detected by the University of Utah in 1991 with an energy of 3.2×10^{20} eV [26]. Cosmic rays are mainly composed of protons (83 %) and alpha particles (13 %) but also of electrons (3 %) and of a large spectrum of heavy ions (1 %) [27]. They are very different from solar radiations in that they have a much lower flux but are significantly more energetic.

Last but not least are the Earth radiation belts also called the Van Allen belts. They consist of trapped particles in the Earth's magnetosphere that spiral along magnetic field lines from pole to pole. These belts have a toroidal shape stretching around the Earth and the inner and the outer belt can be distinguished. The inner belt extends from an altitude of 1000 to 12 000 km and contains both electrons and protons. The outer belt has an altitude that goes from 13 000 to 60 000 km and is made of high energy electrons.

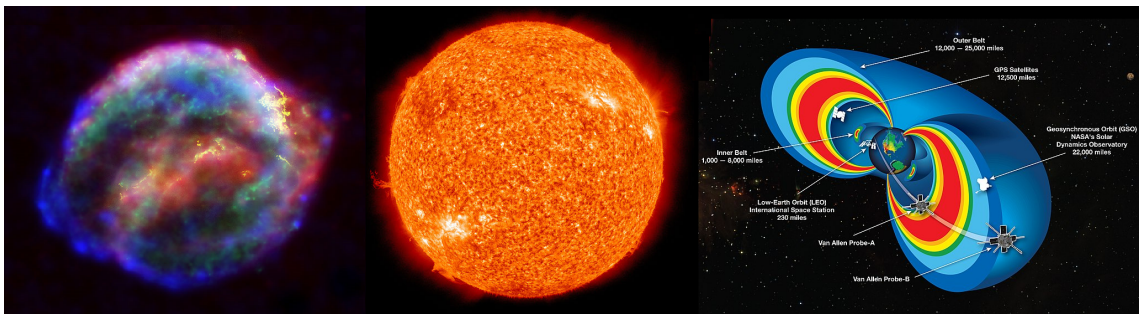

Figure 1.12: The main radiation sources. From left to right: A supernova remnant producing cosmic rays [28], the Sun responsible for solar flares and solar wind [29], the Earth's radiation belts also called Van Allen belts [30].

Table 1.2: Overview of the different radiation sources [27, 31, 32]

Radiation source	Particles	Energy	Fluxes ($cm^{-2}s^{-1}$)
Radiation belt	Electrons	1 keV-30 MeV	$10^2 - 10^7$
	Protons	1 keV-100 MeV	$10 - 10^6$
Solar wind	p^+, e^-, α	<1 keV	3.10^8
Solar flare	p^+, ions, γ rays	$1 - 10^3$ MeV	10^{10}
Cosmic rays	e^-, p^+, α, heavy ions	$1 - 10^{14}$ MeV	1 – 10

In addition to the radiative perspective, the space environment can be detrimental to satellites and spacecrafts through micrometeorite collisions, surface

contamination and electrostatic discharges (ESD). These phenomena can damage severely satellite parts such as solar arrays but are not in the framework of this thesis.

1.2.2 Radiation interaction with matter

As energetic as they are, space radiations can interact with matter in various ways. Thanks to both the magnetosphere and the atmosphere of our planet, high-energy radiations cannot reach its biosphere and interact with critical life features such as DNA. For the same reason, radiation is not a primary concern when engineering system for terrestrial applications [3]. However, the situation is different in space where satellites and spacecrafts constantly operate in a natural radiation environment. To predict the degradation rate and the possible failure of on-board components, we need to understand the underlying irradiation mechanisms. Depending on its energy and nature, the incident particle can interact with electronics materials in different ways.

- **Interaction with the electron cloud**

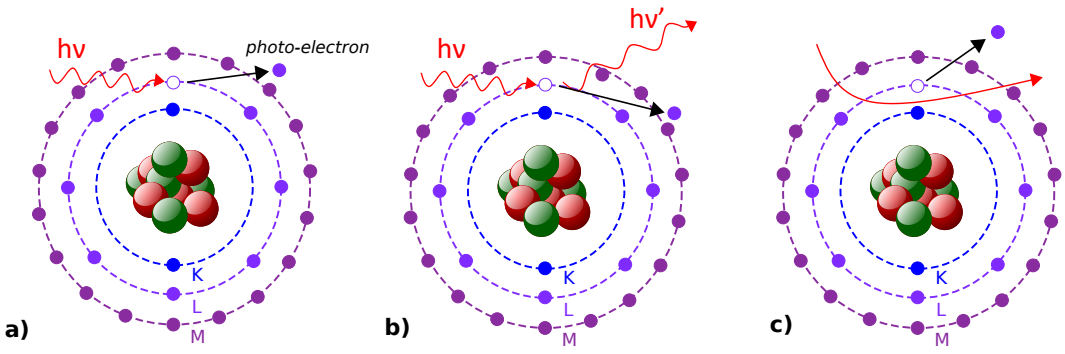

Figure 1.13: The main ionizing interactions occuring between an incident particle and the electron cloud. a) Photoelectric effect b) Compton effect c) electronic Coulombic interaction.

Photons and charged particles such as electrons and protons can interact with the electron cloud of atoms through different processes, generally leading to the ionization of the target atom. When the incident particle is a photon, this ionization can simply result from the photoelectric effect, but also from Compton or Rayleigh diffusion processes. On the other hand, charged particles interact with the electron cloud through Coulombic interactions. Depending on the charge of the incident particle, this interaction can be attractive or repulsive and can either way result in ionization. As particles interact with electron clouds, they lose kinetic energy. This energy loss is transferred to the lattice and is defined as the

[3] To be precise, there are few terrestrial structures where radiation is of critical importance such as nuclear reactors or particle colliders.

total ionizing dose (TID). This latter can be calculated as the multiplication of the particle fluence and the electronic stopping power of the material called the linear energy transfer (LET). While the ionization induced by irradiation can be troublesome for microelectronics (total ionizing dose and single-event effects), for biological matter (especially astronauts) and for devices relying on dielectric and polymers, it does not cause much concern for solar cells.

- **Interaction with the atomic nucleus**

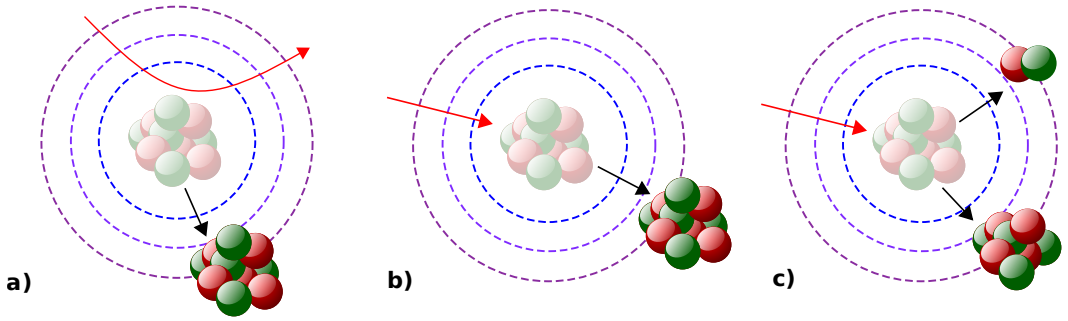

Figure 1.14: The main non-ionizing interactions occuring between an incident particle and an atomic nucleus. a) nuclear Coulombic interaction b) nuclear elastic interaction c) nuclear inelastic interaction (spallation).

Although most of the interactions between particles and atoms occurs through ionizing processes, the remaining non-ionizing interactions are the ones detrimental to the solar cells. High energy photons (E > 1 MeV / λ < 1.2 pm, i.e. gamma rays) can interact with atomic nuclei through two different processes: pair production and photodisintegration. On the one hand, pair production happens when a photon is absorbed by a nucleus, which in turns emits a positron and an electron, whose total kinetic energy equals the energy of the absorbed photon. On the other hand, photodisintegration takes place when a high energy photon is absorbed by a nucleus, which then decays in one or several nucleons.

Regarding other particles, they can interact with the atomic nucleus through three different mechanisms. As it was the case with the electron clouds, charged particles and nuclei can be subject to Coulombic interactions, possibly resulting in the displacement of an atom from its original site. A high-energy particle can also directly collide with an atomic nucleus and eject it from its lattice site: this process is called the nuclear elastic interaction. Finally, the incident particle can be absorbed by a nucleus that then reaches an unstable state and decomposes during its de-excitation process. This last mechanism is called nuclear inelastic interaction or nuclear spallation. A high initial energy is required for incident charged particles to interact with the nucleus since they will lose energy through Coulombic interactions before reaching it. However, Coulombic interactions will not take place with neutral particles such as neutrons, which will more easily react with the nucleus.

Similarly to the ionizing dose that we defined for interaction with the electron cloud, we can introduce the displacement damage dose (DDD) that results from non-ionizing processes. In most cases, the DDD can be calculated as the product of the fluence and the nuclear stopping power called the Non-Ionizing Energy Loss (NIEL). The NIEL is usually found in MeV.cm^2 but, dividing it by the material density, it can also be given as the mass stopping power NIEL$_m$ expressed in MeV.cm^2/g. The NIEL is an important parameter when assessing the impact of the irradiation on solar cells as it relates the particle fluence to the DDD which can in turn be related to the degradation factors of the main photovoltaic parameters (V_{oc}, J_{sc}, FF). The NIEL's value depends on the atomic density η of the irradiated material, its threshold displacement energy E_t and the cross-section σ corresponding to the interaction between the incident particle and a lattice nucleus. It also depends on the Lindhard partition function L that calculates the part of the energy that is actually used to displace atoms [33]. Taking E as the energy, the NIEL can be expressed as:

$$NIEL = \eta \int_{E_t}^{E_{max}} \frac{d\sigma}{dE} L(E)\, dE \tag{1.6}$$

The threshold displacement energy E_t is the minimal energy required to displace an atom from its crystalline site. It is typically higher than the cohesive energy of the material. In the "sudden approximation" it can be simply calculated as the recoil energy of the knocked atom required to overcome its surrounding potential barrier [34]. Table 1.3 shows the threshold energies for typical semiconductors.

Table 1.3: Threshold displacement energy for typical semiconductors

Material	E_t	**Reference**
Si	21 eV	Corbett1966 [35]
Ge	21 eV	Holmström2010 [36]
GaAs	Ga sublattice 10 eV	Lehmann1993 [37]
	As sublattice 10 eV	Hausmann1996 [38]

As we can see in equation 1.6, the NIEL's value depends on the energy of the incident particle. As this particle interacts with the irradiated material, it loses energy which means that its associated NIEL changes. This evolution needs to be taken into account to understand the damage profile in a material as different particles have a different energy dependence in their NIEL. For instance, the NIEL of electrons decreases as they slow down in the matter whereas the protons exhibit the opposite behaviour (Figure 1.15). This means that, unlike the electrons, the protons tend to add more displacement damage at the end of their course.

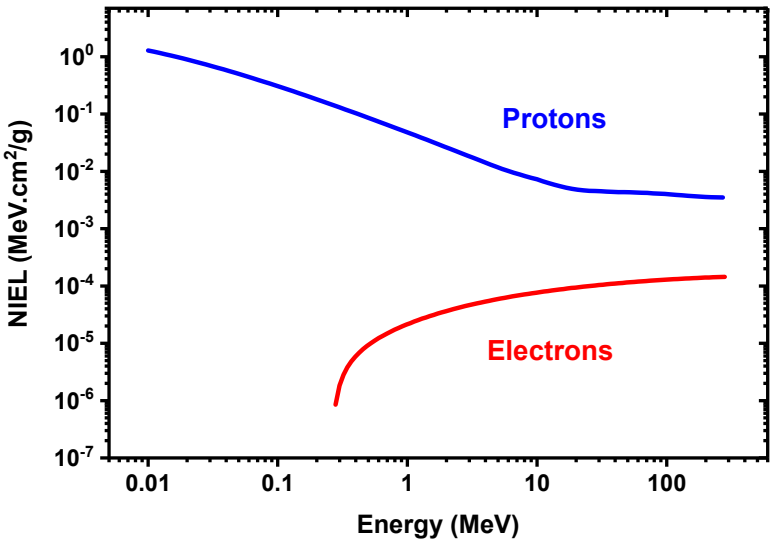

Figure 1.15: NIEL for electrons and protons in GaAs calculated with NEMO codes [39].

1.2.3 Defects introduction

As non-ionizing processes are occurring and atoms are being displaced from their lattice sites, the crystal defect density increases. Depending on the energy that is transferred from the incident particle to the primary knock-on atom (PKA), it can result in different defect configurations [40]. If we consider only binary collisions, the number of displaced atoms can be calculated with the Kinchin-Pease (KP) model as [41]:

$$N(Q) = \begin{cases} 0 & \text{if } Q < E_t \\ 1 & \text{if } E_t < Q < 2E_t \\ \frac{E}{2E_t} & \text{if } 2E_t < Q < \infty \end{cases} \tag{1.7}$$

In this equation, Q is the remaining particle energy after accounting for the energy lost to electronic stopping power E_e.

$$Q = E_0 - E_e \tag{1.8}$$

After conducting computer simulations relying on the binary collision approximation, Norgett, Robinson and Torrens proposed a modified equation (the NRT equation) that takes into account potential recombination processes [42]:

$$N(Q) = \begin{cases} 0 & \text{if } Q < E_t \\ 1 & \text{if } E_t < Q < \frac{2E_t}{0.8} \\ \frac{0.8E}{2E_t} & \text{if } \frac{2E_t}{0.8} < Q < \infty \end{cases} \tag{1.9}$$

For an energy Q lower than the displacement threshold, the PKA will not be ejected from its site ($N = 0$). For an energy higher than E_t but lower than $\frac{2E_t}{0.8}$, the PKA will be displaced without however being able to knock a second atom from its crystal site. As represented in Figure 1.16, it will typically result in a Frenkel pair composed of a vacancy and an interstitial defect. If the energy transferred from the incident particle to the PKA is higher than the displacement threshold (*i.e.* if $Q > \frac{2E_t}{0.8}$), a secondary knock-on atom (SKA) will be ejected from its site.

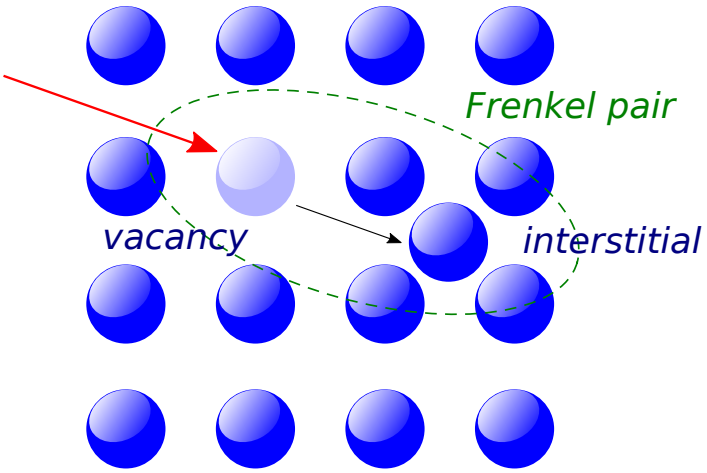

Figure 1.16: Formation of a Frenkel defect induced by a non-ionizing interaction.

For energies transferred to the PKA significantly higher than the displacement threshold (E>1 keV), a cascade of defects will spread in the material. The formation of more complex defects such as double interstitials, double vacancies or defect clusters will also be possible. For energies even higher (E>10 keV), a damage profile presenting multiple subcascades will appear (Figure 1.17).

In addition to the damage resulting from the collision of atoms, the incident particle usually brings a lot of thermal energy to the lattice. This suddenly increases the local temperature of the material in a process called the "thermal spike" that occurs in a femtosecond lap of time. The temperature increase can then be so high that the material locally reaches its melting point which then partially leads to its amorphization after cooling down. On the other hand, the thermal spike mechanism can also locally enhance the atomic diffusion and promote defect recombination (defect annealing) [44, 45]. The annealing of defects can also result from the so-called "radiation enhanced diffusion" mechanism, which typically occurs when irradiation creates vacancies in the lattice [44, 46].

Even though the basic mechanisms of defects formation and defects curing are essentially the same for all the semiconductors, a special attention should be paid to compound semiconductors such as GaAs. Indeed, the atomic structure of GaAs is called "Zincblende" and involves gallium and arsenic atoms distributed in two interpenetrating face-centered cubic lattices. Another type of point defect called "antisite" can then appear if the PKA is a Ga atom (respectively As atom) and replaces an As SKA (respectively Ga). Moreover, the antisite defects can be charged (As^{+}_{Ga}, Ga^{-}_{As}) and act as coulombian scattering centers in the lattice

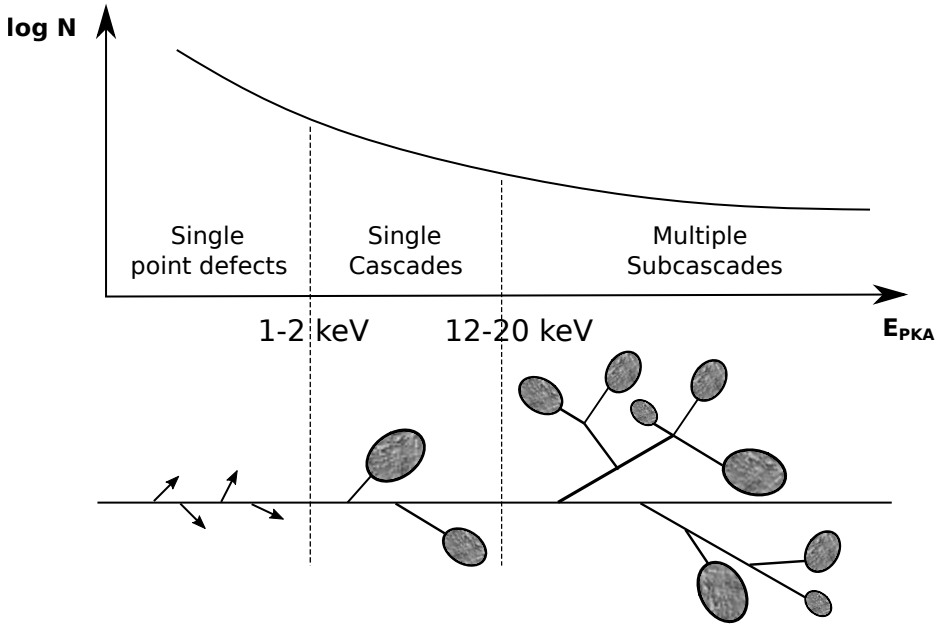

Figure 1.17: Single defects and cascades configuration as a function of the energy of the PKA (inspired from [43]).

[47]. Furthermore, compound semiconductors made of atoms with a large mass difference will exhibit different energy thresholds depending on the nature of the PKA. This is for instance the case for GaN for which $E_{t,Ga} > E_{t,N}$ [48]. On the contrary, the Ga and As atoms have roughly the same mass leading to a very similar displacement energy (see Table 1.3).

1.2.4 Degradation of the solar cell properties

As we mentioned in the first section of this chapter, conventional solar cells are *pn* junctions that can separate the photocarriers through diffusion and drift mechanisms. In the majority of the solar cell architectures, the contribution of drift is negligible compared to diffusion. Assuming a perfectly passivated surface and a uniform carrier generation, the current density of a solar cell in a diffusion regime with no external bias (short-circuit condition) can be calculated as [49]:

$$J_{sc} = qG(L_n + L_p) \tag{1.10}$$

L_n and L_p are the minority carrier diffusion lengths and G is the carrier photogeneration rate. This equation shows that only the carriers photogenerated up to the minority carrier diffusion length from the p/n interface can be collected. Having a long diffusion length is then crucial to obtain high photocurrent. The diffusion length of a minority carrier depends itself on its diffusion coefficient D and on its lifetime τ.

$$L_{n,p} = \sqrt{D_{n,p}.\tau} \tag{1.11}$$

Furthermore, the diffusion coefficient can be related to the temperature and the mobility of the carrier μ through the Einstein relation:

$$D_{n,p} = \frac{\mu_{n,p} kT}{q} \tag{1.12}$$

The carrier mobility is dependent on impurity and defect concentrations. It is also temperature-dependent as carriers are affected by lattice scattering (phonons). Having this expression of the diffusion coefficient, the photocurrent can be written as a function depending on both the minority carrier lifetimes and their mobilities.

$$J_{sc} = qG\left(\sqrt{\frac{kT}{q}\mu_n\tau_n} + \sqrt{\frac{kT}{q}\mu_p\tau_p}\right) \tag{1.13}$$

It is now important to notice that for a given generation rate G, the short-circuit current of a solar cell depends only on μ and τ (under the assumptions made earlier). Under irradiation, these materials properties are usually degraded because of the creation of crystal defects. Indeed, these defects introduce energy states in the material band gap which promotes non-radiative recombination and consequently decreases the minority carrier lifetime τ. The global minority carrier lifetime depends on the recombination rates of non-radiative and radiative processes:

$$\frac{1}{\tau} = \frac{1}{\tau_{rad}} + \frac{1}{\tau_{SRH}} + \frac{1}{\tau_{surf}} + \frac{1}{\tau_A} \tag{1.14}$$

Here, τ_{rad}, τ_{SRH} are the lifetimes respectively associated to the band-to-band radiative recombination and to the bulk non-radiative recombination (SRH). τ_{surf} and τ_A represent the lifetimes related to surface and Auger recombination. In addition, the irradiation induced-defects also degrade the carrier mobility as μ depends itself on the mean time between collisions τ_c, which is reduced by defect scattering. In the following mobility expression, $m*$ is the effective carrier mass:

$$\mu_n = \frac{q\tau_c}{m_e^*} \qquad \mu_p = \frac{q\tau_c}{m_h^*} \tag{1.15}$$

This defect scattering coupled with the decrease of the minority carrier lifetime explains why the diffusion length, and therefore the photocurrent, decreases during irradiation. In the photocurrent expression that we have just developed, it is assumed that the solar cell relies only on diffusion transport. However, in *pn* solar cells with a low base doping concentration and in *pin* architecture, the

depletion region is wide and the drift can no longer be neglected. The current density collected by electrical drift (field aided collection) can be expressed as [50]:

$$J_{drift} = q(n\mu_n + p\mu_p)E_{bi} \tag{1.16}$$

In this equation, E_{bi} is the built-in electric field equal to the built-in potential divided by the width of the depletion region. We can notice that this drift component relies strongly on the carrier mobility and will also be affected by the introduction of defects during irradiation.

As an illustration purpose, the mobility and the lifetime of electrons and holes in molecular beam epitaxy (MBE) grown-GaAs are given in Table 1.4 (T=300 K). It is important to consider that these parameters are very much temperature and doping-dependent [47]. They also largely depend on the growth technique that was used to obtain the GaAs crystal.

Table 1.4: Carrier mobility and lifetime in MBE-grown GaAs [47, 51]

Minority carrier	**Doping level (cm^{-3})**	**Mobility ($cm^2/V.s$)**	**Lifetime (ns)**
electron	$n = 10^{17}$	8000	100
hole	$p = 10^{17}$	400	30

Under irradiation, these values are expected to decrease as defects are introduced. Moss et al. measured the impact of electron irradiation on the minority carrier lifetime in n-type GaAs ($n = 3.5 \times 10^{16}\ cm^{-3}$) performing time-resolved photoluminescence (TRPL) on AlGaAs-GaAs-AlGaAs double heterostructures [52]. Figure 1.18 shows the evolution of the carrier lifetime with 1 MeV electron fluence. On the other hand, Dresner reported n-type GaAs mobility values dropping from 6400 to 443 $cm^2/V.s$ after 1.65×10^{15} cm^{-2} 1 MeV electron irradiation [53].

The open-circuit voltage V_{oc} is also directly affected by the introduction of defects in the crystal. Indeed, this parameter depends greatly on the dark saturation current I_0 as shown in the following equation [50]:

$$V_{oc} = \frac{kT}{q}\ln\left(\frac{I_{ph}}{I_0} + 1\right) \tag{1.17}$$

The dark saturation current I_0 increases when the carrier generation-recombination rate is enhanced by deep-level defects. This consequently leads to the decrease of the open-circuit voltage of the solar cells.

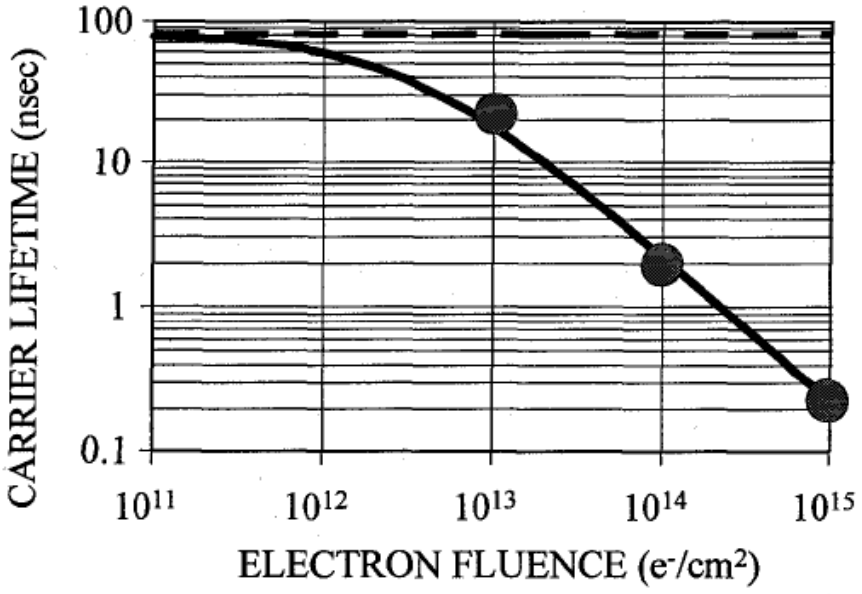

Figure 1.18: Room temperature minority carrier lifetime vs. total 1 MeV electron fluence [52]. The dashed line represents the pre-irradiation lifetime.

1.2.5 Degradation rate modelling

Two methods exist to predict the degradation rate of solar cells under space irradiation.

- **The JPL equivalent damage approach**

The Jet Propulsion Laboratory (NASA) first developed an experimental method to study the degradation occurring in solar cells under irradiation. They observed that the degradation rate depends on the type and the energy of the incident particule and proposed to calculate *relative damage coefficients* (RDC) [54]. The RDC relate the degradation of a photovoltaic parameter (I_{sc}, V_{oc}, FF...) under electrons and protons of a given energy E with the degradation caused by 1 MeV electrons or 10 MeV protons:

$$RDC_e(E) = \frac{\phi(1MeV)}{\phi(E)} \qquad RDC_p(E) = \frac{\phi(10MeV)}{\phi(E)} \tag{1.18}$$

As an exemple, having $RDC_e(E)=0.1$ implies that it takes 10 electrons with energy equal to E to cause as much degradation as a single 1 MeV electron. Multiple experimental irradiation studies are then required to obtain RDC for different energies and particles. Typically, the degradation of solar cells is measured for 8 proton and 4 electron energies [55, 56].

The JPL equivalent damage method is mature and gives reliable empirical

data on the solar cells degradation rate. However, it is expensive and requires a lot of beam time in irradiation facilities.

- **The NRL displacement damage dose approach**

Scientists at the Naval Research Laboratory noted that the degradation of the solar cells could be expressed as a function of the displacement damage dose DDD introduced in Section 1.2.2 [57]. The NIEL of the material for the incident particle energy is calculated and the remaining factors can be plotted against the DDD. In most cases, the remaining factors for different energies at different fluences collapse in a single degradation curve which can be fitted with the following expression [58]:

$$RF(X) = 1 - C.log(1 + \frac{DDD}{D_x}) \tag{1.19}$$

where $RF(X)$ is the remaining factor of a photovoltaic parameter X, and $(C;D)$ are fit parameters.

Some materials exhibit a non-linear dependency of electron damage coefficient on the NIEL leading to different $RF=f(DDD)$ profiles. To address this behaviour, a 1 MeV electron effective dose can be calculated:[4]

$$DDD_{eff} = DDD(E) \times (\frac{NIEL(E)}{NIEL(1MeV)})^{n-1} \tag{1.20}$$

where n is an exponential index >1 that is tuned to superimpose degradation curves.

Considering a linear relation between the DDD and the NIEL for protons and a possibly non-linear relation for electrons, the NRL approach requires only three irradiations (1 proton and 2 electron energies) to predict the degradation of solar cells in space environment. Messenger et al. showed that the NRL method gives results very similar to what can be obtained with the JPL approach, at the notable exception of crystalline silicon solar cells [58]. The NRL displacement damage dose method is then more convenient as it requires less ground-test irradiations to calculate remaining factors.

1.2.6 Irradiation setups for radiation testing

The impact of the space radiations on solar cells and other satellite parts is usually simulated in ground-based facilities. As mentioned in Section 1.2.1, the

[4] 1 MeV electrons were chosen to define an effective dose since they represent a standard in the JPL method and in the space community.

energy of the charged particles encountered in space varies from few keV to thousands of MeV. The particle accelerators used to represent space environment need then to cover this energy range. Furthermore, we saw in Section 1.2.2 that the NIEL variation with energy differs from one particle to another, meaning that devices should ideally be tested under multiple particle irradiation. Studies are usually conducted under electrons and protons exposition as they account for the large majority of space radiations.

Several technologies exist to accelerate particles, the most famous one being the synchrotron which is an *electromagnetic* particle accelerator often used for particle physics experiment. The most iconic synchrotron is the Super Proton Synchrotron (SPS) used at CERN to feed 450 GeV protons to the Large Hadron Collider (LHC) [59]. While synchrotrons are indispensable to obtain very high energy particles, they are extremely large structures that require high investment and a high level of maintenance. A more adequate technology to simulate space radiations is the *electrostatic* accelerator which relies on electric fields to accelerate particles.

There are two main types of electostatic particle accelerator: the Cockroft-Walton (CW) and the Van de Graaff (VdG) generators. CW accelerators are electrical circuits made of a cascade of voltage multiplier elements based on capacitors and diodes. It transforms low-voltage AC into high voltage DC output. This type of accelerator is usually found in a Dynamitron configuration where a RF oscillator is coupled to the circuit to enhance the potential build-up [60].

In VdG generators, an insulator conveyor belt (typically made of rubber) is used to transfer electrical charges from a high voltage electrode to a hollow metallic conductor (called *terminal*). As the belt keeps on rotating and transferring charges, a high potential builds up in the hollow conductor. Charged particles can then be accelerated through the difference of potential between the terminal and the ground, creating a radiation beam. The hollow conductor is generally filled with SF_6 atmosphere as this gas exhibits a very high dielectric constant.

Two upgrades of the VdG generator can commonly be encountered: the tandem and the pelletron configuration. In a tandem generator, negative ions are first accelerated between ground and terminal levels before passing through a *stripper* material. This material strips away electrons from the accelerated anions which, as a result, changes their charge sign (making them cations). The ions are then accelerated a second time leading to an effective energy twice higher than for regular VdG generators[5]. In a pelletron generator, the conveyor belt is replaced by a chain of metal pellets connected by insulating links. Unlike the conveyor belt in VdG generators, the pellets charge through induction interactions which reduces a lot their deterioration by wearing. Pelletron generators usually display high voltage stability and long life time [61].

The main irradiation setups used to study the impact of space radiations on solar cells are listed in Table 1.5.

[5]The multiplication gain can actually be higher for ions with greater oxidation states.

Table 1.5: Review of the main irradiation setups used for solar cell radiation testing.

Lab/Company	City	Country	Accelerator type	Particule	Energy	Beam current	Ref
NIST	Gaithersburg	USA	VdG	electron			[62]
JAEA	Takasaki	Japan	VdG	electron	1-2 MeV		[63]
TU Delft	Delft	Netherlands	VdG	electron	3 MeV		[64]
ONERA	Toulouse	France	VdG	electron, proton	2.5 MeV	20-50 μA (source)	[65]
LSI	Palaiseau	France	Pelletron	electron	0.15 - 2.5 MeV	10 nA-50 μA	[66]
IPN	Orsay	France	Tandem	proton	15 MeV		[67]
JPL	Pasadena	USA	Dynamitron	electron	0.5 - 2.5 MeV	10^8 – 10^{12} e/cm^2/s	[68]
Neo Beam	Middlefield	USA	Dynamitron	electron	0.7 - 5 MeV	1-50 mA	[69]
Boeing	Seattle	USA	Dynamitron	electron, proton	0.01 - 2.5 MeV	3.10^{11}e/cm^2/s - 10^{10}p/cm^2/s	[70]
KFA Jülich	Jülich	Germany		electron			[71]
Toyota Tech Inst	Nagoya	Japan	CW	electron			[72]
CNEA	Buenos Aires	Argentina	Tandem	electron, protons	20 MeV		[73]
RADEF	Jyväskylä	Finland	Tandem Pelletron	proton	1.7 MeV		[74]
XTIPC	Urumqi	China	Tandem	electron, proton	e: 1MeV, p: 3MeV		[75]

1.2.7 State of the art on solar cell degradation

The degradation of solar cells under irradiation is usually plotted as the J_{sc}, V_{oc}, FF or P_{max} remaining factors vs the particle fluence or the calculated DDD. Yamaguchi reported in 1995 a review of solar cells irradiation-induced degradation for different semiconductors materials [72]. The degradation of the output power of III-V and Si solar cells under 1 MeV electron irradiation is plotted in Figure 1.19.

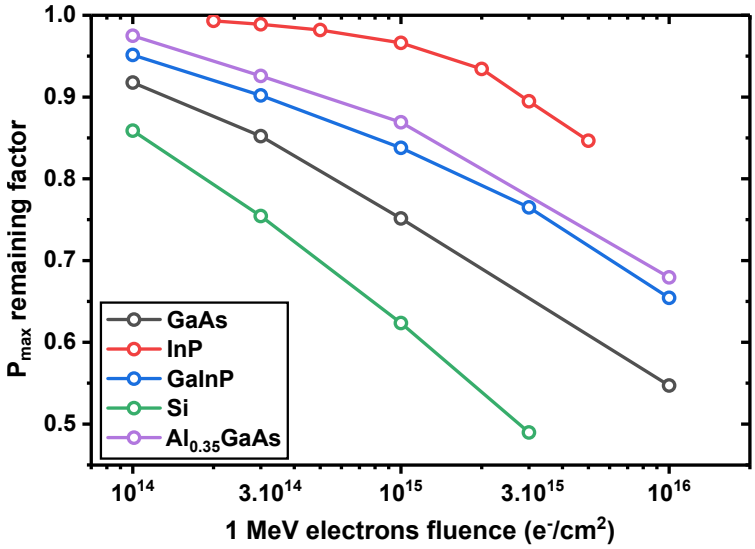

Figure 1.19: Degradation of solar cells output power with 1 MeV electron fluence (data from [72]).

It can first be noticed that the degradation rate is very different from one type of material to another. However, special care needs to be taken when interpreting the solar cell radiation hardness depicted in Figure 1.19. Indeed, it can arise from the intrinsic radiation resistance of the material itself as it is the case for InP-based solar cells: InP was shown to exhibit a very low degradation factor because the defects introduced through irradiation are annealed at room temperature and under illumination [76].

$CuInSe_2$ (CIS) cells are found to be extremely radiation resistant as they virtually do not degrade after $5{\times}10^{15}$ 1 MeV e^-/cm^2 [72]. The radiation hardness of these cells can be explained by the higher optical absorption coefficient of CIS compared to other materials. The thickness of the active region of the CIS solar cells can then be reduced while achieving complete light absorption. Doing so, the photocarriers do not need to diffuse over long distances to be collected, which means that the decrease in the minority carrier diffusion length is not as detrimental as for other cells. The very same phenomenon was observed for ultra-thin GaAs solar cells relying on a 80 nm active region and light trapping structures [77].

A low absorption coefficient is then problematic for a space solar cell because

it implies the need for thick active region structures requiring long minority carrier diffusion lengths. This explains the low radiation hardness of silicon solar cells as depicted in Figure 1.19. Indeed, Si is an indirect-gap semiconductor that consequently exhibits a low absorption coefficient.

Multijunction solar cells have also been extensively tested for radiation hardness as they are widely used in space applications. Figure 1.20 shows the global degradation of the output power of commercial GaInP/GaAs/Ge triple junction solar cells.

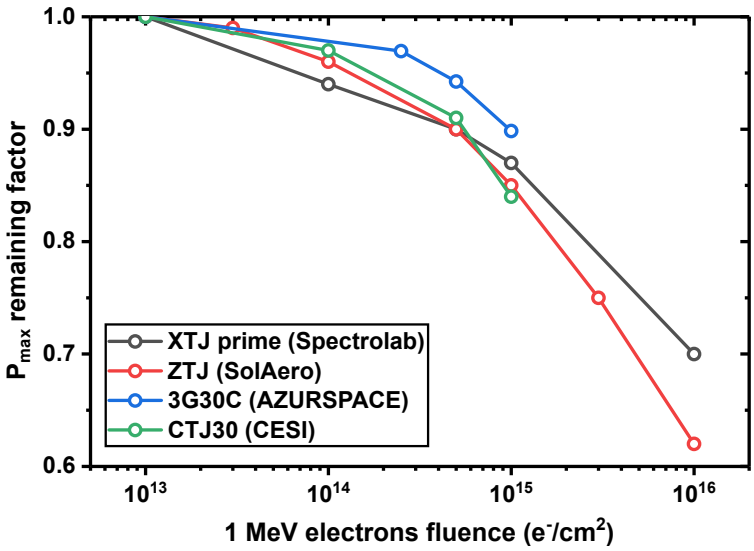

Figure 1.20: Degradation of the output power of commercial 3J solar cells with 1 MeV electron fluence (data from [14, 15, 16, 17]).

The P_{max} remaining factor is very similar from one manufacturer to another. It corresponds to the *global* degradation of the MJSC and does not give precise information concerning the material degradation of the subcells. A special attention should yet be paid to understand and quantify the subcell degradation. Indeed, it is important to determine which cell will be the current-limiting one for a given radiation exposure to mitigate the power loss. To get access to subcells degradation, irradiation studies were conducted on triple junction and on their component solar cells [78, 79]. Park et al. demonstrated that the distribution of defects in irradiated 3J was non-uniform and that this distribution depended on the evolution of the NIEL with the particle energy [78, 80].

Recently, two irradiation studies were conducted on perovskite solar cells (PSC) as this technology is developing extremely fast. Miyazawa et al. reported on PSC with high remaining factors under 1 MeV electron irradiation [81]. Their cells demonstrated a P_{max} remaining factor equals to 0.92 for a 10^{16} e^-/cm^2 fluence. On the other side, Song et al. reported a lower remaining factor ($RF(P_{max})$ = 0.59 after 1.3×10^{15} e^-/cm^2 1 MeV electrons) and found that the transmittance of the glass encapsulation decreased under irradiation (cover glass darkening) [82]. It is likely that the degradation rate of PSC depends on its composition and on its

BOL efficiency. Further work should be carried out to describe the nature of the irradiation-induced defects and correlate it with the PSC degradation.

Chapter 1 conclusion

We have shown in this chapter that the state of the art technology in space photovoltaics is the multi-junction solar cell architecture. Stacking-up subcells with different band gap energies allows indeed to reach higher power to mass ratio which is highly desirable for space applications. Moreover, we have described the deterioration that a solar cell undergoes when exposed to space radiation. Special care should be taken with MJSC as the degradation of one individual subcell can cause large power loss to the whole structure.

The elements developed in this chapter indicate that new materials need to be radiation-tested before they can be implemented in MJSC. In order to overcome the 30 % efficiency of GaInP/GaAs/Ge 3J cells, alternative III-V semiconductors need to be developed and characterized under space representative irradiation. In the next chapter we will focus on a promising alloy for space MJSC integration: the dilute nitride InGaAsN.

Bibliography

[1] E. Becquerel, "Mémoires sur les effets électriques produits sous l'influence des rayons solaires," *Comptes rendus de l'académie des sciences*, vol. 9, p. 561, 1839.

[2] D. M. Chapin, C. S. Fuller, and G. L. Pearson, "A new silicon p-n junction photocell for converting solar radiation into electrical power," *Journal of Applied Physics*, vol. 25, no. 5, pp. 676–677, 1954.

[3] S. Philipps and W. Warmuth, "Photovoltaics Report 2019." Fraunhofer ISE, Tech. Rep. November, 2019.

[4] A. W. Bett, S. P. Philipps, S. S. Essig, S. Heckelmann, R. Kellenbenz, V. Klinger, M. Niemeyer, D. Lackner, and F. Dimroth, "Overview about technology perspectives for high efficiency solar cells for space and terrestrial applications," *28th European Photovoltaic Solar Energy Conference and Exhibition*, vol. 0, pp. 1–6, 2013.

[5] NASA, "Nasa space science data coordinated archive: Vanguard 1." [Online]. Available: https://nssdc.gsfc.nasa.gov/nmc/spacecraft/display.action?id=1958-002B

[6] G. Strobl, G. LaRoche, K.-D. Rasch, and G. Hey, "From Extraterrestrial to Terrestrial Applications," in *High-efficient low-cost photovoltaics: recent developments*. Springer, 2009, ch. 2, pp. 7–27.

[7] S. Bailey and R. Raffaelle, "Space Solar Cells and Applications," in *Solar Cells and Their Applications*. Wiley, 2010, ch. 18, pp. 396–424.

[8] V. M. Andreev, V. R. Larionov, V. D. Rumyantsev, O. M. Fedorova, and S. S. Shamukhamedov, "pAlGaAs–pGaAs–nGaAs solar cells with efficiencies of 19% at AM0 and 24% at AM1.5," *Sov. Tech. Phys. Lett. (Engl. Transl.); (United States)*, vol. 9:10, 1983.

[9] Z. I. Alferov, V. M. Andreev, and V. D. Rumyantsev, "Solar photovoltaics: Trends and prospects," *Semiconductors*, vol. 38, no. 8, pp. 899–908, 2004.

[10] NASA, "International Space Station Solar Array Bifacial Electrical Performance Model Developed." [Online]. Available: https://ntrs.nasa.gov/archive/nasa/casi.ntrs.nasa.gov/20050215028.pdf

[11] ——, "About the space station solar arrays." [Online]. Available: https://www.nasa.gov/mission_pages/station/structure/elements/solar_arrays-about.html

[12] P. K. Chiang, J. H. Ermer, W. T. Nishikawa, D. D. Krut, D. E. Joslin, J. W. Eldredge, B. T. Cavicchi, and J. M. Olson, "Experimental results of GaInP2/GaAs/Ge triple junction cell development for space power systems," *Conference Record of the IEEE Photovoltaic Specialists Conference*, pp. 183–186, 1996.

[13] C. Fetzer, B. Jun, K. Edmondson, S. Khemthong, K. Rouhani, R. Cravens, R. Bardfield, and M. Gillanders, "Production ready 30% efficient triple junction space solar cells," *Conference Record of the IEEE Photovoltaic Specialists Conference*, 2008.

[14] Spectrolab, "Spectrolab datasheets," 2021. [Online]. Available: https://www.spectrolab.com/support.html#datasheets

[15] SolAero, "Ztj space solar cell," 2018. [Online]. Available: https://solaerotech.com/wp-content/uploads/2018/04/ZTJ-Datasheet-Updated-2018-v.1.pdf

[16] AZURSPACE, "Space solar cells," 2021. [Online]. Available: http://www.azurspace.com/index.php/en/products/products-space/space-solar-cells

[17] CESI, "Triple-Junction Solar Cell for Space Applications (CTJ30)." [Online]. Available: https://www.cesi.it/app/uploads/2020/03/Datasheet-CTJ30-1.pdf

[18] NREL, "Best research-cell efficiency chart," 2020. [Online]. Available: https://www.nrel.gov/pv/assets/pdfs/best-research-cell-efficiencies.20200104.pdf

[19] D. Derkacs, R. Jones-Albertus, F. Suarez, and O. Fidaner, "Lattice-matched multijunction solar cells employing a 1 eV GaInNAsSb bottom cell," *Journal of Photonics for Energy*, vol. 2, no. 1, pp. 021 805–1, 2012.

[20] J. Kret, J. Tournet, S. Parola, F. Martinez, D. Chemisana, R. Morin, M. de la Mata, N. Fernández-Delgado, A. Khan, S. Molina, Y. Rouillard, E. Tournié, and Y. Cuminal, "Investigation of AlInAsSb/GaSb tandem cells – A first step towards GaSb-based multijunction solar cells," *Solar Energy Materials and Solar Cells*, vol. 219, p. 110795, 2021. [Online]. Available: https://www.sciencedirect.com/science/article/pii/S0927024820303949

[21] M. S. Leite, R. L. Woo, J. N. Munday, W. D. Hong, S. Mesropian, D. C. Law, and H. A. Atwater, "Towards an optimized all lattice-matched InAlAs/InGaAsP/InGaAs multijunction solar cell with efficiency> 50%," *Applied Physics Letters*, vol. 102, no. 3, p. 033901, 2013.

[22] H. Cotal, C. Fetzer, J. Boisvert, G. Kinsey, R. King, P. Hebert, H. Yoon, and N. Karam, "III-V multijunction solar cells for concentrating photovoltaics," *Energy and Environmental Science*, vol. 2, no. 2, pp. 174–192, 2009.

[23] F. Dimroth, T. N. Tibbits, M. Niemeyer, F. Predan, P. Beutel, C. Karcher, E. Oliva, G. Siefer, D. Lackner, P. Fus-Kailuweit, A. W. Bett, R. Krause, C. Drazek, E. Guiot, J. Wasselin, A. Tauzin, and T. Signamarcheix, "Four-junction wafer-bonded concentrator solar cells," *IEEE Journal of Photovoltaics*, vol. 6, no. 1, pp. 343–349, 2016.

[24] J. F. Geisz, R. M. France, K. L. Schulte, M. A. Steiner, A. G. Norman, H. L. Guthrey, M. R. Young, T. Song, and T. Moriarty, "Six-junction III-V solar cells with 47.1% conversion efficiency under 143 Suns concentration," *Nature Energy*, vol. 5, no. 4, pp. 326–335, 2020. [Online]. Available: http://dx.doi.org/10.1038/s41560-020-0598-5

[25] M. Ackermann, M. Ajello, A. Allafort, L. Baldini, J. Ballet, G. Barbiellini, M. Baring, D. Bastieri, K. Bechtol, R. Bellazzini *et al.*, "Detection of the characteristic pion-decay signature in supernova remnants," *Science*, vol. 339, no. 6121, pp. 807–811, 2013.

[26] S. Webb, *The 'Oh my God' particles*. Springer New York, 2012, pp. 135–158.

[27] S. Bourdarie and D. Boscher, "Space radiation environment," in *Space Radiation Environment and its Effects on Spacecraft Components and Systems*. Cepadues, 2005, ch. I-02, pp. 57–83.

[28] NASA, "Supernova remnant turns 400." [Online]. Available: https://www.nasa.gov/multimedia/imagegallery/image_feature_219.html

[29] ——, "The Sun by the Atmospheric Imaging Assembly of NASA's Solar Dynamics Observatory." [Online]. Available: https://sdo.gsfc.nasa.gov/assets/img/browse/2010/08/19/20100819_003221_4096_0304.jpg

[30] ——, "Radiation belts with satellites." [Online]. Available: https://www.nasa.gov/mission_pages/sunearth/news/gallery/20130228-radiationbelts.html

[31] W. Feldman, J. Asbridge, S. Bame, and J. Gosling, "High-speed solar wind flow parameters at 1 au," *Journal of Geophysical Research*, vol. 81, no. 28, pp. 5054–5060, 1976.

[32] P. Lantos, "The sun, the solar wind and their effects on the earth's environment," in *Space Radiation Environment and its Effects on Spacecraft Components and Systems*. Cepadues, 2005, ch. I-01, pp. 13–56.

[33] J. Lindhard, V. Nielsen, M. Scharff, and P. Thomsen, "Integral equations governing radiation effects," *Mat. Fys. Medd. Dan. Vid. Selsk*, vol. 33, no. 10, pp. 1–42, 1963.

[34] W. Windl, T. J. Lenosky, J. D. Kress, and A. F. Voter, "First-principles investigation of radiation induced defects in Si and SiC," *Nuclear Instruments and Methods in Physics Research Section B: Beam Interactions with Materials and Atoms*, vol. 141, no. 1-4, pp. 61–65, 1998.

[35] J. W. Corbett, *Electron Radiation Damage in Semiconductors*. Academic Press, New York, 1966.

[36] E. Holmström, K. Nordlund, and A. Kuronen, "Threshold defect production in germanium determined by density functional theory molecular dynamics simulations," *Physica Scripta*, vol. 81, no. 3, p. 035601, 2010.

[37] B. Lehmann and D. Bräunig, "A deep-level transient spectroscopy variation for the determination of displacement threshold energies in GaAs," *Journal of applied physics*, vol. 73, no. 6, pp. 2781–2785, 1993.

[38] H. Hausmann, A. Pillukat, and P. Ehrhart, "Point defects and their reactions in electron-irradiated GaAs investigated by optical absorption spectroscopy," *Physical Review B*, vol. 54, no. 12, p. 8527, 1996.

[39] C. Inguimbert and R. Gigante, "Nemo: a code to compute niel of protons, neutrons, electrons and heavy ions," in *2005 8th European Conference on Radiation and Its Effects on Components and Systems*. IEEE, 2005, pp. PG2–1.

[40] K. Nordlund, S. J. Zinkle, A. E. Sand, F. Granberg, R. S. Averback, R. E. Stoller, T. Suzudo, L. Malerba, F. Banhart, W. J. Weber *et al.*, "Primary radiation damage: A review of current understanding and models," *Journal of Nuclear Materials*, vol. 512, pp. 450–479, 2018.

[41] G. Kinchin and R. Pease, "The displacement of atoms in solids by radiation," *Reports on progress in physics*, vol. 18, no. 1, p. 1, 1955.

[42] M. Norgett, M. Robinson, and I. Torrens, "A proposed method of calculating displacement dose rates," *Nuclear engineering and design*, vol. 33, no. 1, pp. 50–54, 1975.

[43] S. Wood, N. Doyle, J. Spitznagel, W. Choyke, R. More, J. McGruer, and R. Irwin, "Simulation of radiation damage in solids," *IEEE Transactions on Nuclear Science*, vol. 28, no. 6, pp. 4107–4112, 1981.

[44] J. Bourgoin and J. Corbett, "Enhanced diffusion mechanisms," *Radiation Effects*, vol. 36, no. 3-4, pp. 157–188, 1978.

[45] F. Seitz and D. Turnbull, *Solid state physics*. Academic Press, 1957.

[46] G. J. Dienes and A. Damask, "Radiation enhanced diffusion in solids," *Journal of Applied Physics*, vol. 29, no. 12, pp. 1713–1721, 1958.

[47] M. R. Brozel and G. E. Stillman, *Properties of Gallium Arsenide*. INSPEC, London, 1996.

[48] F. Gao, H. Y. Xiao, and W. J. Weber, "Ab initio molecular dynamics simulations of low energy recoil events in ceramics," *Nuclear Instruments and Methods in Physics Research Section B: Beam Interactions with Materials and Atoms*, vol. 269, no. 14, pp. 1693–1697, 2011.

[49] P. Wurfel, *Physics of solar cells*. Wiley-Vch, 2005.

[50] J. Gray, "The physics of the solar cells," in *Handbook of Photovoltaic Science and Engineering, Second Edition*. Wiley, 2011, ch. 3, p. 99.

[51] K. Ploog, "Molecular beam epitaxy of III–V compounds," in *III–V Semiconductors*. Springer, 1980, pp. 73–162.

[52] S. C. Moss, L. F. Halle, and D. C. Marvin, "Effects of electron beam irradiation on transient photoluminescence measurements of GaAs and AlGaAs double heterostructures," *IEEE Transactions on Nuclear Science*, vol. 42, no. 6, pp. 2058–2065, 1995.

[53] J. Dresner, "Mobility in epitaxial GaAs under 1-MeV electron irradiation," *Journal of Applied Physics*, vol. 45, no. 9, pp. 4118–4119, 1974.

[54] B. Anspaugh and R. Downing, "Radiation effects in silicon and gallium arsenide solar cells using isotropic and normally incident radiation," 1984.

[55] B. E. Anspaugh, "Proton and electron damage coefficients for GaAs/Ge solar cells," in *The Conference Record of the Twenty-Second IEEE Photovoltaic Specialists Conference-1991*. IEEE, 1991, pp. 1593–1598.

[56] B. E. Anspaugh *et al.*, *GaAs solar cell radiation handbook*. National Aeronautics and Space Administration, Jet Propulsion Laboratory . . . , 1996, vol. 7.

[57] G. P. Summers, E. A. Burke, and M. A. Xapsos, "Displacement damage analogs to ionizing radiation effects," *Radiation measurements*, vol. 24, no. 1, pp. 1–8, 1995.

[58] S. R. Messenger, G. Summers, E. Burke, R. Walters, and M. Xapsos, "Modeling solar cell degradation in space: A comparison of the NRL displacement damage dose and the JPL equivalent fluence approaches," *Progress in Photovoltaics: Research and Applications*, vol. 9, no. 2, pp. 103–121, 2001.

[59] CERN, "The super proton synchrotron." [Online]. Available: https://home.cern/science/accelerators/super-proton-synchrotron

[60] C. S. Nunan, "Present and future applications of industrial accelerators," *Proceedings of the 9th Fermilab Industrial Affiliates Roundtable on Applications of Accelerators*, pp. 55–88, 1989.

[61] National Electrostatics Corp., "Pelletron charging system." [Online]. Available: https://www.pelletron.com/products/pelletron-charging-chains

[62] D. Walker, J. Nocerino, Y. Yue, C. J. Mann, and S. H. Liu, "Subcell light current-voltage characterization of irradiated multijunction solar cell," in *2017 IEEE 44th Photovoltaic Specialist Conference (PVSC)*. IEEE, 2017, pp. 93–95.

[63] T. Ohshima, S. Sato, M. Imaizumi, T. Nakamura, T. Sugaya, K. Matsubara, and S. Niki, "Change in the electrical performance of GaAs solar cells with InGaAs quantum dot layers by electron irradiation," *Solar energy materials and solar cells*, vol. 108, pp. 263–268, 2013.

[64] T. Delft, "Pulsed high-energy electron accelerator facilities." [Online]. Available: https://www.tudelft.nl/en/faculty-of-applied-sciences/about-faculty/departments/chemical-engineering/principal-scientists/laurens-siebbeles/laurens-siebbeles-group/experimental-facilities/pulsed-high-energy-electron-accelerator-facilities

[65] S. Duzellier, L. Artola, G. Hubert, C. Inguimbert, T. Nuns, S. Lewandowski, T. Paulmier, B. Dirassen, R. Rey, and C. Pons, "AXEL lab.: representative ground simulation for investigating radiation effects in materials and electronics," in *2017 17th European Conference on Radiation and Its Effects on Components and Systems (RADECS)*. IEEE, 2017, pp. 1–7.

[66] Polytechnique, "Installation sirius." [Online]. Available: https://portail.polytechnique.edu/lsi/fr/equipements/linstallation-sirius

[67] IPN, "Installations." [Online]. Available: http://ipnwww.in2p3.fr/installations-429

[68] JPL, "Space radiation facilities." [Online]. Available: https://trs.jpl.nasa.gov/bitstream/handle/2014/42836/13-1123_A1b.pdf?sequence=1

[69] C. Vargas-Aburto and R. Uribe, "Electron irradiation facility for the study of radiation damage in large solar cell arrays in the energy range," *Solar energy materials and solar cells*, vol. 87, no. 1-4, pp. 629–636, 2005.

[70] Boeing, "Boeing: Radiation effects laboratory." [Online]. Available: http://www.boeing.com/specialty/radiation-effects-laboratory/index.page#/capabilities

[71] F. Eisen, K. Bachem, E. Klausman, K. Koehler, and R. Haddad, "Ion irradiation damage in n-type GaAs in comparison with its electron irradiation damage," *Journal of applied physics*, vol. 72, no. 12, pp. 5593–5601, 1992.

[72] M. Yamaguchi, "Radiation resistance of compound semiconductor solar cells," *Journal of applied physics*, vol. 78, no. 3, pp. 1476–1480, 1995.

[73] M. Ibarra, J. Garcia, M. Barrera, I. Prario, and M. Alurralde, "A beam line to simulate space environment at TANDAR ion accelerator," in *2nd IAA Latin American Symposium on Small Satellites*, 2019.

[74] U. of Jyväskylä, "Accelerators and ion sources." [Online]. Available: https://www.jyu.fi/science/en/physics/research/infrastructures/accelerator-laboratory/accelerators-and-ion-sources

[75] X. Shen, A. Aierken, M. Heini, J. Mo, Q. Lei, X. Zhao, M. Sailai, Y. Xu, M. Tan, Y. Wu *et al.*, "Degradation analysis of 1 MeV electron and 3 MeV proton irradiated InGaAs single junction solar cell," *AIP Advances*, vol. 9, no. 7, p. 075205, 2019.

[76] M. Yamaguchi, "Radiation-resistant solar cells for space use," *Solar energy materials and solar cells*, vol. 68, no. 1, pp. 31–53, 2001.

[77] L. Hirst, M. Yakes, J. Warner, M. Bennett, K. Schmieder, R. Walters, and P. Jenkins, "Intrinsic radiation tolerance of ultra-thin GaAs solar cells," *Applied Physics Letters*, vol. 109, no. 3, p. 033908, 2016.

[78] S. Park, "Irradiation effect in triple junction solar cells for spatial applications," Ph.D. dissertation, Université Paris-Saclay, 2018.

[79] A. Gauffier, "Caractérisation et modélisation de la dégradation sous irradiations de cellules solaires trijonction," Ph.D. dissertation, Institut Supérieur de l'Aéronautique et de l'Espace, 2008.

[80] S. Park, J. C. Bourgoin, H. Sim, C. Baur, V. Khorenko, O. Cavani, J. Bourcois, S. Picard, and B. Boizot, "Space degradation of 3j solar cells: I—proton irradiation," *Progress in Photovoltaics: Research and Applications*, vol. 26, no. 10, pp. 778–788, 2018.

[81] Y. Miyazawa, M. Ikegami, H.-W. Chen, T. Ohshima, M. Imaizumi, K. Hirose, and T. Miyasaka, "Tolerance of perovskite solar cell to high-energy particle irradiations in space environment," *IScience*, vol. 2, pp. 148–155, 2018.

[82] Z. Song, C. Li, C. Chen, J. McNatt, W. Yoon, D. Scheiman, P. P. Jenkins, R. J. Ellingson, M. J. Heben, and Y. Yan, "High remaining factors in the photovoltaic performance of perovskite solar cells after high-fluence electron beam irradiations," *The Journal of Physical Chemistry C*, vol. 124, no. 2, pp. 1330–1336, 2019.

Chapter 2

InGaAsN as a 1 eV material for MJSC

"*If I have seen further it is by standing on the shoulders of Giants.*" – Isaac Newton

This chapter covers a literature review on the development of InGaAsN as a 1 eV material for MJSC application. The first section introduces molecular beam epitaxy as a major technique to grow InGaAsN. The history of InGaAsN as a solar cell absorber is then detailed in the second section, before focusing on the optoelectronic properties of dilute nitrides. In the third section of this chapter, we conduct a litterature review of reported InGaAsN solar cells properties and their typical crystal defects. In the fourth section, we describe the challenges of InGaAsN subcell integration within MJSC and we end up this chapter reviewing the few irradiation studies conducted on dilute nitrides. In the frame of this thesis, this chapter will allow to:

- position the work of this PhD
- compare our results with the state of the art
- identify the gaps in the literature on InGaAsN for space applications

Contents

2.1 Epitaxial growth techniques

2.1.1 Epitaxial growth principles

Epitaxy is a technique used to grow crystal layers on top of a substrate lattice. The term *epitaxy* derives from the Greek *epi* "above" and *taxis* "arrangement", meaning that epitaxial growth occurs when external atoms are brought to a crystalline surface and arrange in a way it extends the crystal lattice. The most straightforward way to perform epitaxy is to grow layers (called *epilayers*) of the same material as the substrate: it is called *homoepitaxy*. The lattice parameters and the chemical bonds of both the epilayer and the substrate are then identical which generally results in high crystal quality, suitable for electronics and optoelectronics applications.

On the other side, *heteroepitaxy* is used to fabricate structures relying on multiple materials, such as solar cells, lasers or Bragg mirrors. Layers with different atomic compositions can be grown on top of a substrate under 3 different regimes, depending on the lattice-mismatch f between the epilayer and the substrate:

$$f = \frac{a_{layer} - a_{substrate}}{a_{substrate}} \tag{2.1}$$

where a_{layer} and $a_{substrate}$ are the lattice parameters of the epilayer and the substrate, parallel to the interface.

- if the epilayer has the same lattice parameter as the substrate *i.e.* $f = 1$, the crystal growth occurs without stress, as in the case of homoepitaxy. The layer is said to be *lattice-matched* to the substrate (Figure 2.1a).
- if the epilayer has a lattice parameter slightly different from the substrate ($|f| < 2$ %), it can be grown under stress with moderate strain in the crystal. For $f > 0$, the epilayer is subjected to elastic compressive stress from the substrate (Figure 2.1b) , for $f < 0$ it undergoes elastic tensile stress (Figure 2.1c). The lattice parameter of the epilayer perpendicular to the interface is also strained to compensate the deformation of its parallel lattice parameter

(tetragonal deformation). This kind of growth is called **pseudomorphic** and stops when the stored strain energy becomes too high. For a given f, it translates into a critical thickness which was estimated by Matthews and Blakeslee [1].

- if there is a large mismatch between the epilayer and the substrate or if the critical thickness is exceeded, the stored strain energy is released and the system undergoes plastic deformations. Misfit dislocations (MD) emerge at the hetero-interface while threading dislocations (TD) propagate through the entire epilayer (Figure 2.1d). This results in a new effective lattice parameter (virtual substrate) on top of which layers can be grown, as it is done in inverted and upright **metamorphic** MJSC.

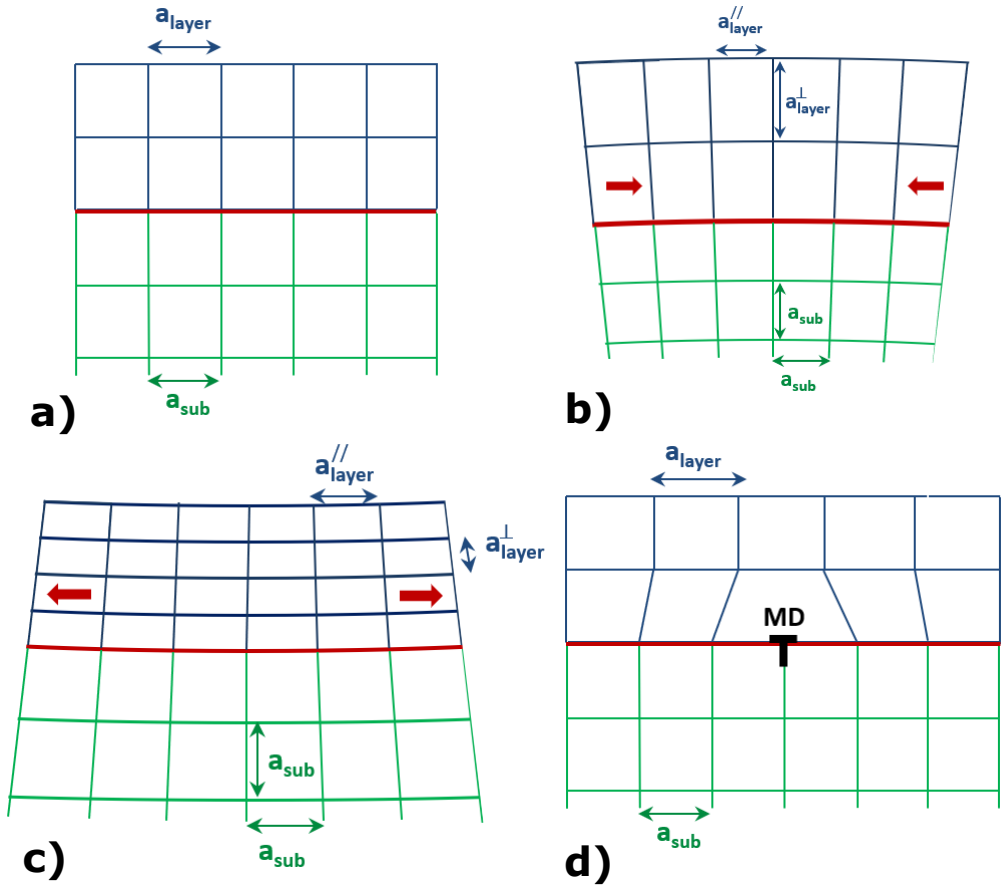

Figure 2.1: a) Heteroepitaxy with lattice-matching of the epilayer b) Pseudomorphic growth of epilayer under compressive stress c) Pseudomorphic growth of epilayer under tensile stress d) Metamorphic growth with misfit dislocation (MD).

There are different epitaxial growth technologies depending on the source of the atoms that impinge the surface of the substrate. **Liquid Phase Epitaxy (LPE)** was the first technique to be developed. It was used to fabricate silicon diodes and transistors in the 1950's and GaAs/AlGaAs structures in the 60's [2]. In LPE, the *adatoms* are brought to the surface through molten metallic solutions and the substrate is typically slided from one melt to another to obtain different layers. It

is based on an near-equilibrium process in which a liquid phase precipitates on a crystalline layer. LPE is a cheap and mature technique that benefits from high growth rates [3].

Vapour Phase Epitaxy (VPE) relies on molecular precursors acting as carriers for the atoms to be incorporated during layer growth. In the case of III-V semiconductors, the precursors of the species are generally organometallic molecules and the technique is called **metal organic vapour phase epitaxy (MOVPE)**. The organometallic molecules are typically thermally cracked on or near the surface through chemical reactions that separates the metal atoms from the organic products. MOVPE was pioneered in the late 60's for III-V materials [4] and became a production technique in the late 80's [3]. In addition to the high crystal quality it leads to, MOVPE has high growth rates and a high throughput because multiple wafers can be processed a the same time. It is also very versatile as there is a wide panel of organometallic precursors available.

Molecular Beam Epitaxy (MBE) is a straightforward growth technique in which atoms or molecules are directly sent to the substrate surface with ballistic transport. It requires a very high level of vacuum and relies on effusion cells that emit molecular beams when heated above the melting point of the element. MBE has low growth rates but leads to high-purity crystals. Furthermore, MBE allows for very precise control of thicknesses and compositions of the layers, enabling pure and abrupt interfaces.

Finally, **Chemical Beam Epitaxy (CBE)** was developed by Tsang in 1984 [5]. This technique lies between MOCVD and MBE in that it relies on gaseous carriers that travel a high-vacuum growth chamber in a molecular beam regime.

2.1.2 Molecular Beam Epitaxy

The term Molecular Beam Epitaxy was coined by Cho in 1970 [6] and rose with the development of commercial ultra high vacuum (UHV) equipments in the 70's. In a MBE system, the atoms are provided by high purity solid sources (typically 6N) contained in effusion cells. These cells are generally made of a pyrolytic boron nitride (PBN) crucible wrapped with heating resistances. A mechanically actionable shutter is also found at the tip of the cell in order to cut a specific atom flux in a short lap of time (≈0.1 s). This flux management enables to grow superfine heterostructures with abrupt interfaces, which is highly desirable for superlattices, quantum wells or tunnel junctions. In addition to their shutter, some effusion cells have a valve that allows to tune the beam flux. This valve can be engineered with a cracking system (valved cracker cells) to dissociate molecules emitted from the solid source (As_4, P_4). Finally, atoms can also be provided through gas or plasma sources as it is the case in CBr_4 injector and RF plasma nitrogen source.

Once the atoms hit the surface, they can undergo different mechanisms, driven by the potential energy distribution of the surface. These mechanisms

are depicted in Figure 2.2, they depend on the chemical nature of the atoms in presence (sticking coefficient) and on the growth conditions (substrate temperature T_g, atom fluxes). Incoming atoms are first adsorbed, becoming adatoms, and then migrate around the surface until they find an energetically favorable incorporation site (absorption). Increasing the substrate temperature enhances the diffusion length of the adatoms, which promotes the layer-by-layer 2D growth generally looked for. However, having a high T_g increases the desorption and the interdiffusion rate and is typically incompatible with non-equilibrium growth.

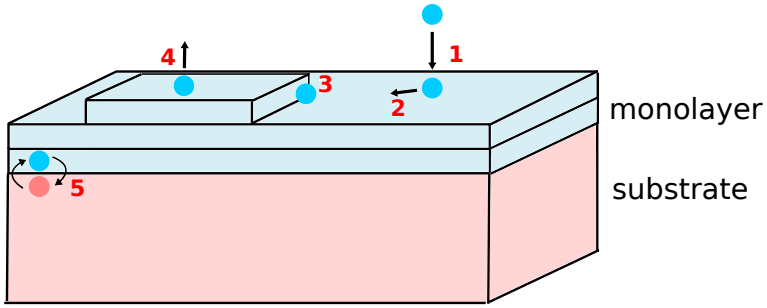

Figure 2.2: Schematics of the basic atomic mechanisms occuring at the surface during growth. 1) adsorption, 2) migration, 3) incorporation/absorption, 4) desorption, 5) interdiffusion.

As mentioned in the previous part, MBE requires UHV conditions (typically lower than 10^{-9} Torr / 10^{-12} bar) to allow ballistic transport and low contamination. The UHV also enables the use of multiple *in-situ* characterization techniques such as reflection high-energy electron diffraction (RHEED), Auger emission spectroscopy (AES), secondary ion mass spectroscopy (SIMS) and X-ray photoelectron spectroscopy (XPS). In addition, ion guns can be used under vacuum for surface cleaning prior to the growth. This UHV is made possible thanks to ion-, cryo-, turbomolecular and titanium sublimation pumps, coupled with nitrogen cooling cryopanels and a hermetic stainless steel growth chamber. A schematic view of the atomic beam fluxes operating under UHV and coupled with RHEED characterization is presented in Figure 2.3.

Since the development of AlGaAs/GaAs first heterostructures, most of the MBE researches and applications have been focused on III-V materials. InSb and GaSb infrared detectors, GaAs solar cells, VCSELs and GaN transistors are III-V devices that can be fabricated with this technique. However, MBE growth of II-VI and IV-VI alloys has also been studied for narrow-bandgap photodetectors ($Hg_{1-x}Cd_xTe$, $PbSe_{0.8}Te_{0.2}$), PbTe lasers and CdTe/CdS solar cells [7].

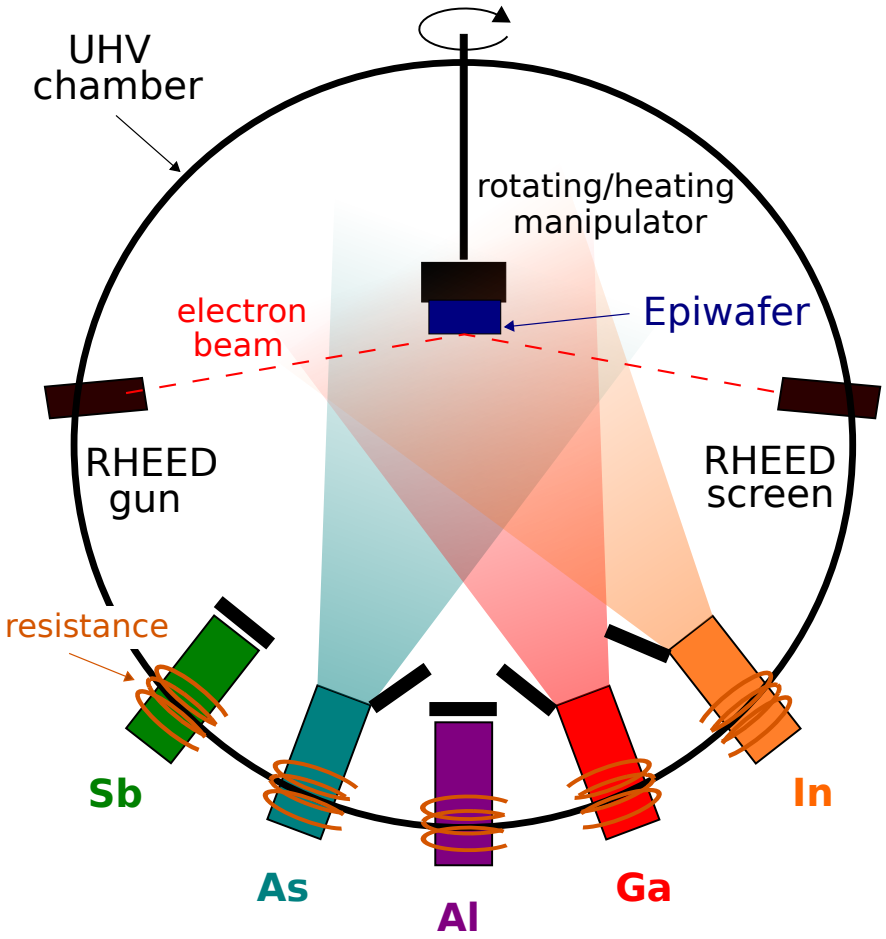

Figure 2.3: Representation of an MBE growth-system with five effusion cells. In this schematic, Sb and Al shutters are closed and InGaAs is being grown on the substrate.

2.2 History of InGaAsN solar cells

2.2.1 Dilute nitride first developments

Dilute nitrides are GaAs-based alloys that contain a small amount of nitrogen. In 1992, as scientists from NTT Lab in Japan were studying nitrogen doping in MOCVD-grown GaAs, they reported an important bandgap red-shift in the resulting material [8], as shown in Figure 2.4. This observation was surprising because $GaAs_{1-x}N_x$ was expected to follow Vegard's law stating that the dilute nitride bandgap should lay between the bandgap of GaAs (1.42 eV) and the bandgap of GaN (3.4 eV).

This serendipity brought a lot of interest to the laser community as near infrared emitting materials were being researched for telecommunication applications. In 1996, a team from Hitachi proposed InGaAsN as a replacement for InGaAsP as the 1.3 μm active material for laser diodes used in optical fiber communications, as InGaAsP/InP laser diodes suffer from poor temperature charac-

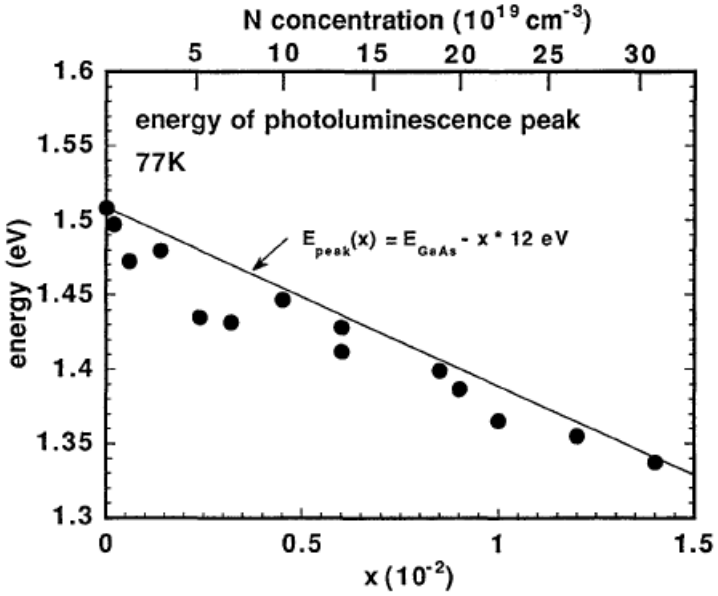

Figure 2.4: Evolution of GaAsN bandgap energy with nitrogen concentration measured by photoluminescence at 77K [8].

teristics [9]. They were the first to introduce both indium and nitrogen in GaAs to form a low-bandgap alloy that could be lattice-matched to GaAs substrate. Indeed, nitrogen is a small atom compared to arsenic which leads the GaAsN epilayers to be grown under tensile stress on GaAs substrates. On the contrary, indium is larger than gallium which provokes compressive stress when InGaAs is grown on GaAs substrates. Furthermore, the bandgap energy of $In_yGa_{1-y}As$ also decreases with the In content. Introducing both nitrogen and indium in a GaAs matrix (with $\frac{x_{In}}{x_N} \approx 2.8$) allows then to remain lattice-matched to GaAs while lowering the alloy bandgap energy, which is depicted in Figure 2.5.

2.2.2 Rising of multi-junction solar cells

In parallel to this, multi-junction solar cells (MJSC) were being developed for space applications and high concentrating photovoltaics (HCPV) systems. The monolithic triple-junction GaInP/GaAs/Ge cells fabrication was demonstrated in 1996 at Spectrolab, exhibiting a 25.7 % efficiency under AM0 exposition [11]. In 2000, NREL and Spectrolab reported a GaInP/GaAs/Ge MJSC with 32.3 % efficiency under 47×AM1.5D concentrated sunlight [12]. Even though this architecture held the world record efficiency by the time, the authors of the article emphasized on the need to develop a 1 eV material to further improve the structure. This observation was referring to the calculations of the MJSC optimal bandgap combination made by Kurtz et al. in 1997 [13], as illustrated in Figure 2.6. These calculations pointed out the need to develop a 1 eV subcell that could either replace Ge bottom cell in a triple junction device or be introduced between GaAs and Ge cells in a 4-junction solar cell. Therefore, the main challenge was to find

a semi-conductor that could both have a 1 eV bandgap and a lattice parameter equal to 5.65 Å in order to be lattice-matched to GaAs or Ge. Researchers from the NREL decided to develop 1 eV solar cells based on a promising new material: InGaAsN.

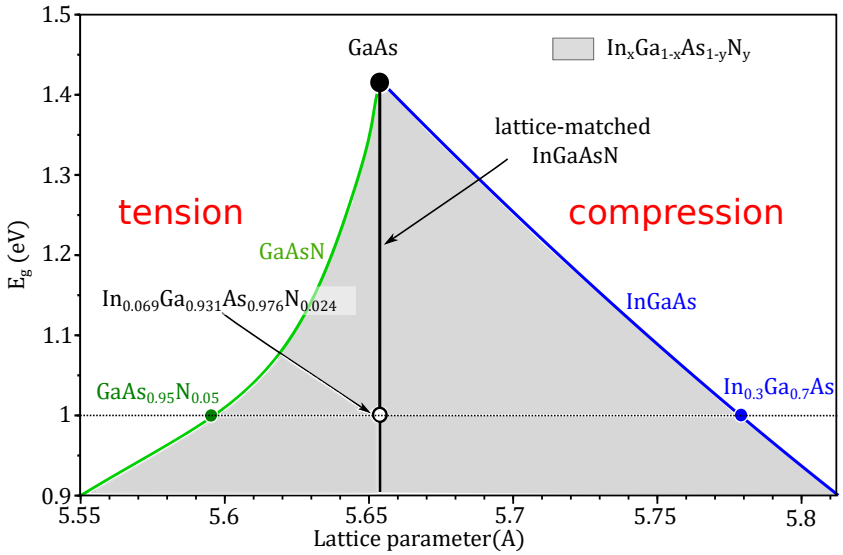

Figure 2.5: Bandgap energy and lattice parameter for the InGaAsN system (inspired from [10]).

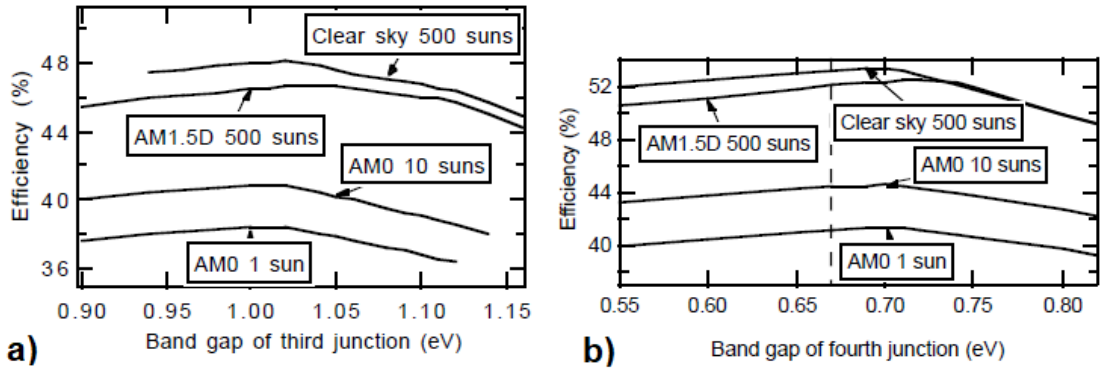

Figure 2.6: a) Maximal theoretical efficiency of a 3J with GaInP and GaAs subcells as a function of the bandgap of the bottom cell b) Maximal theoretical efficiency of a 4J with GaInP, GaAs and a 1-1.05 eV subcell as a function of the bandgap of the 4th junction [13].

2.2.3 1 eV InGaAsN cells

As the InGaAsN alloy was filling the MJSC requirements mentioned earlier (1 eV bandgap and lattice-matched to GaAs and Ge), 1 eV InGaAsN subcells were developed and demonstrated at NREL [14, 15] and at Sandia National Laboratories [16, 17]. The InGaAsN cells were grown with metal organic vapor phase

epitaxy (MOVPE) and were unfortunately plagued with short minority carrier diffusion length. This led to very low quantum efficiencies (on the order of 0.2) and short-circuit current densities equal to 1.8 mA/cm^2 under AM1.5D GaAs-filtered light [15]. Increasing the photocurrent became the top priority as 1 eV subcells were required to photogenerate more than 14 mA/cm^2 under AM0 to be current-matched with the GaInP and GaAs subcells [18].

In order to do that, GaAs/InGaAsN/GaAs *pin* and *nip* junctions were developed. They rely on a drift collection regime which is less sensitive to dilute nitride low diffusion length and higher photocurrents were obtained with these structures. Friedman et al. demonstrated a pn^- cell with a J_{sc} equal to 10.2 mA/cm^2 under AM0>870 nm light [15] and the Fraunhofer ISE in collaboration with Philipps-University Marburg reported on a J_{sc} equal to 10.9 mA/cm^2 under the same illumination condition [19]. To further improve the collection efficiency, efforts were made on lowering the background carrier concentration (BGCC) to increase the width of the space charge region (Figure 2.7). This was notably made possible by using MBE as an alternative to MOVPE, as this latter one was found to lead to higher impurity concentrations [20, 21].

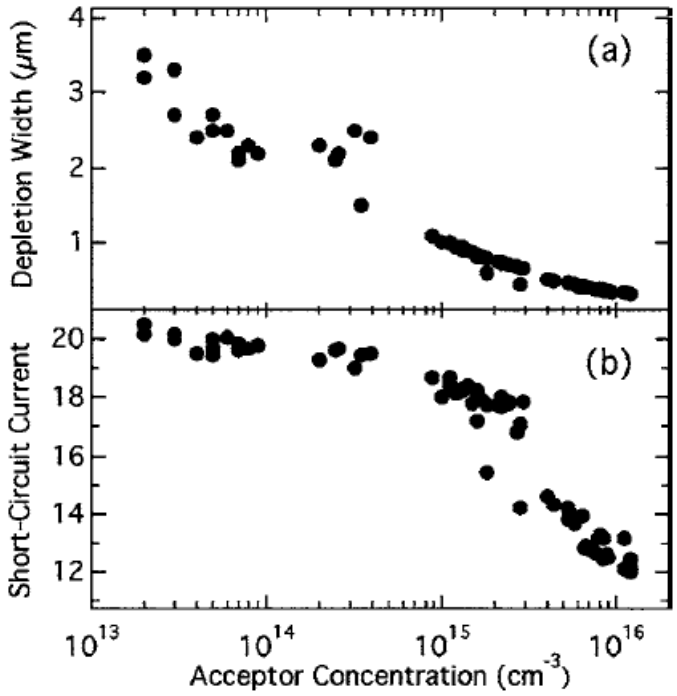

Figure 2.7: Evolution of the depletion width (a) and of the short-circuit current density in mA/cm^2 (under AM1.5 illumination) (b) of InGaAsN solar cells with their acceptor concentration [21].

Another matter was the formation of crystal defects during epitaxial growth. Indeed, N-related defects were found to be responsible for poor open-circuit voltage, diffusion length and quantum efficiency [22, 23]. Different techniques were proposed to prevent the formation of these defects such as the introduc-

tion of antimony as a surfactant during growth and the use of deflector plates in front of the nitrogen source [24]. Photocurrent of 14.8 mA/cm^2 could then be obtained for InGaAsSbN solar cells under AM1.5D>880 nm spectrum. In parallel to this, studies were conducted on post-growth thermal annealing (also called rapid thermal processing or RTP) as it was found to be an effective way of reducing the concentration of these defects [22, 23, 25, 26].

Taking advantage of all this development, Solar Junction announced in 2012 a world record efficiency (at the time) of 43.5 % under concentration for a triple-junction incorporating a InGaAsN-based bottom cell [27]. Although only few details regarding the cell properties were reported by Solar Junction, this GaInP/GaAs/InGaAsNSb constituted a remarkable proof of concept for dilute nitrides in MJSC. Since then, most of the 1 eV-InGaAsN solar cell development has been focusing on the optimization of the thermal annealing [28, 29, 30] and the growth conditions (*As/III* ratio, substrate temperature ...) [31, 32, 33]. The growth and annealing optimizations of 1 eV-InGaAsN enabled the fabrication of high-efficiency triple junction solar cells for space applications, as demonstrated by the Tampere/CESI collaboration [34, 35]. Research is also being carried out at Tampere University on dilute nitrides with both low and high N content, in order to cover a wide range of bandgap energy and introduce more than one $In_yGa_{1-y}As_{1-x}N_x$ subcell in a MJSC [36, 37].

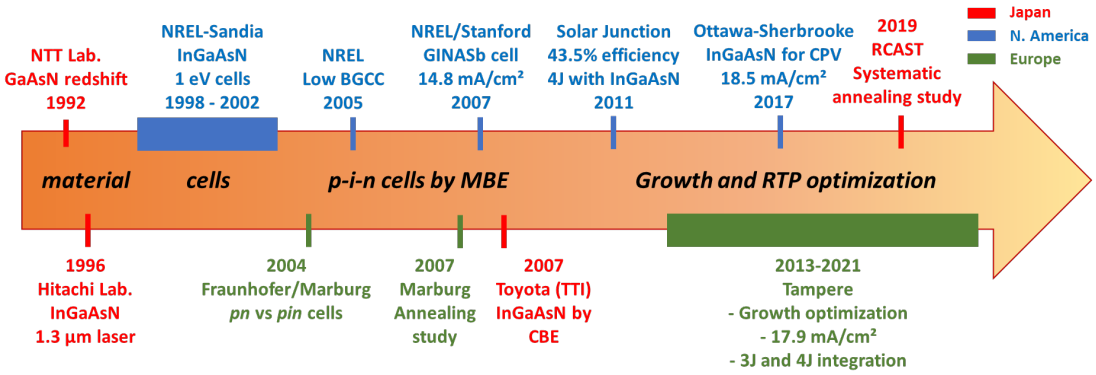

Figure 2.8: Important milestones, findings and contributions in the development of InGaAsN for MJSC applications.

2.3 Optoelectronic properties of dilute nitrides

In this section, we show the effect of nitrogen atoms on the band gap energy of dilute nitrides and we present the most common defects in (In)GaAsN. A focus is made on deep-level transient spectroscopy and a review of defects probed by DLTS is presented. The impact of these crystal defects on the carrier properties is then discussed and we finally introduce thermal annealing as a way of curing them.

2.3.1 Nitrogen effect on the bandgap of GaAs

The bandgap of $(In)GaAs_{1-x}N_x$ depends strongly on the nitrogen content: dilute nitrides exhibit a very large *bowing parameter*. Adding 1 % of nitrogen into GaAs decreases the bandgap energy from 1.424 to approximately 1.25 eV whereas comparatively the bandgap reduction in the $In_yGa_{1-y}As$ system for 1 % indium content is only 15 meV. The bandgap of GaAsN can be estimated with the following equation, where b is the bowing parameter:

$$E_g(GaAs_{1-x}N_x) = (1-x).E_g(GaAs) + x.E_g(GaN) - bx(1-x) \tag{2.2}$$

In addition, the bowing parameter of dilute nitrides was determined to be itself dependent on the nitrogen composition [38]. Tisch et al. gave the following empirical expression of the GaAsN bowing parameter [39]:

$$b(x) = b_0 + b_1 e^{-x/x_1} + b_2 e^{-x/x_2} \tag{2.3}$$

where the fitted values of b_0, b_1, b_2, x_1 and x_2 are respectively 7.5 ± 2.5 eV, 21.1 ± 1.3 eV, 15.9 ± 1.6 eV, 0.26 ± 0.04 % and 3.3 ± 1.3 %.

Knowing that the bandgap energy of InGaAs can also be expressed with a Vegard law corrected with a bowing parameter equal to 0.475 eV [40], we can plot the decrease of the InGaAsN bandgap energy with its nitrogen content (Figure 2.9).

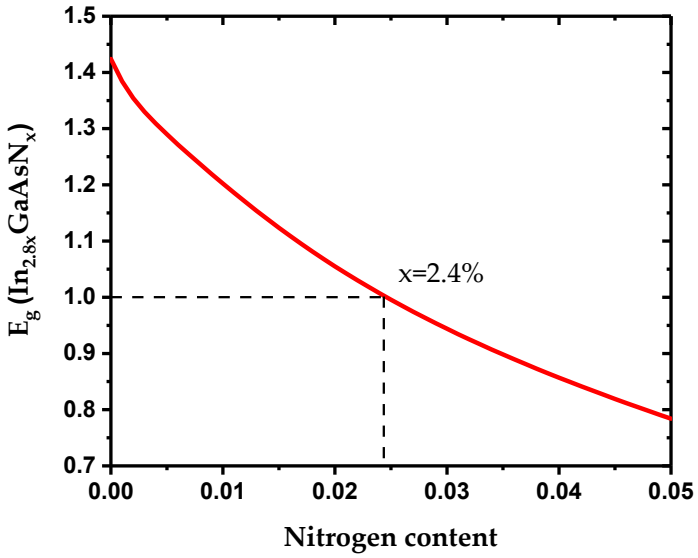

Figure 2.9: Evolution of the InGaAsN bandgap energy with the nitrogen content of the quaternary alloy.

This huge reduction of the bandgap with nitrogen incorporation can be described by the band anti-crossing (BAC) model [41]: Nitrogen atoms are smaller and have a higher electronegativity than As atoms, which leads to the formation of defect states near the edge of the conduction band [42]. These nitrogen-related defects are highly localized and form a narrow band that resonates with the extended states of the (In)GaAs conduction band. This coupling through anticrossing interaction results in the splitting of the conduction band into two subbands E_- and E_+, according to the following equation:

$$E_\pm = \frac{1}{2}(E_N + E_M \pm \sqrt{(E_N - E_M)^2 + 4V_{MN}^2}) \tag{2.4}$$

E_M is the energy of the conduction band edge of the (In)GaAs matrix, E_N is the energy of the nitrogen defect and V_{MN} is a term describing the interaction between those two states. The fundamental bandgap of the dilute nitride becomes then the transition between the maximum of the valence band E_V (that is virtually not affected by N introduction) and the lower branch of the conduction band E_-. Moreover, the splitting between E_- and E_+ increases with the nitrogen concentration, which in turn leads to a decrease in the (In)GaAsN bandgap energy. Transitions from E_+ and $E_- + \Delta_0$ (spin-orbit split-off band) to E_V also exists and can be observed with photoreflectance measurements, as depicted in Figure 2.10 b).

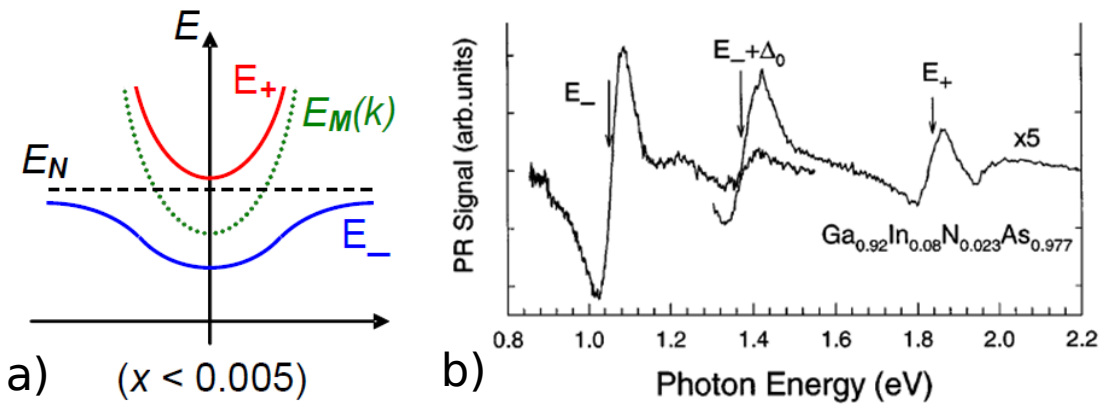

Figure 2.10: a) Schematic of the splitting of the conduction band with nitrogen introduction [42], b) Photoreflectance spectrum of a InGaAsN layer showing the 3 possible transitions from the E_-, $E_- + \Delta_0$ and E_+ levels to the valence band [41].

2.3.2 Characterization of the nature of defects in InGaAsN

In addition to the decrease in the bandgap energy, introducing N atoms in a (In)GaAs matrix usually leads to the creation of *growth* defects (as opposed to *irradiation-induced* defects). Characterizing these defects is crucial in order to prevent their apparition and be able to mitigate their impact on InGaAsN solar cells.

To that end, nanoscale spectroscopy techniques can be used to identify the *atomic nature* of the defect.

Li et al. conducted positron annihilation spectroscopy (PAS) and nuclear reaction analysis (NRA) on InGaAsN layers grown by MBE [43]. They were able to identify both nitrogen interstitials N_i and Ga vacancies V_{Ga} in the dilute nitride crystal. These two defects are represented in Figure 2.11. The presence of nitrogen interstitials in (In)GaAsN was also experimentally observed with NRA coupled with channelling techniques [44, 45, 46]. Furthermore, it is supported by theoretical first-principles calculation showing that the formation of $(N-N)_{As}$ and $(N-As)_{As}$ split interstitials is energetically favourable [47]. $(N-H)_{As}$ in GaAsN layers has also been evidenced by studying local vibration modes (LVM) with Fourier transform infrared spectroscopy (FTIR) [48], and with hard x-ray photoelectron spectroscopy (HXPES)[49]. Another experimental evidence of nitrogen interstitials is the discrepancy between SIMS and high-resolution X-ray diffraction (HRXRD) measurements observed by Fan et al. [50].

As for gallium vacancies, their concentration was reported to increase with the N content by Toivonen et al. using PAS [51] and it was calculated that nitrogen atoms reduce the formation energy of V_{Ga} in (In)GaAsN [52]. The presence of gallium vacancies in dilute nitrides could also originate from the relatively low temperature at which they are grown (T_g typically lower than 500°C in MBE). Indeed, molecular dynamics simulations have shown that V_{Ga} formation is enhanced in GaAs when the growth temperature is lowered [53].

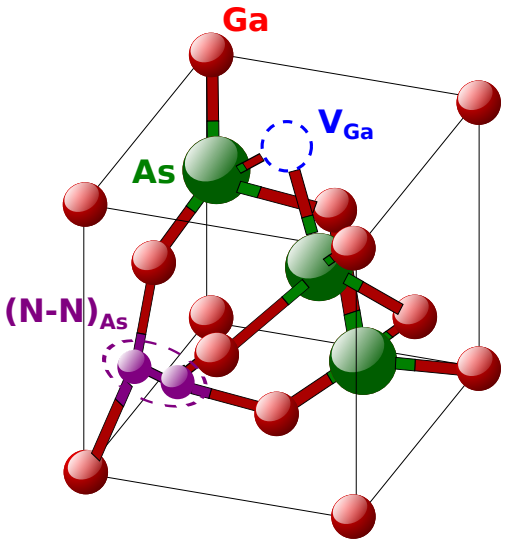

Figure 2.11: Atomic representation of the two main defects in InGaAsN: nitrogen interstitials $(N\text{-}N)_{As}$ and gallium vacancies V_{Ga}. The GaAs zinc blende structure is shown without In atoms as they only account for a few percents of the *III* elements in lattice-matched dilute nitrides.

2.3.3 Deep level transient spectroscopy

Deep level transient spectroscopy, usually shortened as DLTS, is an electrical characterization technique developed in 1974 at Bell laboratories by D. V. Lang [54]. It relies on the analysis of a capacitance transient occurring after a voltage pulse is applied to a *pn* or Schottky junction. Unlike the techniques that were mentioned in the previous section, DLTS characterizes the *electrical nature* of crystal defects.

At equilibrium and under reverse bias, a *pn* junction displays a space charge region (SCR) which can be considered as an insulator separating electrical charges. The junction can then be considered as a parallel plate capacitor whose capacitance is equal to:

$$C = \frac{\epsilon_0 \epsilon_r A}{\omega_{SCR}} \tag{2.5}$$

where ϵ_0 is the vacuum permittivity, ϵ_r is the relative permittivity of the semiconductor, A is the area of the junction and ω_{SCR} is the width of the SCR.

The capacitance of a *pn* junction increases when a positive voltage pulse is applied as the width of the SCR is reduced. Once the voltage pulse is over, charges start to be depleted and the SCR expands again to its initial width. However, carriers that were injected during the pulse can be trapped in deep level states and will be re-emitted to their band only after a certain time τ. This leads to a capacitance transient in the junction that can be measured for different temperatures, as the rate of emission of trapped carriers $e_{e,h}$ depends strongly on this latter parameter:

$$e_{e,h} = N_{C,V} v_{e,h} \sigma_{e,h} \exp(-\frac{E_A}{kT}) \tag{2.6}$$

where $N_{C,V}$ is the effective density of state of the conduction and valence bands, $v_{e,h}$ is the thermal velocity of the carrier , $\sigma_{e,h}$ are the carrier capture cross-sections and E_A is the activation energy of the trap. Considering that $v_{e,h} \propto T^{\frac{1}{2}}$ and $N_{C,V} \propto T^{\frac{3}{2}}$, the emission rate can be re-written as:

$$e_{e,h} = A^*_{e,h} T^2 \sigma_{e,h} \exp(-\frac{E_A}{kT}) \tag{2.7}$$

where $A^*_{e,h}$ is the Richardson constant of the material.

In practice, the capacitance transient is studied by calculating the capacitance difference ΔC at two times t_1 and t_2 after the end of the pulse. As the temperature of the junction is varied, the $[t_1;t_2]$ time window gives different ΔC, as depicted in Figure 2.12.

- At low temperature, the emission rate of the trapped carrier is low and the transient is typically long compared to the time window → ΔC is small.
- Near the peak temperature, the emission time constant is of the same order of magnitude as the time window → ΔC is large.
- At high temperature, the emission rate of the trapped carrier is high and the transient typically short compared to the time window → ΔC is small

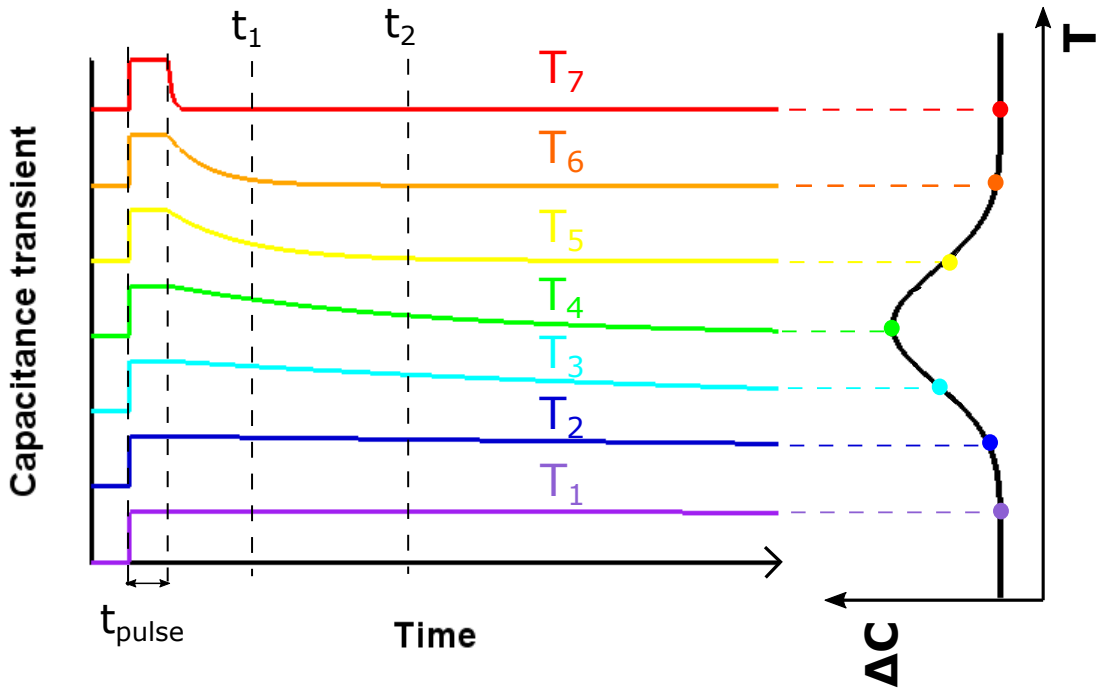

Figure 2.12: Schematics of capacitance transient after applying a voltage pulse and for different temperatures. The DLTS signal $\Delta C = C(t_2) - C(t_1)$ is reported on the right figure along the temperature.

To get the electrical properties of the defect, we analyze the capacitance transient at different temperatures around the DLTS peak. We use Equation 2.7 expressed as an Arrhenius relation:

$$\ln(\frac{e_{e,h}}{T^2}) = \ln(A^*_{e,h}\sigma_{e,h}) - \frac{E_A}{kT} \tag{2.8}$$

By plotting $\ln(\frac{e_{e,h}}{T^2})$ as a function of $\frac{1}{T}$, the "signature" of the defect *i.e.* its capture cross-sections $\sigma_{e,h}$ and its activation energy E_A can be calculated.

Finally, the trap concentration N_t is obtained by measuring ΔC after having completely filled the traps (typically with a long voltage pulse):

$$N_t = 2N_{eff}\frac{\Delta C}{C_\infty} \tag{2.9}$$

where N_{eff} is the effective doping concentration and C_∞ is the capacitance at reverse bias condition.

2.3.4 DLTS characterization of the defects in InGaAsN

Since the early development of dilute nitrides, DLTS has been extensively used to study the electrical properties of defects in InGaAsN. The information DLTS provides can be related to the non-radiative recombination rate and the dark saturation current density, making it a very powerful technique for solar cell analysis. We propose in Table 2.1 a non-exhaustive list of growth-defects probed by DLTS. Irradiation-induced defects in InGaAsN are mentioned in Section 2.5.

It can first be noted that most of the studies do not report on the atomic nature of the measured defects. To be able to associate the defect's crystal structure with its electrical signature, a strong correlation between DLTS and structural characterization needs to be observed. LVM measured by FTIR [55] and SIMS hydrogen analysis [56] were used to establish correlation between DLTS results and N-H bonds concentration. Using DLTS, Elleuch et al. characterized GaAsN layers grown by CBE with hydrogen and deuterium-based precursors. They found a slight shift of the trap activation energies between the two isotopes, indicating that the defects were based on hydrogen [57]. Also, the DLTS traps can be associated to a certain atomic structure when the experimental data fit theoretical prediction. Krispin et al. [58] attributed one of their defect signature to a $(\text{N-As})_{As}$ structure based on *ab-initio* calculations [47].

In addition, we see in Table 2.1 that the reported DLTS results are noticeably different from one author to the next. This arises from the fact that the dilute nitrides characterized in this table are not of the same nature, having different compositions and bandgap energies. Furthermore, the crystal quality of dilute nitrides is strongly dependent on the growth conditions, as illustrated by the shift in activation energy reported for defects in InGaAsN grown under different *As/III* ratios [32].

Table 2.1: Review of reported deep-level defects in dilute nitrides. References marked with * used admittance spectroscopy rather than DLTS. Reported values were averaged for the sake of clarity.

Reference	Growth method	Material	E_t (eV)	σ (cm^2)	N_t (cm^{-3})	Defect
Kwon1999 [59]	MOCVD	1.05 eV InGaAsN	$E_V + 0.1$		3.5×10^{14}	
			$E_V + 0.23$		3.8×10^{14}	
			$E_V + 0.48$		8.2×10^{14}	
Kaplar2002 [23]	MBE	1.05 eV InGaAsN	$E_V + 0.37$	3×10^{-13}	3×10^{14}	
			$E_V + 0.51$	4×10^{-14}	1×10^{14}	
			$E_V + 0.71$	3×10^{-15}	1×10^{14}	
			$E_C - 0.56$	2×10^{-17}	3×10^{13}	
Krispin2003 [58]	MBE	GaAsN	$E_V + 0.8$		1×10^{16}	$(N\text{-}N)_{As}$
			$E_V + 1.1$		1.3×10^{17}	$(N\text{-}As)_{As}$
Johnston2005 [60]	MOCVD	1.3 eV GaAsN	$E_C - 0.2$	5×10^{-16}	1.5×10^{15}	
Khan2007 [22]	MOCVD	(In)GaAsN	$E_C - 0.2$	8.9×10^{-15}	1×10^{16}	
Jackrel2007 [24]	MOCVD	InGaAsN	$E_C - 0.6$	1×10^{-15}	2.6×10^{14}	
		InGaAsNSb	$E_C - 0.53$	5.1×10^{-13}	1.3×10^{14}	
Yamaguchi2012 [55]	CBE	GaAsN	$E_V + 0.15$		3×10^{14}	$(N\text{-}H)_{As}$
			$E_C - 0.33$			$(N\text{-}As)_{As}$
Elleuch2015 [57]	CBE	GaAsN	$E_C - 0.11$			$(N\text{-}H)_{As}$
			$E_C - 0.19$			$(N\text{-}H)_{As}$
Polojärvi2016a [26]	MBE	1eV (In)GaAsNSb	$E_A = 0.56$	4×10^{-14}	1×10^{14}	
Polojärvi2016b [32]	MBE	1eV InGaAsN	$E_A = 0.1 - 0.11$	2×10^{-15}	3×10^{14}	
			$E_A = 0.25 - 0.36$		5×10^{13}	
			$E_A = 0.45 - 0.48$	2×10^{-15}	1×10^{14}	
Baranov2018* [33]	MBE	1eV InGaAsN	$E_A = 0.5$	1×10^{-15}	1×10^{15}	
			$E_A = 0.2$	1×10^{-16}	1×10^{15}	
He2018* [56]	MBE	InGaAsNSb	$E_A = 0.23$	8.4×10^{-15}	7×10^{14}	
			$E_A = 0.39$	3×10^{-13}	1.2×10^{15}	$(N\text{-}H)_{As}$

2.3.5 Carriers properties and transport mechanisms in InGaAsN solar cells

The numerous crystal defects previously mentioned have a large impact on the carriers properties in InGaAsN. Just as for defects, there is a wide spectrum of reported values for carrier lifetime, mobility and diffusion length, depending on the composition and the growth conditions of dilute nitrides.

The hole lifetime in 1 eV InGaAsN(Sb) was measured by time-resolved photoluminescence (TRPL) to range from 0.2 to 0.74 ns ($n \approx 10^{15} - 10^{16}\ cm^{-3}$) [24], which is two orders of magnitude shorter than in GaAs. Gubanov et al. measured an even shorter lifetime of 50 ps in as-grown 1 eV InGaAsN but reported a longer lifetime around 600 ps after thermal annealing [61]. These short carrier lifetimes arise from high non-radiative recombination rate on deep levels introduced by crystal defects. Optimization of the growth conditions can increase the carrier lifetime up to 4 ns, as reported for 0.9 eV InGaAsN [36].

The carrier mobility is also strongly degraded with the introduction of nitrogen. In InGaAsN with N content larger than 1 %, the hole mobility is measured to range from 20 to 150 $cm^2/V.s$ [14, 17, 19, 62]. As for electrons, a much larger mobility decrease is reported: μ_e goes from 8000 in GaAs [63] to values ranging from 170 to 300 $cm^2/V.s$ for $InGaAsN_x$ with $x \in [0.01 - 0.02]$ [17, 43, 62]. Several hypotheses were advanced to explain this significant degradation of the electron transport properties. It could be caused by alloy or impurity scattering, large scale inhomogeneities (typically larger than the electron mean free path) [17] or it could simply arise from the band nature of InGaAsN. Skierbiszewski et al performed PL analysis on GaAsN/GaAs quantum wells and conducted BAC model calculations showing that the decrease in electronic mobility was related to the increase of the electron effective mass m_e^* [64]. Their findings imply that the electron mobility is intrinsically limited in InGaAsN.

Short lifetime and low mobility in InGaAsN lead to low minority carrier diffusion length (*cf* equations 1.11 and 1.12 in Chapter 1). Fitting the IQE of $InGaAsN_{0.02}$ MOVPE-grown solar cells, Kurtz et al. found a hole diffusion length equals to 0.9 μm and an electron diffusion length as low as 0.01 μm [17]. These results were obtained for annealed samples as a previous report showed on similar cells an increase in the hole diffusion length from 0.25 μm to 0.7 μm after annealing at 650 °C for 30 min [16].

Low diffusion length is a major issue for solar cells as minority carriers typically need to diffuse over hundreds of nanometres to be collected. To overcome this limitation, *p-i-n* architectures relying on drift transport were developed. The most standard structure is p-GaAs/NID-InGaAsN/n-GaAs where the dilute nitride layer is non-intentionally doped. Depending on the residual doping and the thickness of the InGaAsN layer, the depletion region can extend across the entire absorber, making the solar cell much less dependent on diffusion length. However, relatively high mobilities are still required for the carriers to drift along the electric field and be collected.

In order to get full absorption of the near infrared light ($\lambda > 870$ nm), structures were designed with an absorber thickness equal or larger than 1 μm. Low residual doping was then needed as the depletion region thickness can be written as:

$$\omega_{SCR} = \sqrt{\frac{2\epsilon_0\epsilon_r}{q} \times (\frac{1}{N_A} + \frac{1}{N_D}) \times V_{bi}} \tag{2.10}$$

where N_A and N_D are the net acceptor and donor concentrations on both sides of the junction, and where V_{bi} is the built-in voltage. In a *p-i-n* architecture, the SCR can be located either at the *p-i* or at the *i-n* interface depending on the type of the BGCC. Assuming the dielectric permittivity of InGaAsN is equal to the one of GaAs (ϵ_r=12.9) and considering a built-in voltage of 0.5 V for a 1 eV solar cell, the residual doping needs to be lower than 7×10^{14} cm^{-3} for the SCR to spread accross more than 1 μm.

To ensure low BGCC, the impurity contamination needs to be reduced as much as possible. Growth with MBE rather than MOVPE was then advocated [20] and BGCC as low as 10^{14} cm^{-3} were demonstrated [21]. However, high residual doping levels are still observed in MBE-grown InGaAsN, arising from acceptor or donor defects. This phenomenon is called "intrinsic-doping" and can only be mitigated through optimization of the growth parameters. Ptak et al. showed that the type and the amplitude of the residual doping could be controlled by changing the growth temperature, leading to very low BGCC at around 520 °C [65]. The *As/III* ratio is also known to have a strong influence on the resulting doping concentration [32, 66].

2.3.6 Effect of post-growth thermal annealing on InGaAsN properties

Post-growth annealing is generally conducted on dilute nitrides as it is reported to cure growth defects [22], increase carrier lifetime [61] and enhance minority carrier diffusion length [16]. The impact of annealing on the residual doping is somewhat still unclear. Some studies report on a decrease in the BGCC with annealing [67] while others conclude on the opposite behaviour [66]. A possible explanation for this discrepancy is the difference in the as-grown material, as the annealing effect was shown to depend largely on the growth temperature [65]. Also, BGCC type conversion was observed in [65] and [66] when the growth conditions were changed. Considering that the residual doping of the MBE-grown layer is mostly intrinsic, type conversion indicates that compensation mechanisms exist in InGaAsN and that curing certain defects through annealing can both decrease or increase the effective BGCC.

Another interesting but restricting behaviour is the blueshift that dilute nitrides typically undergo during thermal annealing (20 to 100 meV). During the epitaxial growth, nitrogen atoms tend to regroup in chain-like structures in the

[001]-direction [68, 69]. The formation of long N-chains in the growth direction was indeed calculated to be energetically favorable in GaAsN [69, 70]. Furthermore, the nitrogen atoms in these chains are typically bonded to Ga atoms because the cohesive energy of GaN (2.24 eV) is larger than for InN (1.93 eV) [71]. However, the InGaAsN alloy tends to minimize its inner strain when it is thermally annealed. Through nitrogen atoms diffusion, long InAs bonds (2.61 Å) and short GaN bonds (1.94 Å) give way to GaAs (2.45 Å) and InN (2.15 Å) orderings. The N nearest-neighbour configuration goes then from Ga to In-rich [25, 72], which raises the InGaAsN conduction band and induces a blueshift [73, 74].

While post-growth thermal annealing is a very effective way of achieving high quality InGaAsN, it can be a problematic step to implement during MJSC monolithic growth. Indeed, degradation of tunnel junctions [75, 76, 77] dopant out-diffusion [78] and InGaAsN bandgap blueshift are multiple issues that can occur after thermal annealing. This constitutes a motivation to try to optimize the growth conditions of InGaAsN in such a way thermal annealing is no longer necessary.

2.4 InGaAsN subcells in MJSC

Through numerous trial and error empirical studies, the growth and the annealing conditions were optimized for InGaAsN solar cells. Photocurrents higher than 15 mA/cm^2 were obtained under AM0>870 nm for $E_g \leq 1$ eV. In Figure 2.13, we calculated the photocurrents of InGaAsN cells integrating their reported quantum efficiency over the AM0 spectrum. It should be noted that in certain cases, high J_{sc} was traded for low fill-factor and V_{oc} [66, 79].

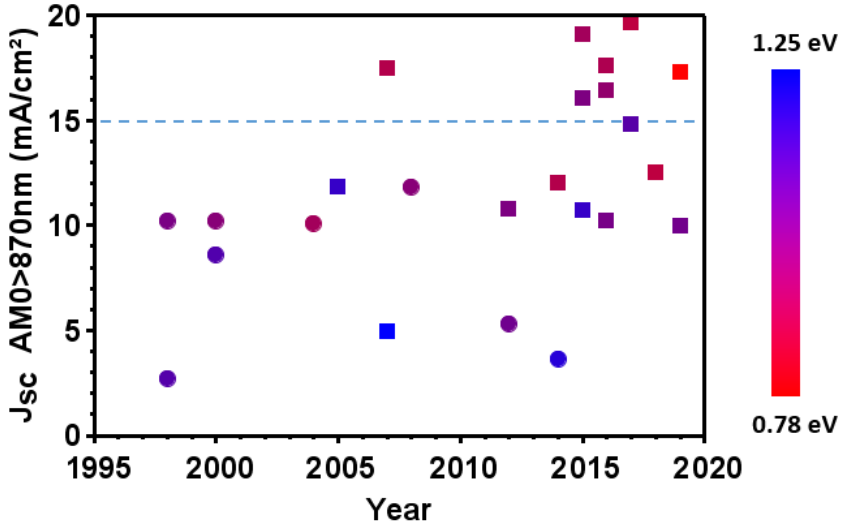

Figure 2.13: Photocurrent of InGaAsN cells calculated from quantum efficiencies reported in the literature. Square and circle markers correspond to MBE and MOCVD-grown samples, respectively. The color of the markers indicates the bandgap of the absorber.

Some InGaAsN subcells could then satisfy the current and lattice-matching conditions. Cells displaying in addition high FF and V_{oc} were then integrated within triple-junction, replacing the Ge bottom cell. Solar Junction reported on a 5.5 mm^2 GaInP/GaAs/InGaAsNSb 3J for CPV applications [27] and a 31 % 3J for space applications was demonstrated by CESI and Tampere University [34].

However, integrating a InGaAsN subcell with $E_g \leq 1$ eV in a MJSC considerably reduces the amount of light available for the Ge bottom cell. Figure 2.14 shows the light management in a hypothetical 4J including a 1.0 eV dilute nitride cell with a 70 % quantum efficiency in the [870-1240 nm] window. The quantum efficiencies of GaInP, GaAs and Ge subcells were taken from AZURSPACE's "3G30-advanced" triple-junction [80].

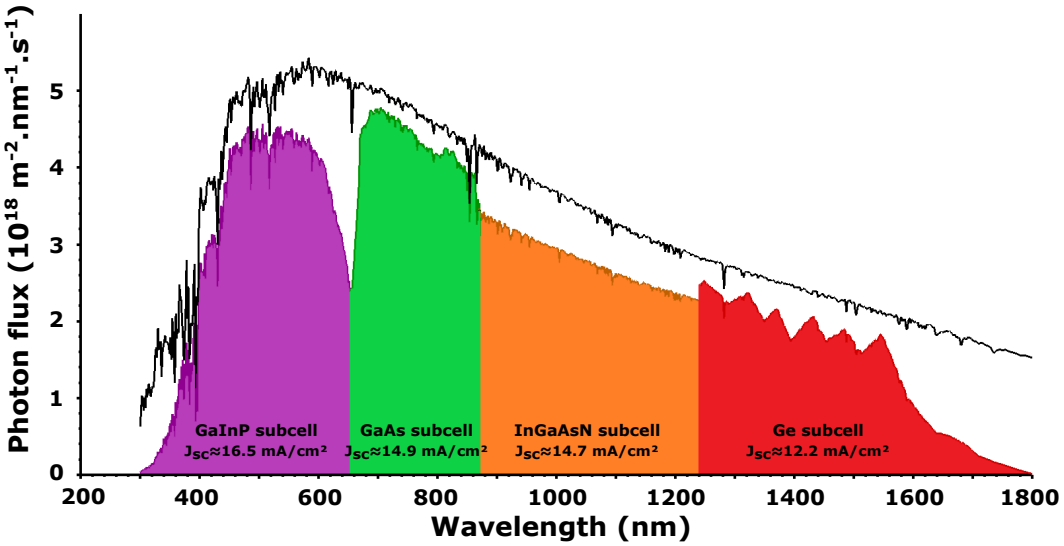

Figure 2.14: Photon flux spectrum with collection efficiency and associated photocurrent in each subcell.

Thinning of the top junctions and dilute nitride subcell with E_g>1 eV are then necessary to respect the current-matching condition. 4J architectures with two $InGaAsN_x$ bottom cells (1.2 and 0.9 eV) were demonstrated with roughly a 11 mA/cm^2 photocurrent under AM1.5D sunlight, leading to 39 % efficiency under 560-sun illumination [37]. On the other hand, Solar Junction announced in 2017 they were developing a dilute nitride-based 4J on Ge for space applications [81]. Modelling was also performed on GaInP/GaInAs/GaNAsSb/Ge 4J using dilute nitride characterization results. It showed that efficiencies as high as 47 % and 33 % under AM1.5D ×1000 and AM0 could be achieved with proper growth and annealing optimizations [82].

2.5 Degradation of InGaAsN under space radiations

For a dilute nitride subcell to be used in MJSC for space applications, it needs to be robust to radiations. A review of the few articles published on this specific topic is conducted here.

Kurtz et al. conducted a first irradiation study on 1 eV InGaAsN solar cells grown by MOVPE in 2002 [83]. They observed a low degradation rate of the cells under 1 MeV electron exposure as illustrated in Figure 2.15. Irradiation with 1 MeV electrons was also performed on optimized InGaAsN subcells grown by MBE, showing a large J_{sc} and V_{oc} decrease [34]. This higher degradation rate probably arises from the better BOL crystal quality, making the material more sensitive to irradiation-induced defects.

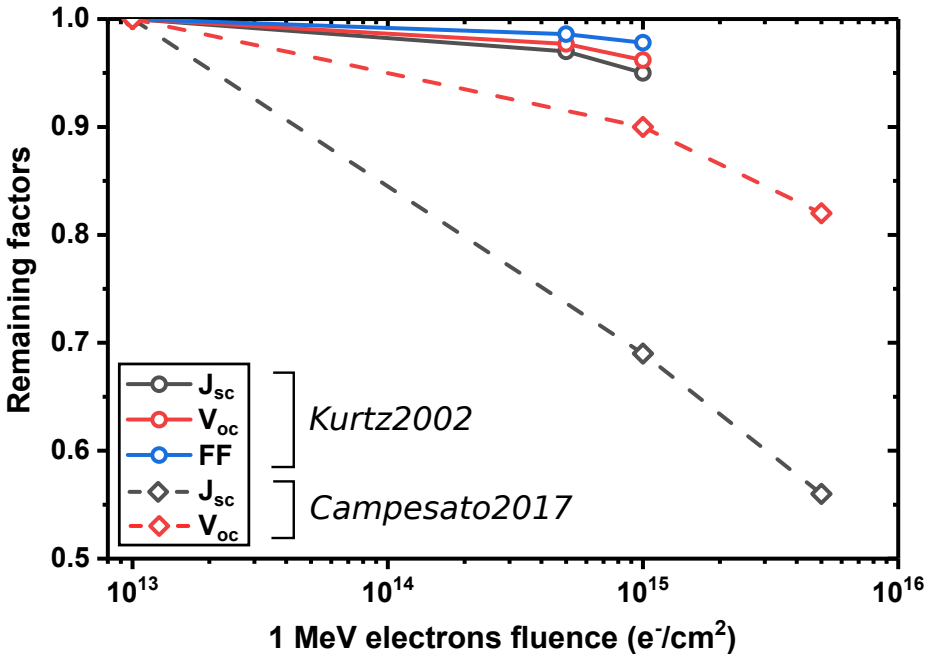

Figure 2.15: Remaining factor of short-circuit current, open-circuit voltage and fill factor of InGaAsN solar cells irradiated with 1 MeV electrons.

An increase in the concentration of N-related electron traps (E_C-0.2) and the introduction of hole traps (E_V+0.75) after 1 MeV electron irradiation was observed by DLTS in p-InGaAsN [84]. Degradation of the photoluminescence signal was also observed in $In_{0.34}GaAsN_{0.012}$ quantum wells irradiated with 2×10^{16} electrons/cm^2 (E_{e^-}=7 MeV) [85]. Interestingly, the PL intensity was found to be the highest for samples irradiated and subsequently annealed at 650 °C. This possibly indicates that point defects introduced through irradiation facilitate atomic diffusion, which enhances the effect of thermal annealing. This increase in the PL intensity after irradiation and annealing was also observed in 1 eV InGaAsN lattice-matched to GaAs [86]. Additionally, a 35 % increase in luminescence intensity was measured after 10^{14} electrons/cm^2 (E_{e^-}=7 MeV) without annealing step. This pointed out a decrease in the non-radiative recombination rate which

was attributed to recombination-enhanced annealing mechanisms.

As for proton irradiation, studies were only conducted on lattice-mismatched dilute nitride layers with very low N content (<0.5 %) [87, 88], showing both introduction and annealing of deep level defects.

Chapter 2 conclusion

InGaAsN has been studied since the early 90's and is today one of the main material candidates to increase MJSC efficiency. Using MBE, low BGCC can be obtained and high photocurrents were achieved. The integration of a dilute nitride cell within MJSC was demonstrated in different architectures. Efforts remain yet to be made on the growth optimization in order to reduce defects concentration and ensure high V_{oc}. Finally, we reviewed irradiation studies and noticed that opposite behaviours were experienced in irradiated InGaAsN. Further studies are required to understand both the degradation and the annealing mechanisms occurring in InGaAsN upon irradiation.

In the framework of this thesis, we propose to characterize thoroughly InGaAsN before and after irradiation to understand these mechanisms. To do that, characterizations of both the material and the solar cell will be conducted in order to correlate optolectronic properties with photovoltaic parameters.

Bibliography

[1] J. Matthews and A. Blakeslee, "Defects in epitaxial multilayers: I. Misfit dislocations," *Journal of Crystal growth*, vol. 27, pp. 118–125, 1974.

[2] M. G. Mauk, "Liquid-Phase Epitaxy," in *Handbook of Crystal Growth*. Elsevier, 2015, pp. 225–316.

[3] P. Capper, S. Irvine, and T. Joyce, "Epitaxial crystal growth: methods and materials," in *Springer Handbook of Electronic and Photonic Materials*. Springer, 2017, pp. 1–1.

[4] H. Manasevit and W. I. Simpson, "The use of metal-organics in the preparation of semiconductor materials: I. Epitaxial gallium-V compounds," *Journal of the Electrochemical Society*, vol. 116, no. 12, p. 1725, 1969.

[5] W. Tsang, "Chemical beam epitaxy of InP and GaAs," *Applied Physics Letters*, vol. 45, no. 11, pp. 1234–1236, 1984.

[6] A. Cho, "Morphology of epitaxial growth of GaAs by a molecular beam method: The observation of surface structures," *Journal of Applied Physics*, vol. 41, no. 7, pp. 2780–2786, 1970.

[7] R. Farrow, "MBE growth of II-VI and IV-VI compounds and alloys," in *Molecular Beam Epitaxy and Heterostructures*. Springer, 1985, pp. 227–262.

[8] M. Weyers, M. Sato, and H. Ando, "Red shift of photoluminescence and absorption in dilute GaAsN alloy layers," *Japanese Journal of Applied Physics*, vol. 31, no. 7A, p. L853, 1992.

[9] M. Kondow, K. Uomi, A. Niwa, T. Kitatani, S. Watahiki, and Y. Yazawa, "GaInNAs: A novel material for long-wavelength-range laser diodes with excellent high-temperature performance," *Japanese journal of applied physics*, vol. 35, no. 2S, p. 1273, 1996.

[10] K. Louarn, "Etude et réalisation de jonctions tunnel à base d'hétérostructures à semiconducteurs III-V pour les cellules solaires multi-jonction à très haut rendement," Ph.D. dissertation, Université Toulouse 3 Paul Sabatier, 2018.

[11] P. K. Chiang, J. H. Ermer, W. T. Nishikawa, D. D. Krut, D. E. Joslin, J. W. Eldredge, B. T. Cavicchi, and J. M. Olson, "Experimental results of $GaInP_2$/GaAs/Ge triple junction cell development for space power systems," *Conference Record of the IEEE Photovoltaic Specialists Conference*, pp. 183–186, 1996.

[12] D. Lillington, H. Cotal, J. Ermer, D. Friedman, T. Moriarty, and A. Duda, "32.3% efficient triple junction $GaInP_2$/GaAs/Ge concentrator solar cells," in *Collection of Technical Papers. 35th Intersociety Energy Conversion Engineering Conference and Exhibit (IECEC)(Cat. No. 00CH37022)*, vol. 1. IEEE, 2000, pp. 516–521.

[13] S. R. Kurtz, D. Myers, and J. M. Olson, "Projected performance of three-and four-junction devices using GaAs and GaInP," in *Conference Record of the Twenty Sixth IEEE Photovoltaic Specialists Conference-1997*. IEEE, 1997, pp. 875–878.

[14] J. Geisz, D. Friedman, J. Olson, S. R. Kurtz, and B. Keyes, "Photocurrent of 1 eV GaInNAs lattice-matched to GaAs," *Journal of Crystal Growth*, vol. 195, no. 1-4, pp. 401–408, 1998.

[15] D. Friedman, J. Geisz, S. R. Kurtz, and J. Olson, "1-eV solar cells with GaInNAs active layer," *Journal of Crystal Growth*, vol. 195, no. 1-4, pp. 409–415, 1998.

[16] S. R. Kurtz, A. Allerman, E. Jones, J. Gee, J. Banas, and B. Hammons, "InGaAsN solar cells with 1.0 eV band gap, lattice matched to GaAs," *Applied Physics Letters*, vol. 74, no. 5, pp. 729–731, 1999.

[17] S. R. Kurtz, A. A. Allerman, C. H. Seager, R. M. Sieg, and E. D. Jones, "Minority carrier diffusion, defects, and localization in InGaAsN, with 2% nitrogen," *Applied Physics Letters*, vol. 77, no. 3, pp. 400–402, 2000.

[18] K. Bertness, S. R. Kurtz, D. J. Friedman, A. Kibbler, C. Kramer, and J. Olson, "29.5%-efficient GaInP/GaAs tandem solar cells," *Applied Physics Letters*, vol. 65, no. 8, pp. 989–991, 1994.

[19] F. Dimroth, C. Baur, A. Bett, K. Volz, and W. Stolz, "Comparison of dilute nitride growth on a single-and 8×4-inch multiwafer MOVPE system for solar cell applications," *Journal of crystal growth*, vol. 272, no. 1-4, pp. 726–731, 2004.

[20] A. Ptak, S. Johnston, S. Kurtz, D. Friedman, and W. Metzger, "A comparison of MBE-and MOCVD-grown GaInNAs," *Journal of crystal growth*, vol. 251, no. 1-4, pp. 392–398, 2003.

[21] A. Ptak, D. Friedman, S. Kurtz, and R. Reedy, "Low-acceptor-concentration GaInNAs grown by molecular-beam epitaxy for high-current p-i-n solar cell applications," *Journal of Applied Physics*, vol. 98, no. 9, p. 094501, 2005.

[22] A. Khan, S. R. Kurtz, S. Prasad, S. Johnston, and J. Gou, "Correlation of nitrogen related traps in InGaAsN with solar cell properties," *Applied physics letters*, vol. 90, no. 24, p. 243509, 2007.

[23] R. Kaplar, S. Ringel, S. R. Kurtz, J. Klem, and A. Allerman, "Deep-level defects in InGaAsN grown by molecular-beam epitaxy," *Applied physics letters*, vol. 80, no. 25, pp. 4777–4779, 2002.

[24] D. B. Jackrel, S. R. Bank, H. B. Yuen, M. A. Wistey, J. S. Harris Jr, A. J. Ptak, S. W. Johnston, D. J. Friedman, and S. R. Kurtz, "Dilute nitride GaInNAs and GaInNAsSb solar cells by molecular beam epitaxy," *Journal of Applied Physics*, vol. 101, no. 11, p. 114916, 2007.

[25] K. Volz, D. Lackner, I. Nemeth, B. Kunert, W. Stolz, C. Baur, F. Dimroth, and A. Bett, "Optimization of annealing conditions of (GaIn)(NAs) for solar cell applications," *Journal of Crystal Growth*, vol. 310, no. 7-9, pp. 2222–2228, 2008.

[26] V. Polojärvi, A. Aho, A. Tukiainen, A. Schramm, and M. Guina, "Comparative study of defect levels in GaInNAs, GaNAsSb, and GaInNAsSb for high-efficiency solar cells," *Applied Physics Letters*, vol. 108, no. 12, p. 122104, 2016.

[27] D. Derkacs, R. Jones-Albertus, F. Suarez, and O. Fidaner, "Lattice-matched multijunction solar cells employing a 1 eV GaInNAsSb bottom cell," *Journal of Photonics for Energy*, vol. 2, no. 1, p. 021805, 2012.

[28] N. Miyashita, N. Ahsan, and Y. Okada, "Generation and collection of photocarriers in dilute nitride GaInNAsSb solar cells," *Progress in Photovoltaics: Research and Applications*, vol. 24, no. 1, pp. 28–37, 2016.

[29] N. Miyashita, Y. He, N. Ahsan, and Y. Okada, "Anneal mediated deep-level dynamics in GaInNAsSb dilute nitrides lattice-matched to GaAs," *Journal of Applied Physics*, vol. 126, no. 14, p. 143104, 2019.

[30] T. Kim, K. Kim, J. Lee, T. Kuech, L. Mawst, N. Wells, S. LaLumondiere, Y. Sin, W. Lotshaw, and S. Moss, "Impact of thermal annealing on bulk InGaAsSbN materials grown by metal-organic vapor phase epitaxy," *Applied Physics Letters*, vol. 104, no. 5, p. 051915, 2014.

[31] A. Aho, V. Polojärvi, V.-M. Korpijärvi, J. Salmi, A. Tukiainen, P. Laukkanen, and M. Guina, "Composition dependent growth dynamics in molecular beam epitaxy of GaInNAs solar cells," *Solar Energy Materials and Solar Cells*, vol. 124, pp. 150–158, 2014.

[32] V. Polojärvi, A. Aho, A. Tukiainen, M. Raappana, T. Aho, A. Schramm, and M. Guina, "Influence of As/group-III flux ratio on defects formation and photovoltaic performance of GaInNAs solar cells," *Solar Energy Materials and Solar Cells*, vol. 149, pp. 213–220, 2016.

[33] A. I. Baranov, A. S. Gudovskikh, D. A. Kudryashov, A. A. Lazarenko, I. A. Morozov, A. M. Mozharov, E. V. Nikitina, E. V. Pirogov, M. S. Sobolev, K. S. Zelentsov *et al.*, "Defect properties of InGaAsN layers grown as sub-monolayer digital alloys by molecular beam epitaxy," *Journal of Applied Physics*, vol. 123, no. 16, p. 161418, 2018.

[34] R. Campesato, A. Tukiainen, A. Aho, G. Gori, R. Isoaho, E. Greco, and M. Guina, "31% European InGaP/GaAs/InGaAs Solar Cells for Space Application," in *E3S web of conferences*, vol. 16. EDP Sciences, 2017, p. 03003.

[35] A. Tukiainen, A. Aho, G. Gori, V. Polojärvi, M. Casale, E. Greco, R. Isoaho, T. Aho, M. Raappana, R. Campesato *et al.*, "High-efficiency GaInP/GaAs/GaInNAs solar cells grown by combined MBE-MOCVD technique," *Progress in Photovoltaics: Research and Applications*, vol. 24, no. 7, pp. 914–919, 2016.

[36] A. Aho, R. Isoaho, L. Hytönen, T. Aho, M. Raappana, V. Polojärvi, A. Tukiainen, J. Reuna, S. Mäkelä, and M. Guina, "Lattice-matched four-junction tandem solar cell including two dilute nitride bottom junctions," *Progress in Photovoltaics: Research and Applications*, vol. 27, no. 4, pp. 299–305, 2019.

[37] A. Aho, R. Isoaho, M. Raappana, T. Aho, E. Anttola, J. Lyytikäinen, A. Hietalahti, V. Polojärvi, A. Tukiainen, J. Reuna *et al.*, "Wide spectral coverage (0.7–2.2 eV) lattice-matched multijunction solar cells based on AlGaInP, AlGaAs and GaInNAsSb materials," *Progress in Photovoltaics: Research and Applications*, 2021.

[38] S.-H. Wei and A. Zunger, "Giant and composition-dependent optical bowing coefficient in GaAsN alloys," *Physical review letters*, vol. 76, no. 4, p. 664, 1996.

[39] U. Tisch, E. Finkman, and J. Salzman, "The anomalous bandgap bowing in GaAsN," *Applied physics letters*, vol. 81, no. 3, pp. 463–465, 2002.

[40] S. Paul, J. Roy, and P. Basu, "Empirical expressions for the alloy composition and temperature dependence of the band gap and intrinsic carrier density in $Ga_xIn_{1-x}As$," *Journal of applied physics*, vol. 69, no. 2, pp. 827–829, 1991.

[41] W. Shan, W. Walukiewicz, J. Ager III, E. Haller, J. Geisz, D. Friedman, J. Olson, and S. R. Kurtz, "Band anticrossing in GaInNAs alloys," *Physical Review Letters*, vol. 82, no. 6, p. 1221, 1999.

[42] S. Turcotte, "Propriétés Optoélectroniques d'Hétérostructures de Ga(In)AsN," Ph.D. dissertation, Ecole Polytechnique de Montréal, 2008.

[43] W. Li, M. Pessa, T. Ahlgren, and J. Decker, "Origin of improved luminescence efficiency after annealing of Ga(In)NAs materials grown by molecular-beam epitaxy," *Applied Physics Letters*, vol. 79, no. 8, pp. 1094–1096, 2001.

[44] S. G. Spruytte, C. W. Coldren, J. S. Harris, W. Wampler, P. Krispin, K. Ploog, and M. C. Larson, "Incorporation of nitrogen in nitride-arsenides: Origin of improved luminescence efficiency after anneal," *Journal of Applied Physics*, vol. 89, no. 8, pp. 4401–4406, 2001.

[45] T. Ahlgren, E. Vainonen-Ahlgren, J. Likonen, W. Li, and M. Pessa, "Concentration of interstitial and substitutional nitrogen in GaN_xAs_{1-x}," *Applied physics letters*, vol. 80, no. 13, pp. 2314–2316, 2002.

[46] M. Reason, H. McKay, W. Ye, S. Hanson, R. Goldman, and V. Rotberg, "Mechanisms of nitrogen incorporation in GaAsN alloys," *Applied physics letters*, vol. 85, no. 10, pp. 1692–1694, 2004.

[47] S. Zhang and S.-H. Wei, "Nitrogen solubility and N-induced defect complexes in epitaxial GaAs: N," *Physica B: Condensed Matter*, vol. 308, pp. 839–842, 2001.

[48] K. Nishimura, H. Suzuki, K. Saito, Y. Ohshita, N. Kojima, and M. Yamaguchi, "Electrical properties of GaAsN film grown by chemical beam epitaxy," *Physica B: Condensed Matter*, vol. 401, pp. 343–346, 2007.

[49] F. Ishikawa, S. Fuyuno, K. Higashi, M. Kondow, M. Machida, H. Oji, J.-Y. Son, A. Trampert, K. Umeno, Y. Furukawa *et al.*, "Direct observation of N-(group V) bonding defects in dilute nitride semiconductors using hard x-ray photoelectron spectroscopy," *Applied Physics Letters*, vol. 98, no. 12, p. 121915, 2011.

[50] W. Fan, S. F. Yoon, T. K. Ng, S. Wang, W. K. Loke, R. Liu, and A. Wee, "Comparison of nitrogen compositions in the as-grown GaN_xAs_{1-x} on GaAs measured by high-resolution x-ray diffraction and secondary-ion mass spectroscopy," *Applied physics letters*, vol. 80, no. 22, pp. 4136–4138, 2002.

[51] J. Toivonen, T. Hakkarainen, M. Sopanen, H. Lipsanen, J. Oila, and K. Saarinen, "Observation of defect complexes containing Ga vacancies in GaAsN," *Applied Physics Letters*, vol. 82, no. 1, pp. 40–42, 2003.

[52] A. Janotti, S.-H. Wei, S. Zhang, S. Kurtz, and C. Van de Walle, "Interactions between nitrogen, hydrogen, and gallium vacancies in $GaAs_{1-x}N_x$ alloys," *Physical Review B*, vol. 67, no. 16, p. 161201, 2003.

[53] D. Murdick, X. Zhou, and H. Wadley, "Low-temperature atomic assembly of stoichiometric gallium arsenide from equiatomic vapor," *Journal of crystal growth*, vol. 286, no. 1, pp. 197–204, 2006.

[54] D. Lang, "Deep-level transient spectroscopy: A new method to characterize traps in semiconductors," *Journal of applied physics*, vol. 45, no. 7, pp. 3023–3032, 1974.

[55] M. Yamaguchi, B. Bouzazi, H. Suzuki, K. Ikeda, N. Kojima, and Y. Ohshita, "(In) GaAsN materials and solar cells for super-high-efficiency multijunction solar cells," in *2012 38th IEEE Photovoltaic Specialists Conference*. IEEE, 2012, pp. 000 831–000 834.

[56] Y. He, N. Miyashita, and Y. Okada, "N-H-related deep-level defects in dilute nitride semiconductor GaInNAs for four-junction solar cells," *Japanese Journal of Applied Physics*, vol. 57, 2018.

[57] O. Elleuch, L. Wang, K.-H. Lee, K. Ikeda, N. Kojima, Y. Ohshita, and M. Yamaguchi, "Identification of N–H related acceptor defects in GaAsN grown by chemical beam epitaxy using hydrogen isotopes," *Journal of Alloys and Compounds*, vol. 649, pp. 815–818, 2015.

[58] P. Krispin, V. Gambin, J. Harris, and K. Ploog, "Nitrogen-related electron traps in Ga (As, N) layers (< 3% N)," *Journal of Applied Physics*, vol. 93, no. 10, pp. 6095–6099, 2003.

[59] D. Kwon, R. Kaplar, S. Ringel, A. Allerman, S. R. Kurtz, and E. Jones, "Deep levels in p-type InGaAsN lattice matched to GaAs," *Applied physics letters*, vol. 74, no. 19, pp. 2830–2832, 1999.

[60] S. Johnston, S. Kurtz, D. Friedman, A. Ptak, R. Ahrenkiel, and R. Crandall, "Electron traps in p-type GaAsN characterized by deep-level transient spectroscopy," in *Conference Record of the Thirty-first IEEE Photovoltaic Specialists Conference, 2005.* IEEE, 2005, pp. 599–602.

[61] A. Gubanov, V. Polojärvi, A. Aho, A. Tukiainen, N. V. Tkachenko, and M. Guina, "Dynamics of time-resolved photoluminescence in GaInNAs and GaNAsSb solar cells," *Nanoscale research letters*, vol. 9, no. 1, pp. 1–4, 2014.

[62] N. Miyashita, Y. Shimizu, N. Kobayashi, Y. Okada, and M. Yamaguchi, "Fabrication of GaInNAs-based solar cells for application to multi-junction tandem solar cells," in *2006 IEEE 4th World Conference on Photovoltaic Energy Conference*, vol. 1. IEEE, 2006, pp. 869–872.

[63] M. R. Brozel and G. E. Stillman, *Properties of Gallium Arsenide*. INSPEC, London, 1996.

[64] C. Skierbiszewski, I. Gorczyca, S. Łepkowski, J. Łusakowski, J. Borysiuk, and J. Toivonen, "The electron effective mass at the bottom of the GaNAs conduction band," *Semiconductor science and technology*, vol. 19, no. 10, p. 1189, 2004.

[65] A. Ptak, D. Friedman, and S. Kurtz, "Effects of temperature, nitrogen ions, and antimony on wide depletion width GaInNAs," *Journal of Vacuum Science & Technology B: Microelectronics and Nanometer Structures Processing, Measurement, and Phenomena*, vol. 25, no. 3, pp. 955–959, 2007.

[66] F. Langer, S. Perl, S. Höfling, and M. Kamp, "p-to n-type conductivity transition in 1.0 eV GaInNAs solar cells controlled by the V/III ratio," *Applied Physics Letters*, vol. 106, no. 6, p. 063905, 2015.

[67] S. Kurtz, R. King, D. Law, A. Ptak, J. Geisz, and N. Karam, "Effects of in situ annealing on GaInNAs solar cells," in *2013 IEEE 39th Photovoltaic Specialists Conference (PVSC)*. IEEE, 2013, pp. 2095–2099.

[68] K. Volz, T. Torunski, and W. Stolz, "Detection of nanometer-sized strain fields in (GaIn)(NAs) alloys by specific dark field transmission electron microscopic imaging," *Journal of applied physics*, vol. 97, no. 1, p. 014306, 2005.

[69] K. Volz, T. Torunski, B. Kunert, O. Rubel, S. Nau, S. Reinhard, and W. Stolz, "Specific structural and compositional properties of (GaIn)(NAs) and their influence on optoelectronic device performance," *Journal of crystal growth*, vol. 272, no. 1-4, pp. 739–747, 2004.

[70] O. Rubel, K. Volz, T. Torunski, S. Baranovskii, F. Grosse, and W. Stolz, "Columnar [001]-oriented nitrogen order in Ga(NAs) and (GaIn)(NAs) alloys," *Applied physics letters*, vol. 85, no. 24, pp. 5908–5910, 2004.

[71] K. M. Kim, J. Lee, and J. H. Ryu, "Thermal annealing effect on nitrogen related defects of GaInNAs semiconductors," *Journal of Ceramic Processing Research*, vol. 16, no. 1, pp. 45–48, 2015.

[72] K. Uno, M. Yamada, I. Tanaka, O. Ohtsuki, and T. Takizawa, "Thermal annealing effects and local atomic configurations in GaInNAs thin films," *Journal of crystal growth*, vol. 278, no. 1-4, pp. 214–218, 2005.

[73] E.-M. Pavelescu, T. Jouhti, M. Dumitrescu, P. Klar, S. Karirinne, Y. Fedorenko, and M. Pessa, "Growth-temperature-dependent (self-) annealing-induced blueshift of photoluminescence from 1.3 μm GaInNAs/GaAs quantum wells," *Applied physics letters*, vol. 83, no. 8, pp. 1497–1499, 2003.

[74] V. Lordi, V. Gambin, S. Friedrich, T. Funk, T. Takizawa, K. Uno, and J. S. Harris, "Nearest-neighbor configuration in (GaIn)(NAs) probed by X-ray absorption spectroscopy," *Physical review letters*, vol. 90, no. 14, p. 145505, 2003.

[75] I. Rey-Stolle, I. García, E. Barrigón, J. Olea, D. Pastor, M. Ochoa, L. Barrutia, C. Algora, and W. Walukiewicz, "On the thermal degradation of tunnel diodes in multijunction solar cells," in *AIP Conference Proceedings*, vol. 1881, no. 1. AIP Publishing LLC, 2017, p. 040005.

[76] P. Colter, B. Hagar, and S. Bedair, "Tunnel junctions for III-V multijunction solar cells review," *Crystals*, vol. 8, no. 12, p. 445, 2018.

[77] W. Dawidowski, B. Ściana, I. Zborowska-Lindert, M. Mikolášek, J. Kováč, and M. Tłaczała, "Tunnel junction limited performance of InGaAsN/GaAs tandem solar cell," *Solar Energy*, vol. 214, pp. 632–641, 2021.

[78] I. García, M. Ochoa, I. Lombardero, L. Cifuentes, M. Hinojosa, P. Caño, I. Rey-Stolle, C. Algora, A. Johnson, I. Davies *et al.*, "Degradation of subcells and tunnel junctions during growth of GaInP/Ga(In)As/GaNAsSb/Ge 4-junction solar cells," *Progress in Photovoltaics: Research and Applications*, vol. 25, no. 11, pp. 887–895, 2017.

[79] M. M. Wilkins, J. Gupta, A. Jaouad, B. Bouzazi, S. Fafard, A. Boucherif, C. E. Valdivia, R. Arès, V. Aimez, H. P. Schriemer *et al.*, "Design of thin InGaAsN (Sb) nip junctions for use in four-junction concentrating photovoltaic devices," *Journal of Photonics for Energy*, vol. 7, no. 2, p. 022502, 2017.

[80] G. Strobl, D. Fuhrmann, W. Guter, V. Khorenko, and W. Köstler, "About AZUR's "3G30-advanced" space solar cell and next generation product with 35% efficiency," in *Proc. 27th Eur. Photovoltaic Sol. Energy Conf. Exhib.*, 2012, pp. 104–108.

[81] F. Suarez, T. Liu, A. Sukiasyan, J. Lang, E. Pickett, E. Lucow, T. Bilir, S. Chary, R. Roucka, I. Aeby *et al.*, "Advances in dilute nitride multi-junction solar cells for space power applications," in *E3S Web of Conferences*, vol. 16. EDP Sciences, 2017, p. 03006.

[82] M. Ochoa, I. García, I. Lombardero, L. Ayllón, L. Cifuentes, I. Rey-Stolle, C. Algora, A. Johnson, J. Davies, K. Tan *et al.*, "Advances towards 4J lattice-matched including dilute nitride subcell for terrestrial and space applications," in *2016 IEEE 43rd Photovoltaic Specialists Conference (PVSC)*. IEEE, 2016, pp. 0052–0057.

[83] S. Kurtz, R. King, K. Edmondson, D. Friedman, and N. Karam, "1-MeV-electron irradiation of GaInAsN cells," in *Conference Record of the Twenty-Ninth IEEE Photovoltaic Specialists Conference*. IEEE, 2002, pp. 1006–1009.

[84] A. Khan, J. Gou, M. Imazumi, and M. Yamaguchi, "Interaction of electron irradiation with nitrogen-related deep levels in InGaAsN," *Applied Physics Letters*, vol. 91, no. 4, p. 043503, 2007.

[85] E.-M. Pavelescu, A. Gheorghiu, M. Dumitrescu, A. Tukiainen, T. Jouhti, T. Hakkarainen, R. Kudrawiec, J. Andrzejewski, J. Misiewicz, N. Tkachenko *et al.*, "Electron-irradiation enhanced photoluminescence from GaInNAs/GaAs quantum wells subject to thermal annealing," *Applied physics letters*, vol. 85, no. 25, pp. 6158–6160, 2004.

[86] E. Pavelescu, R. Kudrawiec, N. Bălţăţeanu, S. Spânulescu, M. Dumitrescu, and M. Guina, "Enhancement in photoluminescence from 1 eV GaInNAs epilayers subject to 7 MeV electron irradiation," *Semiconductor science and technology*, vol. 28, no. 2, p. 025020, 2013.

[87] B. Bouzazi, N. Kojima, Y. Ohshita, and M. Yamaguchi, "Effect of electron and proton irradiation on recombination centers in GaAsN grown by chemical beam epitaxy," *Current Applied Physics*, vol. 13, no. 7, pp. 1269–1274, 2013.

[88] Q. Lei, A. Aierken, M. Sailai, M. Heini, X. Shen, X. Zhao, R. Hao, J. Mo, Y. Zhuang, and Q. Guo, "150 KeV proton irradiation effects on photoluminescence of GaInAsN bulk and quantum well structures," *Optical Materials*, vol. 97, p. 109375, 2019.

Chapter 3

Study of the MBE growth conditions of InGaAsN

In this chapter, we study the impact of the MBE growth conditions on the optoelectronic properties of InGaAsN.

The first section introduces the materials and methods used to grow InGaAsN layers and solar cells. The solar cell structure and the growth conditions are also detailed and a focus is made on the growth defects that were observed in both GaAs and InGaAsN.

The second section of this chapter presents the material study that we have conducted on our epilayers. This part is divided into three subsections dedicated to structural, optical and electrical characterizations.

Contents

3.1 Epitaxial growth of InGaAsN layers

3.1.1 MBE growth setup and in-situ characterization tools

MBE growth setup

In this thesis, we used a semi-automated RIBER412 solid source MBE system, which is a ultra-high vacuum growth setup dedicated to research and development. It is equipped with five main vacuum modules:

- The **loadlock chamber** where substrates mounted on molybdenum platen are introduced
- The **cluster tool** acting as a substrate transfer system connecting the other chambers
- The **storage chamber**
- The **treatment chamber** where substrates are thermally degassed
- The **growth chamber** where the epitaxial deposition takes place

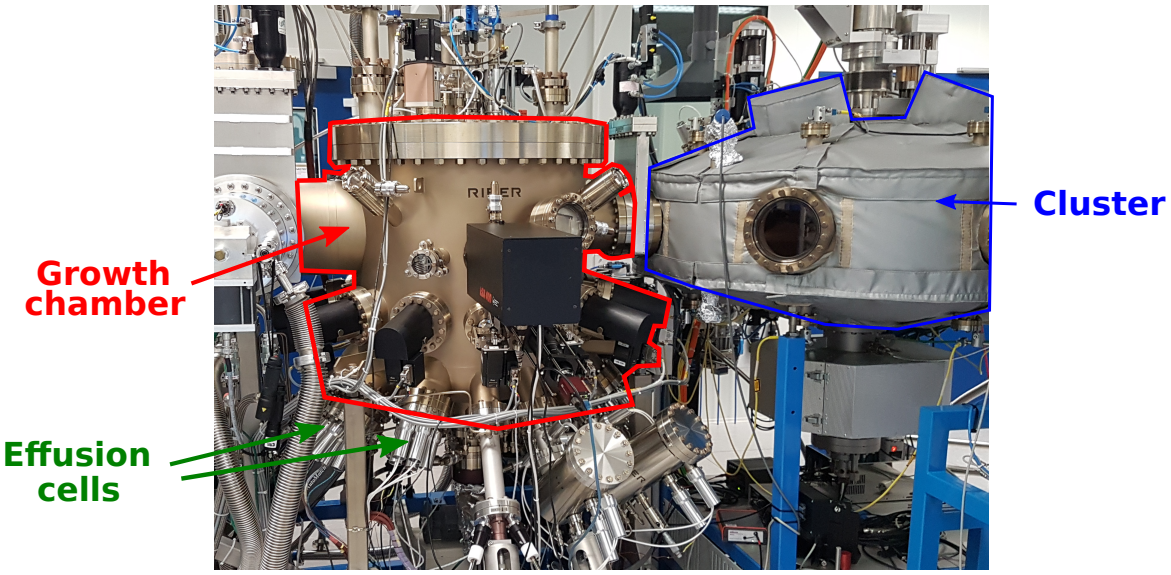

Figure 3.1: The RIBER412 system in the LAAS-CNRS clean-room. The left-hand side corresponds to the growth chamber, the right-hand side corresponds to the cluster.

The growth chamber is equipped with a substrate heater (T<750 °C) and a LN_2 cryopanel removing heat and maintaining a very low pressure (P<10^{-9} Torr). It also provides twelve cell ports oriented towards the wafer placed face-down on its Mo platen:

- 8 standard effusion cells: gallium×2, aluminium×2, indium, antimony, bismuth and silicon
- 2 arsenic valved cracker cells providing uncracked As_4 tetramers
- 1 CBr_4 injector providing carbon
- 1 RF valved plasma nitrogen source

Our growth setup is equipped with a RF valved plasma nitrogen source: a N_2 gas is introduced in a RF chamber where it is excited and transformed into a nitrogen plasma. This plasma is composed of electrons, N_2 molecules, N atoms and N^+ - N^{++} ions. As energetic ions were shown to introduce defects during the InGaAsN growth [1], the outlet of the source includes a valve that acts as a metallic plate eliminating ion species [2, 3]. The geometry of this outlet is an alternative to deflection plates also used to remove ion species [4].

In-situ characterization tools

To ensure optimal growth in real-time, we used *in-situ* characterization tools.

The **surface roughness** was monitored with an optical diffusion setup: the wafer was shone with white light and filmed with a camera placed normally to the substrate. Furthermore, a reflectivity characterization setup including a diffraction grating was employed to measure the spectral reflectance and control the evolution of the surface roughness during the epitaxial growth. A RHEED apparatus was also used to monitor surface reconstructions.

The RHEED tool was also used to infer the **substrate temperature** (see Section 3.1.4), along with Band Edge Thermometry (BandiT) and coupled with a thermocouple located behind the substrate. The temperature set in the RIBER CrystalXE software relies on the thermocouple read value, which was found to be significantly different from the effective temperature (ΔT>100 °C)).

In addition, the epilayers were **structurally** characterized with spectral reflectivity measurements (through light interferences) and with a high sensitivity curvature measurement setup developed in-house [5]. In this characterization, a matrix of light spots is shone upon the wafer where it undergoes specular reflection. The reflection of this pattern is then recorded through a camera and analysed with the EZ-CURVE software to infer the curvature $1/R$ of the epilayer which is being grown. As represented in Figure 3.2, distortion of the reflected image will occur if the epilayer is grown under a compressive or a tensile stress.

Using Stoney's equation, the stress×thickness product $\sigma_e h_e$ of the epilayer can be calculated in real time:

$$\sigma_e h_e = \frac{M_s h_s^2}{6R} \tag{3.1}$$

where M_s and h_s are the biaxial modulus and the thickness of the GaAs substrate, respectively. Knowing the growth rate, we can plot the evolution of $\sigma_e h_e$

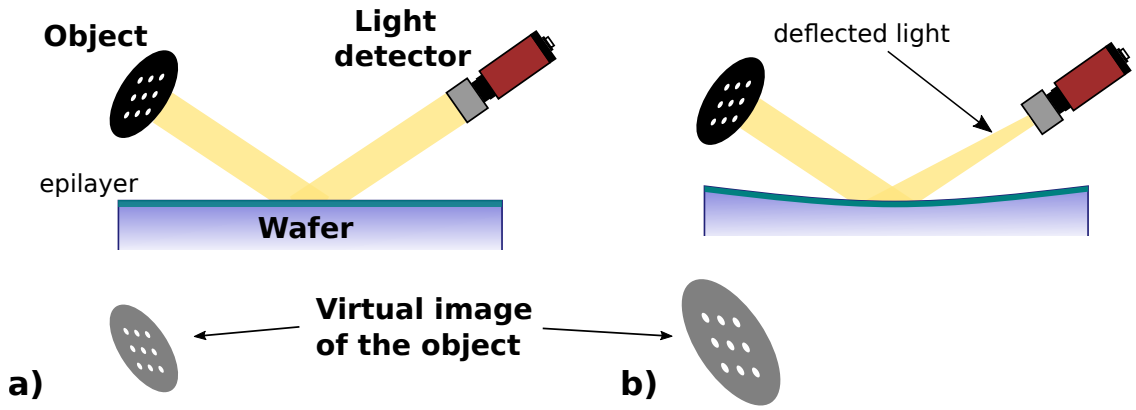

Figure 3.2: Schematics of the principle of the *in-situ* curvature measurement characterizing a) a lattice-matched epilayer and b) an epilayer grown under tensile stress.

against the thickness of the epilayer h_e. The slopes of this graph correspond to the stress under which a layer was grown at a given thickness.

Optical flux monitoring (OFM) and *in-situ* photoluminescence are additional characterization techniques being developed in our growth system. However, they were not used within the framework of this thesis.

InGaAsN growth

We have grown our dilute nitride layers and our solar cells on 4-inch GaAs (001) AXT substrates. As we have seen in the last chapter, InGaAsN is a quaternary alloy that can be grown lattice-matched to GaAs. To achieve lattice-matching, the In/N atomic ratio must be kept around 2.8 during the entire growth. The *in-situ* curvature measurement setup was then a crucial tool when growing InGaAsN because the nitrogen plasma intensity is found to be unstable over time. From our estimations, nitrogen flux instabilities can be larger than 20 %, which translates into equivalent InGaAsN composition inhomogeneities.

In addition to the plasma instability, we observe a considerable latency in the system between the moment the valve aperture is changed and the moment the N flux reaches its new level. Hysteresis phenomena also occur when the valve aperture is modified and then brought back to its initial value. The curvature measurement was therefore of great help to maintain a steady and adequate nitrogen flux.

In the case of InGaAsN, $\sigma_e > 0$ indicates that the layer is grown under tensile stress, which means that the lattice parameter of the epilayer is smaller than the lattice parameter of GaAs. This implies that the nitrogen concentration is too high (or alternately the indium concentration too low) and that the N beam flux should be decreased. Oppositely, $\sigma_e < 0$ indicates compressive stress, which translates in an lack of N atoms (or alternately an excess of In atoms). As it will be shown in Section 3.2.1, the RF power and the N_2 gas flow were set constant and the atomic nitrogen flux was tuned through the valve aperture of the cell.

3.1.2 Growth calibrations

Before growing InGaAsN samples, a calibration of the beam flux or beam equivalent pressure (BEP) is always conducted. GaAs-based compounds are generally grown under arsenic overpressure while the growth rate of these alloys is controlled with the gallium BEP (since the sticking coefficient of *III* elements approaches 1). As for arsenic, its flux is also precisely measured since the *As/III* BEP ratio is known to strongly affect the crystal quality of InGaAsN (see 2.3). We use a beam flux gauge (Bayard-Alpert) to measure the BEPs and we tune these latter ones with the temperature of the effusion cell or with the valve aperture in the case of arsenic. The cell temperature T_c and its BEP follow an Arrhenius relation:

$$BEP = A \exp\left(\frac{-B}{kT_c}\right) \tag{3.2}$$

where A and B are fit parameters.

Because we need to account for the uncertainties in the beam flux measurement and for the sticking coefficients of the *III* elements, we cannot only rely on BEP values. To relate the cell temperature T_c to the composition of alloys such as InGaAs and AlGaAs, quantum wells or superlattices are grown and analysed with X-ray diffraction (XRD) or photoluminescence (PL). By fitting the diffractogram of the calibration stack with simulated results on the Bruker Leptos 7 software, and by measuring the band to band PL transition, the composition of the calibration layers can be deduced.

For doping calibration, we grow 1 μm-thick GaAs layers with different silicon and carbon BEP. Small pieces are then cut from these samples and indium contacts are deposited on their corners to perform Hall measurements with the Van der Pauw method. The Hall voltage and the sheet resistivity are obtained from this measurement, which allow us to calculate the doping level and the mobility of the GaAs layer.

3.1.3 Structure of the InGaAsN samples

In this thesis, InGaAsN alloys were epitaxially grown either as thick layers (bulk layers) for our material property characterization studies or within solar cells as the absorber layer. InGaAsN bulk layers and solar cells were then used as test vehicles for our irradiation studies detailed in Chapter 5.

The NID-InGaAsN thick layers were grown on *n*-doped GaAs substrates[1] to enable electrical characterizations such as DLTS and impedance-voltage measurements, through an ohmic contact on the rear of the substrate and a Schottky contact on top of InGaAsN. The thickness of the bulk layers was set at 0.9 or 1.5 μm to ensure large SCR extension in case of very low residual doping.

[1] We assumed here that the residual doping would be n-type.

The solar cells are *p-i-n* heterostructures where the *p*-emitter and the *n*-base doped layers are GaAs with $n = p = 2 \times 10^{18}\ cm^{-3}$ and where *i* designates the non-intentionally doped (NID) InGaAsN layer. This latter InGaAsN layer is called the absorber and the SCR ideally spans across its whole thickness. As we mentioned in 2.3.5, a compromise between absorption and collection must be made when choosing the thickness of the InGaAsN active layer. We grew standard structures with a 1 μm-thick absorber to allow comparison with other published results [4, 6]. SEM and XRD characterizations showed that the InGaAsN layer of samples A1 to A4 was slightly thinner than targeted ($\approx$ 940 nm). The *n*-type doping of GaAs and AlGaAs layers was obtained with silicon whereas the *p*-type doping was achieved with carbon.

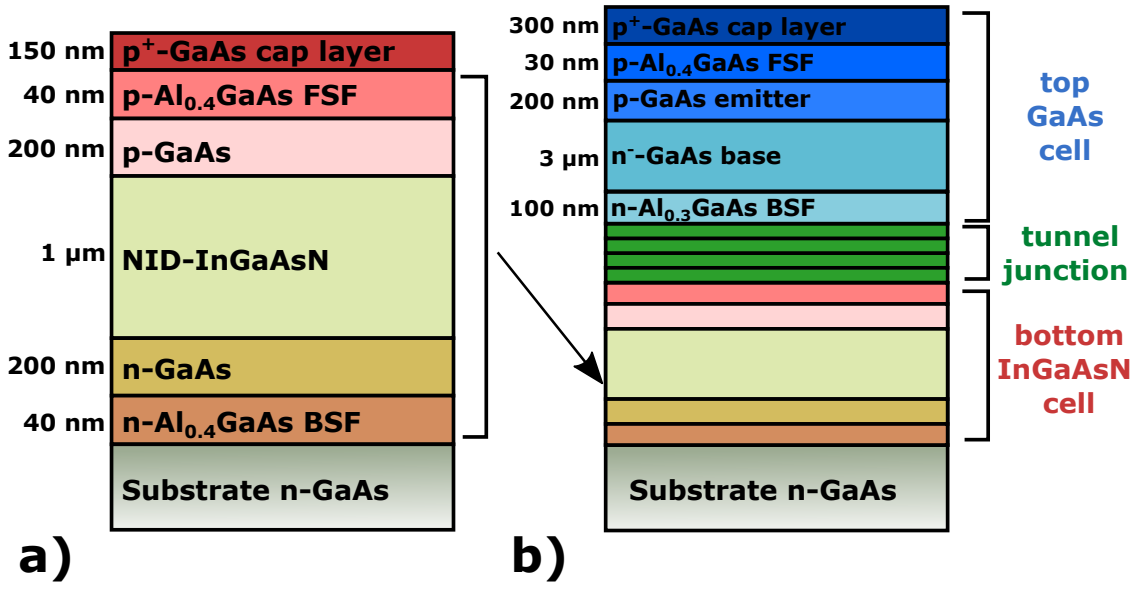

Figure 3.3: a) Structure of a InGaAsN solar cell epitaxial stack. b) Architecture of a GaAs/InGaAsN tandem solar cell stack including a tunnel hetero-junction.

As it can be seen in Figure 3.3 a), the structure of the cells also includes a highly p-doped GaAs cap layer ($p^+ = 1.5 \times 10^{19}\ cm^{-3}$) on the frontside that enables ohmic contact once metal is deposited on top of the cell. Furthermore, *p*-type and *n*-type $Al_{0.4}Ga_{0.6}As$ layers ($n = p = 2 \times 10^{18}\ cm^{-3}$) act as front surface field (FSF, also called *window*) and back surface field (BSF), respectively. Having a wider bandgap than GaAs, doped-$Al_{0.4}Ga_{0.6}As$ repels minority carriers, which suppresses surface recombination (see Appendix A.1) and bulk recombination in the cap layer and in the substrate. This field effect can be seen in the band diagram presented in Figure 3.4.

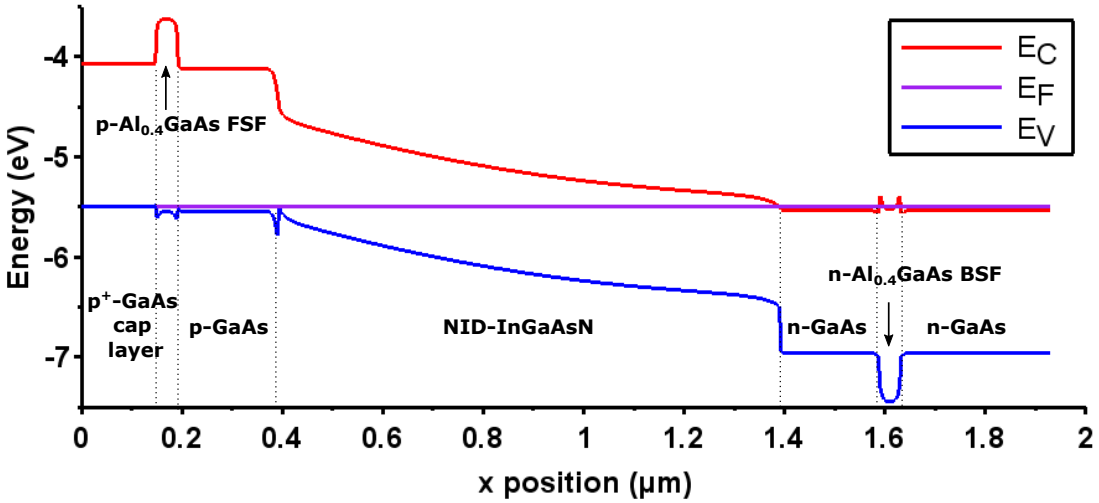

Figure 3.4: Simulation of the band diagram of an InGaAsN *p-i-n* solar cell obtained with SimWindows. The doping of the InGaAsN absorber was set at n^{-}=10^{15} cm^{-3}.

Finally, we have grown a GaAs/InGaAsN tandem solar cell (Figure 3.3 b), taking advantage of a tunnel heterojunction developed at LAAS [7, 8]. This tunnel junction is composed of two highly doped 50 nm GaAs layers with n^{+} = 1.5×10^{19} cm^{-3} and p^{+} = 10^{20} cm^{-3} in which we added a n^{+} 6 nm-$In_{0.12}Ga_{0.88}As$ and a p^{+} 4 nm-$GaAs_{0.12}Sb_{0.88}$ quantum well to enhance tunnelling properties.

The thickness of the InGaAsN absorber layer of the bottom cell was set at 1.15 μm in contrast to the 1 μm thickness of the single junctions. The top GaAs solar cell was grown with a standard *pn* structure with p = 10^{18} cm^{-3} in the emitter and n = 2×10^{17} cm^{-3} in the base. This structure includes a $Al_{0.3}Ga_{0.7}As$ BSF and a $Al_{0.4}Ga_{0.6}As$ window, as well as a p^{+} GaAs cap layer. For *I-V* analysis and irradiation purposes, a single junction GaAs solar cell was also grown with the same structure.

3.1.4 Growth conditions

Before growing layers, the first step of our epitaxial growth procedure is to degas the substrate by heating it at 350 °C under ultra-high vacuum in the treatment chamber. The substrate is then introduced in the growth chamber where it starts to rotate at 12 *rpm* to guarantee homogenous atomic fluxes and homogeneous heat repartition. Afterwards, the native surface oxide is removed at 620 °C. This action is performed under an As flux to compensate the arsenic desorption occurring at this temperature. A GaAs buffer is then grown with the same doping concentration as the substrate (n = 2×10^{18} cm^{-3}). This buffer layer is typically 300 nm-thick and is grown at 580 °C with a As/Ga BEP ratio equal to 2.

Additionally, the nitrogen plasma is cracked by flowing N_2 gas at 3 sccm under a 450 W RF excitation power. The plasma is then moved to a high brilliance

regime (measured with a photodiode) by reducing the flow rate to 0.2-0.3 sccm.

To assess the impact of the growth conditions on the $InGaAsN_x$ optoelectronic properties, we have grown solar cells and bulk layers with different nitrogen contents x, substrate or growth temperatures T_g, and with different arsenic overpressures *As/III*. The average nitrogen content of each sample was determined from PL measurements (Section 3.2.2), assuming In/N = 2.8. The influence of bismuth as a growth surfactant was also investigated, as it was reported to smooth the surface during growth [9, 10] and enhance nitrogen incorporation [9, 11]. The growth conditions of each sample are summarized in Table 3.1. As a convention for semi-conductor compounds, the N content value relates to the proportion of nitrogen among the other *V*-elements.

Table 3.1: Growth conditions of the InGaAsN layers

Structure	Name	N (%)	T_g (°C)	As/III	G. rate (μm/h)	ID LAAS
Solar cells	A1	1.6	465	12 (+Bi)	0.3	A1124
	A2			12		A1125
	A3		445	10		A1187
	A4		485			A1188
	A5	2.0	430	7.5	0.15	A1298
	A6	1.6	465	12	0.3	A1375
Bulk layers	B1	2	465	11	0.3	A1233
	B2		465	8		A1236
	B3	2.3	430	7.5	0.15	A1368
	B4	1.2	465	12	0.3	A1369
Bottom cell (tandem)	T1	2	430	7.5	0.15	A1320

Samples A2 and A6 were grown in the same conditions but two years apart. As it can be seen in the fifth column of this table, most of the InGaAsN layers were grown at 0.3 μm/h. On the other hand, three samples (A6, B3 and T1) with higher nitrogen content were grown at 0.15 μm/h since our RF plasma source could not deliver a N flux high enough to grow them at 0.3 μm/h. Besides, the growth temperature of these samples was lowered to 430 °C as the surface roughness was found to be very high for $InGaAsN_{x>2\%}$ samples grown at 480 and 445 °C (see Figure 3.5).

The effective substrate temperature was inferred from the measured temperature T_0 at which the (2x4)→c(4x4) GaAs surface reconstruction transition took place. This transition was observed with RHEED under an As BEP equal to 1.2×10^{-5} Torr and was reported to occur at 525 °C by Labella et al. [12], as shown in Figure 3.6.

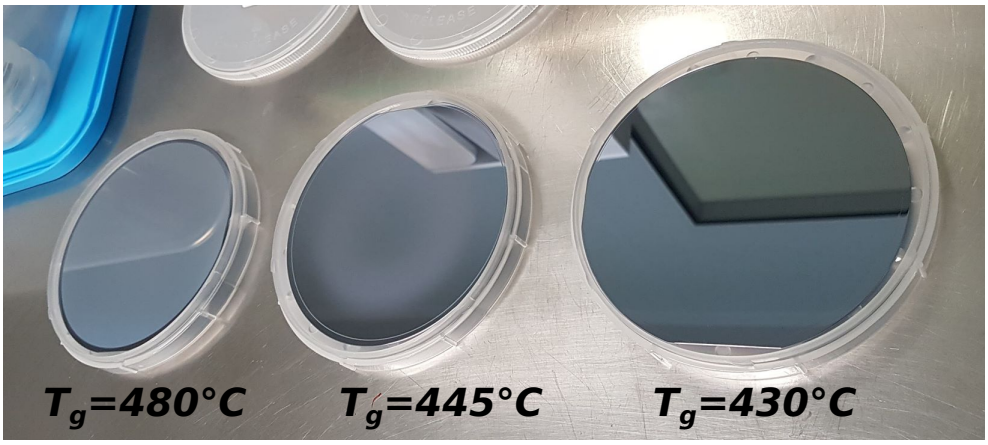

Figure 3.5: InGaAsN layers grown on 4-inch GaAs substrate at 480, 445 and 430 °C. The picture was taken at a tilted angle to highlight roughness and diffuse reflection.

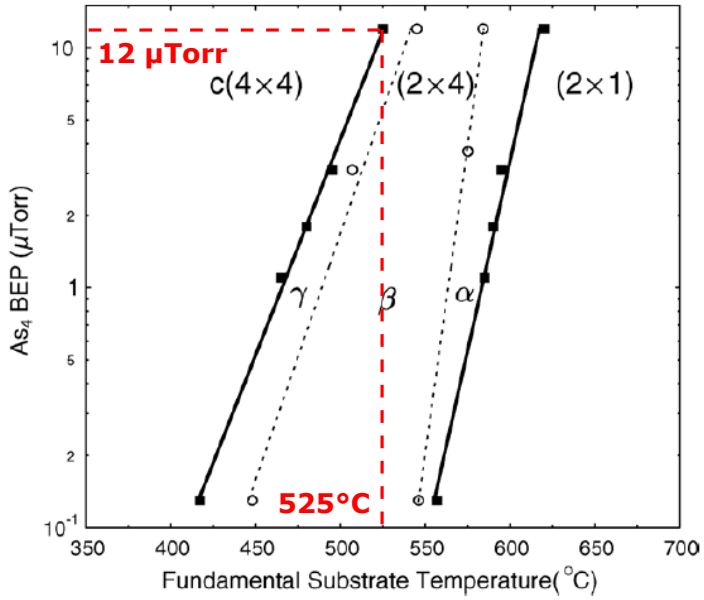

Figure 3.6: Surface reconstruction phase diagram of a GaAs (001) surface for different temperatures and As pressures [12]

3.1.5 Oval defects mitigation

Oval defects are large scale features (μm range) typically encountered in GaAs grown by MBE. These defects have a very specific morphology: in (001)-grown GaAs, they are elongated in the <110> direction and present a dark spot at their centre. Their formation results from a particle contamination of the surface before or during the epitaxial growth, acting as a nucleation point for the growth in {111} secondary planes [13, 14], as represented in Figure 3.7. The particles can originate from carbon contamination during the substrate preparation [13], or from con-

tamination occuring during the transfer of the substrate into the growth reactor [15]. It can also arise from the presence of Ga_2O_3 oxide native in the Ga melt, decomposing into Ga_2O suboxides that evaporate and form $Ga_2O_3 + Ga$ clusters on the wafer [16]. Finally, oval defects were also reported to appear because of the spitting of Ga droplets from the effusion cell directly to the surface [17]. This spitting is caused by droplets made of Ga particles covered by GaAs shells, which are present on the crucible walls of the cell and regularly fall in the gallium melt.

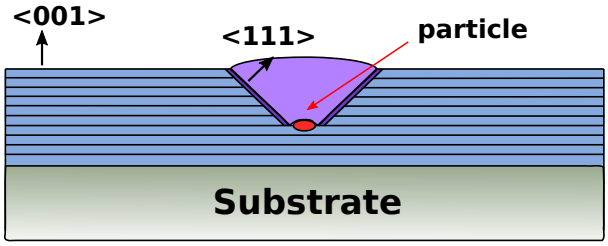

Figure 3.7: Schematic of the structure of an oval defect in MBE grown GaAs

At the beginning of our last growth campaign in 2021, we noticed a high density of macroscopic defects (10000-20000 cm^{-2}) on a 10 μm-thick GaAs layer grown for residual doping measurement. We characterized this sample with a Hitachi S-4800 scanning electron microscopy (SEM) system which confirmed that our sample was plagued with oval defects. As it can be seen in Figure 3.8, secondary planes started to grow in the <111> directions and a large polycrystal was formed at their centre, where the differently oriented twinned crystals intersected.

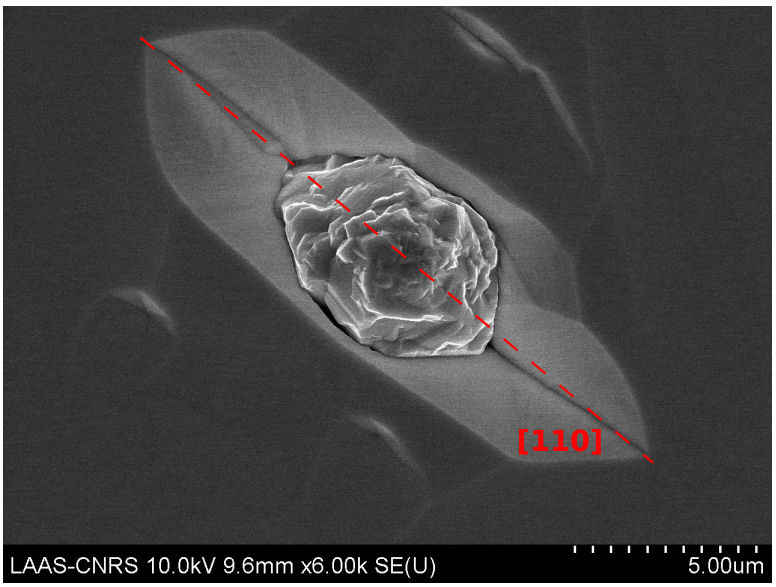

Figure 3.8: SEM image of an oval defect in GaAs, elongated in the [110] direction

As our growth procedure relies on "epi-ready" substrates that do not require surface preparation, and as the wafer transfer is performed under high vacuum, the origin of the contamination was thought to be the effusion cell. We did not have any direct way to assess the hypothesis of Ga_2O suboxides contamination

but we could observe droplets at the tip of the PBN crucible of the Ga6 effusion cell, as depicted in Figure 3.9.

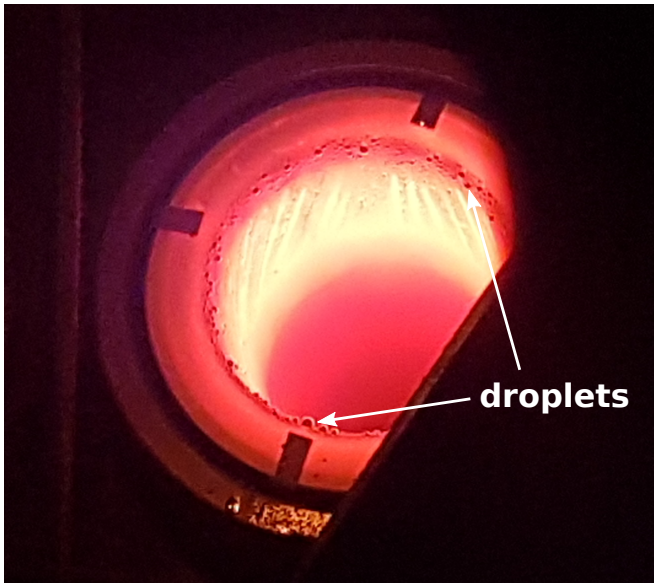

Figure 3.9: Picture of the Ga6 effusion cell (with open shutter) taken through the viewport of the MBE chamber. Droplets can be seen all around the tip of the PBN crucible.

We tried to troubleshoot this problem by heating up the tip of the crucible while keeping the base of the cell at a low temperature, and having the shutter open. No apparent changes could be observed with our camera after 20 hours of this procedure but we noticed a progressive decrease in the beam flux with the Bayard-Alpert gauge, probably meaning that droplets were being evaporated.

As this "cleaning" procedure was found to be highly time-consuming, we decided to conduct our last growth campaign with the other Ga effusion cell available in our MBE system. The density of oval defects on a 10 μm-thick GaAs layer grown with the Ga11 cell was found to be very low, which confirmed that the Ga6 cell was the origin of the particle contamination.

3.1.6 Self-replicated defects in InGaAsN

In addition to the oval defects, we encountered in InGaAsN with higher nitrogen content (> 2 %) groups of defects with a very unique structure. During the growth of both B3 and a 500 nm-thick $InGaAsN_x$ calibration sample (named C, grown with the same parameters as B3 but with the Ga6 effusion cell), we measured *in-situ* a slow decrease in the wafer reflectivity. A decrease in the reflectivity usually means that the surface roughness is increasing but in our case the drop of reflectivity could only be observed along one direction. *Ex-situ* optical microscopy showed a large density of elongated structures resembling oval defects without having any feature at their centre.

We characterized sample C with SEM to get a better understanding of the

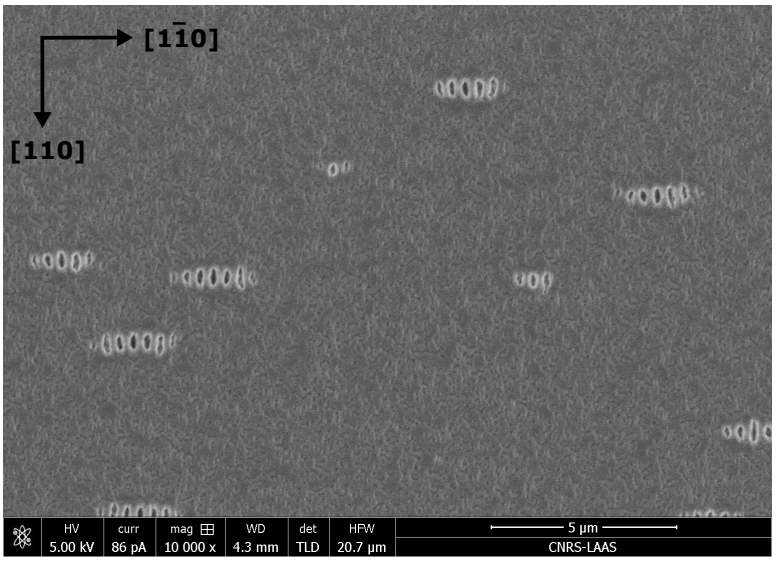

Figure 3.10: SEM image of self-replicated defects in the InGaAsN sample C

nature of these defects. As shown in Figure 3.10, the elongated structures that were observed with optical microscopy are in fact series of aligned defects, stretched themselves in the [110] direction. These defects exhibit the intriguing characteristics of being aligned, evenly spaced and almost always found in an odd number. Drawn by these properties and inspired from elements that will be discussed later on, we decided to call them "*self-replicated defects*". The concentration of these defects is very low near the edge of the wafer but it was found to increase significantly when approaching its centre. This indicates a non-homogeneity of the growth that will be addressed with the PL results presented in Section 3.2.2.

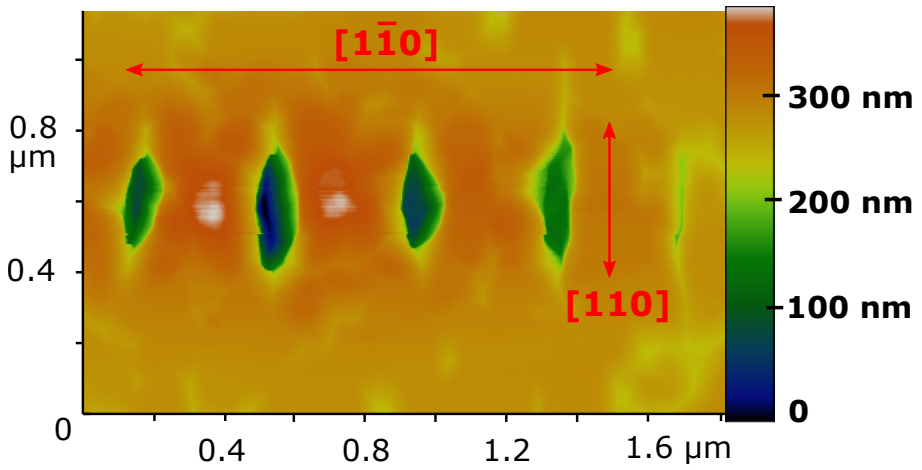

Figure 3.11: AFM image of the self-replicated defects morphology (sample C)

As depicted in the atomic force microscopy (AFM) image shown in Figure 3.11, these defects are actually ≈ 300 nm-deep holes separated by hillocks. We investigated these depressions with focused ion beams (FIB) to see if they had stemmed from particles contamination. A $\approx 5 \times 5\ \mu m^2$ square was etched away

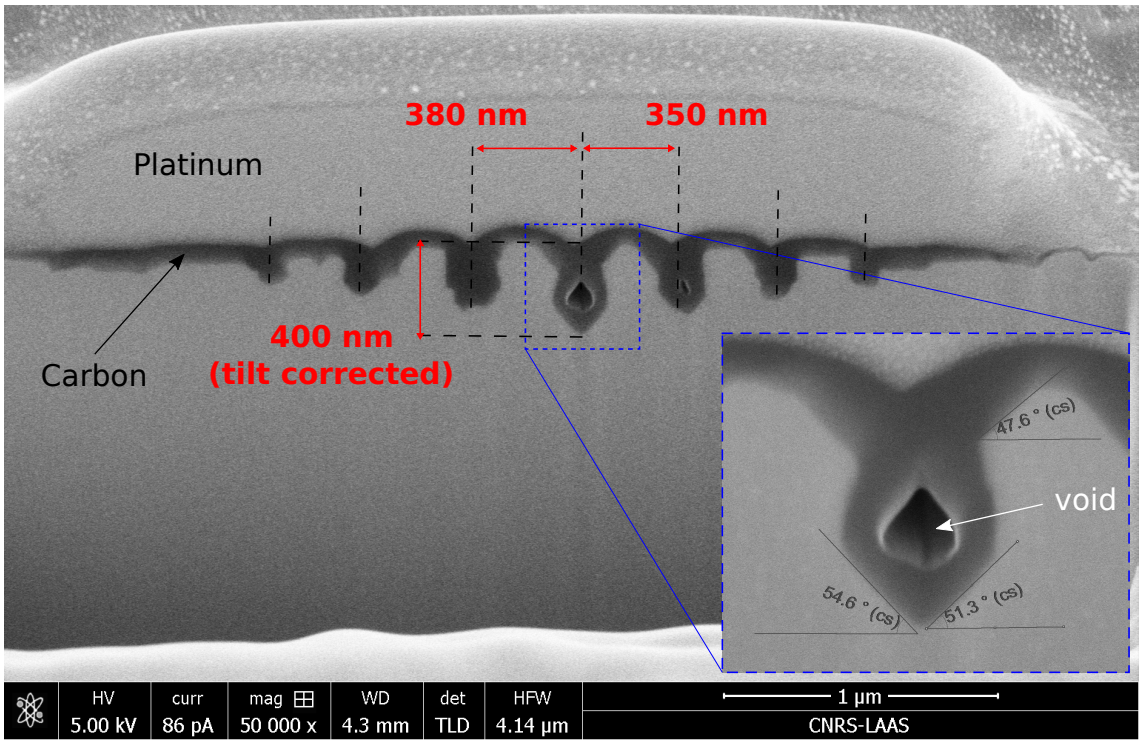

Figure 3.12: 45°-tilted SEM image of a (100) FIB cut in sample C, revealing the depth profile of the self-replicated defects, filled with carbon. The bottom right inset image was taken at ×250 000.

with Ga^{3+} ions to uncover the depth profile of the defects in the (110) plane. In Figure 3.12, we can clearly see that these features are evenly spaced and organized around a central defect. This central defect is deeper than the rest, which indicates that it was the first to appear during the growth. Two replicates were then formed at roughly the same moment and third and fourth order replications appeared later on. A high degree of symmetry can also be observed at the defect scale as shown in the inset of Figure 3.12 where we distinguish secondary growth planes with a $\approx 50°$ angle. These planes correspond likely to the [111] growth direction ($\theta = 54.74°$). Interestingly, a second FIB cut realised in the $(\bar{1}10)$ plane revealed that secondary planes were growing with a $\approx 26°$ angle, which indicates [113] growth direction ($\theta = 25.24°$).

To our best knowledge, this kind of defect has never been observed in InGaAsN. Besides their morphology, three elements allow us to discriminate these structures from oval defects. First, the group of self-replicated defects is much larger than an oval defect would be, considering the low thickness of the layer ($\approx$ 500 nm). Second, the concentration of these groups of defects was found to be much greater than the concentration of oval defects observed in a 10 μm-GaAs layer grown with the same effusion cell. Finally, we can see with the FIB cut that the central defect is roughly 400 nm deep, meaning that it first appeared in the InGaAsN layer and did not stem in the GaAs buffer.

From these elements we hypothesize that a first defect appeared in InGaAsN because of a nitrogen-related surface disordering. Nitrogen segregation or N ions

not deflected by the metallic plates could be the cause of this first surface damage. Then, the local disorder possibly led to preferential growth in the [111] and [113] directions. Different surface diffusion and incorporation rates of nitrogen and indium atoms in the secondary growth planes could have generated local stress field that were then compensated by the formation of another defect. This would explain the group symmetry and the constant spacing between two holes.

These explanations are highly speculative and more characterizations should be performed to understand the formation of these defects. In particular, microphotoluminescence, cathodoluminescence and X-ray spectroscopy (EDX, XPS) could bring a lot of information regarding the local compositions and the levels of stress. Additionally, InGaAsN layers of several thicknesses should be grown to check if the number of self-replicated defects increases with the thickness. Lastly, growing periodically AlAs thin layers within InGaAsN would be a great way of observing the layer-by-layer growth history [18].

3.2 Impact of the growth conditions on InGaAsN material properties

3.2.1 Structural characterization

Curvature measurement

As described in Section 3.1.1, we monitored in real time the curvature of the layers during growth. It allowed us to tune the nitrogen valve aperture and find the adequate N flux, as illustrated in Figure 3.13.

Figure 3.14 a) shows the time evolution of the curvature of the InGaAsN absorber of four solar cells (A1, A2, A3 and A4) as a function of the accumulated thickness of the InGaAsN layer. The curves of this graph also indicate the stress × thickness product as it is directly proportional to the curvature (see Equation 3.1). The stress at a given thickness was then calculated from the slopes of this graph and the corresponding strain value was obtained using Hooke's law:

$$\sigma_e = \epsilon_{//} \times \frac{(C_{11} + 2C_{12})(C_{11} - C_{12})}{C_{11}} \tag{3.3}$$

where C_{11} and C_{12} are the elastic constants of the epilayer approximated as the values known for $In_{0.05}Ga_{0.95}As$. We found a good consistency of the literature reporting on InGaAs elastic constant [19, 20, 21] unlike for GaAsN alloys where no consensus seems to exist [22, 23].

The lattice parameter of the InGaAsN epilayer is then deduced from the strain value:

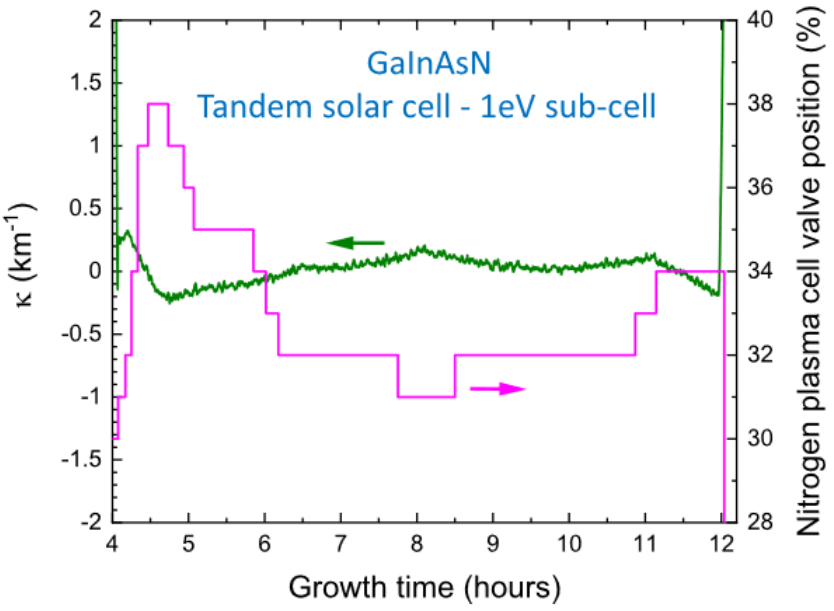

Figure 3.13: In green: time evolution of the curvature κ measured during the growth of the InGaAsN absorber layer of the tandem solar cell T1. The pink curve corresponds to the valve aperture of the nitrogen plasma cell. The figure was taken from [5].

$$\epsilon_{//} = \frac{a_{GaAs} - a_{InGaAsN}}{a_{InGaAsN}} \Leftrightarrow a_{InGaAsN} = \frac{a_{GaAs}}{1 + \epsilon_{//}} \tag{3.4}$$

From this lattice parameter we inferred the nitrogen content x of $InGaAsN_x$ using a double Vegard law and assuming the indium content is 0.045 (assumed from PL measurements).

$$\begin{aligned} a_{In_{0.045}GaAsN_x} &= (1 - x - 0.045) \times a_{GaAs} + x \times a_{GaN} + 0.045 \times a_{InAs} \\ \Leftrightarrow x &= \frac{a_{In_{0.045}GaAsN_x} - 0.955 \times a_{GaAs} - 0.045 \times a_{InAs}}{a_{GaN} - a_{GaAs}} \end{aligned} \tag{3.5}$$

where a_{GaN} and a_{InAs} are the lattice parameters of GaN and InAs equal to 4.520 and 6.058 Å, respectively [24]. Finally, we can directly relate the measured curvature $1/R$ to the nitrogen content x. Using equation 3.1, we can write:

$$\frac{1}{R} = \frac{6h_e}{h_s^2} \times \frac{\sigma_e}{M_s} \tag{3.6}$$

Knowing that $\sigma_e = M_e \times \epsilon_{//}$ and assuming that the GaAs and InGaAsN biaxial moduli are equal, we can re-write equation 3.6 as:

$$\frac{1}{R} = \frac{6h_e}{h_s^2} \times \epsilon_{//} \tag{3.7}$$

From equations 3.4 and 3.5 we can reformulate $\epsilon_{//}$, leading to the final expression:

$$\frac{1}{R} = \frac{6h_e}{h_s^2} \times \left(\frac{a_{GaAs}}{(0.955 - x).a_{GaAs} + x.a_{GaN} + 0.045.a_{InAs}} - 1 \right) \tag{3.8}$$

Using this equation and the data from Figure 3.14 a), the evolution of the nitrogen content x within the InGaAsN absorber of the four solar cells is depicted in Figure 3.14 b).

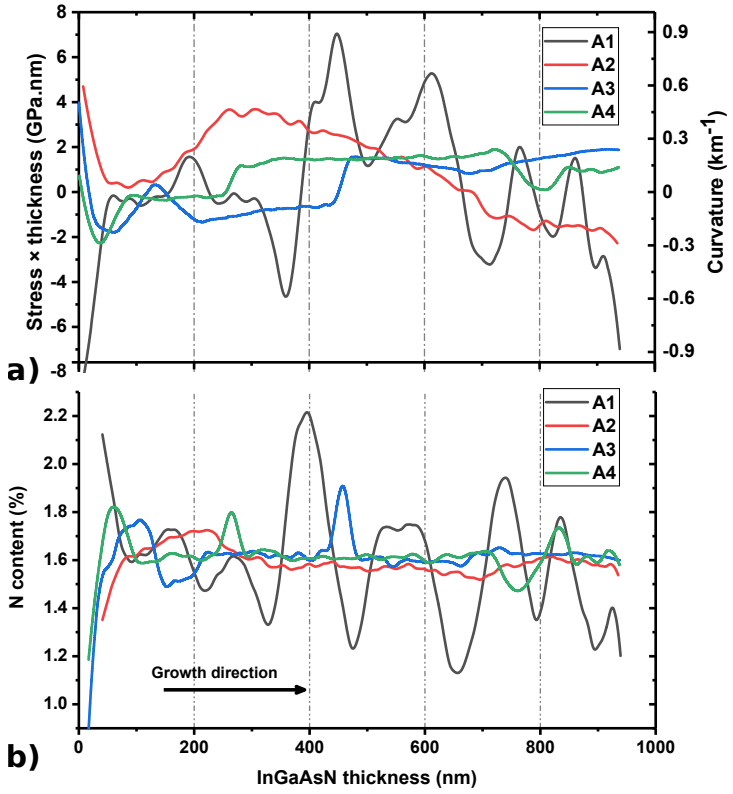

Figure 3.14: a) Stress×thickness evolution during the InGaAsN growth of samples A1 to A4. b) Nitrogen composition profiles along the InGaAsN layer deduced from a).

We can see that sample A1 (black curve) exhibits large nitrogen oscillations (± 1 % absolute) because our procedure for adjusting the aperture of the N plasma valved cell was not optimized. However, the three other solar cells display a very steady nitrogen content along the entire InGaAsN layer.

Something important to keep in mind when looking at the curvature graphs is that the value of $1/R$ is not nearly as important as the *variation* of the curvature as well as its second derivative. To avoid having sharp oscillations in our curvature profile, we have grown samples B3, B4 and A6 with another valve management procedure. This new procedure consists in waiting a longer time (typically 10 min) after changing the valve aperture to avoid *overshoots* where we go from one

type of stress to another. The curvature and the nitrogen profiles of the three samples grown with this method are depicted in Figure 3.15.

One can see that despite the large stress × thickness values, the nitrogen contents of these samples is quite steady, except for the few oscillations exhibited by B3 (purple curve). Furthermore, we can see in sample B3 that the first 200 nm of InGaAsN were grown with a lack of nitrogen, which shows the limitation of this valve management procedure.

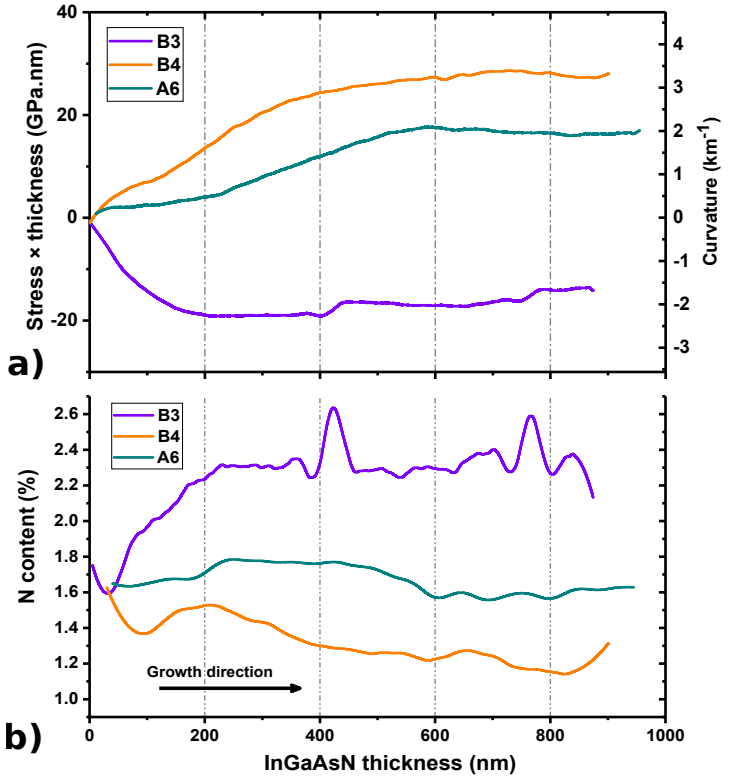

Figure 3.15: a) Stress×thickness evolution during the InGaAsN growth of samples B3, B4 and A6. b) Nitrogen composition profiles along the InGaAsN layer deduced from a).

XRD analysis

To assess the impact of the nitrogen content oscillations on the structural properties of the InGaAsN layer, we conducted XRD measurements with a *Bruker D8 Discovery* system equipped with a K-alpha1 X-Ray source (λ = 1.54059 Å). Figure 3.16 shows the XRD characterization of samples A1 and A2, which respectively exhibit large and low nitrogen oscillations. The diffractogram of sample A6 grown with the second valve aperture procedure is also plotted in Figure 3.16. Samples A1, A2 and A6 are solar cells with the same targeted nitrogen content and the same stack structure.

First, we can see that for the three samples, the InGaAsN diffraction peak strictly coincides with the substrate response. The full widths at half maximum

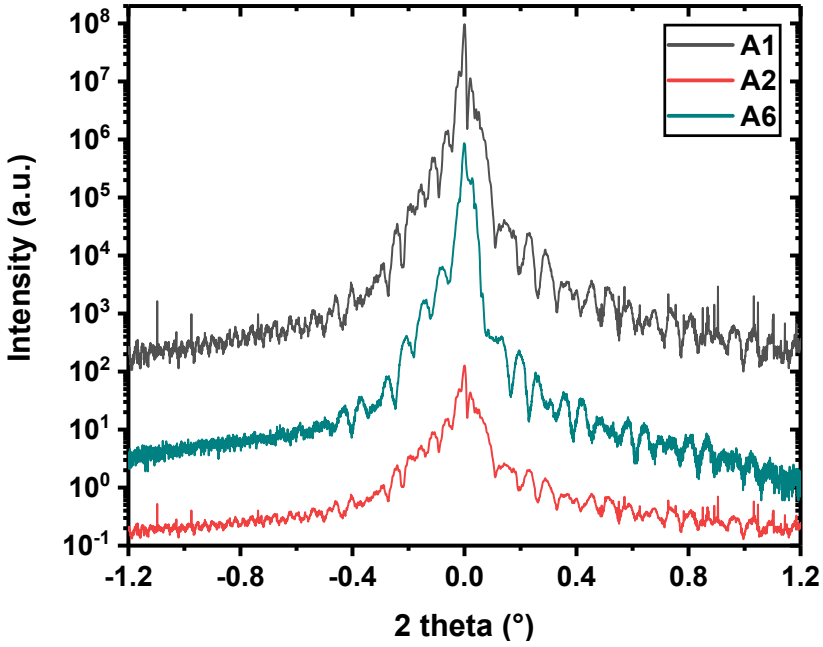

Figure 3.16: (004)-diffractogram of samples A1, A2 and A6. The diffractograms were logarithmically y-shifted for the sake of clarity.

(FWHM) are 34.34, 33.86 and 35.82 arcseconds for samples A1, A2 and A6, respectively. These very low values indicate that the lattice mismatch f is virtually null in these samples. This result is in agreement with the steady nitrogen profiles found for A2 and A6 (Figures 3.14 and 3.15). However, it appears that the N oscillations exhibited by sample A1 do not have any impact on its diffractogram, possibly because they are too thin compared to the thickness of the InGaAsN layer.

SIMS analysis

To characterize the layer compositions of our solar cells, we sent a sample from wafer A2 to Probion Analysis (*Bagneux, France*) in order to obtain secondary ion mass spectroscopy (SIMS) data. Three analyses were conducted. First, we looked for the contents of Al, Ga, As, In, and N to get the atomic compositions of the AlGaAs layers (BSF and window) and of the InGaAsN absorber. Second, we assessed the dopant concentrations (Si and C) for comparison with the targeted doping levels. Finally, we investigated the contamination levels in our sample. We searched for oxygen and hydrogen atoms as these species are frequently encountered in MBE grown InGaAsN [25, 26, 27, 28]. Besides, as we have seen in Chapter 2 - Section 2.3.2, a special attention should be paid to the introduction of hydrogen in dilute nitrides, as (N-H) split interstitials are thought to be a major crystal defect in InGaAsN. Additionally, we measured the concentration levels of calcium and boron, as traces of these elements were found in [27] and [25], respectively.

Figure 3.17 shows the content of the five main elements in our solar cells,

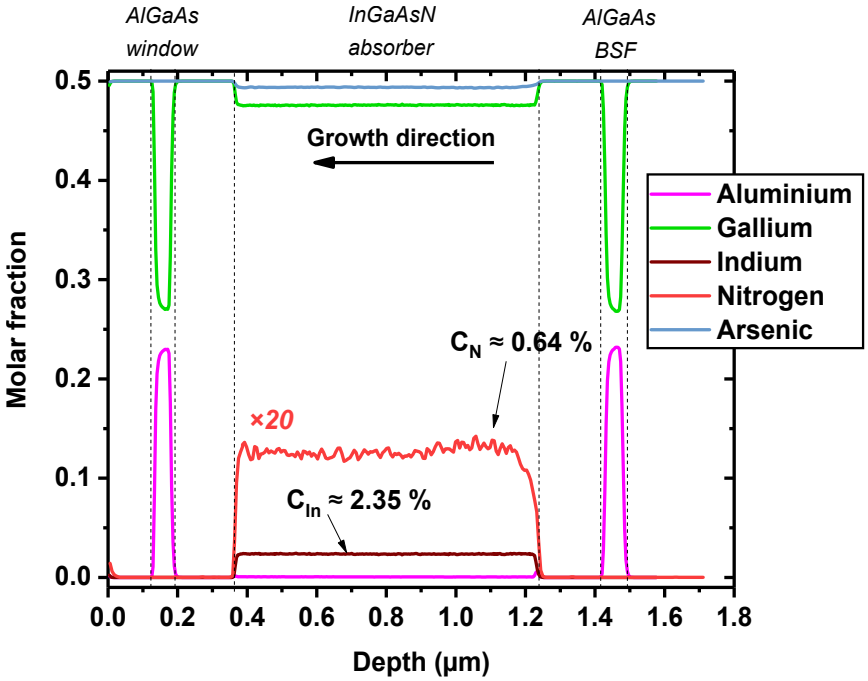

Figure 3.17: A2 SIMS profiles of the molar fractions for the five main elements in our solar cells: Al, Ga, In, N and As. The nitrogen profile was multiplied by 20 for the sake of clarity.

expressed in global molar fraction. We can see that the window and BSF layers have aluminium and gallium molar fractions approximately equal to 0.23 and 0.27, which corresponds to a $Al_{0.46}Ga_{0.54}As$ alloy, consistent with the $Al_{0.4}Ga_{0.6}As$ targeted composition.

The In molar fraction in InGaAsN measured by SIMS is 2.35 % (4.7 % of the *III*-elements), similar to the content determined through PL characterization (4.5 %). However, the nitrogen content measured by SIMS (≡ 1.28 %) is found to be much lower (from a relative point of view) than the 1.6 % expected by PL measurement. Besides, this low value gives a In/N ratio equal to 3.67 which does not concur with the 2.8 empirical ratio reported in the literature for lattice-matched InGaAsN. This discrepancy could arise from measurement uncertainties as the SIMS nitrogen calibration was conducted using a GaAs sample with very low nitrogen concentration (impurities). Furthermore, the discrepancy could originate from the calculation of the nitrogen molar fraction realised by dividing the N concentration obtained by SIMS by the atomic density of InGaAsN[2]. This calculation is conducted assuming that the InGaAsN atomic density is equal to the atomic density of GaAs (4.42 at.cm^{-3}), which is only true for a defect-free crystal, lattice-matched on GaAs, and in which In and N atoms are exclusively located in substitutional sites.

[2]The As content is then deduced from the N molar fraction.

Even though we obtain different nitrogen contents x through SIMS and curvature characterizations, the evolutions of x with the thickness/depth of the absorber layer are found to be in close agreement, as depicted in Figure 3.18.

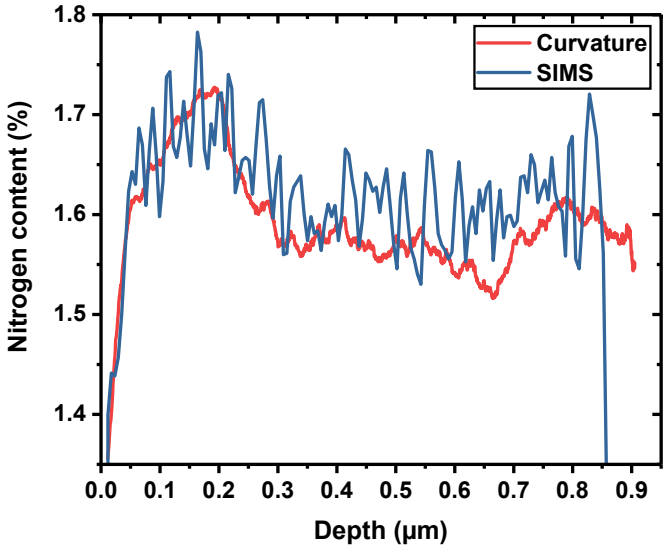

Figure 3.18: Nitrogen content profile in the absorber layer of sample A2, deduced from curvature and SIMS analysis. For the purpose of comparison, the SIMS profile was y-shifted to match the curvature values.

Figure 3.19 presents the dopant concentrations throughout the solar cell structure. The carbon concentration in the GaAs emitter and in the AlGaAs window is virtually the same as the targeted doping concentration (2×10^{18} cm^{-3}). On the other hand, the C concentration measured in the cap layer is roughly twice larger than what was expected, which is fortunately beneficial to our structure as it promotes ohmic contact of the front metallization. Carbon atoms were also found in the rest of the structure at a $\approx 3 \times 10^{16}$ cm^{-3} residual concentration. Although Probion Analysis confirmed us this level of carbon, we remain sceptical about this result, for three main reasons: i) we cannot find any carbon source inside the growth system possibly leading to this level of contamination, ii) carbon is a p-type dopant and ECV profiling showed a n-type residual doping (see Section 3.2.3) and iii) the residual carbon concentration in InGaAsN is found to be identical as the C concentration in the substrate.

Furthermore, a high concentration of carbon atoms was detected at the substrate interface. This shows that carbon contamination still exists on our *epi-ready* GaAs substrates, even after performing degassing and deoxidation steps.

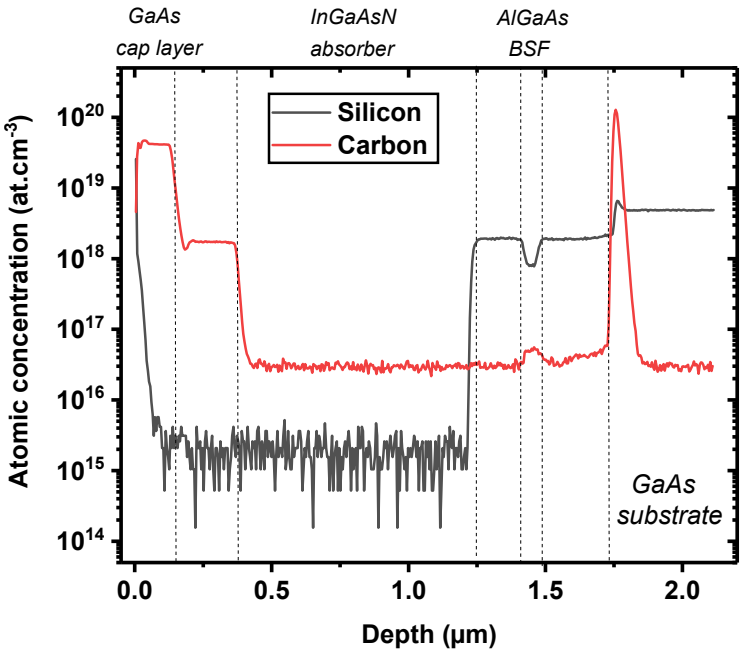

Figure 3.19: A2 SIMS profiles of the dopant concentrations: Si and C

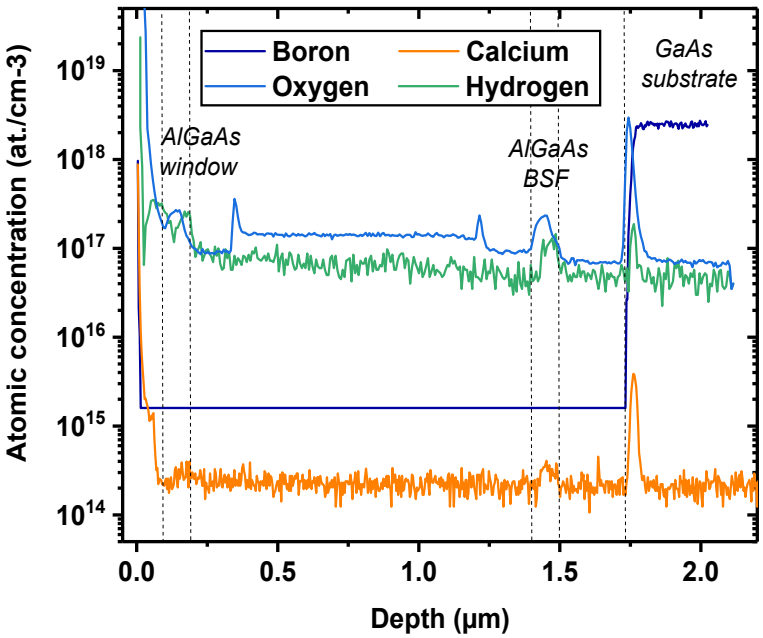

Figure 3.20: A2 SIMS profiles of investigated contaminants. The H, B and Ca contents are below the detection threshold in the cell but present at the surface and in the substrate.

Silicon was found to be below the detection limit in the *p*-doped layers and the Si concentration was measured to be $\approx 2 \times 10^{18}$ cm^{-3} in the *n*-GaAs layers, just as targeted. A lower silicon content is yet measured in the BSF layer, which cannot be explained by SIMS matrix effects and arises rather from a higher growth rate

of the AlGaAs layer.

Finally, Figure 3.20 shows the concentration levels of four possible contaminants. Only the oxygen concentration was measured to be above the detection limit in the solar cell, at a level higher than 10^{17} cm^{-3}. Besides, we can see that oxygen atoms were incorporated more in the window and BSF layers, which is a well known behaviour in AlGaAs alloys [29]. The oxygen atoms are thought to originate from the aluminium or the gallium melt [30]. Boron atoms could also be probed in the GaAs substrate and we can notice that calcium and oxygen atoms are present at the substrate interface.

Subsection highlights:

- The oscillations of the nitrogen content can be mitigated with optimized valve aperture management.
- All of the InGaAsN layers are globally lattice-matched to their substrate at room temperature.
- SIMS analysis shows atomic compositions similar to targeted values.

3.2.2 Characterization of InGaAsN optical properties

To measure the bandgap energy and compare the non-radiative recombination rates of our dilute nitrides, we conducted photoluminescence experiments on our samples. The PL peak intensity of a material is a good indicator of its crystal quality as it is directly proportional to the radiative recombination rate. During the laser excitation step, free-carriers are generated and move along in the lattice for a certain duration. Then, a competition between two recombination mechanisms occurs as photocarriers have the opportunity to recombine radiatively or non-radiatively. A perfect crystal does not have any defect and thus no energy state exists within the bandgap: the recombination is exclusively radiative and the PL signal is maximal. In real crystals, defects in the lattice exist and the higher their concentration, the lower the PL intensity.

The PL signal of the bulk layers was measured at LAAS with a 15 mW - 488 nm laser excitation source. The InGaAsN absorbers within the A1, A2, A3 and A4 solar cells were characterized at LPCNO (*Toulouse, France*) with Hélène Carrère, using a 950 nm Ti-sapphire pulsed laser. We also assessed the impact of post-growth thermal annealing on the luminescence properties of our bulk layers. To do that, a 750 °C rapid thermal processing (RTP) was conducted under N_2 atmosphere during 30 seconds (see more information in Chapter 4).

Figure 3.21 shows the PL spectra of samples B1 and B2, grown with the same conditions except for the *As/III* ratio. We can see that the PL signal is stronger for sample B2, grown with a lower arsenic overpressure. As shown on the figure, the uncertainty of the PL measurement for bulk layers was calculated to be ± 15

%. The peak wavelength for the two as-grown samples is approximately equal to 1170 nm, which corresponds to a 1.055 eV bandgap energy.

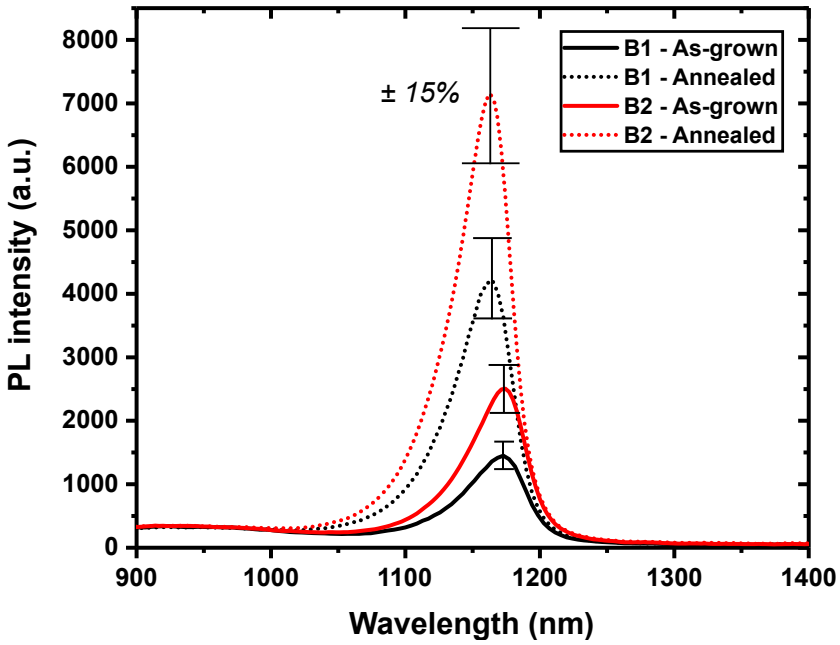

Figure 3.21: PL spectra of sample B1 and B2 measured at 300 K before and after thermal annealing.

In addition, Figure 3.21 shows the impact of the thermal annealing on the luminescence properties. Both of the samples exhibit a bandgap blueshift of ≈ 10 nm and a 180 % increase in their PL signal after annealing. These findings are in line with the literature review conducted in Chapter 2 (2.3.6). The beneficial effect of thermal annealing on the luminescence was also observed for samples B3 and B4, as depicted in Figure 3.22. This latter figure also shows that the PL intensity decreases with the nitrogen content, which can be explained by the higher concentration of nitrogen-related defects. In addition, a 10 nm blueshift is observed for B4 while no significant change in the peak wavelength was recorded for B3.

All of these samples were cautiously taken from the centre of their respective 4-inch wafer because we observed a radial inhomogeneity in the PL intensity. The luminescence was found to be greater near the middle of the wafer as depicted in Figure 3.23 a). An *in-situ* BandEdge cartography of a 4-inch GaAs wafer surface showed a higher temperature at the centre compared to the edge (Figure 3.23 b)), which could explain the discrepancy in the PL signal. This difference in local growth temperature could also be the cause of the inhomogeneous self-replicated defects concentration mentioned earlier.

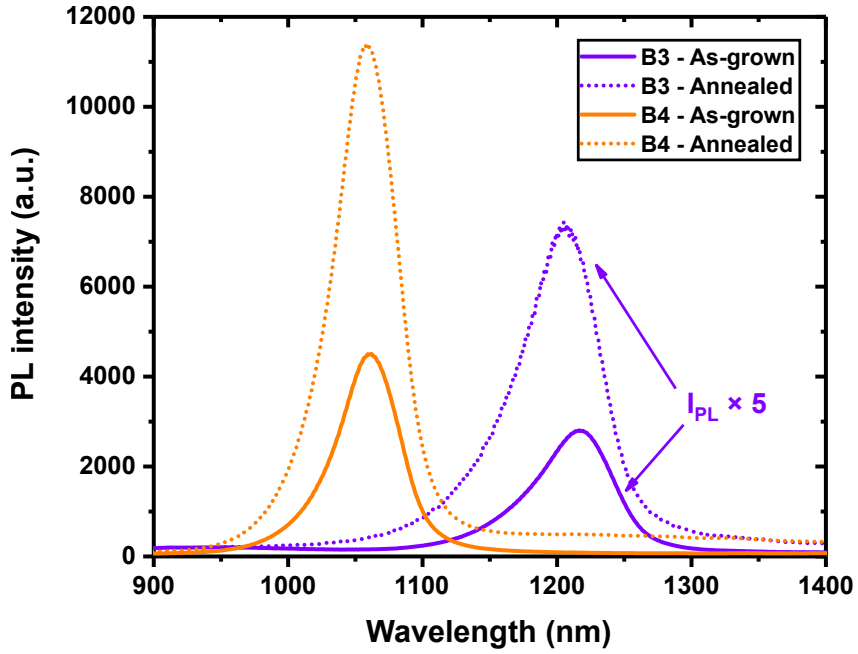

Figure 3.22: PL spectra of samples B3 and B4 measured at 300 K before and after thermal annealing.

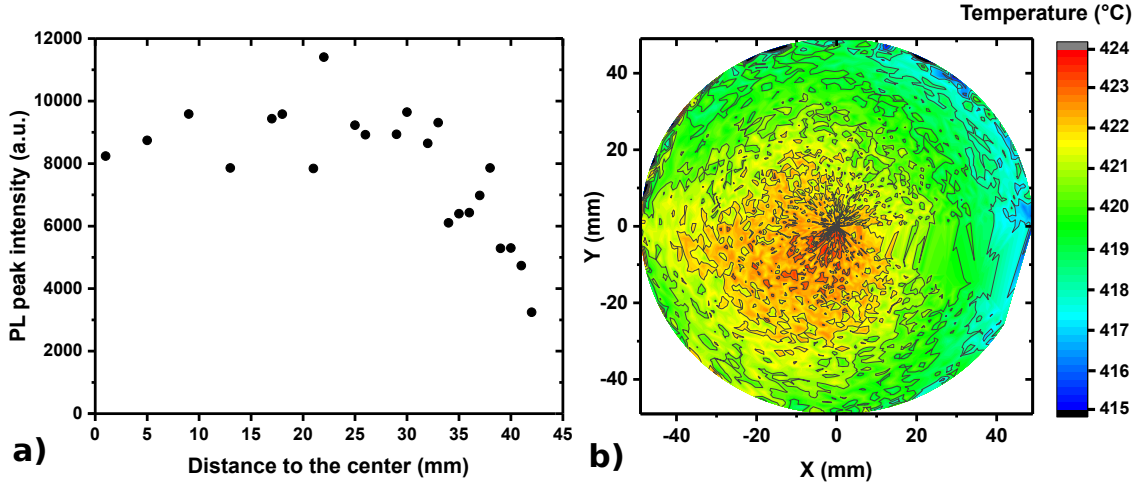

Figure 3.23: a) Evolution of the PL peak intensity of samples B2 with the distance to the centre of the wafer, b) Growth temperature cartography of a 4-inch GaAs NID substrate.

The PL response of the InGaAsN absorber within the solar cells was measured with a 950 nm laser. We used a laser with a wavelength greater than 870 nm and lower than 1100 nm in order to pass through the AlGaAs and GaAs most superficial layers and excite solely the dilute nitride alloy. From PL measurements at 300 K we determined the bandgap of the InGaAsN absorbers to be 1.11 eV. However, low signal/noise ratios were obtained at room temperature so we measured the PL emission at 10 K, as presented in Figure 3.24.

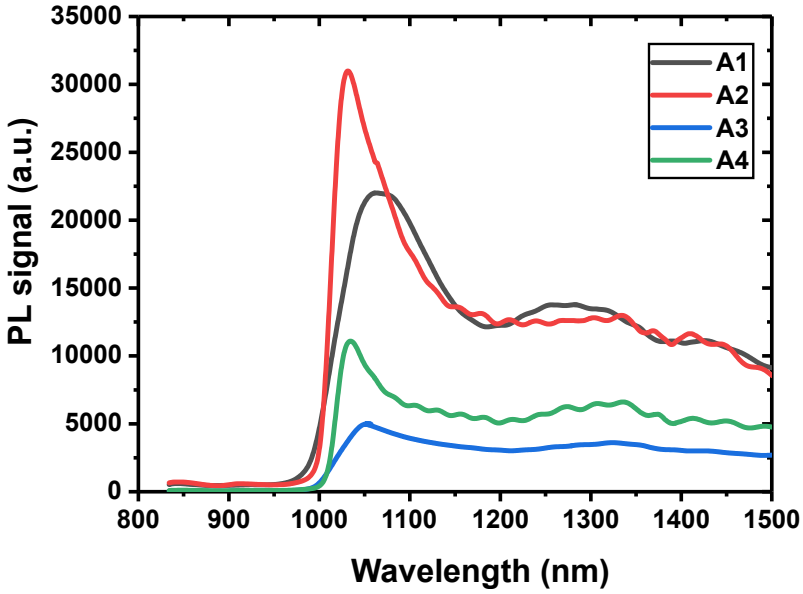

Figure 3.24: PL spectra of InGaAsN solar cells measured at 10 K. The broad peak appearing at higher wavelength originates from the n^+-doped GaAs substrate.

We can clearly see that sample A1 and A2, grown with a *As/III* ratio equal to 12, exhibit a higher PL intensity than A3 and A4, grown with a ratio equal to 10. This finding is contrary to what was observed for bulk layers in Figure 3.21 but one should keep in mind that the nitrogen content was higher in those latter samples.

The surfactant effect of bismuth could not be demonstrated as the PL signal of sample A1 was found to be lower than for A2 (grown at the same T_g and *As/III*). It is possible that the bismuth flux used during growth (2.6×10^{-8} Torr) was too low to promote the surfactant effect [9]. The PL comparison might also be biased from the sharp nitrogen content oscillations observed in A1 (Figure 3.14).

The variation in the nitrogen composition within A1 is also thought to be responsible for its broader PL peak: assuming the InGaAsN absorption coefficient is equivalent to the GaAs one red-shifted by 240 nm, the absorption depth of the 950 nm laser is approximately equal to 440 nm. Both the photogeneration and the radiative recombination of carriers can then take place at different depths (and thus for different bandgap values). Looking at Figure 3.14, we can see the nitrogen content oscillating from 1.2 to 2 % in the most superficial 400 nm. The bandgap energy of $In_{0.045}GaAsN_x$ is calculated to be 1.15 eV (λ =1075 nm) for x=1.2 % and 1.07 eV (λ =1157 nm) for x=2 %, which explains the broadness of the PL emission peak.

We also studied the temperature dependence of the PL signals of the InGaAsN bulk layers. To do that, samples were put in a closed-cycle helium cryostat where their photoluminescence spectra were recorded from 8 to 300 K. Figure 3.25 shows the bandgap energy evolution with the temperature for sample B2

and B4, at both as-grown and annealed conditions. It was found that sample B1, B2 and B3 exhibit the same behaviour: their bandgap energy follows the empirical Varshni relation given in Equation 3.9 [31].

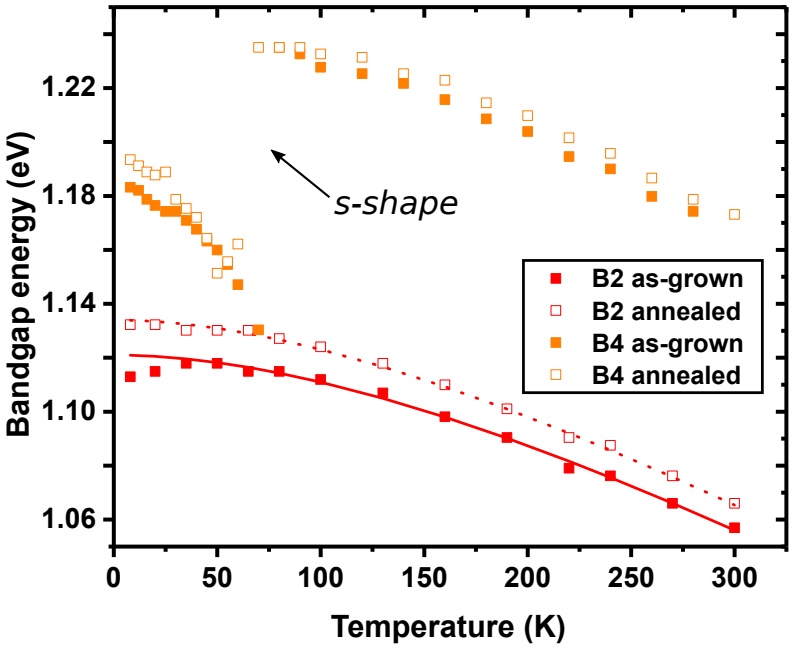

Figure 3.25: Evolution of the bandgap energy of samples B2 and B4, as-grown and annealed. Varshni fits are represented in solid and dotted lines for B2.

$$E_g(T) = E_g(0) - \frac{\alpha T^2}{T + \beta} \tag{3.9}$$

where α and β are the Varshni coefficients and $E_g(0)$ is the bandgap energy of the material at 0 K. As it can be seen in Figure 3.25, a good fit was found for sample B2 with the following parameters:

Table 3.2: $InGaAsN_{0.02}$ Varshni parameters

Sample	E_0	α	β
B2 as-grown	1.121	5.11×10^{-4}	408.2
B2 annealed	1.134	5.06×10^{-4}	363.2

Even though small discrepancies at T<50 K could be observed between the Varshni fits and the experimental data of sample B1, B2 and B3, large s-shapes could only be observed in sample B4. These s-shapes are typical signatures of exciton localization in dilute nitrides.

At low temperature, photogenerated carriers tend to bound in the exciton state which can be confined on potential fluctuations [32]. In InGaAsN, these fluctuations can originate from composition inhomogeneities or crystal defects creating band-tail states. The exciton binding energy being lower than the bandgap energy, the PL emission occurs at higher wavelength when excitons are localized at lower temperatures. However, this exciton recombination-regime disappears at higher temperature as thermal energy dissociate excitons into free carriers.

In the case of sample B4, strong localization can be observed until $\approx$ 60 K, with an s-shape very similar to literature reports [33, 34]. However, we notice here two unexpected features. First, the thermal annealing does not suppress the s-shape while it is supposed to cure crystal defects and homogenize the material. Second, it is counter-intuitive that s-shape is only observed in the *lower* nitrogen content sample (x=1.2 %), displaying the highest photoluminescence intensity (Figure 3.22) and the lowest DLTS signal (see Section 3.2.3 below). This demonstrates that exciton localization does not necessarily correlate with deep-level defects detrimental to the optoelectronic properties.

Subsection highlights:

- The PL intensity of InGaAsN is enhanced by thermal annealing.
- Higher nitrogen content in InGaAsN leads to lower PL signal.
- We observe a high sensitivity of the PL intensity on the *As/III* ratio.

3.2.3 Characterization of InGaAsN electrical properties

ECV profiling

As it was demonstrated in Chapter 2, InGaAsN solar cells usually rely on a *pin* architecture to take advantage of drift collection in the space charge region. However, this collection regime is only possible when the residual doping (BGCC) is low enough for the SCR to spread across hundreds of nanometres. Knowing the doping concentrations in our InGaAsN layers is then essential to our work and we used electrochemical capacitance-voltage (ECV) and mercury probe measurements to access this information.

The ECV characterizations were performed at the III-V Lab (*Palaiseau, France*) in collaboration with Jean Decobert and Nicolas Vaissière. The front surface of the samples was put against an electrolyte solution to obtain Schottky-like contacts and allow etching of the semiconductors. The doping profiles of the layers were then evaluated by alternating C-V profiling steps and etch steps. Just like SIMS, ECV has the convenient ability to provide data from multiple layers within any epitaxial stack such as a solar cell. Figure 3.26 shows the n-type doping profile of the top layers of the five solar cells.

We can first see that the doping levels measured in the GaAs substrate corres-

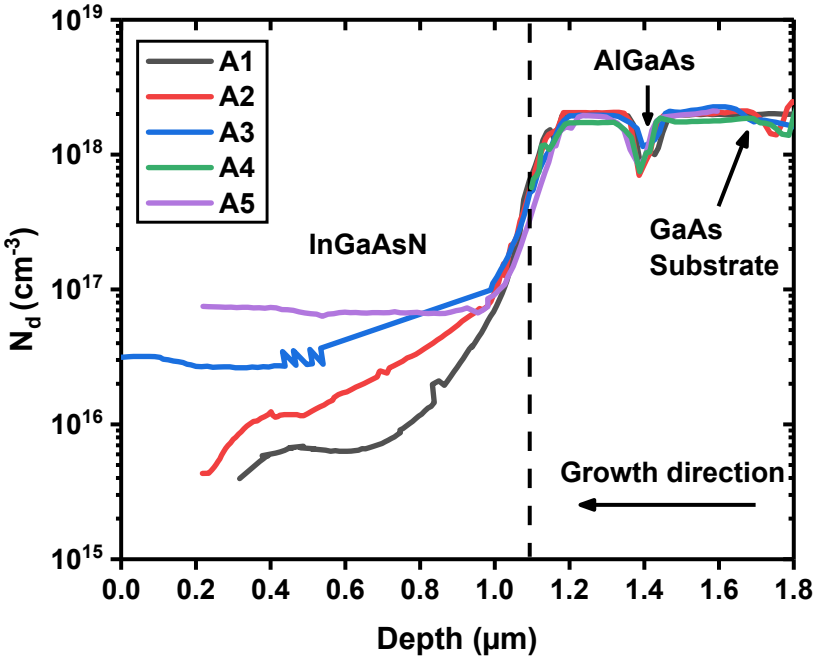

Figure 3.26: *n*-type doping profile of the InGaAsN solar cells

Table 3.3: BGCC and SCR extension in the InGaAsN absorber layers

	A1	A2	A3	A4	A5
BGCC (cm^{-3})	7×10^{15}	8×10^{15}	3×10^{16}	$< 4 \times 10^{15}$	7×10^{16}
SCR extension (nm)	320	300	150	> 420	100

pond to the wafer specifications ($n \approx 2 \times 10^{18}$ cm^{-3}). Exactly like the dopant SIMS profiles in the solar cells (Figure 3.19), we observe a lower doping concentration of the BSF layer compared to the GaAs buffer and base. For all five samples, the residual doping of the InGaAsN absorber was found to be *n*-type. The InGaAsN doping level in sample A4 was found to be below the detection limit ($n < 4 \times 10^{15}$ cm^{-3}).

The doping tail around the InGaAsN/GaAs interface is likely to arise from inhomogeneous etching depth, exposing at the surface simultaneously the NID-InGaAsN and *n*-GaAs layers. Indeed, profilometry measurement of the etching base after ECV showed a depth variation as high as 90 nm, which is of the same order of magnitude as the doping tail extent. The effective BGCC values for each solar cell were then taken far away from the GaAs interface and summarized in Table 3.3. The InGaAsN residual doping concentration in A6 solar cell was not measured but is estimated to be similar to A2, grown in the same conditions. The associated thicknesses of the space charge regions at 0 V were calculated using Equation 2.10 from Chapter 2.

Having a *n*-type residual doping is somewhat intriguing as SIMS measure-

ments revealed carbon contamination in the InGaAsN layers. As we argued in Section 3.2.1, this carbon contamination could result from measurement issues. In the case of an actual carbon contamination, this would suggest that: i) doping is mostly intrinsic in our solar cells, ii) it arises from donor defects such as $(N\text{-}H)_{As}$ [35] and iii) our dilute nitrides are subject to doping compensation mechanisms.

It is also interesting to notice that there is no correlation between the PL intensity and the BGCC of the absorbers. Samples A3 and A4, grown with *As/III*=10 but at a different temperature, exhibit both similarly low PL emission but display a significant difference in BGCC. An explanation is that donor and acceptor defects - responsible for the doping level - are generally shallow and do not behave like strong recombination centres. On the other hand, an anti-correlation can be found for the 4 first solar cells between the growth temperature and the BGCC[3]. This is qualitatively and quantitatively in close agreement with observations made by Ptak et al. [36] on 1.15 eV as-grown InGaAsN, showing the *n* to *p*-type transition to occur between 510 and 530 °C.

The *p*-type doping levels measured in the cap layers (not shown here) were found to closely match the carbon contents determined with SIMS (4-5×10^{19} cm^{-3}).

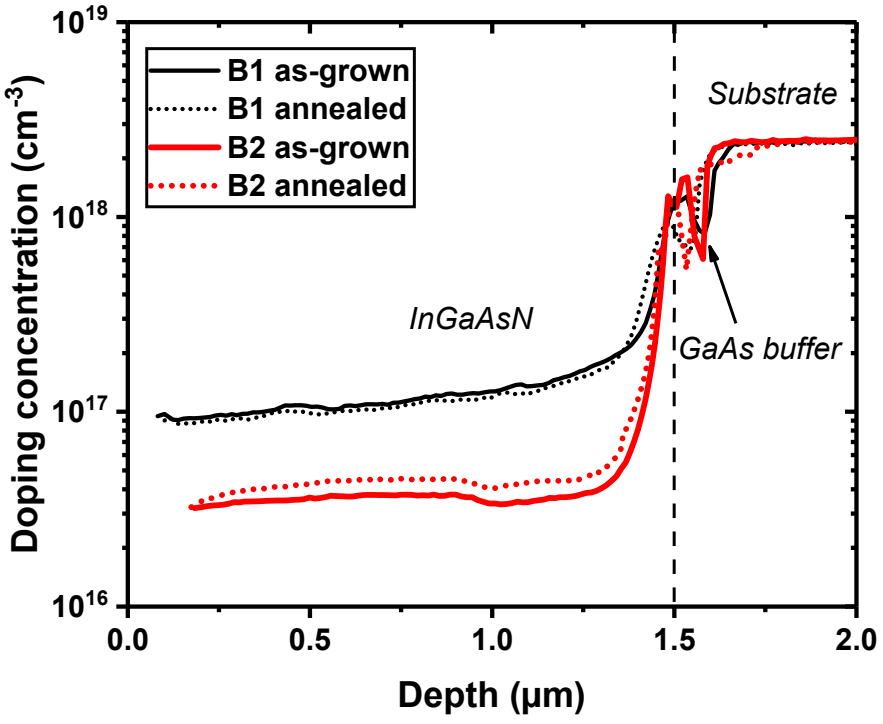

Figure 3.27: *n*-type doping profile of B1 and B2 InGaAsN bulk layers

The residual doping concentration was also measured in InGaAsN bulk layers to assess the impact of both the *As/III* ratio and the 750 °C post-growth annealing

[3]Sample A5 was left out this analysis because of its higher nitrogen content, which is believed to be the cause of its higher residual doping concentration.

on samples with 2 % nitrogen. Figure 3.27 shows that the BGCC is an order of magnitude higher in these $InGaAsN_{0.02}$ samples, just as the A5 solar cell grown with the same nitrogen content. Furthermore, we can see a strong influence of the arsenic overpressure on the residual doping as sample B2 grown at *As/III*=8 exhibit a BGCC approximately three times lower than B1 grown at *As/III*=11.

The post-growth annealing step was found to have a negligible effect on the doping level of B1 while it led to a slight BGCC increase in sample B2. This latter change in the residual doping can arise from the creation of donor defects in the lattice or alternately from the curing of acceptor levels.

To obtain the residual doping concentrations in B3 and B4, we performed *C-V* measurements using a MDC Hg-probe. This tool enables *C-V* profiling without having to process and metallize our samples. Liquid mercury is brought to the front surface within two concentric rings acting as the contact electrodes. The *C-V* profiles were acquired at 30 kHz using the ECV-results of samples B1 and B2 as calibration data.

Figure 3.28 shows once again that the nitrogen content has a major influence on the residual doping in $InGaAsN_x$. However, no monotonic relation between x and the BGCC can be inferred since B3 with 2.3 % N exhibits lower residual doping than B1. In a general way, we believe that comparing samples with different nitrogen content is complex because it implicitly requires to keep all other parameters constant, while the optimal MBE-growth parameters are themselves highly nitrogen-dependent. Thus, only general trends and qualitative results should be considered when comparing samples with a different N content.

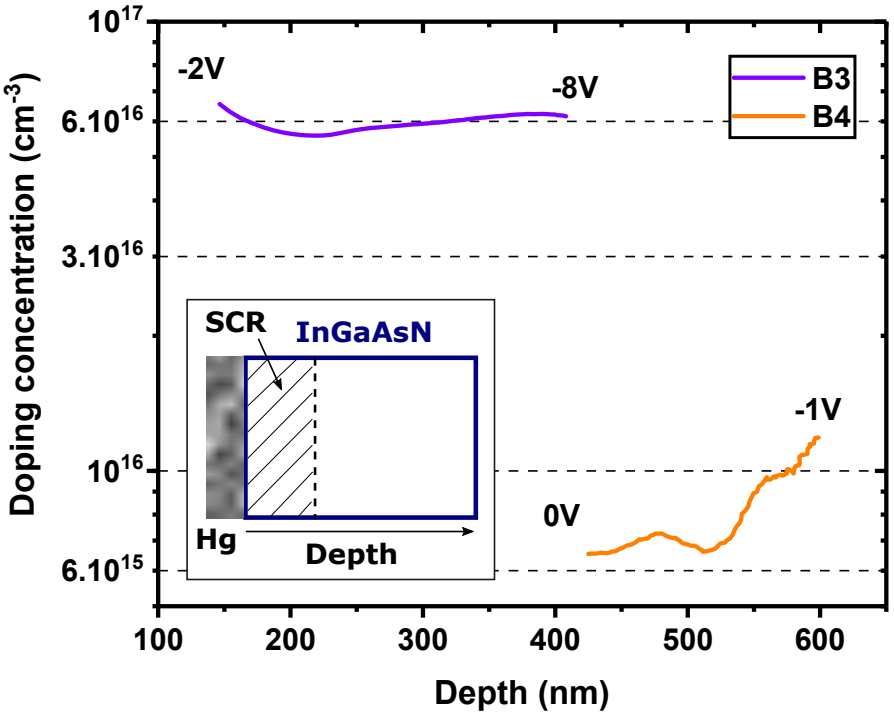

Figure 3.28: B3 and B4 doping profiles obtained with capacitance-voltage measurements

DLTS characterization

As mentioned earlier, the BGCC analysis gives information related to shallow defects. A complementary material study was conducted using current-deep level transient Fourier spectroscopy (i-DLTFS) to characterize deeper defects. To do that, basic technological process steps were realised in clean room to obtain Au/InGaAsN Schottky diodes with a 400 μm diameter. These process steps are essentially the same as for the solar cells and will be described in the next chapter.

Current-based rather than capacitance-based DLTS method was used because parasitic capacitances were present at 1 MHz in all our diodes. These parasitic capacitances are thought to originate from the back-side contact between the n^+-GaAs substrate and the AuGeNi metallization.

A Phystech DL8000 spectrometer and its analysis software were used to characterize our samples. In Figure 3.29, we compared the DLTS response of B1 and B2, setting the reverse voltage to -1 V and using a 0.5 ms filling pulse of 0 V. The current transient was recorded between 10 and 50 ms after the end of the pulse. As the residual doping of our samples is *n*-type, the majority carriers are electrons and only electron traps will be investigated here.

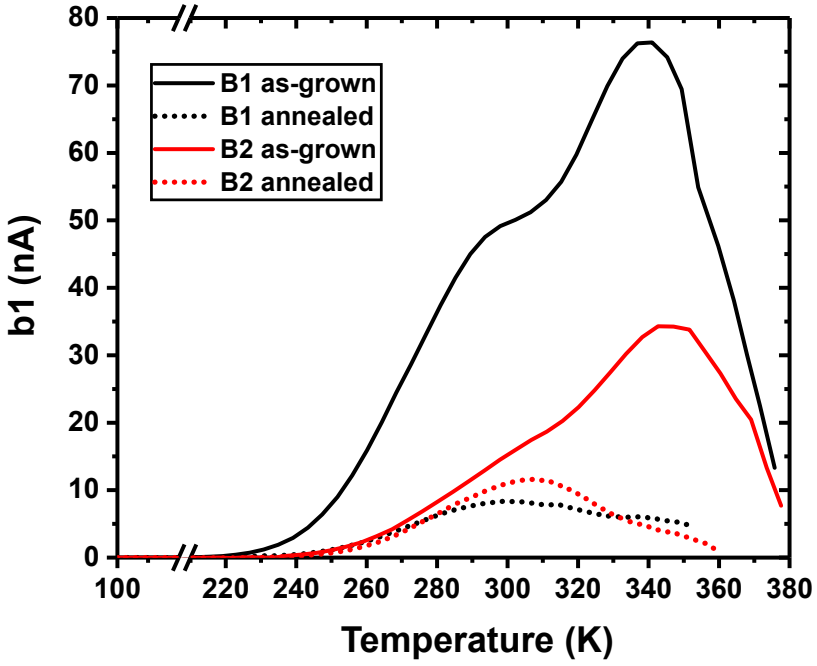

Figure 3.29: DLTS spectra of samples B1 and B2 before and after thermal annealing

We can first notice a considerable difference in the DLTS signal between B1 and B2. This indicates that sample B2, grown with a lower *As/III* ratio, has a lower defects concentration than sample B1. Furthermore, the effect of RTP can also be observed in terms of signal intensity: both samples show a decrease in their defect concentrations after thermal annealing. These results concur with the PL observations made on the same samples in Figure 3.21, meaning that the deep levels probed here act as powerful non-radiative recombination centres.

Even though the signal intensities gives a first comparative insight, we can see in Figure 3.30 a) that the DLTS spectra results from the convolution of two peaks arising from two electron traps, E1 and E2. We separated the contribution of each peak and plotted the Arrhenius regression of $\mathrm{Ln}(e_n/T^2)$ over $1000/T$ to calculate the activation energy of these traps (Figure 3.30 b)).

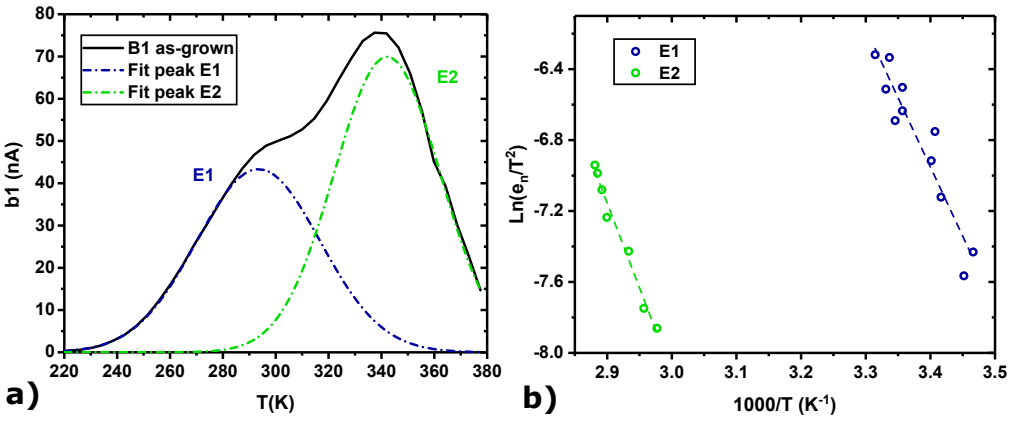

Figure 3.30: a) Peak deconvolution of the DLTS spectra measured for B1 as-grown b) E1 and E2 Arrhenius plots with linear fits in dashed line.

Depending on the samples and the measurement parameters, the activation energy of E1 ranges from 0.53 to 0.68 eV. This trap lies then in the very middle of the InGaAsN bandgap which is detrimental to its optoelectronic properties. This E1 defect is conjectured to be a nitrogen split interstitial $(\mathrm{N\text{-}N})_{As}$ as its activation energy was theoretically calculated to be 0.66 eV below the conduction band [37].

The evaluation of the activation energy for the second trap was found to be highly dependent on the reverse voltage, which possibly indicates a Poole-Frenkel effect. For U_r=-3 V, we calculated an activation energy ranging from 0.64 to 0.74 eV while it was estimated to be 0.74-0.85 eV at U_r=-1 V. This second trap is also very deep and has an energy state closer to the valence band. We can see in Figure 3.29 that in both samples, E2 is very effectively cured by thermal annealing.

To access the capture cross-section of the defects σ, we calculated the Richardson constant A^* associated with the Au/InGaAsN Schottky junction. To do that, we measured the dark current of sample B2 at various temperatures and used the thermoionic current equation:

$$I_0 = A^* T^2 \exp \frac{-q\Phi_B}{kT} \tag{3.10}$$

where Φ_B is the Schottky barrier energy [38]. As shown in Figure 3.31, we plotted $\mathrm{Ln}(I_0/T^2)$ over $1/T$ to obtain the Richardson constant.

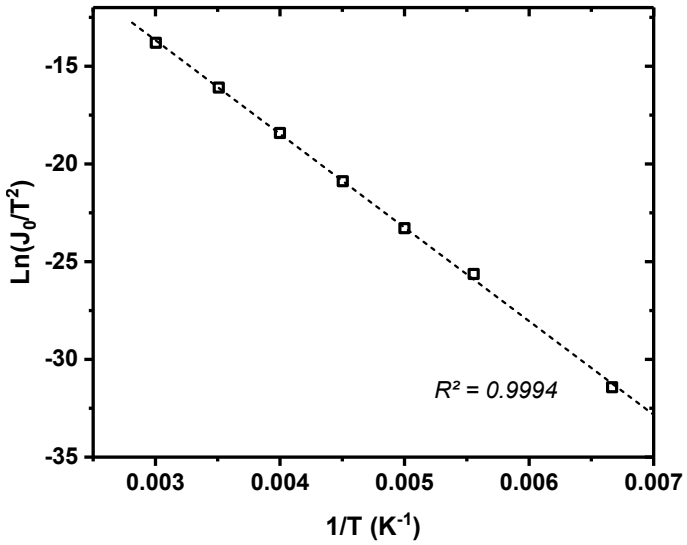

Figure 3.31: $\mathrm{Ln}(\mathrm{I_0/T^2}) = f(1/\mathrm{T})$ Arrhenius plot for sample B2 with linear fit in dashed line.

We found a Schottky barrier of 0.41 eV and a Richardson constant equal to 2.0 $\mathrm{A/cm^2/K^2}$. With this latter parameter, we can extract σ from the y-intercept of the DLTS Arrhenius plot. The cross-capture section is estimated to range from 0.29 to 2.7×10^{-13} $\mathrm{cm^2}$ for E1 and from 0.33 to 3.3×10^{-13} $\mathrm{cm^2}$ for E2. These large section values could mean that we are probing complex structures instead of point defects. Alternately, it could arise from defects positively charged which exhibit a larger electron capture radius through Coulombic attraction.

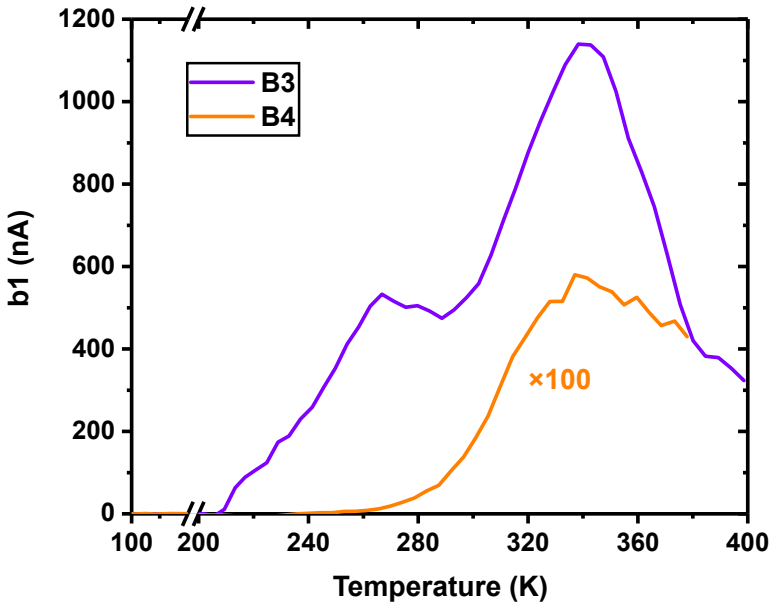

Figure 3.32: DLTS spectra of samples B3 and B4

The E1 and E2 electron traps could also be observed for samples with a different N composition. Figure 3.32 shows the DLTS response of B3 and B4, respectively grown with 2.3 and 1.2 % nitrogen. These spectra were obtained with a reverse voltage equal set to -3 V. As it can be seen with the amplitude of the signal, the defects concentration in B3 is much larger than for B1 and B2, whereas the DLTS intensity exhibited by B4 is found to be very low. This goes in-line with the assumption that we are probing nitrogen-related defects whose concentration increases with the N content.

Subsection highlights:

- The BGCC in all our InGaAsN layers is *n*-type and depends highly on the growth conditions and on the nitrogen content.
- Post thermal annealing does not lead to BGCC reduction.
- Post growth annealing strongly reduces the density of deep level defects measured with DLTS.
- The *As/III* ratio has a high influence on the density of deep level defects measured with DLTS.
- The defects probed by DLTS are very deep and display a large capture cross-section: they act as powerful recombination centres.

Chapter 3 conclusion

In this chapter, we have seen that a special attention should be paid when growing dilute nitrides.

Firstly, the nitrogen flux needs to be controlled and tuned in real time in order to ensure lattice-matched conditions within the whole InGaAsN layer. We meet this requirement by using an *in-situ* curvature measurement system developed in-house. In addition to the monitoring ability it provides, this technique allows us to determine the nitrogen content profile within the absorber of our solar cells.

Secondly, the contamination levels and the microscopical defect concentrations must be kept as low as possible. Observation and characterization of self-replicated and oval defects were conducted, and mitigation strategies were proposed for the latter ones. The contamination levels were assessed with SIMS and it was shown that carbon and oxygen atoms are unintentionally present in our structures.

Thirdly, we observed that the InGaAsN properties are highly dependent on its growth conditions. Specifically, photoluminescence and DLTS characterizations indicated that the density of non-radiative recombination centres can be reduced by optimizing the *As/III* ratio and by performing post-growth annealing. ECV profiles showed that the residual doping concentration tends to increase with the nitrogen content and that the BGCC could be lowered by increasing the growth

temperature. However, we know that doping compensation mechanisms exist in InGaAsN and no correlation was observed between the BGCC and the PL/DLTS results.

Finally, we also exposed that the optimal growth conditions depend strongly on the nitrogen content: a *As/III* ratio higher than 10 leads to stronger PL signal for InGaAsN with 1.6 % while samples with 2 % N exhibited better optoelectronics properties when grown at *As/III*=8. Furthermore, the growth temperature had to be reduced for samples with higher nitrogen content to limit surface roughness.

The material characterizations conducted here will be largely exploited in the next chapter, in order to explain the photovoltaic properties of our InGaAsN solar cells.

Bibliography

[1] T. Kageyama, T. Miyamoto, S. Makino, F. Koyama, and K. Iga, "Optical quality of GaNAs and GaInNAs and its dependence on RF cell condition in chemical beam epitaxy," *Journal of crystal growth*, vol. 209, no. 2-3, pp. 350–354, 2000.

[2] J. Harmand, G. Ungaro, L. Largeau, and G. Le Roux, "Comparison of nitrogen incorporation in molecular-beam epitaxy of GaAsN, GaInAsN, and GaAsSbN," *Applied Physics Letters*, vol. 77, no. 16, pp. 2482–2484, 2000.

[3] H. Carrère, A. Arnoult, A. Ricard, X. Marie, T. Amand, and E. Bedel-Pereira, "Nitrogen-plasma study for plasma-assisted MBE growth of 1.3 μm laser diodes," *Solid-State Electronics*, vol. 47, no. 3, pp. 419–423, 2003.

[4] D. B. Jackrel, S. R. Bank, H. B. Yuen, M. A. Wistey, J. S. Harris Jr, A. J. Ptak, S. W. Johnston, D. J. Friedman, and S. R. Kurtz, "Dilute nitride GaInNAs and GaInNAsSb solar cells by molecular beam epitaxy," *Journal of Applied Physics*, vol. 101, no. 11, p. 114916, 2007.

[5] A. Arnoult and J. Colin, "Magnification inferred curvature for real-time curvature monitoring," *Scientific Reports*, vol. 11, no. 1, pp. 1–11, 2021.

[6] M. M. Wilkins, J. Gupta, A. Jaouad, B. Bouzazi, S. Fafard, A. Boucherif, C. E. Valdivia, R. Arès, V. Aimez, H. P. Schriemer *et al.*, "Design of thin InGaAsN (Sb) nip junctions for use in four-junction concentrating photovoltaic devices," *Journal of Photonics for Energy*, vol. 7, no. 2, p. 022502, 2017.

[7] K. Louarn, "Etude et réalisation de jonctions tunnel à base d'hétérostructures à semiconducteurs III-V pour les cellules solaires multi-jonction à très haut rendement," Ph.D. dissertation, Université Toulouse 3 Paul Sabatier, 2018.

[8] K. Louarn, Y. Claveau, C. Fontaine, A. Arnoult, L. Marigo-Lombart, I. Massiot, F. Piquemal, A. Bounouh, N. Cavassilas, and G. Almuneau, "Thickness Limitation of Band-to-Band Tunneling Process in GaAsSb/InGaAs Type-II Tunnel Junctions Designed for Multi-Junction Solar Cells," *ACS Applied Energy Materials*, vol. 2, no. 2, pp. 1149–1154, 2019.

[9] S. Tixier, M. Adamcyk, E. Young, J. Schmid, and T. Tiedje, "Surfactant enhanced growth of GaNAs and InGaNAs using bismuth," *Journal of crystal growth*, vol. 251, no. 1-4, pp. 449–454, 2003.

[10] T. Liu, S. Chandril, A. Ptak, D. Korakakis, and T. Myers, "Bismuth surfactant effects for GaAsN and beryllium doping of GaAsN and GaInAsN grown by molecular beam epitaxy," *Journal of crystal growth*, vol. 304, no. 2, pp. 402–406, 2007.

[11] E. Young, S. Tixier, and T. Tiedje, "Bismuth surfactant growth of the dilute nitride $GaNxAs_{1-x}$," *Journal of crystal growth*, vol. 279, no. 3-4, pp. 316–320, 2005.

[12] V. P. LaBella, M. R. Krause, Z. Ding, and P. M. Thibado, "Arsenic-rich GaAs (001) surface structure," *Surface science reports*, vol. 60, no. 1-4, pp. 1–53, 2005.

[13] M. Bafleur, A. Munoz-Yague, and A. Rocher, "Microtwinning and growth defects in GaAs MBE layers," *Journal of Crystal Growth*, vol. 59, no. 3, pp. 531–538, 1982.

[14] N. Chand and S. Chu, "A comprehensive study and methods of elimination of oval defects in MBE-GaAs," *Journal of crystal growth*, vol. 104, no. 2, pp. 485–497, 1990.

[15] S.-L. Weng, C. Webb, Y. Chai, and S. Bandy, "Particulates: An origin of GaAs oval defects grown by molecular beam epitaxy," *Applied physics letters*, vol. 47, no. 4, pp. 391–393, 1985.

[16] S.-L. Weng, "Ga2O3: The origin of growth-induced oval defects in GaAs molecular beam epitaxy," *Applied physics letters*, vol. 49, no. 6, pp. 345–347, 1986.

[17] K. Takahashi, H. Kawada, S. Ueda, M. Furuse, and S. Shirayone, "The origins and elimination of oval defects in GaAs layers grown by molecular beam epitaxy," *Journal of Vacuum Science & Technology A: Vacuum, Surfaces, and Films*, vol. 9, no. 3, pp. 854–857, 1991.

[18] P. Atkinson and D. Ritchie, "GaAs facet formation and progression during MBE overgrowth of patterned mesas," *Journal of crystal growth*, vol. 278, no. 1-4, pp. 482–487, 2005.

[19] A. De Bernabe, C. Prieto, L. González, Y. González, and A. Every, "Elastic constants of $in_xga_{1-x}as$ and $in_xga_{1-x}p$ determined using surface acoustic waves," *Journal of Physics: Condensed Matter*, vol. 11, no. 28, p. L323, 1999.

[20] I. Institute, "Physical properties of gallium indium arsenide (gainas)." [Online]. Available: http://www.ioffe.ru/SVA/NSM/Semicond/GaInAs/

[21] P. Vyas, B. Thakore, P. Gajjar, and A. Jani, "Elastic constants of $Ga_xIn_{1-x}As$ semiconductor," in *AIP Conference Proceedings*, vol. 1349, no. 1. American Institute of Physics, 2011, pp. 1113–1114.

[22] J. Berggren, M. Hanke, and A. Trampert, "Bowing effect in elastic constants of dilute ga (as, n) alloys," *Applied Physics Letters*, vol. 108, no. 18, p. 183106, 2016.

[23] M. Reason, X. Weng, W. Ye, D. Dettling, S. Hanson, G. Obeidi, and R. Goldman, "Stress evolution in GaAsN alloy films," *Journal of applied physics*, vol. 97, no. 10, p. 103523, 2005.

[24] I. Vurgaftman, J. á. Meyer, and L. á. Ram-Mohan, "Band parameters for III-V compound semiconductors and their alloys," *Journal of applied physics*, vol. 89, no. 11, pp. 5815–5875, 2001.

[25] H. Carrère, "Conception, élaboration et caractérisation de structures à puits quantiques GaInAsN/GaAs pour composants optoélectroniques émettant à 1,3 um," Ph.D. dissertation, INSA Toulouse, 2002.

[26] A. Ptak, S. Johnston, S. Kurtz, D. Friedman, and W. Metzger, "A comparison of MBE-and MOCVD-grown GaInNAs," *Journal of Crystal Growth*, vol. 251, no. 1-4, pp. 392–398, 2003.

[27] A. Ptak, D. Friedman, S. Kurtz, and R. Reedy, "Low-acceptor-concentration GaInNAs grown by molecular-beam epitaxy for high-current p-i-n solar cell applications," *Journal of Applied Physics*, vol. 98, no. 9, p. 094501, 2005.

[28] N. Miyashita, Y. He, N. Ahsan, T. Agui, H. Juso, T. Takamoto, and Y. Okada, "Incorporation of hydrogen into MBE-grown dilute nitride GaInNAsSb layers in a MOCVD growth ambient," *Solar Energy Materials and Solar Cells*, vol. 185, pp. 359–363, 2018.

[29] S. Naritsuka, O. Kobayashi, K. Mitsuda, and T. Nishinaga, "Oxygen incorporation mechanism in AlGaAs layers grown by molecular beam epitaxy," *Journal of crystal growth*, vol. 254, no. 3-4, pp. 310–315, 2003.

[30] T. Achtnich, G. Burri, and M. Ilegems, "Study of oxygen incorporation in AlGaAs layers grown by molecular-beam epitaxy," *Journal of Vacuum Science & Technology A: Vacuum, Surfaces, and Films*, vol. 7, no. 4, pp. 2537–2541, 1989.

[31] Y. P. Varshni, "Temperature dependence of the energy gap in semiconductors," *physica*, vol. 34, no. 1, pp. 149–154, 1967.

[32] A. Kaschner, T. Lüttgert, H. Born, A. Hoffmann, A. Y. Egorov, and H. Riechert, "Recombination mechanisms in GaInNAs/GaAs multiple quantum wells," *Applied Physics Letters*, vol. 78, no. 10, pp. 1391–1393, 2001.

[33] Y. Tsai, B. Barman, T. Scrace, G. Lindberg, M. Fukuda, V. Whiteside, J. Keay, M. Johnson, I. Sellers, M. Al Khalfioui *et al.*, "Probing the nature of carrier localization in GaInNAs epilayers by optical methods," *Applied Physics Letters*, vol. 103, no. 1, p. 012104, 2013.

[34] T. Thomas, N. Kasamatsu, K. H. Tan, S. Wicaksono, W. K. Loke, S. F. Yoon, A. Johnson, T. Kita, and N. Ekins-Daukes, "Time-resolved photoluminescence of MBE-grown 1 eV GaAsSbN for multi-junction solar cells," in *2015 IEEE 42nd Photovoltaic Specialist Conference (PVSC)*. IEEE, 2015, pp. 1–5.

[35] A. Janotti, S. Zhang, S.-H. Wei, and C. Van de Walle, "Effects of hydrogen on the electronic properties of dilute GaAsN alloys," *Physical review letters*, vol. 89, no. 8, p. 086403, 2002.

[36] A. Ptak, D. Friedman, and S. Kurtz, "Effects of temperature, nitrogen ions, and antimony on wide depletion width GaInNAs," *Journal of Vacuum Science & Technology B: Microelectronics and Nanometer Structures Processing, Measurement, and Phenomena*, vol. 25, no. 3, pp. 955–959, 2007.

[37] S. Zhang and S.-H. Wei, "Nitrogen solubility and induced defect complexes in epitaxial GaAs:N," *Physical Review Letters*, vol. 86, no. 9, p. 1789, 2001.

[38] A. Srivastava, B. Arora, and S. Guha, "Measurement of Richardson constant of GaAs Schottky barriers," *Solid-State Electronics*, vol. 24, no. 2, pp. 185–191, 1981.

Chapter 4

Development of InGaAsN PIN subcells for MJSC integration

This chapter presents the development and the characterization of InGaAsN solar cells as a continuity of the material study conducted in Chapter 3. The first section describes in detail the technological process steps used to fabricate solar cells. The second section presents the *I-V* and EQE characterizations performed on InGaAsN solar cells and includes a discussion regarding the performance of the solar cells and the impact of the growth conditions.

Contents

4.1 Solar cell fabrication process

As described in the last chapter, we grew our solar cell epitaxial stacks on 4-inch GaAs substrates. For convenience sake, we fabricated 0.25 and 1 cm^2 solar cells by processing quarters of wafer. The following subsections describe our clean room process and the development of key technological steps.

4.1.1 Post-growth thermal annealing

Post-growth thermal annealing is usually conducted on dilute nitrides to cure growth defects and enhance their optoelectronic properties. This step is typically realised through rapid thermal annealing/processing (RTA/RTP) under N_2 inert atmosphere. At LAAS, we use an As-One setup from AnnealSys in which our samples are heated at 700 or 750°C for 30 seconds. A complicated aspect of this process step is that arsenic desorbs from GaAs above 520°C. To compensate and prevent As-depletion from the surface of the wafer during RTP, we put it in contact with the frontside of another GaAs substrate.

While this procedure generally reduces the As desorption rate, we encountered systematic problems with the RTP. First, the annealing often led to inhomogeneous surface roughness visible to the naked eye. Second, the impact of annealing was not found to be very replicable. Finally, some of our samples were plagued with large scale damage after the RTP step. These damages include cracks, breakage and wafer curving. They are thought to originate from an uneven repartition of the heat flux on our samples, leading to a very high level of thermal stress.

Therefore, as our thermal annealing procedure was found to be not robust enough, most of the solar cells were processed as-grown. Yet, we managed to process and characterize annealed solar cells and observed that thermal annealing could lead to both positive and negative effects (see Section 4.2.1). We have also decided to develop an "RTP-free" technological recipe as annealing can be a quite complicated step to implement in the growth of a 4-junction solar cell. Indeed, degradation of tunnel junctions [1, 2, 3], dopant out-diffusion [4] and InGaAsN bandgap blueshift are multiple issues that can occur after thermal annealing.

4.1.2 Ti/Au front metallization

Front metallization grid

As illustrated in Figure 4.1, we have used two photolithography masks to define the front metal grid of our solar cells. The first mask was designed by Kévin Louarn during his PhD thesis [5], it consists in 0.25 and 1 cm^2 square solar cell patterns featuring two large busbars (L=1 mm) connected with thin fingers (L=10 μm). There are four grid densities (shadowing) available on this mask: 0 (no finger), 3.33 %, 5 % and 10 %. In addition to the solar cells, this mask has TLM grid and small diode[1] patterns used for DLTS characterization.

The second mask was designed by Moana Desbordes during his internship in 2020 dedicated to the analysis of perimeter recombination in GaAs solar cells (see Annexe A). This mask provides a wider panel of geometries for the front

[1]Here, the term "diode" designates full metallization structures where there is no illumination area.

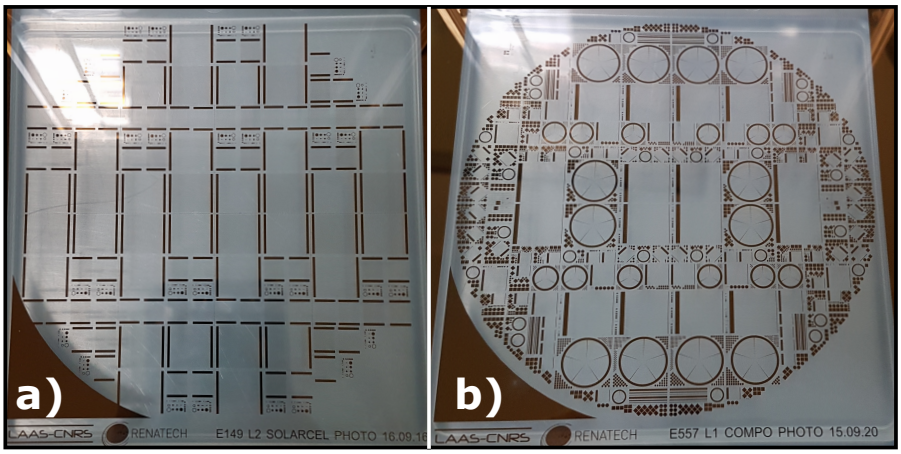

Figure 4.1: The two photolithography masks used to deposit the front metallization grid, designed by a) Kévin Louarn and b) Moana Desbordes.

metallization grid. Three sizes can be found for square, tilted square and round solar cells. The front grid relies here on a thin busbar connected to a large one by fingers with a 3.33 % density. Moreover, this photolithography mask can be used to process small diodes of different shapes with higher perimeter/area ratio (see Appendix A.2).

Optimizing the front metal grid is essential in photovoltaics and a compromise is usually made between shadowing and collection. Indeed, a low metal grid density reduces the metal contact shadowing, which increases the amount of light reaching the active layer. However, a large spacing between two fingers can also limit the collection of carriers in the window layer.

During this PhD thesis, we started by using the first mask and then switched to the second one for two reasons. Firstly, we noticed through EQE measurements that the lateral diffusion in the window layer was sufficiently high to rely on low grid densities. Secondly, we used the second mask to study the impact of both the shape and the size of solar cells on their dark saturation current (see Appendix A.2). All of the solar cells characterized in Section 4.2 were square-shaped with an 0.25 and 1 cm^2 designated illumination area.

Photolithography

Our masks are used to conduct a photolithography step on our samples. After a thorough surface cleaning (acetone/iso-propanol/DI water), a 5 μm NLOF layer is deposited on our wafer by spin-coating. NLOF is a negative resist: it is originally soluble in a developer (MFCD26 in our case) but becomes resistant to this chemical after it re-polymerizes under UV light exposure. Following the enduction step, the resist is baked for 90 s at 110 °C and insolated with UV passing through our mask in a MA6 Gen 4 system (*SUSS MicroTec*). Then, the sample undergoes post-exposure baking (PEB) and is plunged into the MFCD26 developer for $\approx$ 1 min. By the end of this photolithography procedure, the surface is entirely covered by NLOF resist, except for future metallization regions that were not exposed to UV light (Figure 4.2 a)).

Metal deposition

Before depositing metal on the patterned frontside, we deoxidize the surface of the GaAs cap layer to ensure an ohmic contact with low resistivity. The samples partially covered with resist are immersed in a 10 % HCl solution for ≈ 1-2 min. Immediately after this deoxidation step, the wafers are placed into an EVA600 setup (*Alliance Concept*) where Ti and Au are successively deposited. In this machine, the deposition occurs through thermal evaporation where metal targets are heated under electron irradiation. A first 50 nm titanium layer is deposited to ensure the contact adherence followed by a 200 nm gold layer which displays very low resistivity (Figure 4.2 b)).

Once the metallization step is finished, the NLOF resist is removed in a process step called "lift-off", revealing the metal grid (Figure 4.2 c)). The resist lift-off is realised by immersing the samples in acetone for at least one hour.

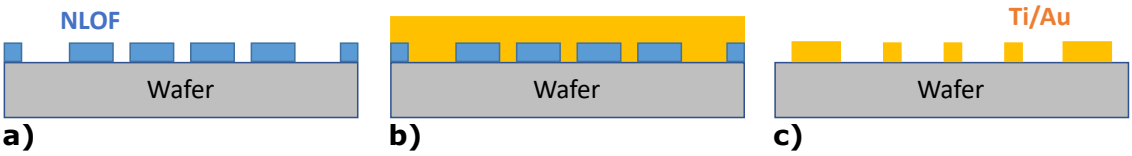

Figure 4.2: Schematics of the front contact deposition steps: a) after photolithography patterning, b) after Ti/Au thermal evaporation and c) after resist-removal (lift-off).

Contact resistance

The specific contact resistance (SCR) of the interface between the metal and the GaAs cap layer ($p^+ = 1.5 \times 10^{19}$ cm^{-3}) was determined through transfer length method (TLM). This technique consists in measuring the total electrical resistance between two metal pads located on the same wafer side and separated with a given spacing. The measured value results then from the contribution of the contact resistance R_c at the two metal/semiconductor interfaces and the resistance of the GaAs cap layer R_{GaAs} (we assume here that the resistance in the metal is null).

$$R_t = 2R_c + R_{GaAs} \tag{4.1}$$

By measuring R_t for different values of the contact spacing d, the length of the electrical current path in the semiconductor is varied, which changes R_{GaAs}. We then plot R_t as a function of d and calculate R_c from the y-intercept (additionally, the sheet resistance of the GaAs cap layer can be obtained with the slope). Dividing the contact resistance by the effective area of the metal pad, we obtain the specific contact resistance.

In our design, we measured a quite low SCR equal to 1.01×10^{-6} $\Omega.cm^2$, which guarantees a negligible voltage drop (due to ohmic resistance at the frontside) during the solar cell operation.

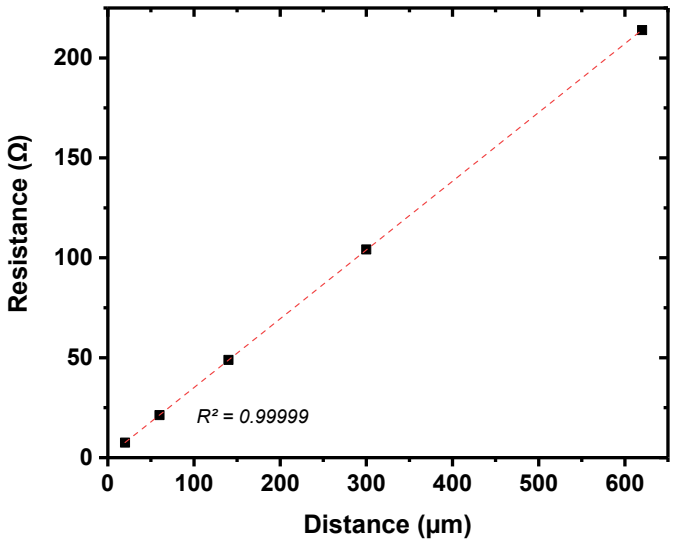

Figure 4.3: Evolution of the contact resistance with the distance between the two Ti/Au pads.

4.1.3 Mesa etching

We etch mesa between our solar cells for two main reasons: i) it isolates electrically each *pin* diode (only their *n*-side is connected through the substrate), ii) it precisely defines the designated illumination area of our cells.

Photolithography

The photolithography step for mesa etching is basically the same as for defining the metallization grid, except that we use here ECI which is a positive photoresist. This means that insolated resist becomes soluble to the developer and that the Cr patterns on our mesa masks correspond to regions that will remain covered by the resist.

Wet etching

A phosphoric acid solution ($H_2O/H_3PO_4/H_2O_2$ with 25/3/1 volume proportion) is used to etch the mesa of the cells. After the solution is prepared, a calibration of the etch rate is done with profilometer measurements. Considering the structure of our InGaAsN *pin* solar cells, the targeted etch depth lies between 1.6 and 2 μm, which corresponds to a 7-12 min etching duration. Once the mesa are completed, we rinse our sample and remove the resist with acetone.

4.1.4 Cap layer removal

The GaAs cap layer is used to minimize the front contact resistance. However, being highly-doped, it displays a large absorption coefficient in the whole

spectral range (free carrier absorption), which reduces the amount of light reaching the InGaAsN absorber. To prevent this parasitic absorption, we etch the uncovered cap layer with citric acid ($C_6H_8O_7$). This latter compound is used with 10 % hydrogen peroxide (H_2O_2) as this solution offers high selectivity of the GaAs etching over AlGaAs ternary alloys [6]. Through calibrations, we measured the etching rate to be approximately 4 nm/s which corresponds to a $\approx$ 40 seconds wet etching to remove the 150 nm cap layer.

4.1.5 AuGeNi/Au back metallization

AuGeNi is one of the main alloys used to contact *n*-type GaAs with moderate doping concentration. This alloy can provide ohmic contact with relatively low resistance thanks to the interdiffusion of species occurring once the junction is annealed [7]. In particular, germanium atoms diffuse into GaAs where they act as donor impurities, which increases the *n*-type doping level at the interface. A special care should be paid to the annealing temperature as the formation of AuGe and AuGa alloys is responsible for metal "balling up" and spiking, respectively [7].

The backside metallization is carried as a last process step because AuGeNi was found to be damaged during our wet eching procedures (mesa and cap layer removal). To achieve high-quality contact interface, we start by etching the rear substrate surface with the phosphoric solution mentioned earlier. Indeed, the backside of the wafer is subjected to arsenic desorption during the epitaxial growth of the cells, which leads to poor surface quality. During this etching step, the already-processed frontside is protected with a 10 μm-thick resist layer.

After deoxidation, a 250 nm layer of $Au_{0.65}Ge_{0.24}Ni_{0.11}$ was deposited on the backside of our wafers with the sputtering method. All of the samples, except for A6, B3 and B4, were metallized at IES (*Montpellier, France*) with Frederic Pichot, using an Alcatel SCM 600. The three remaining samples were processed in LAAS with an AC450CT from Alliance Concept. Both of these sputtering setups rely on argon cation bombardment. A 200 nm gold layer was then deposited on top of AuGeNi.

As it was mentioned, the quality of the GaAs/AuGeNi contact depends strongly on the annealing recipe. We conducted an optimization campaign by measuring the dark current-voltage characteristics of samples annealed at different temperatures for 90 seconds under H_2N_2 atmosphere.

We can see in Figure 4.4 that the contact resistance (defined as the inverse of the slope) is very high for unannealed samples and that ohmic behaviour is only obtained for T>350 °C. We chose 350 °C as an annealing temperature for our solar cell fabrication process as the contact resistance was found to increase for higher temperatures. In addition to low conductance, the morphology of the AuGeNi metal pads was found to seriously degrade after annealing at 400 °C (roughening and large scale inhomogeneities).

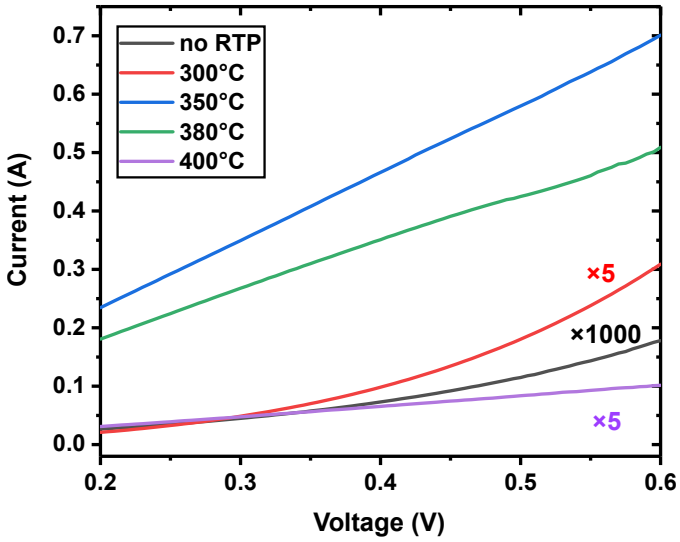

Figure 4.4: Dark *I-V* characteristics of GaAs/AuGeNi junctions annealed at different temperatures.

By the end of this process step, the final structure of the solar cell is achieved, as represented in Figure 4.5.

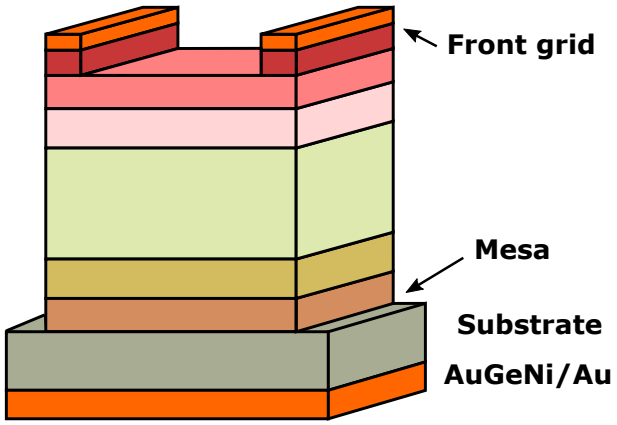

Figure 4.5: Structure of a processed solar cell. The dimensions are not to scale.

4.1.6 Mounting on sample holder

To facilitate the characterization of our solar cells and later on their irradiation, we separated them by cleaving the wafer (Figure 4.6). The 1 cm^2 cells were then glued on a 2×2 cm^2 aluminium nitride (AlN) support with EPO-TEK H20E. This glue is both an electrical and a thermal conductor based on a silver-filled epoxy system. The AlN support is an electrical insulator patterned with gold metallization used to transfer the front and rear contacts. Its dimensions and the positioning of the cell are given in Figure 4.7 a). Unlike alumina (Al_2O_3), AlN has

a relatively high thermal conductivity, which is highly desirable in our irradiation studies.

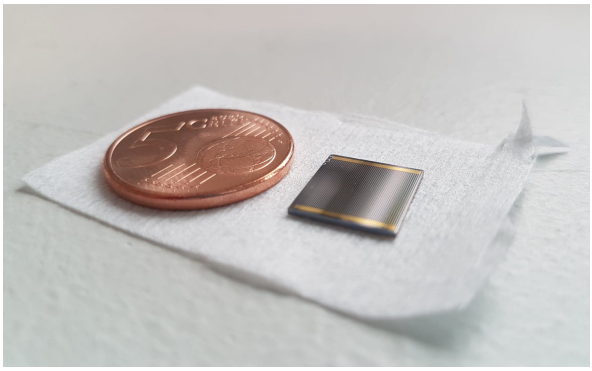

Figure 4.6: Picture of a 0.25 cm^2 solar cell placed next to a 5 euro cent coin as a scale reference.

Once the cell is pasted on the AlN sample holder, Al-wire-bonding is realised to transfer the front contact to the smaller gold pad, as it can be seen in Figure 4.7 b). As for the rear of the cell, it can be directly contacted with the larger pad.

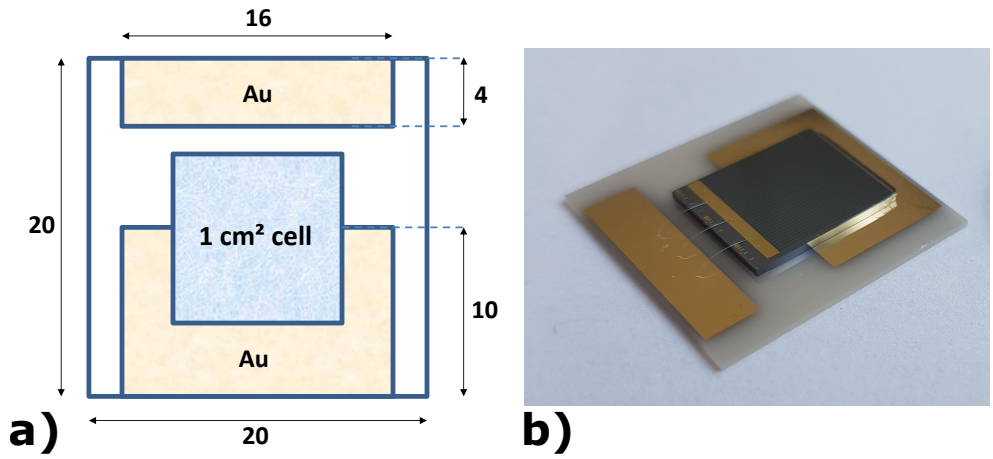

Figure 4.7: a) Dimensions (in *mm*) of the Au-patterned AlN support b) Picture of a solar cell pasted on an AlN support with wire-bonding electrical transfer.

4.2 InGaAsN solar cell characterization

4.2.1 Single junction solar cells

Spectral response

The quantum efficiency of a solar cell is defined by the number of carriers collected in short-circuit condition (V=0 V) divided by the number of exciting photons in a given wavelength range. Measuring the quantum efficiency spectrum of a solar cell gives valuable information on the absorption and collection losses occurring in the device.

We performed *external* quantum efficiency (EQE) measurements at IES with Stéphanie Parola, using a halide lamp coupled with an Oriel monochromator. The light intensity was calibrated with Si and Ge reference photodiodes. A lock-in amplifier system was used to ensure high signal/noise ratios. We also measured the reflectance $R(\lambda)$ of our solar cells with FTIR spectroscopy and we used this latter attribute to calculate the *internal* quantum efficiency IQE:

$$IQE(\lambda) = \frac{EQE(\lambda)}{1 - R(\lambda)} \tag{4.2}$$

The IQE corresponds to the number of collected carriers divided by the number of photons **entering** the solar cell. We calculated the IQE of 0.25 and 1 cm^2 InGaAsN solar cells and did not find any influence of the cell size, which reflects the preponderance of the bulk recombinations over the perimeter ones. Figure 4.8 presents the IQE spectra of six 0.25 cm^2 InGaAsN solar cells, measured at room temperature.

In the following analysis, we assume that the absorption coefficient is the same in every solar cell except A5, as the band gap energy of these samples is identical. Since these solar cells rely on the same structure and were fabricated with the same technological process, a difference in quantum efficiency can only originate from a difference in *collection* efficiency. For the sake of convenience, the growth parameters of the different samples are summarized in Table 4.1.

Similarly to the PL results, we observe that samples A1, A2 and A6, grown with a higher *As/III* ratio, exhibit overall better quantum efficiencies than A3 and A4. However, we can see that even though A4 displays poor IQE for short wavelengths, its collection efficiency is similar to the high *As/III* samples for λ>870 nm (870 nm corresponds to the cut-off wavelength of GaAs). On the other hand, we observe the opposite behaviour for A3 as its IQE steadily decreases from $\approx$ 700 to 1050 nm. This difference originates from the field-aided collection regime of the solar cells: low energy photons (long λ) penetrate deeper in the material and create photocarriers far away from the p-GaAs/n^--InGaAsN junction. Because of their short diffusion length, minority carriers are mostly collected when they are swept by the electric field of the depletion region. The higher collection

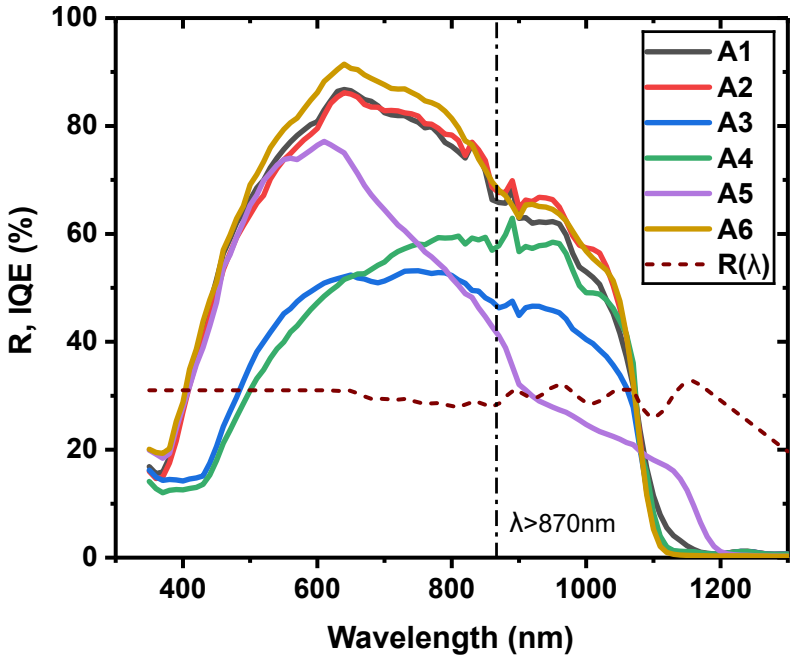

Figure 4.8: Internal quantum efficiency of the six InGaAsN solar cells and their spectral reflectance.

efficiency of A4 compared to A3 is then attributed to its lower residual doping and its wider SCR. Despite displaying lower PL intensity (higher non-radiative recombination rate), sample A4 can photogenerate as much current as A1, A2 and A6 under AM0>870 nm light (AM0 filtered by GaAs).

In samples A1, A2 and A6, the remarkable difference of quantum efficiency between λ<870 nm and λ>870 nm arises from the heterostructure nature of the cell. Photons with a wavelength shorter than 870 nm can be absorbed in the *p*-GaAs emitter and the resulting photocarriers are more likely to be collected in this region because of longer diffusion length in GaAs. Thus, the IQE at λ<870 nm is higher because it results from absorption in both GaAs and InGaAsN.

We also notice from Figure 4.8 the low quantum efficiency displayed by A5,

Table 4.1: Growth conditions of the InGaAsN solar cells

Sample name	N content (%)	T_g (°C)	As/III ratio
A1	1.6	465	12 (+Bi)
A2			12
A3		445	10
A4		485	
A5	2.0	430	7.5
A6	1.6	465	12
T1	2.0	430	7.5

grown with a higher nitrogen content. This result is a direct consequence of: i) the higher defect concentration measured by DLTS for samples grown with more nitrogen and ii) the high BGCC measured in this sample (N_d=7×10^{16} cm^{-3}). The effect of increased N composition is also visible through the cut-off wavelength of A5 (lower band gap energy), which is roughly 80 nm more important than in the other samples. However, even with a narrower band gap, this InGaAsN solar cell can only deliver low current densities.

As the external quantum efficiency measurements are performed under short-circuit conditions, we can calculate the corresponding photocurrent by integrating the spectral response over the appropriate spectrum. The spectral response (SR) is equal to the generated current divided by the power of the excitation light at a given wavelength. It can be expressed as:

$$SR(\lambda) = EQE(\lambda) \times \frac{\lambda q}{hc} \tag{4.3}$$

Integrating the product of SR and the spectral irradiance H_0 gives the photocurrent density:

$$J_{sc} = \int_{\lambda_1}^{\lambda_g} SR(\lambda) \times H_0(\lambda)\, d\lambda \tag{4.4}$$

where λ_1 corresponds to the lower limit of the spectrum and λ_g to the cut-off wavelength of the solar cell. To evaluate the J_{sc} of our solar cells, we used Gueymard's AM0 spectrum [8] and we took λ_1=0 and λ_1=870 nm to simulate full and GaAs-filtered AM0 expositions, respectively. The J_{sc} results will be used and presented in the light current-voltage measurements subsection .

Impact of thermal annealing

All the quantum efficiency measurements presented above were obtained with as-grown solar cells while a thermal annealing step is usually conducted to improve the optoelectronic properties of dilute nitrides. Even though the PL intensity of bulk layers was found to increase after annealing (see 3.2.2), a PL investigation on InGaAsN solar cells revealed the opposite behaviour. Moreover, we observed different evolutions of the BGCC with thermal annealing and we then decided to assess the impact of rapid thermal processing on the IQE of our cells.

Figure 4.9 shows the evolution of the IQE spectra of samples A3 and A4 – grown at 445 °C and 485 °C, respectively – after annealing at 700 and 750 °C. Two opposite effects occur here: the quantum efficiency slightly increases for A3 while it drastically decreases for sample A4. ECV measurements showed a six-fold decrease in the residual doping of A3 after 750 °C annealing whereas this step led to a ≈10 times increase in the BGCC for A4. As we said earlier, having a wide space charge region is essential to collect minority carriers (holes) in InGaAsN. The change in residual doping level upon annealing is likely to arise from the

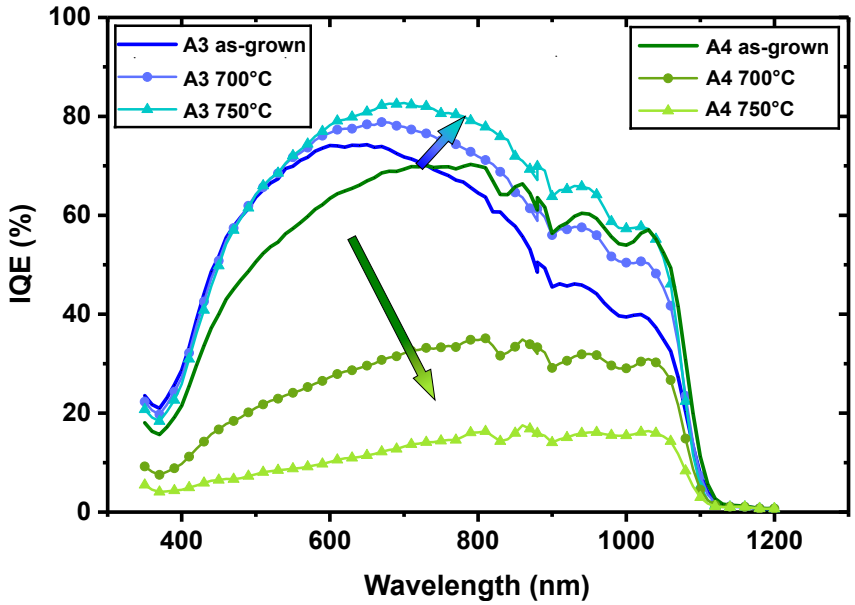

Figure 4.9: Impact of thermal annealing on the internal quantum efficiency of A3 and A4.

curing of acceptor or donor defects. For instance, the curing of donor defects in A3 could be the reason for the increase in its IQE whereas A4 could have experienced curing of acceptor defects.

The IQE of sample A1 was also found to degrade after thermal annealing, although no noticeable change in the BGCC could be observe with this sample. This indicates that the decrease in quantum efficiency can only be ascribed to a decrease in the minority carrier lifetime, which suggests an increase in the deep-level defects concentrations.

Dark current-voltage measurements

Dark current-voltage (DIV) characterization is a simple and powerful technique to access multiple diode properties such as the dark saturation current, the ideality factor and the parasitic resistances. Figure 4.10 shows the DIV characteristics of six 1 cm^2 InGaAsN solar cells, mounted on their AlN holder.

For every cell, the asymmetry of the DIV profile indicates a low level of shunt (high R_{sh}). The shunt and the series resistances were calculated using the following equations:

$$R_{sh} = \left(\frac{\delta V}{\delta I}\right)_{V=0} \qquad R_s = \left(\frac{\delta V}{\delta I}\right)_{V=V_{oc}} \tag{4.5}$$

As summarized in Table 4.2, the shunt resistance is high in every solar cells. Series resistances were found to be quite similar in every samples at the notable exception of A5. A large and reproducible series resistance ($R_s \in$ [110 - 135] Ω/cm^2) was found in the seven solar cells processed from the A5 wafer. Know-

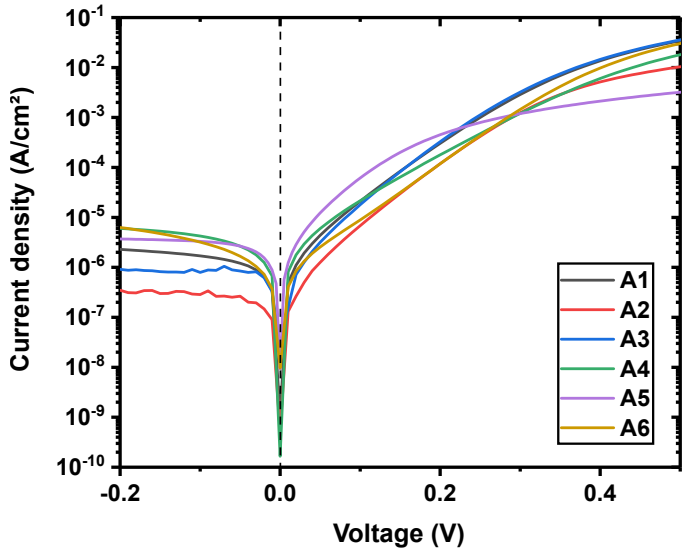

Figure 4.10: Dark *J-V* characteristics of InGaAsN solar cells, measured at room temperature. The reverse current density was taken as an absolute value for the sake of clarity.

ing that the fabrication process and the cell architecture were identical for the six wafers (from A1 to A6), this high series resistance necessary arises from the InGaAsN layer. Although we did not identify the responsible underlying mechanism, it is interesting to note that A5 was grown with a higher nitrogen composition. This potentially reveals a correlation between R_s and the N content in InGaAsN.

Table 4.2: Diode properties of the InGaAsN solar cells

	A1	**A2**	**A3**	**A4**	**A5**	**A6**
$R_{sh}(\Omega/cm^2)$	22500	93400	29800	13100	9400	25400
$R_s(\Omega/cm^2)$	10.9	22.1	15.0	24.5	122	9.1
$J_0(\mu A/cm^2)$	1.2	0.32	0.78	2.2	5.1	0.7

In addition to the parasitic resistances, we calculated the dark saturation current density from these curves. As we can see in Table 4.2, the saturation current is more important in sample A5, grown with a higher nitrogen content. This indicates a larger carrier recombination rate which is consistent with the low PL intensity and the high DLTS signal exhibited by samples grown with N≥2 % (see 3.2.2). Moreover, the lower saturation currents observed for samples A2 and A6 (grown in the same conditions) are in line with the superior PL intensity displayed by A2. This result is another evidence of fewer recombination centres in 1.11 eV samples grown with a higher arsenic overpressure. As for A3 and A4, the absence of correlation between their PL intensity and their J_0 can simply be explained by the size of their depletion region. Having a lower residual doping (see 3.3), A4 has a wider SCR which enhances its recombination rate.

Finally, the ideality factor n was extracted from our DIV characteristics, as de-

picted in Figure 4.11. We could not calculate meaningful n values for A5 because of its high series resistance.

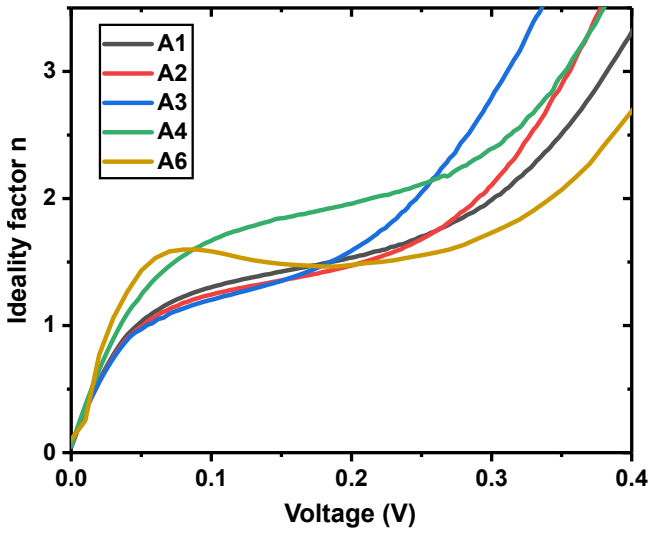

Figure 4.11: Evolution of the ideality factor with voltage.

As we will see in the next subsection, the maximum power voltage V_{mp} ranges from 0.2 to 0.27 V, depending on the cell. We can see that for all the samples the ideality factor lies between 1.5 and 2 in this region. In the Shockley-Read-Hall theory, an ideality factor equal to 1 indicates that the recombination occurs mostly in the quasi neutral regions [9]. On the other hand, n=2 implies that the recombination rate depends on both carrier types, which means that most of the recombination takes place within the depletion region. The high ideality factor of sample A4 is then consistent with its large SCR (>420 nm).

We did not observe any significant impact of the grid condition, the size and the shape of the solar cells on their DIV characteristics. This suggests that the recombination in the InGaAsN solar cells is much more important in the bulk than it is on the surface. This finding goes in line with the high defect concentration and the low minority carrier lifetime generally reported in InGaAsN.

Light current-voltage measurements

We measured the light *I-V* characteristics (LIV) of our solar cells at ONERA with an Oriel solar simulator equipped with a Xenon arc lamp and a AM0 filter. The solar cells were characterized on their holder and were thermoregulated at 25 °C with a water-cooled copper plate.

The light power of the solar simulator was calibrated with reference triple junction and single junction GaAs solar cells from AZURSPACE. Although our Oriel simulator is an ABA class system which indicates spectral mismatches lower than 25 % [10], we observed large discrepancies between measured photocurrents and values calculated from the EQE spectra. The AM0 flux calibrations performed with the GaAs and the 3J reference solar cells ensure spectral matching in the UV-visible range because the triple junction is current-limited by the

GaInP top cell. However, it is possible that the solar spectrum displays an excessive infrared component compared to the AM0 reference spectrum. For the sake of coherence with spectral response measurements, we adjusted the LIV characteristics of the cells to match the photocurrents calculated with EQE spectra.

Figure 4.12 shows the current-voltage response of the six InGaAsN solar cells. It can first be noticed that samples A1, A2 and A6, grown with a higher *As/III* ratio, exhibit better *J-V* characteristics, which translates into higher power densities. As observed with the n(V) profiles, A6 is somewhat different from A2 (grown with the same conditions). Both samples have approximately the same J_{sc} and V_{oc} but A6 displays a much higher fill factor, as summarized in Table 4.3.

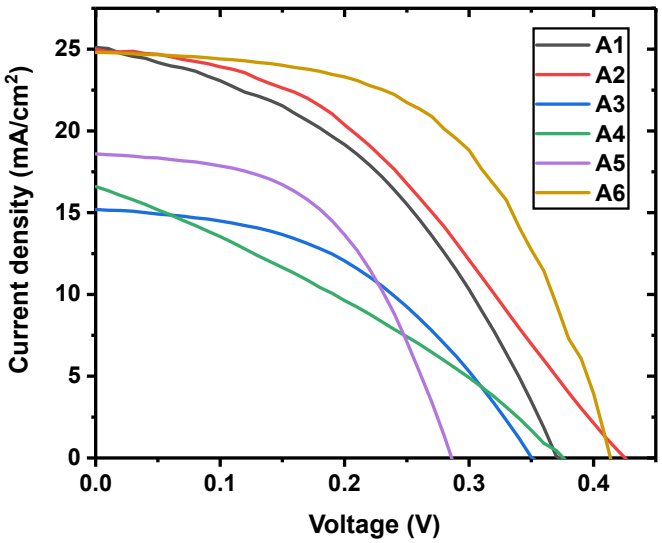

Figure 4.12: *J-V* characteristics of the six InGaAsN solar cells measured under AM0 sunlight.

In addition to shunt and series resistances, the fill factor values depend on the BGCC of the absorber. Indeed, the variation of the SCR width with voltage is more important in solar cells with low residual doping, which leads to large reduction of the collection efficiency when the voltage is increased [11, 12]. This behaviour can easily be mistaken with shunt as it leads to high *J-V* slopes near V=0 V. This is particularly true for sample A4 which has the lowest BGCC. We evidenced in Figure 4.13 that the shunt-like characteristic arises from the voltage-dependent collection of the *pin* structures. For both A3 and A4, the superposition principle is not respected and we can see that the discrepancy between the LIV and the shifted DIV is stronger for lower residual doping.

Figure 4.12 also shows that despite having a higher nitrogen content and a narrower bandgap, the A5 solar cell photogenerates less current than A1, A2 and A6. This concurs with our previous materials and diode observations and suggests that most of the photocarriers recombine before they can be collected. In addition, the bandgap–V_{oc} deficit of A5 is very important ($W_{oc} = E_g - V_{oc} = 1.05 - 0.29 = 0.76$ eV), which indicates a large recombination rate in the active layer.

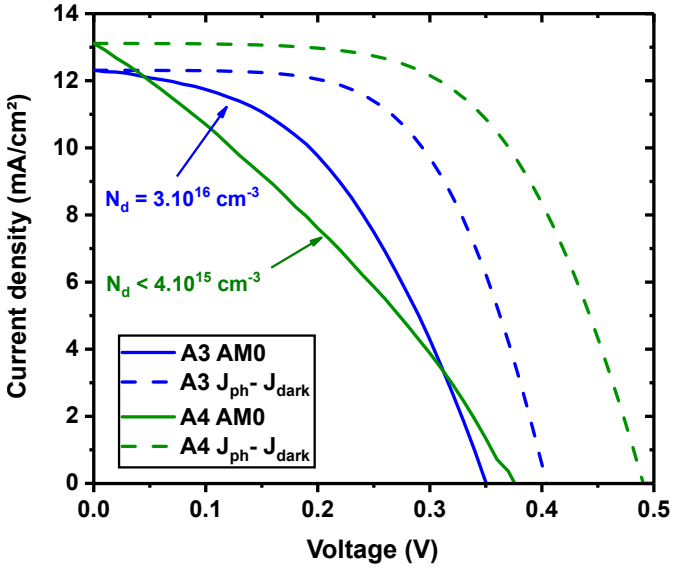

Figure 4.13: Comparison of the AM0 *J-V* and the photocurrent-shifted dark *J-V* characteristics for samples A3 and A4.

Table 4.3: InGaAsN solar cells properties for a AM0 illumination

	A1	**A2**	**A3**	**A4**	**A5**	**A6**
$J_{sc}(mA/cm^2)$	25.1	25.0	15.2	16.6	18.6	24.8
$V_{oc}(V)$	0.375	0.43	0.35	0.375	0.29	0.41
$FF(\%)$	43.6	43.5	45.8	32.0	52	55.3

Characterizing the solar cells under AM0 exposition presents two limitations. Firstly, the measured values of J_{sc}, V_{oc} and FF are not representative of what an InGaAsN subcell could deliver within a MJSC. Indeed, high energy photons of the AM0 spectrum are absorbed in the GaInP and GaAs top cells and cannot be harvested by the dilute nitride subcell. Secondly, part of the AM0<870 nm light is absorbed and collected within the 200 nm GaAs emitter rather than the InGaAsN absorber.

The *I-V* response of the InGaAsN solar cells was then measured under AM0>870 nm illumination as this latter spectrum represents the incident light reaching the InGaAsN subcell in a MJSC. To do that, we placed on the optical path a Newport long-pass filter with a 865-1200 nm transmittance range.

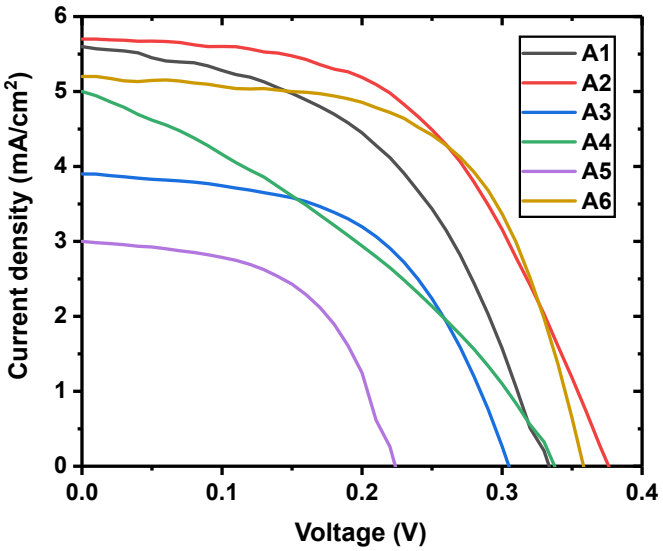

Figure 4.14: *J-V* characteristics of the six InGaAsN solar cells measured under AM0>870 nm sunlight

As we can see in Figure 4.14, the best InGaAsN solar cells are able to photogenerate ≈ 5.7 mA/cm^2 under light representing integration condition. Again, we observe that growing 1.11 eV InGaAsN with an *As/III* ratio equal to 12 (rather than 10) leads to better photovoltaic properties. Our devices were fabricated without anti-reflection coating and we calculated from the IQE that the J_{sc} could reach 7.96 mA/cm^2 if surface reflectance was suppressed.

Although the photocurrent difference between A2 and A6 (grown in the same conditions but two years apart) might originate from their slightly different bandgap energies, we notice a higher FF and a lower V_{oc} for sample A6. This somehow illustrates the difficulty to obtain perfect reproducibility in the epitaxial process, as slow deviation of the *As/III* ratio and the growth temperature were shown to induce considerable change in the materials properties.

Table 4.4: InGaAsN solar cells properties for a AM0>870 nm illumination

	A1	**A2**	**A3**	**A4**	**A5**	**A6**
$J_{sc}(A/cm^2)$	5.59	5.75	3.86	5.02	2.96	5.21
$V_{oc}(V)$	0.335	0.375	0.305	0.340	0.225	0.355
$FF(\%)$	48.3	52.6	54.1	34.6	58.9	60.4

We also investigated the dispersion of the performance of cells processed from the same wafer. Despite the PL inhomogeneity accross the wafer evidenced in Section 3.2.2, Figure 4.15 shows a relatively low dispersion of the *J-V* curves for 1 cm^2 square solar cells processed from the A6 wafer. This reproducibility is crucial because it allows the comparison between cells taken from different wafers.

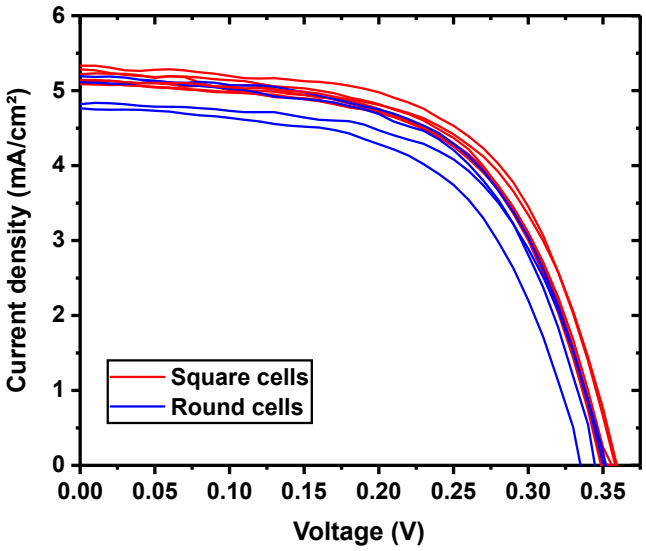

Figure 4.15: AM0>870 nm *J-V* characteristics of seven square (red) and four round (blue) solar cells processed from the A6 wafer.

However, we can clearly see that round solar cells exhibit poorer photovoltaic properties. This could arise from their smaller size (≈ 0.785 cm^2) or from their shape exposing mesa-etched surfaces in all the crystallographic directions. Nonetheless, no influence of the size and shape of the InGaAsN cells could be observed on their dark *J-V* characteristics (see Appendix A.2). The lower V_{oc} and J_{sc} of round solar cells could also originate from their radial metal grid although the shading factor was the same as for square cells.

4.2.2 Tandem solar cell

Spectral response

Our tandem solar cell is a two-terminal device including two subcells connected in series. To measure the spectral response of one of the subcells, we need to optically bias the other one to allow current to flow across the device. To do that, we used a Xenon lamp coupled with filters:

- To measure the EQE of the GaAs top cell, we used a 1000 nm long-pass filter to bias the bottom cell.
- To measure the EQE of the InGaAsN bottom cell we used a 850 nm low-pass filter to bias the top cell.

Optical bias cannot be used alone because it leads to the polarization of the tandem solar cell, which prevents the short-circuit condition required for the EQE measurement. A capacitor is then connected in series to the tandem as a counter electrical bias: in a DC configuration (DC current is generated by the biasing

light), the capacitor is in open-circuit condition and forces the biased solar cell to be at V_{oc}, which prevents polarization of the measured subcell. In the AC configuration (AC current is generated by the monochromatic excitation light and the lock-in system), the capacitor is in short-circuit condition and the photocurrent crossing the tandem solar cell can be measured.

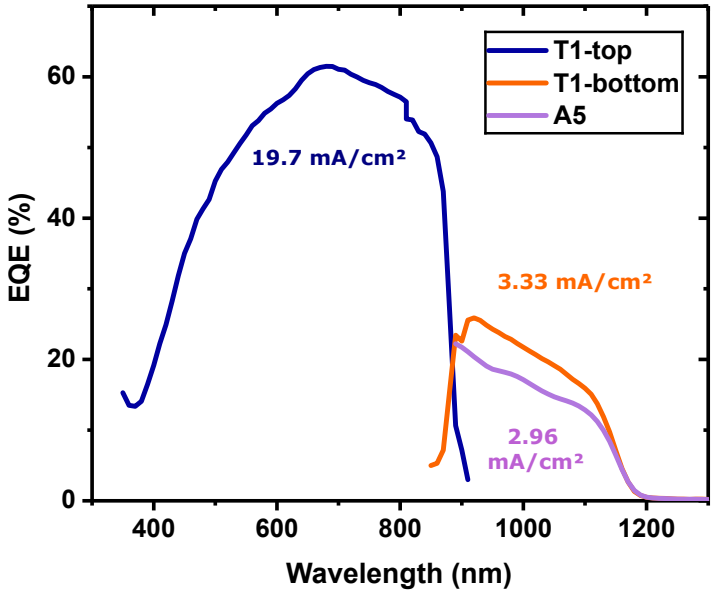

Figure 4.16: External quantum efficiency spectra of the subcells of the tandem solar cell T1 and of the InGaAsN single junction solar cell A5.

Figure 4.16 shows the external quantum efficiency of the GaAs/InGaAsN tandem solar cell T1. We observe a large EQE difference between the two subcells which translates into a huge current-mismatch within the tandem structure. Indeed, we integrated the EQE spectra and found that the GaAs top cell could generate up to 19.7 mA/cm^2 whereas the InGaAsN top cell could only deliver 3.33 mA/cm^2. We also notice a difference between the EQE of the bottom cell and the InGaAsN single cell A5, grown in the same conditions. This difference originates from the thicker InGaAsN absorber in the bottom cell (1.15 μm) compared to the monojunction (1 μm), which limits the transmission loss (non-absorption) in the device.

The EQE spectra of the tandem solar cell highlight material and architecture issues. As we noticed earlier, the dilute nitride with higher nitrogen content (N=2 %) displays relatively poor optoelectronic properties (high recombination rate and high residual doping) leading to low collection efficiency. The material needs further growth optimization to achieve longer diffusion length and wider depletion region. In addition, the architecture of the tandem solar cell could also be optimized to balance the photocurrents of the subcells and permit current-matching. Thinning the GaAs top cell would lead to an increase in the available light for the bottom cell which would enhance its photocurrent without having detrimental effect on the tandem solar cell. Increasing further the thickness of the InGaAsN active layer could also minimize transmission losses and increase the

photocurrent.

Dark current-voltage measurements

The dark *J-V* characteristic of the GaAs/InGaAsN tandem solar cell T1 was also investigated, along with its component subcells. To do that, a GaAs solar cell was fabricated with the same structure as T1's top cell.

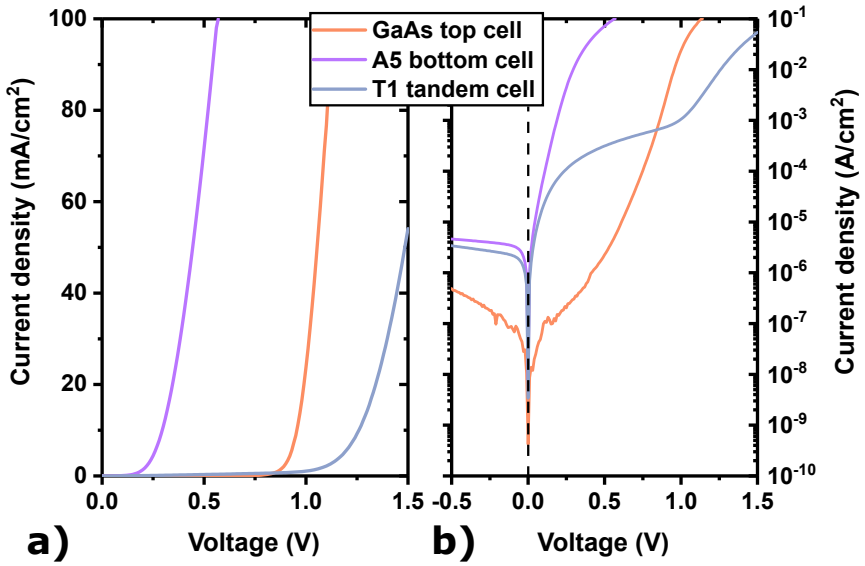

Figure 4.17: Linear and logarithmic dark *J-V* characteristics of the GaAs/InGaAsN tandem (T1) and its component subcells measured at room temperature.

As we can see in Figure 4.17 a), the *knee*-voltage of T1 is approximately equal to the sum of the *knee*-voltages of its subcells. Just as the open-circuit voltage under illumination, it arises from the series-connected architecture of the tandem solar cell. Furthermore, we notice in Figure 4.17 b) that the dark current of the tandem solar cell is dominated by the recombination in the InGaAsN bottom cell. Indeed, the saturation current density of the tandem is equal to 3.6 μA/cm^2 which is much closer to the J_0 value for A5 (5.1 μA/cm^2) than for the GaAs top cell ($\approx$ 0.02 μA/cm^2).

Light current-voltage measurements

Similarly to monojunction solar cells, we measured the *I-V* characteristics of the tandem T1 under AM0 sunlight. However, unlike for EQE measurements we cannot dissociate the response of each subcell in our two-terminal device. To access subcell informations such as fill factor and open-circuit voltage, we also characterized a GaAs and an InGaAsN (A5) component cell under AM0 and AM0>870 nm light, respectively. The *J-V* curves of the tandem and the component solar cells are shown in Figure 4.18.

Just as for the EQE measurements, we observe a large current-mismatch from the two component solar cells. This results in a low photocurrent in the tandem cell limited by the contribution of the InGaAsN bottom cell. The small difference

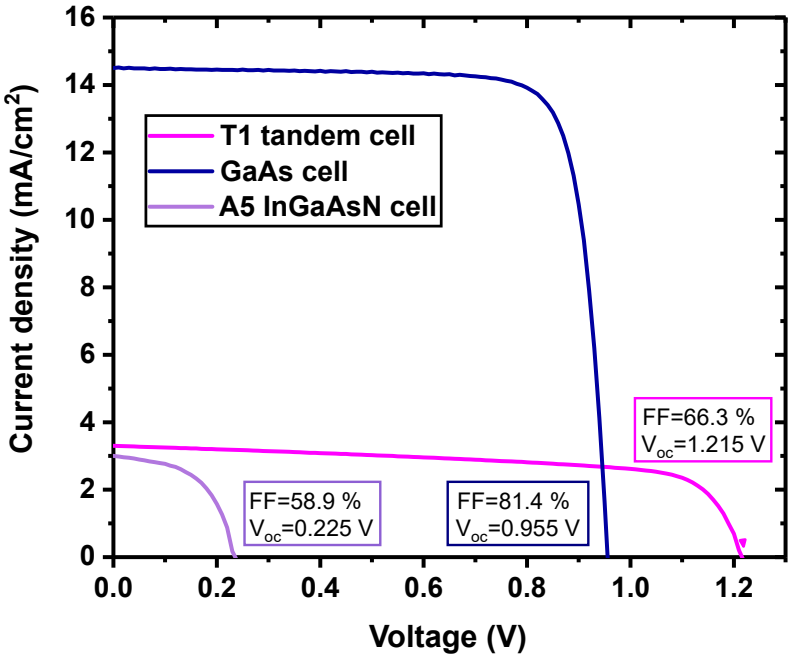

Figure 4.18: Light *J-V* characteristics of a tandem and two single junction solar cells. The *J-V* responses were measured under AM0 for T1 and the GaAs solar cell and under AM0>870 nm for the InGaAsN solar cell A5.

between the J_{sc} exhibited by A5 and T1 originates from their different absorber thicknesses, as addressed in the EQE subsection. Additionally, we can see that the GaAs solar cell photogenerates less current (14.5 mA/cm^2) than the top cell of the tandem (19.7 mA/cm^2). This arises from a doping calibration error which led to an excessive *n*-type doping (4×10^{18} cm^{-3}) in the $3\mu m$ GaAs base of the monojunction.

Figure 4.18 also shows the open-circuit voltage and the fill factor of the cells. As expected, the voltage of the series-connected subcell adds up and we have approximately V_{oc}(tandem)=V_{oc}(top)+V_{oc}(bottom). This equality of the open-circuit voltages also demonstrates the absence of voltage drop across the subcells interface. Indeed, the tunnel junction used in this tandem solar cell (more informations in 3.1.3) relies on a heterostructure providing peak tunneling current density as high as 1300 A/cm^2 [13]. Finally, the relatively low fill factor of the tandem solar cell is thought to originate from the high series resistance of the InGaAsN subcell.

4.2.3 Discussion

The solar cell characterization results (EQE, DIV and LIV) are consistent with the material properties reported in Chapter 3. Among the five 1.11 eV samples, those grown with a higher *As/III* ratio (A1, A2 and A6) exhibit better photovoltaic characteristics. The photovoltaic performances of the InGaAsN solar cell depend strongly on two factors: the BGCC which defines the thickness of the space charge region and the minority carrier lifetime which defines the diffusion length. Sample A4 demonstrates that having a low residual doping is necessary but not sufficient to ensure high output power. Indeed, this sample displays a large SCR which grants it a fairly high J_{sc}, but its excessive non-radiative recombination rate (deduced from PL measurements) leads to a very short diffusion length. The fill factor of such a sample is also strongly affected because of the voltage-dependency of the field-aided collection regime.

In addition, the analysis of the solar cells characteristics shows that there is no correlation between the BGCC and the NRR rate. We know that the *n*-type residual doping in our dilute nitrides is intrinsic and arises from crystal defects. These defects have probably a shallow energy level near the conduction band, making them donor defects. On the other hand, deep-level defects are likely to be responsible for the higher recombination rate without playing a significant role in the doping level. Identifying the crystal nature and the thermodynamic properties of deep and shallow levels appears then necessary to develop: i) epitaxial growth recipes that prevent their apparition and ii) annealing procedures that cure them.

In our case, we observed antinomic effects of the thermal annealing on quantum efficiency. Both the IQE increase displayed by A3 and the IQE decrease exhibited by A4 were shown to correlate with a change in residual doping. This indicates that thermal annealing plays a major role in curing or introducing shallow defects. Besides, the increase in BGCC experienced by A4 upon annealing could also originate from the curing of compensating acceptor defects.

Our best solar cells exhibit a 5.75 mA/cm^2 photocurrent under AM0>870 nm, as calculated with EQE measurements. By suppressing the reflection losses with a perfect anti-reflection coating (ARC), these solar cells could generate up to 7.96 mA/cm^2. This value is too low to satisfy the current-matching condition in a GaInP/GaAs/InGaAsN MJSC ($\approx$ 15 mA/cm^2) but remains one of the highest photocurrents reported for as-grown InGaAsN solar cells. We have identified three main routes to increase further the photovoltaic performances (J_{sc}, V_{oc} and FF):

- **Increasing the nitrogen and indium contents** would lower the band gap energy, which would redshift the absorption threshold and increase the amount of light available to the InGaAsN solar cell. Integrating the photon flux of AM0 between 870 and 1120 nm (cut-off wavelength of our five N=1.6 %/1.11 eV solar cells), we show that the highest photocurrent achievable is 15.05 mA/cm^2. Lowering the band gap energy to 1.0 eV would bring this

maximum J_{sc} limit to 20.99 mA/cm^2.

- As illustrated by the relatively poor properties exhibited by sample A5, obtaining high photocurrent with lower band gap solar cells is only possible if we maintain low BGCC and high carrier lifetime. The second and probably most important route to enhance the InGaAsN solar cells properties is to conduct thorough **growth optimizations**. Identifying optimal growth temperature and *As/III* ratio for a given nitrogen concentration is here the primary concern.
- **Increasing the thickness of the InGaAsN active layer** would limit the transmission losses. Provided that the collection efficiency is not degraded, this would result in higher photocurrent. This architecture investigation is motivated by the higher quantum efficiency exhibited by the InGaAsN bottom cell (1.15 μm-thick absorber) compared to A5 (1 μm).

In addition to these routes, developing a reliable, reproducible and efficient annealing procedure could cure growth defects and ensure decent optoelectronic properties. However, we believe it is possible to develop a RTP-free growth recipe providing solar cells satisfying the current-matching condition. Such a recipe would avoid high thermal loads and could be integrated within the growth process of a 4-junctions solar cell.

Chapter 4 conclusion

Through *I-V* and EQE measurements, we have characterized InGaAsN single junction and GaAs/InGaAsN tandem solar cells. We have correlated the photovoltaic characteristics with the materials properties measured in Chapter 3. The impact of the field-aided collection regime was discussed and two crucial features were used to explain the performances of the solar cells : the residual doping or BGCC and the non-radiative recombination rate related to the minority carrier lifetime. Both of these parameters arise from growth defects of different natures and we observed that their apparition can be mitigated through optimization of the growth parameters. Solar cells grown with a *As/III* ratio equal to 12 exhibit the best *J-V* characteristics and could deliver up to 7.96 mA/cm^2 under AM0>870 nm.

While further optimization is needed to obtain InGaAsN solar cells satisfying the current-matching condition, our solar cells constitute relevant irradiation test vehicles. This chapter and the previous one provide essential informations about the BOL (beginning of life) properties of the solar cells. The next and final chapter will investigate the evolution of these properties upon irradiation.

Bibliography

[1] P. Colter, B. Hagar, and S. Bedair, "Tunnel junctions for III-V multijunction solar cells review," *Crystals*, vol. 8, no. 12, p. 445, 2018.

[2] I. Rey-Stolle, I. García, E. Barrigón, J. Olea, D. Pastor, M. Ochoa, L. Barrutia, C. Algora, and W. Walukiewicz, "On the thermal degradation of tunnel diodes in multijunction solar cells," in *AIP Conference Proceedings*, vol. 1881, no. 1. AIP Publishing LLC, 2017, p. 040005.

[3] W. Dawidowski, B. Ściana, I. Zborowska-Lindert, M. Mikolášek, J. Kováč, and M. Tłaczała, "Tunnel junction limited performance of InGaAsN/GaAs tandem solar cell," *Solar Energy*, vol. 214, pp. 632–641, 2021.

[4] I. García, M. Ochoa, I. Lombardero, L. Cifuentes, M. Hinojosa, P. Caño, I. Rey-Stolle, C. Algora, A. Johnson, I. Davies *et al.*, "Degradation of subcells and tunnel junctions during growth of GaInP/Ga(In)As/GaNAsSb/Ge 4-junction solar cells," *Progress in Photovoltaics: Research and Applications*, vol. 25, no. 11, pp. 887–895, 2017.

[5] K. Louarn, "Etude et réalisation de jonctions tunnel à base d'hétérostructures à semiconducteurs III-V pour les cellules solaires multi-jonction à très haut rendement," Ph.D. dissertation, Université Toulouse 3 Paul Sabatier, 2018.

[6] C. Juang, K. Kuhn, and R. Darling, "Selective etching of GaAs and Al0.30Ga0.70As with citric acid/hydrogen peroxide solutions," *Journal of Vacuum Science & Technology B: Microelectronics Processing and Phenomena*, vol. 8, no. 5, pp. 1122–1124, 1990.

[7] A. Baca, F. Ren, J. Zolper, R. Briggs, and S. Pearton, "A survey of ohmic contacts to III-V compound semiconductors," *Thin Solid Films*, vol. 308, pp. 599–606, 1997.

[8] C. A. Gueymard, "The sun's total and spectral irradiance for solar energy applications and solar radiation models," *Solar energy*, vol. 76, no. 4, pp. 423–453, 2004.

[9] J. L. Gray *et al.*, *The physics of the solar cell*. Citeseer, 2003, vol. 2.

[10] A. International, "Standard specification for solar simulation for terrestrial photovoltaic testing," 2010.

[11] D. Friedman, J. Geisz, S. R. Kurtz, and J. Olson, "1-eV solar cells with GaInNAs active layer," *Journal of Crystal Growth*, vol. 195, no. 1-4, pp. 409–415, 1998.

[12] F. Langer, S. Perl, S. Höfling, and M. Kamp, "p-to n-type conductivity transition in 1.0 eV GaInNAs solar cells controlled by the V/III ratio," *Applied Physics Letters*, vol. 106, no. 6, p. 063905, 2015.

[13] K. Louarn, Y. Claveau, L. Marigo-Lombart, C. Fontaine, A. Arnoult, F. Piquemal, A. Bounouh, N. Cavassilas, and G. Almuneau, "Effect of low and staggered gap quantum wells inserted in GaAs tunnel junctions," *Journal of Physics D: Applied Physics*, vol. 51, no. 14, p. 145107, 2018.

Chapter 5

Degradation study of the InGaAsN solar cells under irradiation

In this chapter, we assess the radiation hardness of the InGaAsN solar cells that were developed in the framework of this thesis. The material and method section introduces first the irradiation setup that was used and justifies the fluence levels chosen here. The second section presents the 1 MeV irradiation study that was conducted on InGaAsN solar cells and bulk layers grown in different epitaxial conditions. In Section 3, we describe the degradation of a GaAs/InGaAsN tandem solar cell and its component subcells under 1 MeV electron irradiation. Afterwards, a fourth section is dedicated to the impact of 1 MeV proton irradiation on InGaAsN samples (solar cells and bulk layers). Finally, a discussion section is presented to relate the degradation mechanisms observed under both electron and proton irradiations.

Contents

5.1 Materials and methods

5.1.1 Irradiation setup

The electron and proton irradiations presented in this thesis were conducted in the MIRAGE chamber, which belongs to the the AXEL laboratory in ONERA Toulouse [1]. MIRAGE is a high vacuum irradiation chamber (P<5 $\times$ 10^{-7} mbar) equipped with a quartz window and electrical feedthrough allowing for *in-situ* light *I-V* (LIV) measurements. The samples to be irradiated are mounted on a movable stage which can both translate and rotate in one direction (z-θ table). Additionally, the chamber is equipped with a thermoregulation system providing monitoring over a wide temperature range [-150 °C; 400 °C].

Two beam lines are connected to MIRAGE to provide electron and proton irradiation. As illustrated in Figure 5.1, the AXEL laboratory relies on two Van de Graaff accelerators which can be used simultaneously for electron/proton combined irradiation. The energy limitations in MIRAGE are E$\in$ [0.4 - 1.3 MeV] for electrons and E$\in$ [0.045 - 2 MeV] for protons.

In order to irradiate large areas, the electron beam is scattered through a 120 μm aluminium foil whereas the proton beam is swept using electromagnetic lenses (steerers). The flux calibration is performed before irradiation using Faraday cups placed in the target plane. In typical configuration, the current or flux inhomogeneity is lower than 10 % on 140 mm $\times$ 140 mm for electrons and lower than 20 % for protons.

5.1.2 Sample holder and light I-V measurements

We used a 150 mm $\times$ 80 mm copper plate as an irradiation sample holder. Four solar cells on their AlN support were mechanically clamped to the plate with screwed aluminium pieces, as depicted in Figure 5.2. To allow *in-situ I-V* characterization, both the front and the rear sides of the solar cell need to be contacted to a SMU unit. The back contact can be taken directly on the copper plate (ground) since it is connected to the rear gold pad through the Al parts

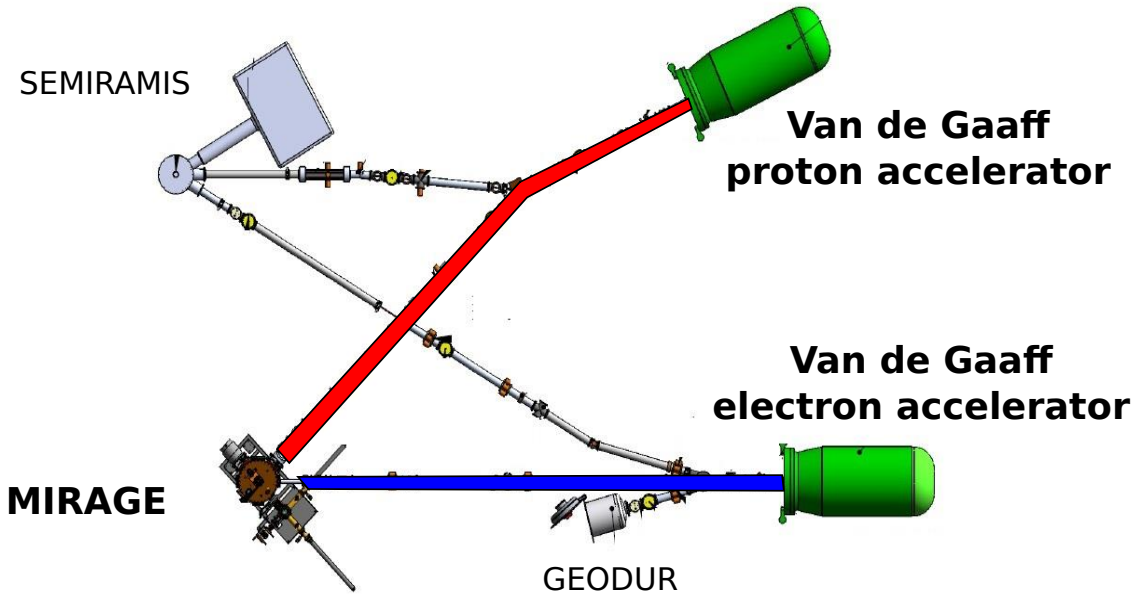

Figure 5.1: Schematic of the AXEL laboratory in ONERA showing the beam lines between MIRAGE and the Van de Graaff generators. SEMIRAMIS and GEODUR are other irradiation chambers that were not used for this thesis.

(right hand side of Figure 5.2). On the other hand, the top contact is electrically isolated from the plate thanks to the AlN supports and the Al_2O_3 screw. The front of the cell is then contacted with a wire soldered on the aluminium part, as shown in Figure 5.3 a).

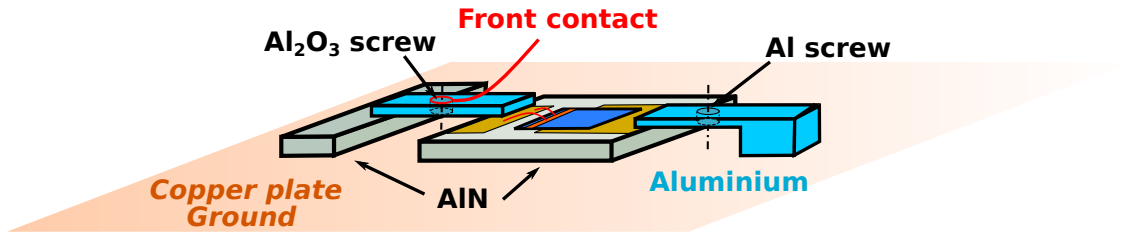

Figure 5.2: Schematics of the contacting of the solar cell (and its AlN support) mounted on a copper sample holder.

Alongside the 1 cm^2 solar cells, InGaAsN bulk samples and 0.25 cm^2 non-contacted cells were placed on the copper plate, as shown in Figure 5.3 a). These smaller samples were either indium or EPOTEK-pasted on AlN supports and were dedicated to PL, DLTS and EQE characterizations.

Finally, Figure 5.3 b) shows the mounting of the copper plate on the irradiation stage, which is conducted after calibrating the beam flux through Faraday cups vertical scanning. The sample holder is then lowered and faced towards the beam line prior to irradiation (normal incidence).

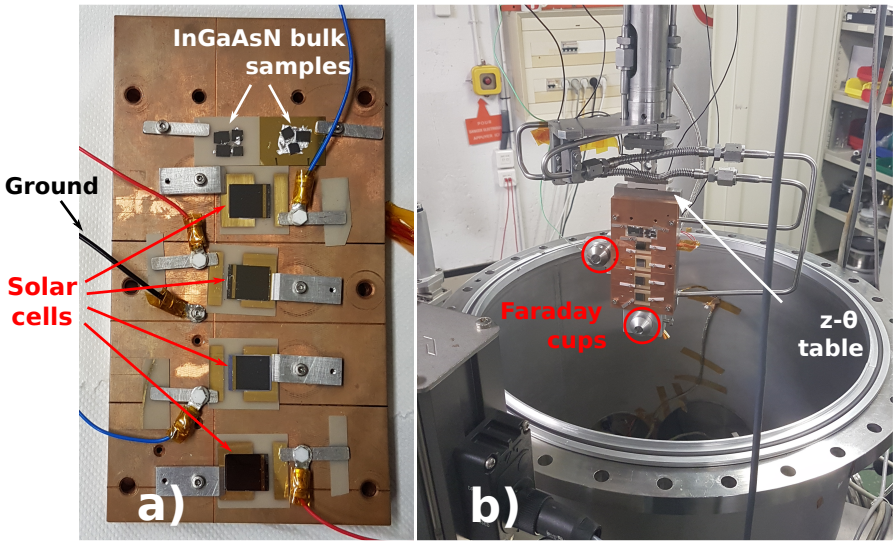

Figure 5.3: a) Picture of the samples fixed on the copper plate, b) Picture of the copper plate attached to MIRAGE irradiation stage.

5.1.3 Electron and proton fluence levels

Ground test facilities allows to simulate the impact of radiation assuming that accelerated irradiation tests (*e.g.* 10^{15} e^-/cm^2 in few hours) are representative of real-time space irradiation (10^{15} e^-/cm^2 in several years). This is a strong assumption and we observed in our first campaign an effect ot the irradiation flux on the degradation behaviour.

To characterize the radiation hardness of the InGaAsN solar cells, we decided to irradiate them with 1 MeV electrons and protons (irradiation standard) and fluences ranging from 10^{15} to $5\times$ 10^{15} electrons/cm^2 and 10^{11} to 10^{13} protons/cm^2. These are typical fluence values enabling comparison with published studies from the literature. Furthermore, we simulated the 1 MeV electron and proton fluences corresponding to a 15-years space mission in geostationary earth orbit (GEO) with the OMERE software [2]. Using the AE8 and AP8 radiation belt models at solar maximum conditions, we obtain 10^6 $e^-/cm^2/s$ and 5×10^3 $p^+/cm^2/s$ fluxes corresponding to final fluences of 4.7×10^{14} e^-/cm^2 and 2.7×10^{12} p^+/cm^2 for 1 MeV electrons and protons, respectively. These fluences are slightly lower than our ground test maximal fluences but one should bear in mind that only 1 MeV particles from the radiation belts were accounted for in the OMERE simulation. Very high energy particles are also found in real space environment, originating from the solar wind, solar flares and galactic cosmic rays.

5.2 1 MeV electron irradiation on InGaAsN subcells

5.2.1 Test plan

To study the impact of 1 MeV electrons on 1.11 eV InGaAsN solar cells, we irradiated samples from the A1, A2, A3 and A4 wafers. Three InGaAsN solar cells labelled as A1a, A2a and A4a along a GaAs solar cell used as a degradation reference (G1) were irradiated with four intermediate steps with cumulative fluences as presented in the test plan of Table 5.1.

Table 5.1: Test plan of the irradiation steps

	Fluence step (cm^{-2})	**Irrad. current density** (nA/cm^2)	**Total fluence** (cm^{-2})
Ex-situ IV measurement			
1 MeV electrons irrad.	5×10^{13}	6.7	5×10^{13}
Ex-situ IV measurement			
1 MeV electrons irrad.	5×10^{13}	5.5	10^{14}
Ex-situ IV measurement			
1 MeV electrons irrad.	4×10^{14}	5.6	5×10^{14}
Ex-situ IV measurement			
1 MeV electrons irrad.	5×10^{14}	5.2	10^{15}
Ex-situ IV measurement			

In this campaign, the electron flux was kept low (<8 nA/cm^2) and the samples were not thermoregulated. *Ex-situ I-V* measurements (both DIV and LIV) were conducted between each irradiation step.

A second set of samples exclusively composed of InGaAsN cells (A1b, A2b, A3b and A4b) was directly irradiated at 10^{15} e^-/cm^2, with a 8 nA/cm^2 average irradiation current density ($\approx 5 \times 10^{10}$ $e^-/cm^2/s$). InGaAsN bulk layers for PL and DLTS characterization and 0.25 cm^2 InGaAsN solar cells dedicated to EQE measurements were also irradiated during this run.

5.2.2 Degradation of the J-V characteristics

Table 5.2 summarizes the epitaxial growth conditions corresponding to the solar cells irradiated in this campaign.

The degradation of the four cumulatively irradiated solar cells can be observed with their LIV characteristics obtained under AM0 illumination. Figure 5.4 shows that the three InGaAsN samples degraded much less than the GaAs solar cell (G1) in terms of both J_{sc} and V_{oc}. This discrepancy in the degradation rates is likely to arise from the different absorber materials as discussed later on. However, it could also originate from the architecture and the collection regime

Table 5.2: Growth conditions of the electron-irradiated InGaAsN solar cells

Sample name	N content (%)	T_g (°C)	As/III ratio
A1	1.6	465	12 (+Bi)
A2			12
A3		445	10
A4		485	

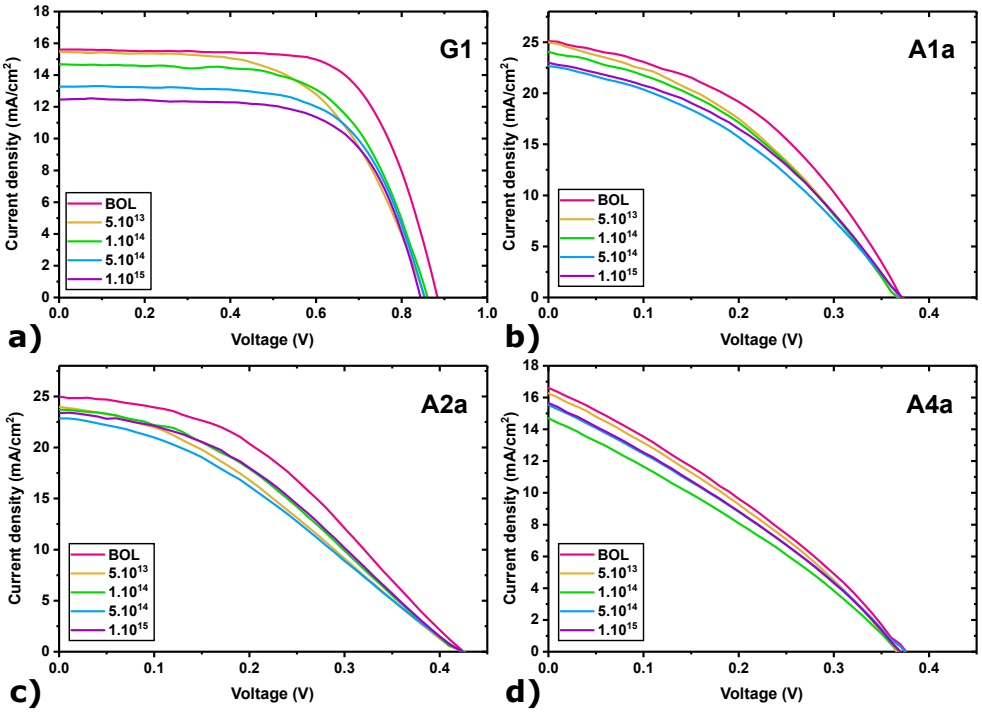

Figure 5.4: Evolution of the *J-V* characteristics measured under AM0 illumination at different fluences (e^-/cm^2) for samples G1, A1a, A2a and A4a.

of the solar cells. The InGaAsN cells rely on a *pin* structure which mostly collects photocarriers through drift in the SCR whereas the GaAs cell G1 is highly dependent on the minority carrier diffusion length along its 3 μm-thick base. The introduction of non-radiative recombination centres in the active material is then more detrimental to conventional *pn* junctions than *pin* architectures.

The fill factor was found to degrade more in A1a and A2a ($\Delta FF/FF_{BOL} \approx 6.5$ %) than in sample G1 ($\Delta FF/FF_{BOL} \approx 2.4$ %). Interestingly, the fill factor of sample A4 only degraded by less than 2 %, which shows that the shunt introduced by irradiation is quite negligible compared to the effect of the field-aided collection.

The relative degradation of the open-circuit voltage after 10^{15} e^-/cm^2 was calculated to be ≈ 4.5 % for the GaAs cell and less than 1.5 % for the InGaAsN cells. The V_{oc} is a good indicator of the recombination rate in a solar cell, which suggests that this latter parameter did not increase much after irradiating the

InGaAsN solar cells. Besides, we did not observe any change in the J_0 of the InGaAsN cells after irradiation whereas the dark current density of the GaAs solar cell was found to increase, as depicted in Figure 5.5.

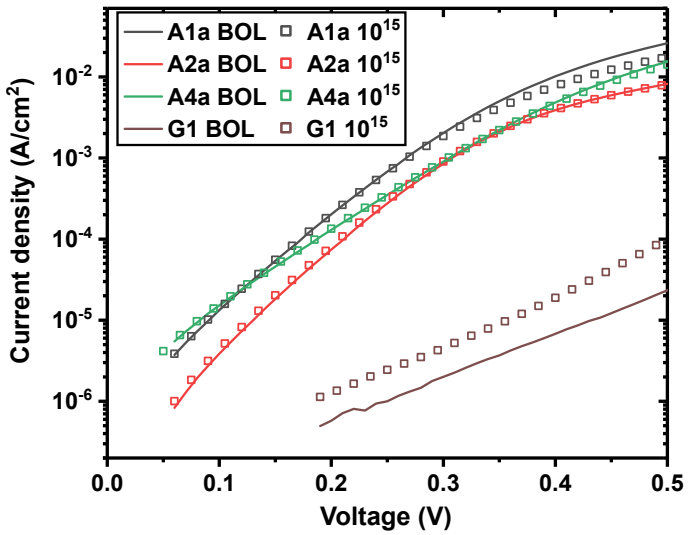

Figure 5.5: Dark *J-V* characteristics of solar cells A1a, A2a, A4a and G1 before and after 10^{15} e^-/cm^2 1 MeV-electrons cumulative irradiation.

A monotonic decrease in the photocurrent of sample G1 can be observed in Figure 5.4 a). This degradation of the carrier collection arises from the introduction of crystal defects shortening the minority carrier diffusion length (see 1.2.4 in Chapter 1). The GaAs solar cell was irradiated as a reference and its degradation rate was compared with data from the literature. Figure 5.6 shows the remaining factors of the short-circuit current for sample G1 and GaAs solar cells taken from published studies [3, 4, 5].

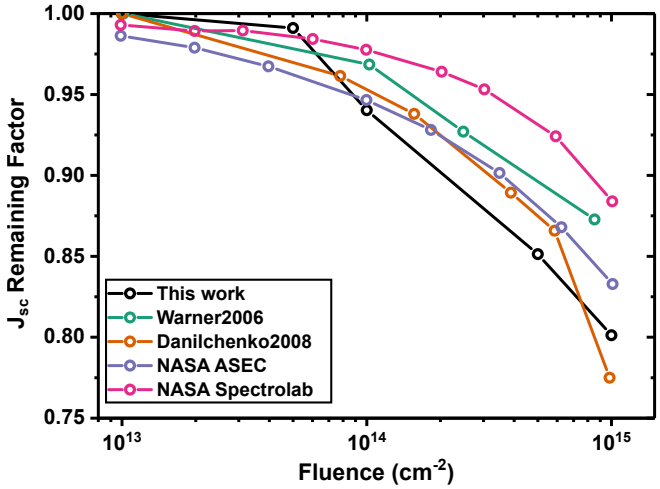

Figure 5.6: Remaining factor of the J_{sc} as a function of the 1 MeV electron fluence. The literature data were taken from [3, 4, 5]

For our GaAs solar cell, the BOL condition was plotted as a 10^{13} fluence for the sake of clarity. The J_{sc} degradation rate exhibited by our GaAs solar cell is in good agreement with the results reported in the literature [4, 5], thus validating our choice to take it as a reference in our study.

The degradation of the light *J-V* characteristics under irradiation for the InGaAsN solar cells was also analysed for AM0>870 nm illumination, as presented in Figure 5.7. As observed under AM0, the V_{oc} is virtually not affected by the irradiation and the fill factor degraded more in samples A1a and A2a (6.7 and 3.1 %) than in A4a (2 %). The photocurrent degradation rates of A1a and A2a are found to be slightly lower for AM0>870 nm than for AM0 unfiltered light (Table 5.3). Since in the former case carriers are only generated in the InGaAsN layer, this discrepancy could reflect the higher degradation rate of the GaAs emitter compared to the InGaAsN absorber.

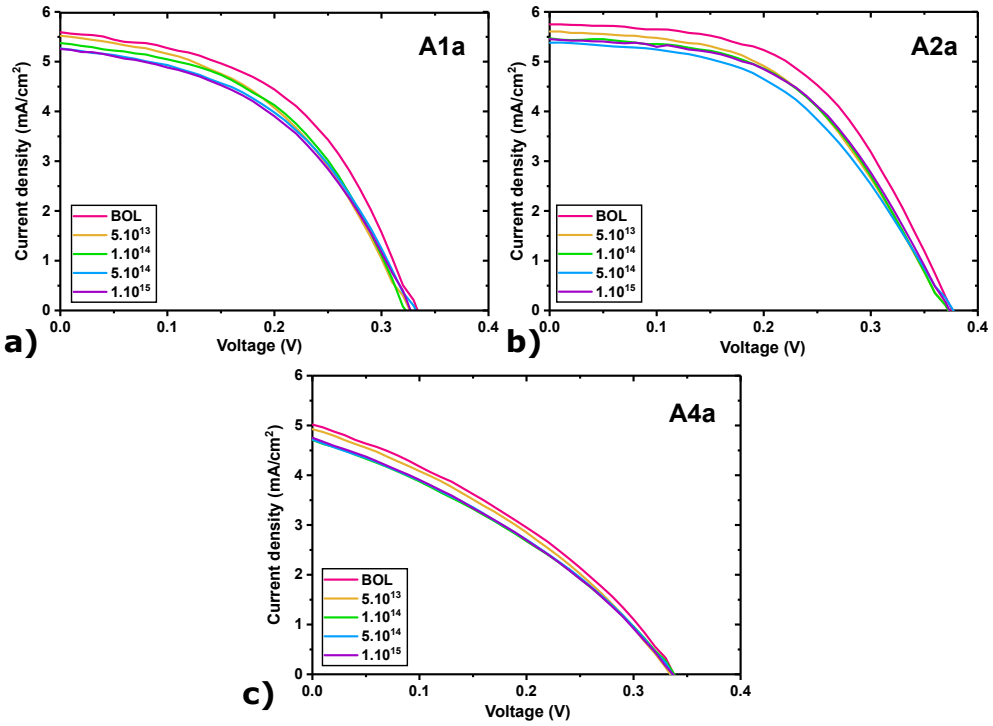

Figure 5.7: Evolution of the *J-V* characteristics measured under AM0>870 nm illumination at different fluences (in e^-/cm^2) for samples A1a, A2a and A4a.

Table 5.3: J_{sc} remaining factors after 10^{15} e^-/cm^2 1 MeV electrons irradiation

	A1a	**A2a**	**A4a**	**G1**
RF(J_{sc}) AM0	0.916	0.935	0.931	0.799
RF(J_{sc}) AM0>870 nm	0.940	0.948	0.940	

The evolution of the filtered-light J_{sc} remaining factor with the 1 MeV electrons fluence is shown in Figure 5.8 for the cumulatively irradiated samples (A1a, A2a and A4a) and for the directly irradiated ones (A1b, A2b, A3b and A4b). We

observe a considerable degradation difference between those two sets of samples at EOL (10^{15} e^-/cm^2). The average J_{sc} degradation is 1.3 % for direct irradiation and 5.7 % for cumulatively irradiated solar cells.

In addition, we can see that A1a and A2a experienced a non-monotonic degradation of their photocurrent with a slight J_{sc} increase observed at higher fluences. While this enhancement behaviour lies within the uncertainty of the measurement, it could also arise from the same mechanisms responsible for the lower degradation exhibited by samples directly irradiated to 10^{15} e^-/cm^2.

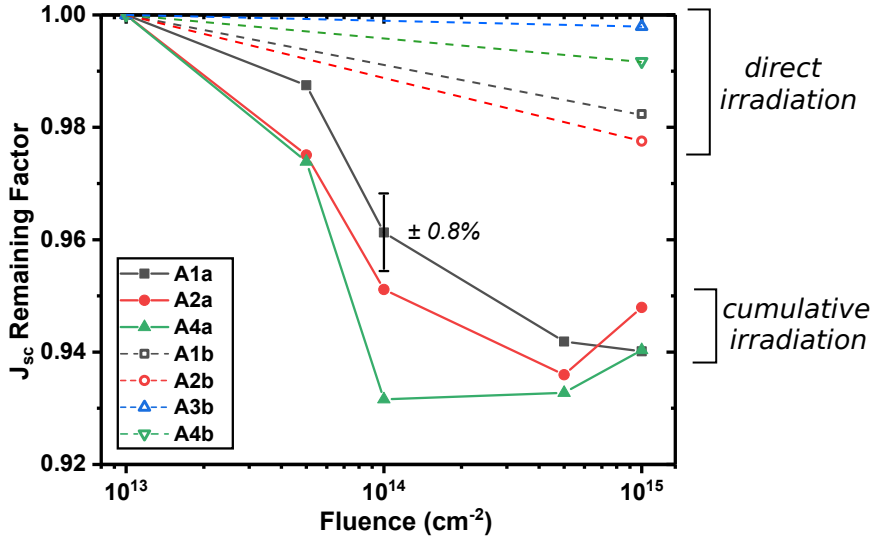

Figure 5.8: Remaining factor of the J_{sc} (AM0>870 nm) as a function of the 1 MeV electron fluence. The BOL condition is here plotted as a 10^{13} fluence. The 0.8 % measurement uncertainty is only shown once but applies to all the data points.

In this campaign, the samples were not thermoregulated during the irradiation process and could have experienced overheating. Indeed, temperature monitoring in our second irradiation campaign (see Section 5.3.1) showed that even under thermoregulation, samples could overheat during the irradiation process. The amount of overheating depends on both the electron flux and the fluence (defining the duration of the irradiation step), which means that the cumulatively irradiated solar cells reached higher temperature during the two final irradiation steps (+4×10^{14} and +5×10^{14} cm^2). As for the second set of samples, it was directly irradiated to final fluence with a higher electron flux (8 nA/cm^2 compared to 5-6 nA/cm^2), which probably caused a large overheating.

The sample heating under irradiation is attributed to the recoil energy transferred to knock-on atoms, leading to local thermal spikes in the lattice. With the temperature rising, the atomic diffusion increases, which enhances recombination of irradiation-induced defects [6]. A second mechanism promoting defect-recombination is the creation of vacancies throughout irradiation [7]. Depending on the irradiation flux, the vacancies reach a certain steady-state concentration (higher than the thermodynamic equilibrium), which enhances the atomic diffusion. Considering these two enhanced diffusion mechanisms, solar cells irradi-

ated with a higher electron flux and at higher temperature are expected to show lower degradation rate.

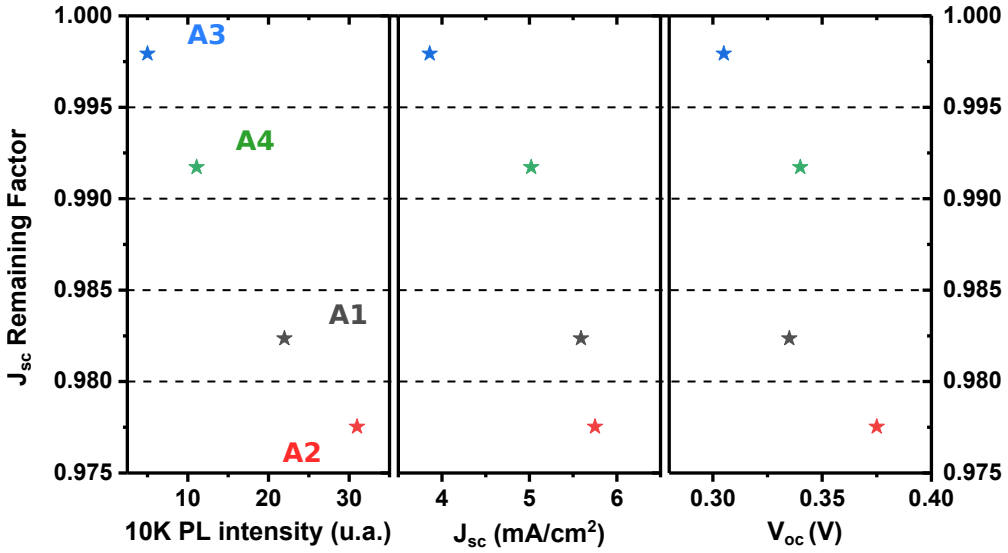

Figure 5.9: EOL J_{sc} remaining factor of the directly irradiated samples as a function of their: a) BOL PL intensity measured at 10 K, b) BOL J_{sc}, c) BOL V_{oc}. The J_{sc} and V_{oc} values correspond to a AM0>870 nm illumination.

The J_{sc} degradation after 10^{15} e^-/cm^2 direct irradiation is slightly different from one sample to the next and we observed a correlation between the BOL performances of the solar cells and their photocurrent degradation rate. Figure 5.9 shows the J_{sc} remaining factor of A1b, A2b, A3b and A4b plotted as a function of their BOL PL intensity, J_{sc} and V_{oc}. The strong correlation between the PL signal and RF(J_{sc}) as well as between the initial photocurrent and RF(J_{sc}) could imply that the low minority carrier lifetime caused by growth defects overshadows the impact of irradiation induced-defects. This effect would also explain the much lower degradation rate exhibited by InGaAsN compared to GaAs solar cells and was discussed by Lang et al. for GaInAsP solar cells [8]. As we can see in Figure 5.9 c), the correlation between the J_{sc} remaining factor and the V_{oc} is not as strong as for the two other parameters. This could be due to the difference in ideality factor between A4 and the rest of the cells arising from its lower residual doping.

5.2.3 Impact of electron irradiation on the quantum efficiency

The quantum efficiency of 0.25 cm^2 solar cells was measured before and after direct electron irradiation. Figure 5.10 shows the IQE spectra of the solar cells at BOL and EOL conditions[1] (10^{15} e^-/cm^2). Samples A3 and A4 exhibit a very low degradation of their quantum efficiency in the λ>870 nm spectral range, which correlates with the slight J_{sc} loss observed in the previous section. On the other

[1]We assume here that the optical reflectance of our solar cells was not affected by irradiation.

hand, A1 and A2 display opposite behaviours as their IQE increased after irradiation. At EOL, both of these samples show enhanced collection efficiency over the 650-1120 nm spectral window. No degradation of the IQE for short wavelengths can be observed in any of the samples. This indicates that the diffusion length within the 200 nm GaAs emitter was not severely affected by the irradiation.

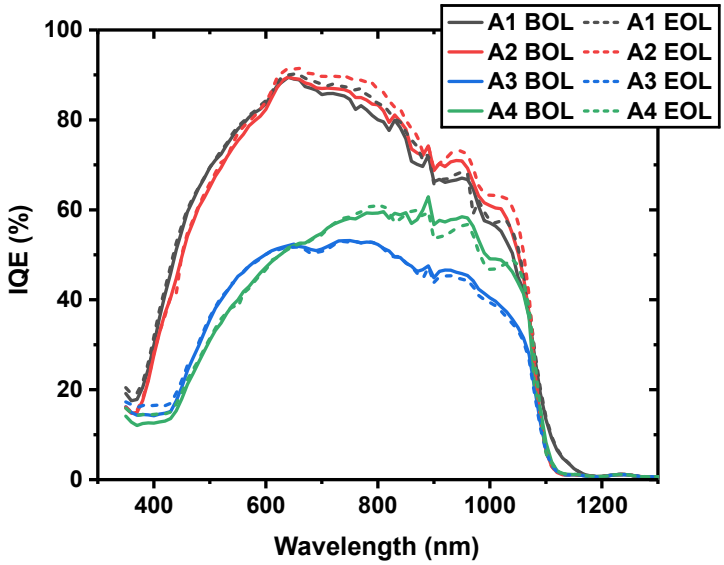

Figure 5.10: IQE spectra of samples A1, A2, A3 and A4 before and after 10^{15} e^-/cm^2 1 MeV electron direct irradiation.

The "annealing" experienced by samples A1 and A2 does not concur with the small J_{sc} degradation measured with the *I-V* characterization. This discrepancy could arise from the experimental uncertainty of the measurements (EQE and *I-V*) or from sample to sample variation, although our proton irradiation study showed a very high degradation homogeneity in InGaAsN solar cells (see Section 5.4). It could also originate from different irradiation conditions as i) 0.25 cm^2 EQE cells were placed at the very top of the sample holder (see Figure 5.3) and we have to account for a roughly 10 % electron beam inhomogeneity ii) the EQE cells were pasted on an electrical insulator which possibly led the samples to charge during irradiation.

As discussed earlier, the temperature and the irradiation flux are expected to play a major role in the defect introduction rate because of enhanced atomic diffusion mechanisms. The same mechanisms could provoke annealing of growth defects present at BOL in the InGaAsN absorber. Besides, Pavalescu et al. reported an enhancement of the PL intensity of 1 eV InGaAsN bulk layers after 7 MeV electrons irradiation [9]. They observed a 35 % and a 23 % increase in the PL signal after 10^{14} e^-/cm^2 and 10^{15} e^-/cm^2 irradiation, respectively. This luminescence enhancement was attributed to the curing of growth defects through recombination-enhanced annealing processes: the irradiation current creates a large number of free carriers that release enough energy upon recombination to induce defect annealing. This hypothesis is supported by numerous studies reporting on defect annealing in III-V *pn*-junctions under high carrier injection [10, 11, 12].

5.2.4 Characterization of irradiated InGaAsN bulk layers

We assessed the impact of the electron irradiation through PL and DLTS characterizations performed on the InGaAsN bulk layers B1 and B2 (grown at *As/III*=11 and 8, respectively). Part of these samples were irradiated *as-grown* (AG) while others were subjected to a post-growth thermal annealing at 750 °C (RTP) before direct electron irradiation at 10^{15} e^-/cm^2.

Figure 5.11 shows the room temperature photoluminescence spectra of the as-grown and annealed samples before and after irradiation. The luminescence of the as-grown samples is found to be higher at EOL condition: B1-AG and B2-AG exhibit a 156 % and a 98 % PL increase after irradiation, reaching PL intensities close to their corresponding annealed samples at BOL. However, unlike thermal annealing, the irradiation did not induce a bandgap blueshift in the dilute nitride. Similarly to results reported by Pavalescu et al., the PL enhancement corresponds to the reduction of the non-radiative recombination centres density. This means that annealing of growth defects occurred through irradiation which concurs with the IQE results obtained with as-grown solar cells.

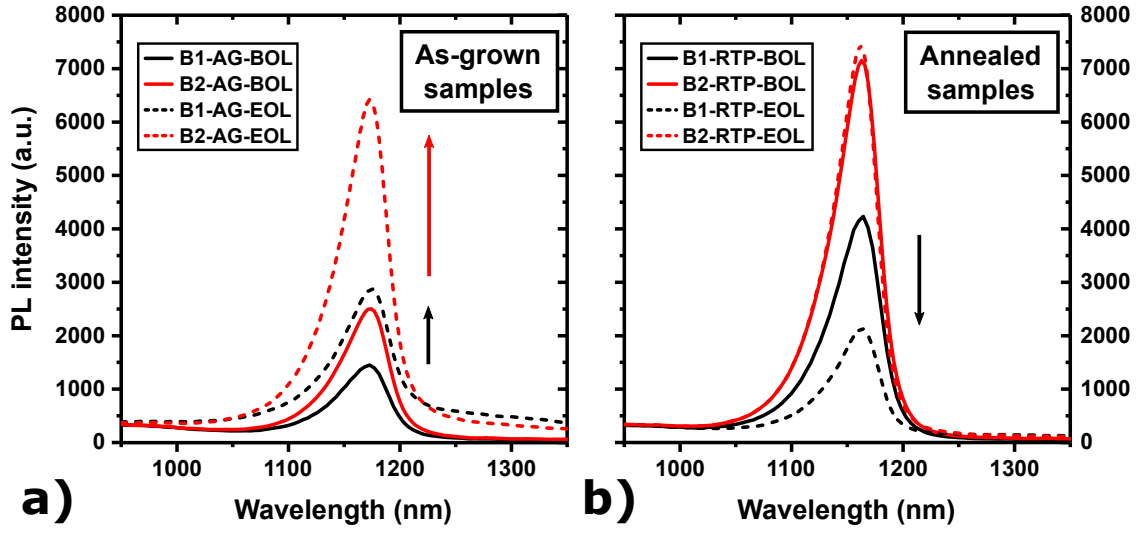

Figure 5.11: PL spectra before and after 1 MeV electrons irradiation for a) as-grown and b) annealed samples.

The electron irradiation did not promote defect curing in the thermally annealed samples, as shown in Figure 5.11 b). Rather, we can see that it degraded the PL intensity of sample B1-RTP and virtually did not affect the luminescence of B2-RTP. We can argue that a part of the defects that could have been cured under irradiation was simply absent at BOL condition, thanks to the post-growth thermal annealing. However, this hypothesis does not explain the PL degradation in sample B1-RTP. It is then possible that the difference in the InGaAsN radiation response arises from the preferential bonding in the quaternary. Indeed, nitrogen atoms are reported to go from a Ga-N bonding configuration to an In-N one after annealing (see Chapter 2, Section 2.3.6), which could affect the defect energy formation and consequently the radiation hardness of the material.

To investigate both the defect introduction and the defect annealing occuring through irradiation, we conducted DLTS analysis on the same InGaAsN layers. The acquisition conditions were the same as in the Section 3.2.3 of Chapter 3, *i.e.* V_r=-1 V, V_r=0 V and t_p=500 μs. Figure 5.12 a) shows that, for the as-grown samples, the BOL and EOL DLTS spectra are identical. Similarly, no notable effect of the irradiation can be observed for B2-RTP in Figure 5.12 b). However, the B1-RTP sample shows a somewhat lower DLTS signal after irradiation, corresponding to a decrease in the E1 defect concentration (see Chapter 3, Section 3.2.3).

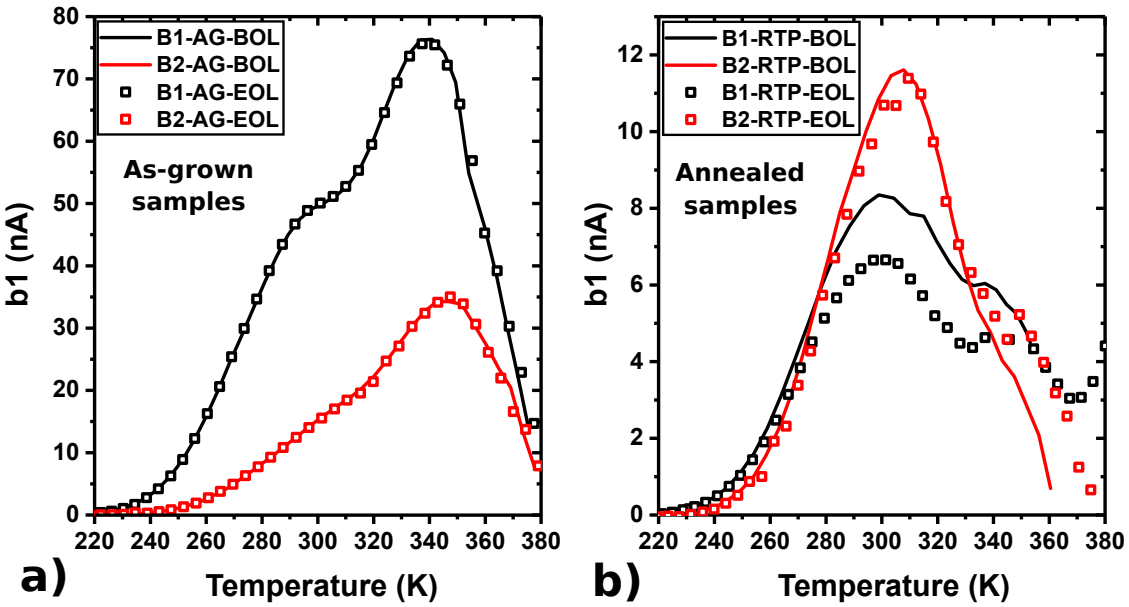

Figure 5.12: DLTS spectra before and after 1 MeV electrons irradiation for a) as-grown and b) annealed samples. Note that the two figures do not share the same y-axis scale.

The DLTS results presented here do not correlate with the PL observations made on the same samples. First, the luminescence enhancement after irradiation in the as-grown samples does not relate to a decrease in the E1 and E2 trap densities. Second, sample B1-RTP exhibits a degradation of its PL intensity while showing a slight decrease in its DLTS signal.

The DLTS measurements were performed at reverse bias, which means that the spectra only show the response of the majority carriers in our samples. The DLTS analysis is thus limited to electron traps and does not give information regarding the holes. It is then possible that the irradiation led to hole trap annealing in the InGaAsN as-grown layers, resulting in a PL enhancement. Indeed, Kwon et al. reported a DLTS study on *p*-type InGaAsN showing high concentrations of hole traps in as-grown samples that were sharply reduced after thermal annealing [13]. Oppositely, simultaneous introduction of hole recombination centres and annealing of electron traps could explain the PL and DLTS behaviour exhibited by sample B1-RTP.

Another way to interpret the DLTS results is to consider that the InGaAsN layers display high growth defect concentrations, which might hide the impact

of defect introduction/annealing taking place under irradiation. This hypothesis is supported by the correlation previously shown between the solar cells BOL properties and their J_{sc} remaining factor (Figure 5.9).

5.2.5 Conclusion of the section

We irradiated with 1 MeV electrons InGaAsN samples grown with different conditions. The average degradation rate of the InGaAsN solar cells is found to be much lower than for their GaAs counterpart, which can be partly explained by the difference in BOL optoelectronical properties. However, we also observed annealing phenomena in as-grown dilute nitrides through increase in quantum efficiency (solar cells) and in PL signal (bulk layers). We attribute this growth defect annealing behaviour to an increase in the atomic diffusion permitted by irradiation-induced vacancies, and to the recombination enhanced annealing mechanism. In addition, comparison between cumulative and direct electron irradiation suggests that the annealing of growth defects is enhanced at higher sample temperature and higher irradiation flux. Finally, we could not observe significant changes in the DLTS spectra after irradiation. This indicates that the introduction or the annealing rate of electron traps is negligible compared to the BOL electron traps densities.

5.3 1 MeV electron irradiation on GaAs/InGaAsN tandem solar cell

5.3.1 Test plan

Considering that the InGaAsN solar cells are intended to be integrated within a MJSC structure, we assessed the impact of 1 MeV electrons irradiation on the GaAs/InGaAsN tandem solar cell T1. A GaAs component cell (G2) was also irradiated to represent the degradation of the top cell in T1 along with an as-grown and an annealed InGaAsN solar cell representing the bottom cell. The four solar cells were cumulatively irradiated with five fluences and *in-situ I-V* measurements were performed between each step. Afterwards, a photo-annealing study was conducted by exposing the solar cells to AM0 sunlight for 30 and 60 minutes. The irradiation fluences and current densities are summarized in Table 5.4.

Table 5.4: Test plan of the irradiation steps

	Fluence step (cm^{-2})	**Irrad. current density** (nA/cm^2)	**Total fluence** (cm^{-2})
In-situ IV measurement			
1 MeV electrons irrad.	3×10^{13}	1.4	3×10^{13}
In-situ IV measurement			
1 MeV electrons irrad.	7×10^{13}	4.7	10^{14}
In-situ IV measurement			
1 MeV electrons irrad.	2×10^{14}	17.2	3×10^{14}
In-situ IV measurement			
1 MeV electrons irrad.	7×10^{14}	25.8	10^{15}
In-situ IV measurement			
1 MeV electrons irrad.	4×10^{15}	23.4	5×10^{15}
In-situ IV measurement			
30 minutes AM0 exposition			
In-situ IV measurement			
60 minutes AM0 exposition			
In-situ IV measurement			

During this campaign, the samples were thermoregulated at 26 °C and the temperature of the copper holder was monitored during the whole process. The evolution of this temperature over two days of irradiation is depicted in Figure 5.13[2]. We can see that even though the stage was thermoregulated, it experienced overheating during the three last irradiation steps. This is clearly the result of longer irradiation times and higher electron fluxes.

Figure 5.13 shows that the copper holder reached a temperature as high as 45.5 °C during the last irradiation process. The temperatures given here were recorded by a thermocouple placed onto the copper plate. Considering the thermal

[2]Part of the $+4.10^{15}$ fluence step was conducted during the 27/10/2020, not shown here.

resistances at the interface between this plate and the AlN sample holder, and between the AlN holder and the solar cells, we can reasonably assume that the samples reached even higher temperatures.

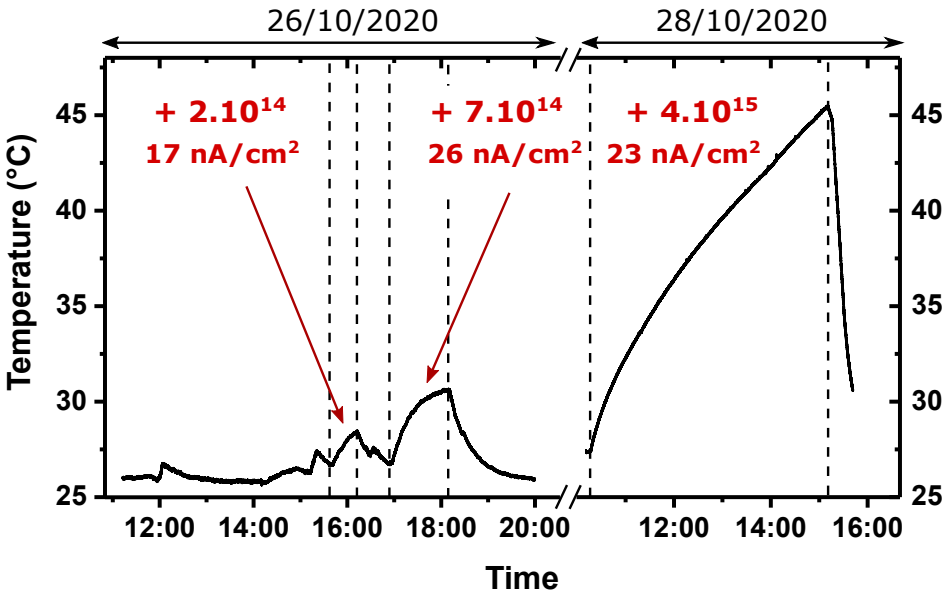

Figure 5.13: Evolution of the stage temperature during two days of irradiation. The fluence steps (e^-/cm^2) and the irradiation current densities are indicated for three specific steps.

5.3.2 Degradation of the J-V characteristics

Figure 5.14 shows the degradation of the *J-V* characteristics of the four cells measured *in-situ* under AM0 exposition. As in the previous irradiation campaign, we observe a very low degradation rate for the InGaAsN samples (A5). The photocurrent decrease after 5×10^{15} e^-/cm^2 electron irradiation is equal to 3.2 % and 2.5 % for samples A5-BOL and A5-RTP, respectively. The A5 solar cells exhibit then a greater radiation hardness than their A1, A2, A3 and A4 counterparts (see 5.2.2). This is completely in line with the poorer BOL optoelectronic properties measured in sample A5, grown with a higher nitrogen content. The photovoltaic parameters (J_{sc}, V_{oc} and *FF*) of A5-AG and A5-RTP are virtually not affected by irradiation because the introduction (or the annealing) of defects through irradiation is negligible compared to the growth defects concentration.

The light *J-V* characteristics of the GaAs solar cell exhibit a monotonic decrease consistent with successive defect introductions. However, the degradation rate of this GaAs sample is found to be quite low compared to our previous irradiation results and compared to reports from the literature. After 1×10^{15} e^-/cm^2, the photocurrent decreased only by 5 % in G2, whereas it decreased by 20 % in sample G1, irradiated at the same fluence in the last campaign. We attribute this enhanced radiation hardness to the high doping level in the base of the G2 solar cell (n = 4×10^{18} cm^{-3}). Indeed, the minority carrier lifetime decreases with the

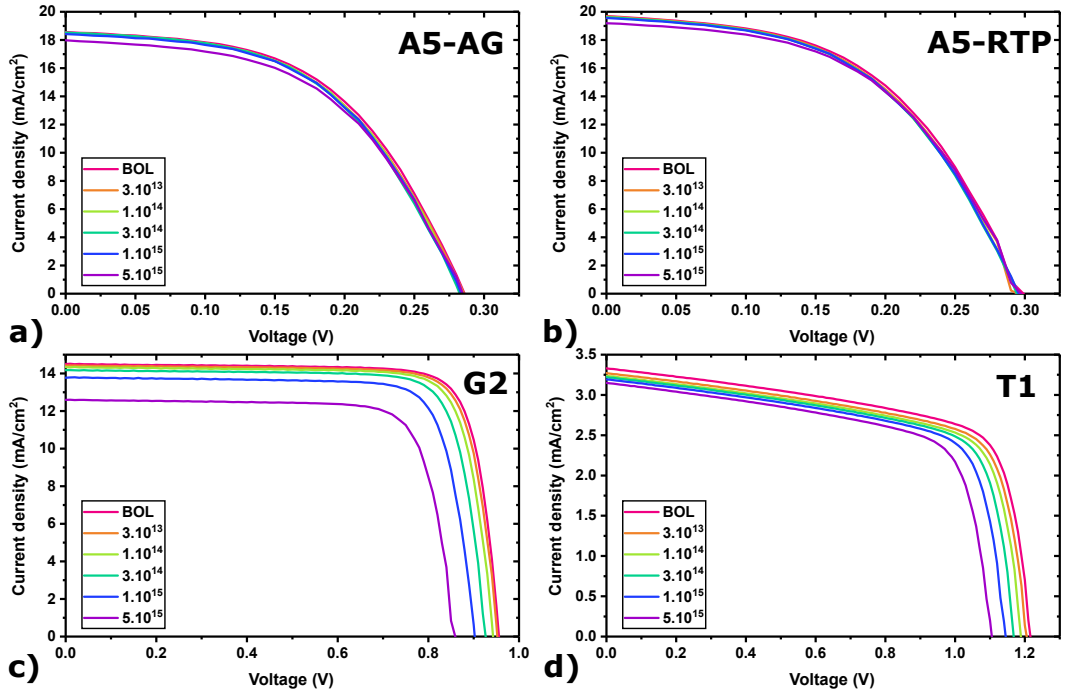

Figure 5.14: Evolution of the *J-V* characteristics measured under AM0 illumination at different fluences (in e^-/cm^2).

doping concentration, which implies that the diffusion length is already low at BOL in the 3 μm-thick GaAs base.

Finally, Figure 5.14 d) shows a steady degradation of the *J-V* profile of the tandem solar cell under electron irradiation. Interestingly, we observe a very similar V_{oc} deterioration between the GaAs component cell and T1 ($\approx$ 0.1 V loss at final fluence). This arises from the non-degradation of the open-circuit voltage in the InGaAsN bottom cell and from the series connected architecture leading to $V_{oc}(T1) = V_{oc}(G) + V_{oc}(A5)$. As for the 0.18 mA/cm^2 decrease in J_{sc} found for sample T1, it originates from the photocurrent degradation of the current-limiting subcell *i.e.* the InGaAsN bottom cell. To correlate this J_{sc} loss to the degradation of the InGaAsN component cells A5, we measured their BOL and EOL *J-V* characteristics under AM0>870 nm illumination, as represented in Figure 5.15.

The A5-AG and A5-RTP cells exhibit a very low degradation rate, similarly to what was observed under AM0 exposition. The as-grown sample shows an even lower photocurrent degradation than the tandem solar cell, implying that the InGaAsN subcell in T1 deteriorated slightly more than A5-AG. This is consistent with the 150 nm-thicker absorber in the InGaAsN bottom cell of T1 (compared to A5), making it more sensible to diffusion length shortening.

We could not observe any impact of the 30 and 60 minutes AM0 exposition on the light and dark *J-V* characteristics of the cells. This suggests that defect annealing cannot occur under photo-excitation alone, which implies that the level of carrier injection under AM0 is not high enough to provoke the recombination enhanced annealing mechanism.

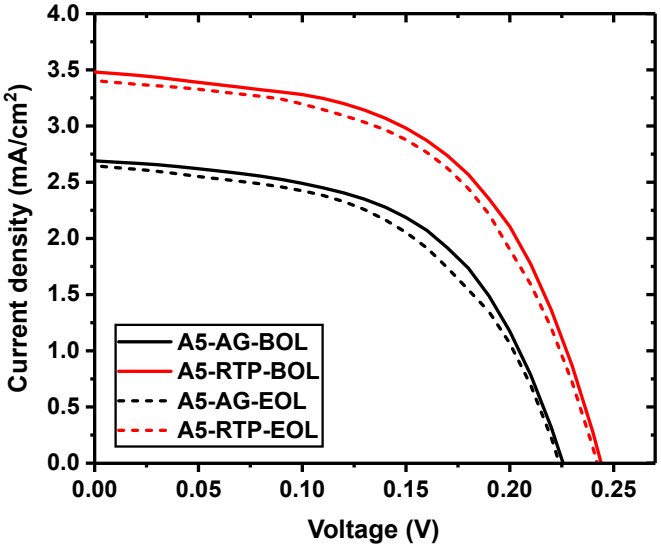

Figure 5.15: Comparison of the BOL and EOL (5×10^{15} e^-/cm^2) *J-V* characteristics of samples A5-AG and A5-RTP measured under AM0>870 nm filtered light.

5.3.3 Degradation of the quantum efficiency

Figure 5.16 shows the quantum efficiency degradation of the two subcells within the tandem solar cell T1. The corresponding J_{sc} are indicated next to the EQE spectra. As expected, the degradation is much more important in the GaAs top cell than in the InGaAsN bottom cell. However, the large decrease in the quantum efficiency exhibited by the top cell is not detrimental to T1 since the bottom cell remains unequivocally the limiting subcell.

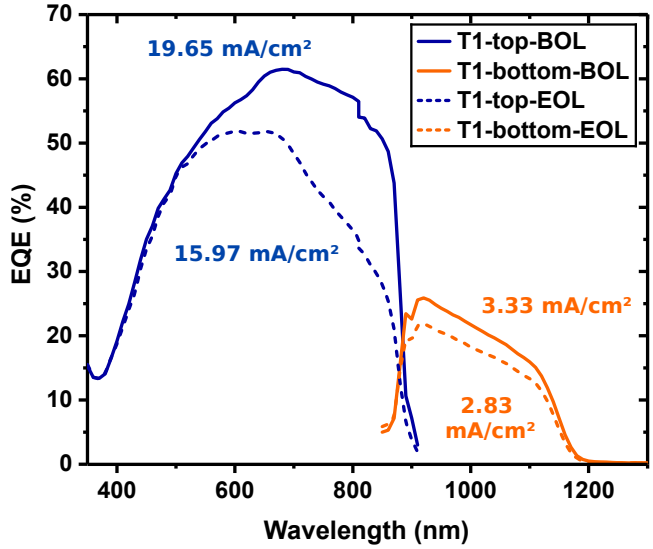

Figure 5.16: EQE spectra of T1's subcells before and after 5×10^{15} e^-/cm^2 irradiation.

The quantum efficiency of the InGaAsN subcell is degraded after 5×10^{15} e^-/cm^2 and we can see that the calculated J_{sc} decreased by 0.5 mA/cm^2. This

degradation is larger than what was measured with the *J-V* characteristics. It might stem from cell to cell dispersion in the T1 wafer as BOL and EOL results presented in Figure 5.16 correspond to different solar cells (indeed, all the EQE measurements presented in this section were conducted posterior to the irradiation campaign).

The impact of the electron irradiation on the component solar cells A5 (as-grown and annealed) and G2 is shown in Figure 5.17. As noticed with the light *J-V* results, the A5 samples do not exhibit significant degradation. The EQE shape of the A5 solar cells probably reflects the contribution of the GaAs emitter for photons of wavelengths shorter than 870 nm. Since the collection efficiency in the 400-870 nm spectral window is only found to slightly degrade, we can assume that the electron diffusion length remained longer than the thickness of the p-GaAs emitter (200 nm) after irradiation.

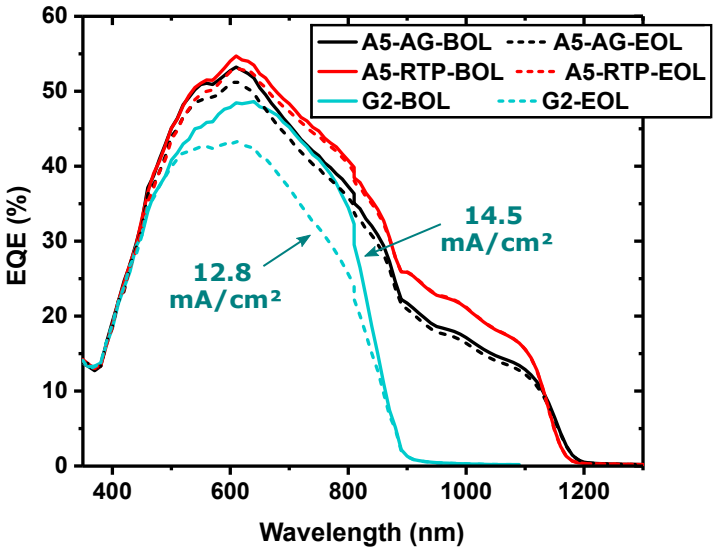

Figure 5.17: EQE spectra of the component cells measured before and after 5×10^{15} e^-/cm^2 electron irradiation.

The photocurrent degradation of the GaAs component cell G2 is highlighted by the J_{sc} values indicated in 5.17. The 1.7 mA/cm^2 photocurrent loss is in excellent agreement with the *J-V* results shown previously.

5.3.4 Conclusion of the section

The degradation of our GaAs/InGaAsN tandem solar under electron irradiation can be explained by two phenomena. Firstly, the defect introduction in the GaAs top cell leads to a higher recombination rate and a lower open-circuit voltage in the subcell, which consequently reduces the V_{oc} of the tandem solar cell. Secondly, the shortening of the minority carrier diffusion length in the InGaAsN bottom cell throughout irradiation decreases its collection efficiency and thus its photocurrent. Since the dilute nitride cell is the current-limiting element,

it causes a global J_{sc} decrease in the tandem solar cell.

Overall, the bottom and component InGaAsN solar cells studied in this section appears to be radiation-harder than the cells irradiated in the previous campaign. This directly results from their higher nitrogen content and their lower BOL optoelectronic properties.

5.4 1 MeV proton irradiation on InGaAsN subcells

5.4.1 Test plan

In addition to electrons, solar cells used in space applications are exposed to protons, as discussed in Chapter 1 (1.2.1). We then assessed the radiation hardness of our InGaAsN solar cells under 1 MeV proton irradiation with four solar cells taken from the A6 wafer. This latter wafer was grown in the same conditions as A2 (T_g=465 °C, *As/III*=12) and exhibits similar BOL properties (see Chapter 4).

The cells were cumulatively irradiated with *in-situ J-V* measurements and a photo-annealing study was conducted, similarly to the previous campaign. As shown in Table 5.5, the fluence target levels were two orders of magnitude lower than for 1 MeV electrons irradiation. Lower fluences were used because i) in space, the proton flux is typically lower than the electron flux (see 5.1.3) and ii) the NIEL of protons is much larger than for electrons (see Chapter 1, 1.2.2). The two first irradiation steps were realised with 1.8 MeV instead of 1 MeV proton energy because of communication issues. Considering the low fluence values corresponding to these two steps, this energy shift should not bring meaningful change in the results.

Table 5.5: Test plan of the irradiation steps

	Fluence step (cm^{-2})	**Irrad. current density** (nA/cm^2)	**Total fluence** (cm^{-2})
In-situ IV measurement			
1.8 MeV protons irrad.	3×10^{11}	0.4	3×10^{11}
In-situ IV measurement			
1.8 MeV protons irrad.	7×10^{11}	0.6	10^{12}
In-situ IV measurement			
1 MeV protons irrad.	2×10^{12}	0.7	3×10^{12}
In-situ IV measurement			
1 MeV protons irrad.	7×10^{12}	1.2	10^{13}
In-situ IV measurement			
30 minutes AM0 exposition			
In-situ IV measurement			
60 minutes AM0 exposition			
In-situ IV measurement			

The samples were thermoregulated at 26 °C during the proton irradiations and we did not observe any significant temperature increase of the stage, even throughout the last irradiation step (+7×10^{12} p^+/cm^2). This steady temperature arises from the moderate fluence levels used here: both the proton flux and the irradiation time were kept low during this campaign.

As mentioned earlier, 1 MeV protons interact more with matter than electrons of the same energy, which results in a lower penetration depth. Additionally, we

have seen in Chapter 1 (1.2.2) that the NIEL of the protons in GaAs increases as the particles lose energy. This means that protons create a large amount of defects in the semi-conductor at the end of their course. To determine the average penetration depth of 1 MeV protons in our samples, we conducted SRIM simulations [14], as represented in Figure 5.18.

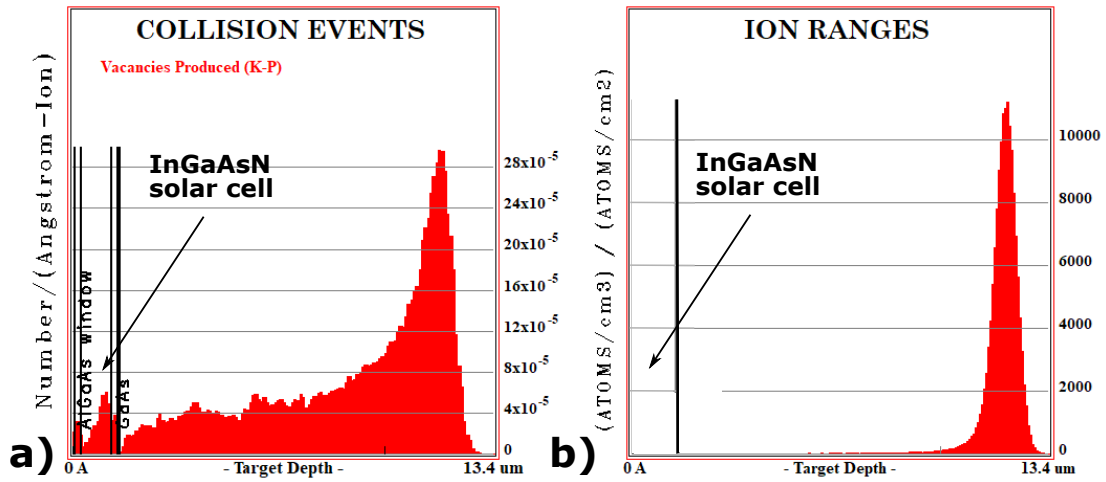

Figure 5.18: SRIM simulation of a) the number of collisions and b) the particle range in our samples under 1 MeV protons irradiation.

Figure 5.18 a) shows that the number of collision events, calculated using the K-P model, increases with the depth of the sample until it reaches a maximum at $\approx 12\ \mu m$. Most of the protons are then implanted at this latter depth (Figure 5.18 b)), which corresponds to the GaAs substrate. Considering the relatively low thickness of the InGaAsN solar cells ($\approx 1.5\ \mu m$ in total), we can assume that the defect introduction rate is constant and homogeneous within the devices.

5.4.2 Degradation of the J-V characteristics

Figure 5.19 shows the degradation of the light *J-V* characteristics (AM0 illumination) of the InGaAsN cells throughout 1 MeV protons irradiation. The four solar cells named A6a, A6b, A6c and A6d exhibit very similar degradation rates. This confirms both the proton flux homogeneity and the uniform radiation response of samples taken from the same wafer.

Unlike for electron irradiation, we can clearly see a monotonic degradation of the *J-V* curves caused by the protons. The remaining factors of the three main photovoltaic parameters (J_{sc}, V_{oc} and FF) are plotted along the proton fluence in Figure 5.20. The remaining factors of GaAs solar cells taken from the literature [15, 16, 17] are also plotted for comparison purpose.

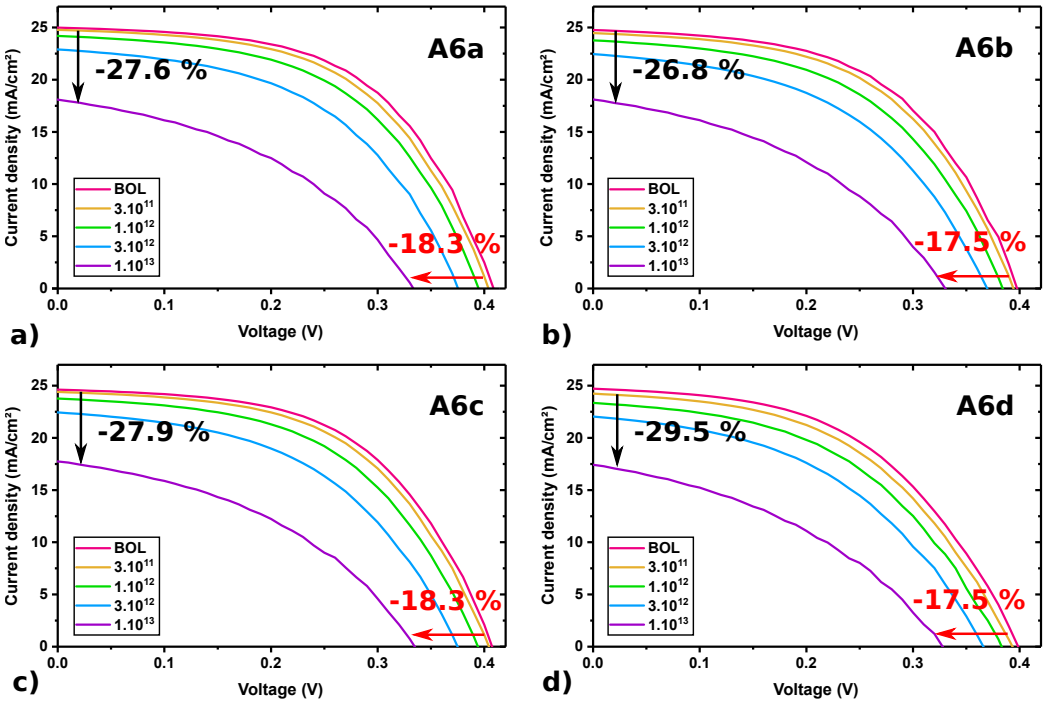

Figure 5.19: *J-V* characteristics of the A6 solar cells measured under AM0 at different fluences (p^+/cm^2). The degradation of the J*sc* and the V_{oc} are indicated in black and red, respectively.

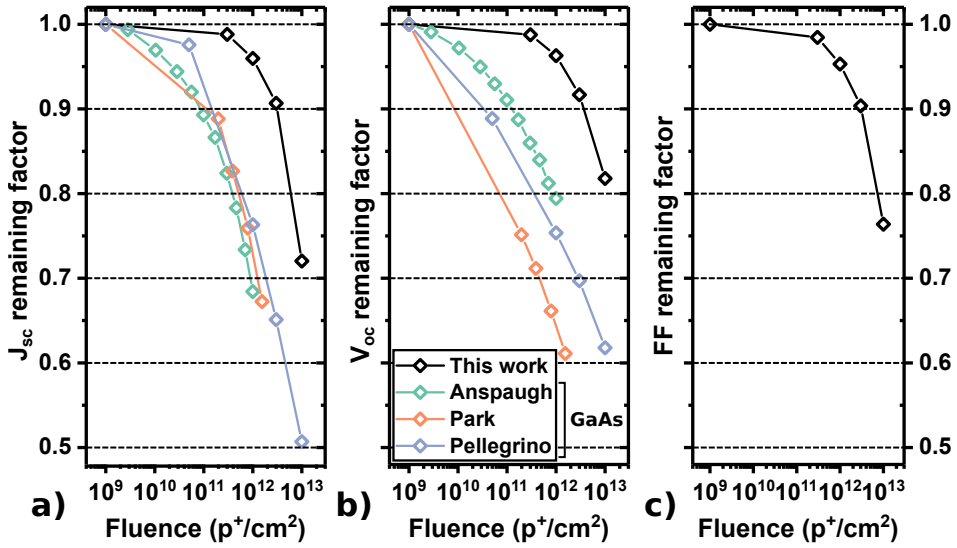

Figure 5.20: A6 average remaining factors of the a) J_{sc}, b) V_{oc} and c) *FF* along the proton fluence (p^+/cm^2). The J_{sc} and V_{oc} remaining factors are also plotted for GaAs solar cells taken from the litterature [15, 16, 17].

In the InGaAsN solar cells, the photocurrent is the parameter that degraded the most throughout irradiation but, unlike for 1 MeV electrons, the open-circuit voltage and the fill factor were also considerably reduced. While we observe

large degradation rates in our InGaAsN solar cells, these samples still exhibit much greater radiation hardness than conventional GaAs solar cells.

Similarly to electron irradiation, the decrease in photocurrent through irradiation can be ascribed to the shortening of the hole diffusion length in the InGaAsN absorber. However, the RFs presented in Figure 5.20 correspond to an AM0 illumination, which means that part of the photocurrent originates from absorption and collection in the GaAs emitter. As it was just mentioned, GaAs undergoes severe degradation under 1 MeV protons irradiation which implies that the emitter contribution is expected to decrease as the fluence increases. This behaviour is discussed in further details in the next section (5.4.3). Current-voltage measurements under AM0>870 nm light were then performed before and after the proton irradiation to exclusively analyse the degradation within the InGaAsN absorber (Figure 5.21).

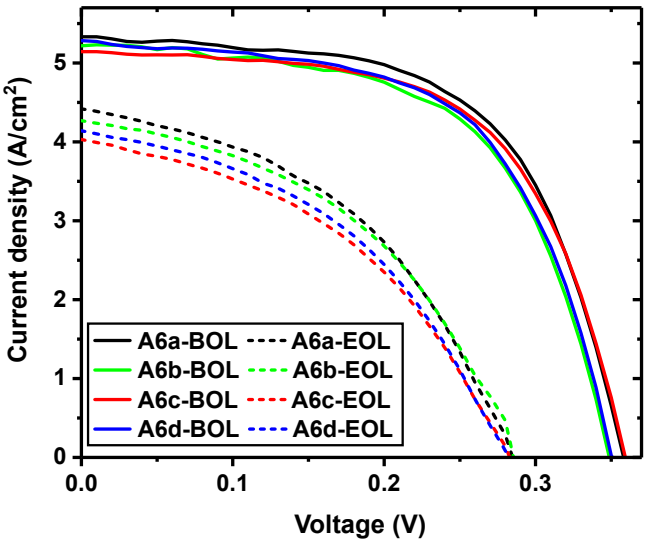

Figure 5.21: Comparison of the BOL and EOL (10^{13} p^+/cm^2) *J-V* characteristics of A6 solar cells measured under AM0>870 nm filtered light.

The average degradation of the photocurrent measured under AM0>870 nm light is 19 %, which is less than the degradation observed under AM0 illumination (≈ 28 %). This discrepancy highlights the higher degradation rate of the GaAs emitter compared to the InGaAsN absorber.

As mentioned earlier, the significant degradation of the V_{oc} measured after proton irradiation, for both AM0 and AM0>870 nm illumination, contrasts with what was observed with 1 MeV electrons. Such a reduction in the open-circuit voltage indicates a raise in the non-radiative recombination rate. This can be observed through the increase in the dark current density, as represented in Figure 5.22 for sample A6a (the other solar cells exhibit similar behaviour).

Moreover, the fill factor was also reduced under proton irradiation, as the photocurrent became more voltage-dependant. This can arise from the contribution of the field aided collection which increases as the minority carrier diffusion

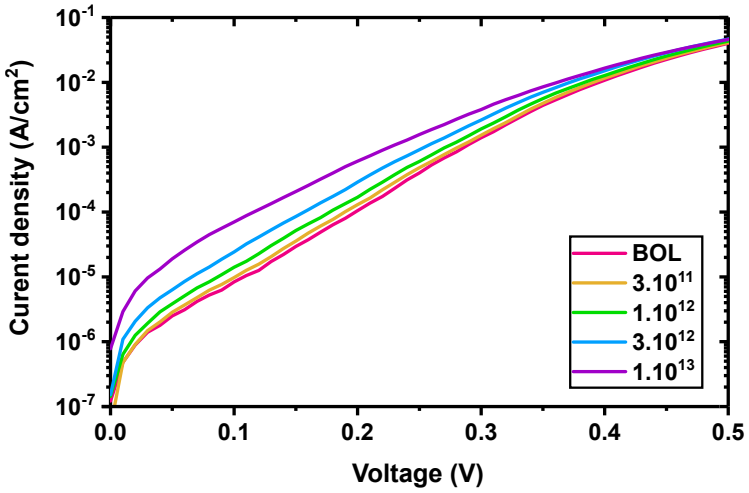

Figure 5.22: Evolution of the dark *J-V* characteristic of sample A6a with the proton fluence (p^+/cm^2).

length gets shorter. This phenomenon was observed for GaAs solar cells irradiated with electrons and protons [18]. Another possible explanation for the fill factor reduction is the electric field dependence of defect recombination. This mechanism was proposed by Park et al. for charged defects introduced in GaInP and GaAs solar cells [16]. Free carriers generated in the space charge region can resist the coulombic attraction of a trap thanks to the kinetic energy provided by the electric field (Poole- Frenkel effect). As the voltage is increased in the *pn* junction, the SCR shortens, which results in a lower number of defects located within the electric field. Less photocarriers are then able to escape trapping, leading to a current degradation.

Finally, we noticed that exposing the solar cells to AM0 light during 30 and 60 minutes did not have any impact on the *J-V* characteristics. The same conclusion as for electron irradiation can then be drawn: the crystal defects introduced through proton irradiation are photo-stable and cannot be annealed through AM0 carrier injection.

5.4.3 Degradation of the quantum efficiency

Figure 5.23 a) shows the degradation of the external quantum efficiency after 10^{13} p^+/cm^2 protons irradiation. The BOL value corresponds to a non-irradiated reference solar cell taken from the A6 wafer. As depicted in Figure 5.23 b), the spectral absorbance A of the 200 nm GaAs emitter was calculated with the Beer-Lambert relation:

$$A = 1 - T = 1 - exp(-\alpha(\lambda).t) \tag{5.1}$$

where T is the emitter transmittance, t is the thickness of the emitter and $\alpha(\lambda)$

is the absorption coefficient of GaAs [19]. The internal reflections in the solar cell are assumed to be negligible.

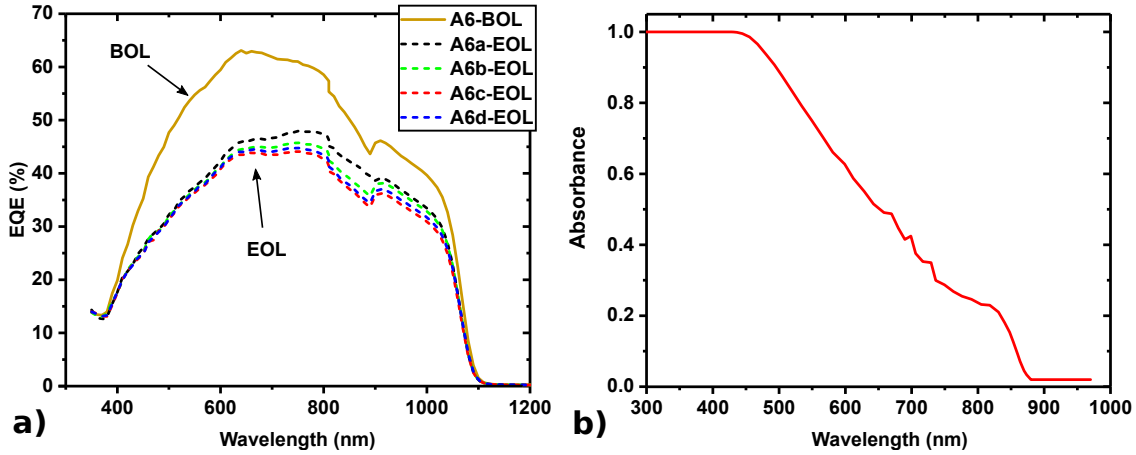

Figure 5.23: a) EQE spectra of A6 solar cells before and after 10^{13} p^+/cm^2 protons irradiation. b) Spectral absorbance of the 200 nm GaAs emitter.

In agreement with the photocurrent decrease observed in the previous section, the quantum efficiency of the A6 solar cells drops after irradiation. The EQE degradation is more important for wavelengths shorter than 870 nm, which is consistent with the *J-V* characterization. As mentioned earlier, this difference in the EQE decrease is due to the large degradation experienced by the GaAs emitter. The spectral absorbance of the 200 nm GaAs emitter plotted in Figure 5.23 b) shows that a considerable amount of light is absorbed in this very layer. As an example, more than half of the λ<600 nm photons are absorbed in GaAs and do not reach the InGaAsN absorber.

The spectrally heterogeneous EQE degradation behaviour exhibited by the A6 samples is then explained by: i) the major contribution of the GaAs emitter highlighted with the absorptance spectra and ii) the large decrease in the diffusion length in proton-irradiated GaAs, inferred from the literature.

5.4.4 Characterization of irradiated InGaAsN bulk layers

The degradation of the materials properties was analyzed through PL and DLTS characterizations conducted on as-grown InGaAsN bulk layer samples taken from the B1, B2, B3 and B4 wafers. The growth conditions corresponding to these samples can be found in Table 5.6.

The degradation of the optical properties of InGaAsN after proton irradiation can be observed with the PL measurements presented in Figure 5.24. The PL intensity of B3 exhibits a 30 % decrease after irradiation while the photoluminescence of B4 is virtually not affected by the protons (ΔI_{PL}<4 %, lower than the measurement uncertainty). This large difference in the PL decrease concurs with

Table 5.6: Growth conditions of the proton-irradiated InGaAsN bulk layers

Sample name	N content (%)	T_g (°C)	As/III ratio
B1	2	465	11
B2			8
B3	2.3	430	7.5
B4	1.2	465	12

our previous observations showing that the samples with better BOL properties (lower nitrogen content) exhibit higher degradation rates.

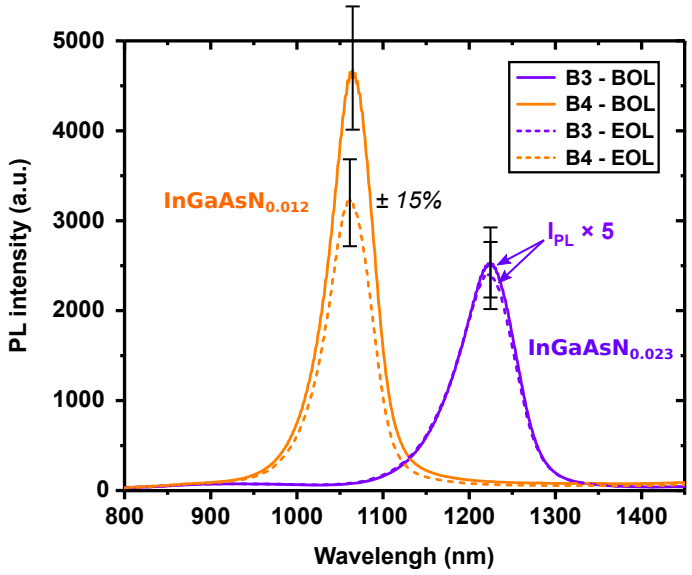

Figure 5.24: PL spectra of samples B3 and B4 before and after $10^{13}/cm^2$ 1 MeV protons irradiation.

Since the A6 solar cells irradiated in this campaign have a nitrogen content equal to 1.6 %, the PL degradation of their InGaAsN absorber is expected to lie closer to 30 % than 4 %. This degradation of the PL intensity is related to the increase in the non-radiative recombination rate, which is also responsible for the decrease in J_{sc} and V_{oc} observed in the previous section. In order to understand the mechanisms causing the NRR to increase, we performed DLTS on the same B3 and B4 samples, as depicted in Figure 5.25 a). The DLTS spectra were obtained with the following acquisition conditions: V_r=-3 V, V_r=0 V and t_p=1 ms.

The DLTS signal of sample B3 is found to increase after irradiation. This highlights defects introduction, which is in line with the slight degradation of the PL intensity of this sample. In order to discriminate the relative increase in the concentration of the two main defects E1 and E2, the BOL and EOL DLTS spectra of sample B3 were fitted with Gaussian peaks, as shown in Figure 5.25 b). We observe an increase in the DLTS signal for the two peaks, which indicates that the proton irradiation is indeed responsible for the introduction of E1 and E2 defects.

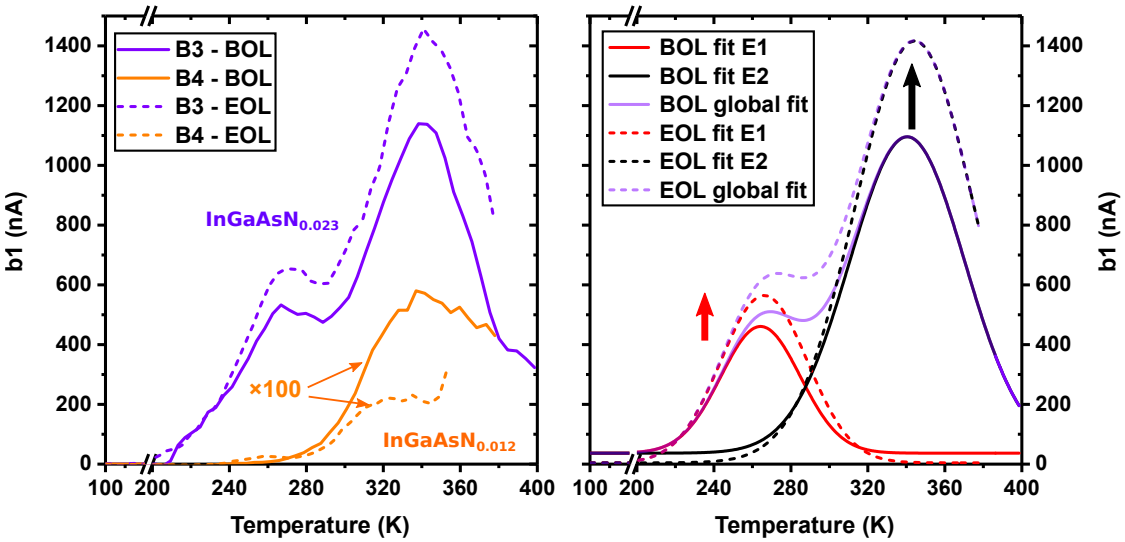

Figure 5.25: a) DLTS spectra of samples B3 and B4 before and after $10^{13}/cm^2$ 1 MeV protons irradiation. b) Fits of the E1 and E2 peaks in the B3 sample at BOL and EOL conditions.

The EOL DLTS spectrum of sample B4 exhibits a decrease compared to its BOL condition. This is somewhat unexpected as a reduction in the DLTS signal usually implies an enhancement of the optoelectronic properties, whereas the luminescence of this very sample was found to degrade through irradiation. No satisfactory explanation could be found to explain this inconsistency but we did notice low signal over noise ratios in the B4 measurements, especially for temperatures higher than 350 K.

Figure 5.26 presents the impact of 1 MeV protons irradiation on the DLTS spectra of the 2 % nitrogen content samples B1 and B2. The acquisition conditions were set as V_r=-1 V, V_r=0 V and t_p=500 μs. Similarly to what was observed with 1 MeV electrons, the DLTS spectra of the annealed samples are not found to vary much after irradiation. The as-grown A6 InGaAsN solar cells irradiated in the same campaign have a comparable nitrogen content (1.6 %), and were found to significantly degrade after proton irradiation. We can then assume that defects were introduced, and considering the steady DLTS spectra exhibited by the *n*-type InGaAsN bulk layer, we can deduce that these defects act as hole traps.

Interestingly, it can be noticed that both the as-grown and annealed B1 samples exhibit the same behaviour after irradiation: a slight decrease in the intensity corresponding to the E1 defect and an increase in the signal corresponding to E2. In addition, we observe a global increase in the DLTS intensity of the annealed samples after irradiation, which contrasts with the behaviour displayed by the as-grown samples. This is likely due to the higher radiation hardness attributed to samples with poorer BOL optoelectronic properties, as discussed in the previous sections.

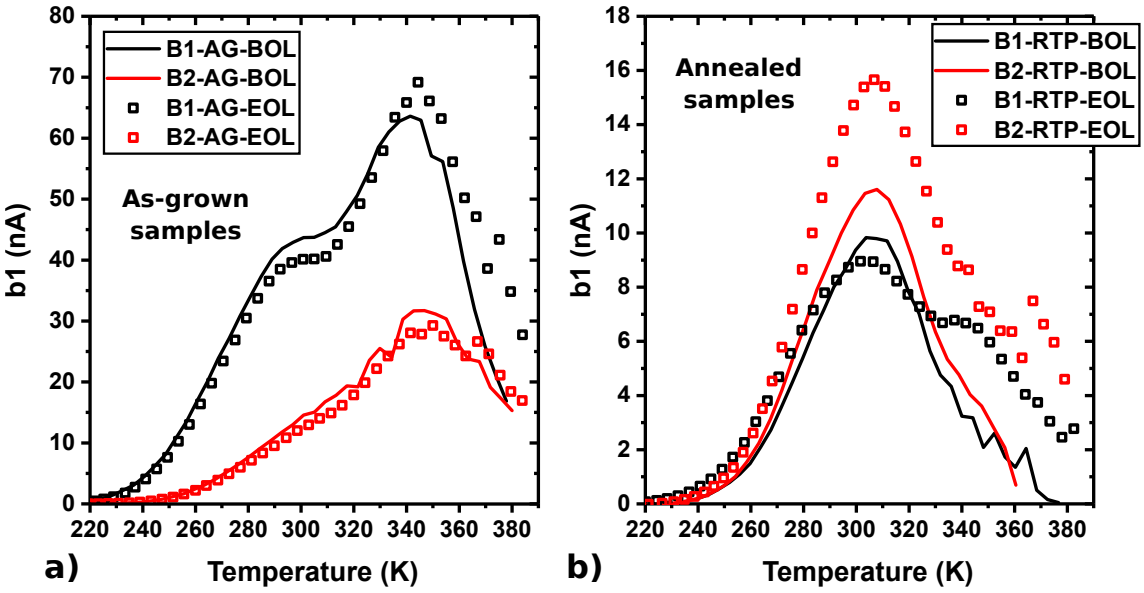

Figure 5.26: DLTS spectra before and after $10^{13}/cm^2$ 1 MeV protons irradiation, for a) as-grown and b) annealed B1 and B2 samples. Note that the two figures do not share the same y-axis scale.

5.4.5 Conclusion of the section

The 1 MeV protons irradiation is found to induce a notable and reproducible degradation of the *J-V* characteristic and the spectral response of InGaAsN solar cells. Although a considerable degradation of their photovoltaic parameters was observed, the InGaAsN cells appears to be much more radiation resistant to 1 MeV protons than their GaAs counterpart. Besides, we noticed that part of the degradation experienced by the InGaAsN cells could be ascribed to the deterioration of the GaAs emitter properties.

As for 1 MeV electrons, the PL analysis showed that the radiation hardness to 1 MeV protons is highly dependent on the BOL properties. In addition, the DLTS spectra were not found to be strongly affected by the protons, indicating that most of the irradiation-induced defects act as hole traps.

5.5 Discussion

Comparison of the degradation factors of InGaAsN solar cells

The irradiation studies conducted in this chapter present different degradation rates, depending on both the sample and the irradiation particle. In order to compare the degradation induced by electrons and protons, the displacement damage dose (DDD) associated to these particles is usually calculated (see Chapter 1, Section 1.2.2). Assuming that InGaAsN has a NIEL value equivalent to

GaAs and taking the irradiation fluences corresponding to the three campaigns, we calculated the DDD induced by 1 MeV electrons and 1 MeV protons in the InGaAsN solar cells [3]. The photocurrent remaining factors obtained under AM0 light can then be plotted as a function of their respective DDD, as depicted in Figure 5.27.

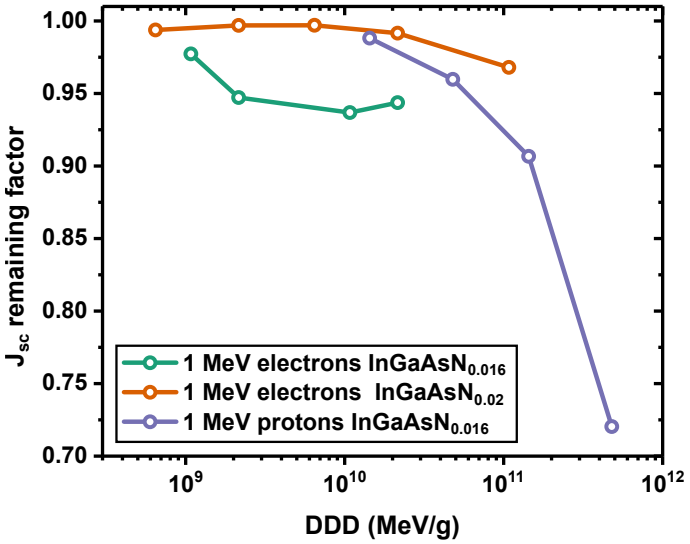

Figure 5.27: Remaining factor of the J_{sc} (AM0 light) as a function of the DDD.

Considering the DDD rather than the particle fluence, we can see that the large *J-V* and EQE degradations observed under proton irradiation result entirely from the higher NIEL energy of 1 MeV protons, as compared to 1 MeV electrons. The RF(J_{sc}) data presented in Figure 5.27 do not perfectly collapse in a single degradation curve because of two main factors: the **difference in BOL properties** and the **irradiation conditions**.

The impact of the BOL properties on the radiation hardness can be observed with three elements:

- The photocurrent remaining factors of the InGaAsN$_{0.016}$ solar cells (E_g=1.11 eV) irradiated in the first campaign were found to correlate with the BOL properties of the cells (J_{sc}, V_{oc} and PL intensity). The samples that displayed the better BOL photovoltaic properties were also the ones that degraded the most.

- The characterization studies presented in both Chapter 3 and Chapter 4 show that optoelectronic properties such as the PL intensity tend to decrease with the nitrogen content. On the other hand, the *J-V* characteristics of the cells grown with a 2 % nitrogen content were found to degrade less than those exhibiting a 1.6 % N content. This difference in the degradation rate can be observed in Figure 5.27, where the J_{sc} remaining factor is larger

[3] We also assume here a linear relation between the DDD and the NIEL, although it is not always the case with electron irradiation.

for the high N content samples. Similarly, the photoluminescence intensity was found to degrade more under irradiation for samples exhibiting lower nitrogen composition.

- The InGaAsN solar cells are found to be much more resistant to electrons and protons than GaAs cells. Although this could arise from a difference in the intrinsic material radiation resistance, or from the *pin* architecture, it more likely originates from a difference in the BOL minority carrier diffusion length.

This finding is intuitive because the degradation of the photovoltaic properties is related to the relative change in the defect concentration ($\frac{\Delta N_t}{N_t}$), rather than the absolute irradiation-induced defect concentration. We know from PL and BGCC measurements that the growth defect concentration in InGaAsN is important. Moreover, the low quantum efficiencies exhibited by the InGaAsN cells in the near infrared region indicate short minority carrier diffusion length. The impact of irradiation-induced defects is then mitigated by the predominance of growth defects in InGaAsN.

The second factor playing an important role in the degradation behaviour is the irradiation condition and more specifically the irradiation flux. In the first electron irradiation campaign, a significantly lower degradation rate was observed in InGaAsN samples irradiated with a higher electron flux. Additionally, annealing behaviours were observed in these samples as the PL intensity of InGaAsN bulk layers was found to increase after 10^{15} e^-/cm^2 irradiation.

Irradiation-induced annealing

The annealing phenomena observed in irradiated semiconductors are often explained by the recombination-enhanced annealing mechanism, suggesting that defects can be cured thanks to the local energy brought by non-radiative recombination of injected carriers [6, 9, 10, 11]. This phenomenon might be partly responsible for the annealing experienced by some InGaAsN samples, but it is not a *sufficient* condition. Indeed, AM0 exposition does not lead to defect annealing in InGaAsN, even though it injects more free carriers ($\approx 2\times10^{17}$ cm^{-2}/s^{-1} if we only consider photons with λ<870 nm) than the 1 MeV electron irradiation ($\approx 5\times10^{16}$ cm^{-2}/s^{-1} if we consider a 5×10^{10} $e^-/cm^2/s$ flux and only ionization interactions). This means that another factor related to the irradiation flux must be accounted for. The high concentration of vacancies introduced throughout the irradiation is believed to be this second necessary condition, as vacancies are reported to enhance the atomic diffusion and promote defect recombination [6, 7]. Overall, the dependency of the InGaAsN radiation response on the irradiation flux could be a limitation to the ground test accelerated simulation.

GaAs emitter degradation

The photocurrent remaining factors of the solar cells presented in Figure 5.27 correspond to a AM0 illumination. However, we noticed lower degradation rates when looking at the current measured under AM0>870 nm filtered light. This is

due to the contribution of the 200 nm GaAs emitter in the global absorption and collection of the InGaAsN solar cells. Under irradiation, the electron diffusion length in the *p*-type GaAs layer shortens, which reduces the number of electrons reaching the *n*-type InGaAsN absorber. The EQE at wavelengths shorter than 870 nm was not found to vary after 5×10^{15} e^-/cm^2 **electron** irradiation, which indicates that the diffusion length remained larger than 200 nm. On the other hand, we have observed with EQE measurements that most of the J_{sc} degradation experienced by InGaAsN solar cells irradiated with 1 MeV **protons** was in fact due to the deterioration of the GaAs emitter.

Even though the degradation of the emitter needs to be accounted for when characterizing InGaAsN subcells, it does not impact the performances of the InGaAsN bottom cell integrated in a tandem or MJSC architecture. Indeed, once placed under a GaAs subcell, no carriers can be generated in the emitter of the InGaAsN hetero-junction solar cell.

Limitations of the DLTS analysis

Finally, we could not observe significant change in most of the DLTS spectra after electron and proton irradiations, even though annealing or degradation behaviours were observed with PL measurements conducted on identical samples. This probably arises from the *n*-type doping of our InGaAsN thick layers restricting the DLTS measurement to the majority carrier traps *i.e.* to the electron traps. Yet, the introduction or the annealing of defects acting as hole traps in the InGaAsN absorber is a more important parameter since it defines the minority carrier diffusion length. A perspective to study further the radiation response of our InGaAsN solar cells would be then to grow *as-hoc p*-type InGaAsN bulk layers and to characterize them with the DLTS technique. Such samples could be obtained by introducing carbon atoms as *p*-type dopants to compensate the *n*-type intrinsic doping.

Comparison with previous studies

As mentioned in Chapter 2 (2.5), only few studies report on the degradation of InGaAsN under space-representative irradiation. Kurtz et al. [20] and Campesato et al. [21] assessed the impact of 1 MeV electron irradiation on InGaAsN solar cells and found significantly different degradation rates. This discrepancy is clearly the result of the large difference in BOL properties. At BOL, the InGaAsN solar cells from [21] deliver enough current to be current-matched in a triple-junction, which implies a low defects concentration in the absorber. This cell is then much more sensitive to irradiation-induced defects, which explains the low J_{sc} remaining factor it displays after 5×10^{15} e^-/cm^2. However, the remaining factors reported in these two latter studies are not representative of the actual degradation rates in the MJSC configuration since the *J-V* characteristics were measured under the full AM0 spectrum. We emphasize in this thesis the importance of considering the GaAs emitter degradation by:

- Measuring the *J-V* characteristics under both AM0 and AM0>870 nm illuminations.

- Conducting quantum efficiency measurements.
- Studying the degradation of a GaAs/InGaAsN tandem solar cell.

Furthermore, the global evolution of the *J-V* characteristics under irradiation can overshadow opposite and compensating mechanisms in the absorber. Materials characterizations such as PL and DLTS were conducted on electron-irradiated InGaAsN and showed both defect introduction [22, 23] and defect annealing [9]. However, these changes in the material properties were not related to degradation (or enhancement) of InGaAsN solar cell devices. We show in this chapter that the degradation of the photovoltaic performances of InGaAsN subcells under electron irradiation correlates with the PL properties and that it cannot be attributed to introduction of electron traps.

Finally, it can be noticed that the literature is lacking studies on the degradation of InGaAsN solar cells under proton irradiation. To our best knowledge, this thesis is the first to report on this subject. As for electrons, we demonstrated an innovative and thorough study including material characterization (PL and DLTS) and *J-V* measurements on InGaAsN single junction and GaAs/InGaAsN tandem solar cells, under both AM0 and AM0>870 nm lights.

Chapter 5 conclusion

InGaAsN solar cells and InGaAsN bulk layers were irradiated with 1 MeV electrons and 1 MeV protons. The proton irradiation was found to impact much more the photovoltaic properties of the cells because of the high NIEL of those particles. We observed different degradation rates of the InGaAsN cells and we showed that the radiation hardness was highly dependent on the BOL photovoltaic performances of the samples. This dependency on the initial optoelectronic properties also explains the higher radiation resistance exhibited by the dilute nitride devices compared to GaAs solar cells. Another factor affecting the radiation hardness of the InGaAsN solar cells is the irradiation flux. Lower degradation rates and even annealing mechanisms were observed in InGaAsN samples irradiated with a high electron flux.

The degradation of the *J-V* characteristics was shown to be different under AM0 and AM0>870 nm illumination, which highlights the degradation of the GaAs emitter. This was also observed with EQE measurements and with a GaAs/InGaAsN tandem solar cell irradiated with 1 MeV electrons. We demonstrated that the degradation of this device can be described by the open-circuit voltage degradation of its GaAs top cell and the photocurrent reduction of its InGaAsN bottom cell.

Bibliography

[1] S. Duzellier, L. Artola, G. Hubert, C. Inguimbert, T. Nuns, S. Lewandowski, T. Paulmier, B. Dirassen, R. Rey, and C. Pons, "AXEL lab.: representative ground simulation for investigating radiation effects in materials and electronics," in *2017 17th European Conference on Radiation and Its Effects on Components and Systems (RADECS)*. IEEE, 2017, pp. 1–7.

[2] TRAD, "Outil de Modélisation de l'Environnement Radiatif Externe." [Online]. Available: https://www.trad.fr/en/download/

[3] J. H. Warner, S. R. Messenger, R. J. Walters, G. P. Summers, J. R. Lorentzen, D. M. Wilt, and M. A. Smith, "Correlation of electron radiation induced-damage in GaAs solar cells," *IEEE Transactions on nuclear science*, vol. 53, no. 4, pp. 1988–1994, 2006.

[4] B. Danilchenko, A. Budnyk, L. Shpinar, D. Poplavskyy, S. Zelensky, K. Barnham, and N. Ekins-Daukes, "1 MeV electron irradiation influence on GaAs solar cell performance," *Solar energy materials and solar cells*, vol. 92, no. 11, pp. 1336–1340, 2008.

[5] B. E. Anspaugh *et al.*, *GaAs solar cell radiation handbook*. National Aeronautics and Space Administration, Jet Propulsion Laboratory, 1996, vol. 7.

[6] J. Bourgoin and J. Corbett, "Enhanced diffusion mechanisms," *Radiation Effects*, vol. 36, no. 3-4, pp. 157–188, 1978.

[7] G. J. Dienes and A. Damask, "Radiation enhanced diffusion in solids," *Journal of Applied Physics*, vol. 29, no. 12, pp. 1713–1721, 1958.

[8] R. Lang, J. Schön, J. Lefèvre, B. Boizot, F. Dimroth, and D. Lackner, "Radiation hardness and post irradiation regeneration behavior of GaInAsP solar cells," *Solar Energy Materials and Solar Cells*, vol. 211, p. 110551, 2020.

[9] E. Pavelescu, R. Kudrawiec, N. Bălţăţeanu, S. Spânulescu, M. Dumitrescu, and M. Guina, "Enhancement in photoluminescence from 1 eV GaInNAs epilayers subject to 7 MeV electron irradiation," *Semiconductor science and technology*, vol. 28, no. 2, p. 025020, 2013.

[10] M. Yamaguchi, T. Okuda, and S. J. Taylor, "Minority-carrier injection-enhanced annealing of radiation damage to InGaP solar cells," *Applied physics letters*, vol. 70, no. 16, pp. 2180–2182, 1997.

[11] D. Lang, L. Kimerling, and S. Leung, "Recombination-enhanced annealing of the E1 and E2 defect levels in 1-MeV-electron–irradiated n-GaAs," *Journal of Applied Physics*, vol. 47, no. 8, pp. 3587–3591, 1976.

[12] D. Stievenard and J. Bourgoin, "Defect-enhanced annealing by carrier recombination in GaAs," *Physical Review B*, vol. 33, no. 12, p. 8410, 1986.

[13] D. Kwon, R. Kaplar, S. Ringel, A. Allerman, S. R. Kurtz, and E. Jones, "Deep levels in p-type InGaAsN lattice matched to GaAs," *Applied physics letters*, vol. 74, no. 19, pp. 2830–2832, 1999.

[14] J. F. Ziegler, M. D. Ziegler, and J. P. Biersack, "SRIM–The stopping and range of ions in matter (2010)," *Nuclear Instruments and Methods in Physics Research Section B: Beam Interactions with Materials and Atoms*, vol. 268, no. 11-12, pp. 1818–1823, 2010.

[15] B. E. Anspaugh, "Proton and electron damage coefficients for GaAs/Ge solar cells," in *The Conference Record of the Twenty-Second IEEE Photovoltaic Specialists Conference-1991*. IEEE, 1991, pp. 1593–1598.

[16] S. Park, J. C. Bourgoin, H. Sim, C. Baur, V. Khorenko, O. Cavani, J. Bourcois, S. Picard, and B. Boizot, "Space degradation of 3J solar cells: I—Proton irradiation," *Progress in Photovoltaics: Research and Applications*, vol. 26, no. 10, pp. 778–788, 2018.

[17] C. Pellegrino, A. Gagliardi, and C. G. Zimmermann, "Difference in space-charge recombination of proton and electron irradiated GaAs solar cells," *Progress in Photovoltaics: Research and Applications*, vol. 27, no. 5, pp. 379–390, 2019.

[18] M. Salzberger, M. Rutzinger, C. Nömayr, P. Lugli, and C. G. Zimmermann, "Voltage-dependent photocurrent in irradiated GaAs solar cells," *Progress in Photovoltaics: Research and Applications*, vol. 26, no. 5, pp. 317–323, 2018.

[19] E. D. Palik, *Handbook of optical constants of solids*. Academic press, 1998, vol. 2.

[20] S. Kurtz, R. King, K. Edmondson, D. Friedman, and N. Karam, "1-MeV-electron irradiation of GaInAsN cells," in *Conference Record of the Twenty-Ninth IEEE Photovoltaic Specialists Conference*. IEEE, 2002, pp. 1006–1009.

[21] R. Campesato, A. Tukiainen, A. Aho, G. Gori, R. Isoaho, E. Greco, and M. Guina, "31% European InGaP/GaAs/InGaAs Solar Cells for Space Application," in *E3S web of conferences*, vol. 16. EDP Sciences, 2017, p. 03003.

[22] A. Khan, J. Gou, M. Imazumi, and M. Yamaguchi, "Interaction of electron irradiation with nitrogen-related deep levels in InGaAsN," *Applied Physics Letters*, vol. 91, no. 4, p. 043503, 2007.

[23] E.-M. Pavelescu, A. Gheorghiu, M. Dumitrescu, A. Tukiainen, T. Jouhti, T. Hakkarainen, R. Kudrawiec, J. Andrzejewski, J. Misiewicz, N. Tkachenko *et al.*, "Electron-irradiation enhanced photoluminescence from GaInNAs/GaAs quantum wells subject to thermal annealing," *Applied physics letters*, vol. 85, no. 25, pp. 6158–6160, 2004.

Conclusion and Perspectives

The aim of this thesis was to assess the degradation of InGaAsN solar cells under space-representative irradiation. To fulfil this objective, we have first grown dilute nitride layers with molecular beam epitaxy, we have then fabricated InGaAsN solar cells and we have finally irradiated these samples with electrons and protons. The following section summarizes the main results reported in each chapter.

Main results

The two first chapters of this thesis introduced the scientific and historical background related to the topic of this thesis. More specifically, **Chapter 1** introduced concepts such as the photovoltaic effect, the multi-junction solar cell structure, the space radiative environment and the interaction between radiation and matter. The degradation of the photovoltaic performances of solar cells in space was explained by the increase in non-radiative recombination rate and by the shortening of the minority carrier diffusion length. **Chapter 2** was dedicated to the InGaAsN quaternary alloy and the historical development that was conducted on this material to use it as a 1 eV absorber in a MJSC. This chapter showed that the minority carrier lifetime is generally low in InGaAsN, because of nitrogen-related crystal defects. Yet, it was shown that high photocurrent cells could be achieved through optimization of the growth conditions and use of a *pin* structure relying less on the diffusion length. **Chapter 2** also highlighted the lack and limitations of irradiation studies conducted on InGaAsN solar cells.

The molecular beam epitaxy recipes used to grow InGaAsN solar cells and bulk layers were described in **Chapter 3**. We showed that an adequate and steady nitrogen flux providing lattice-matching conditions could be obtained thanks to our *in-situ* curvature measurement setup. The epitaxial growth conditions were changed from one sample to the next and we noticed a large impact of the *As/III* ratio on the optoelectronic properties of InGaAsN through PL and DLTS characterizations. The latter characterization technique evidenced two deep electron traps, with approximately 0.6 and 0.8 eV activation energies. The growth temperature was found to play a major role in the residual doping of the dilute nitride layers: solar cells grown at 485 °C and 445 °C display an absorber BGCC equal to $4{\times}10^{15}$ cm^{-3} and $3{\times}10^{16}$ cm^{-3} (respectively), as revealed by ECV measurements.

SIMS data showed that the *n*-type residual doping of the InGaAsN absorber does not arise from atomic contamination but rather from intrinsic doping mechanisms *i.e.* from donor defects.

The InGaAsN solar cell fabrication process and the thorough characterization study conducted on those cells were presented in **Chapter 4**. The *I-V* and EQE measurements performed on single junction and tandem solar cells showed behaviours that correlate with the material properties measured in the previous chapter. In particular, we showed that InGaAsN solar cells grown at lower temperature exhibit low fill factors due to the predominance of the field aided collection regime, which can directly be ascribed to their low residual doping / wide space charge region. The best as-grown $InGaAsN_{0.016}$ solar cells (E_g=1.1 eV) were obtained with an *As/III* ratio equal to 12 and could photogenerate approximately 8 mA/cm^2 in MJSC integration condition. These results were published in an article in the **IEEE Journal of Photovoltaics** [1]. A GaAs/$InGaAsN_{0.02}$ tandem solar cell was also characterized and exhibited a low current (3.3 mA/cm^2)/high voltage (1.215 V) profile. The low photocurrent of the tandem was attributed to the non-optimized bottom cell, displaying a 2 % nitrogen content. We proposed in this chapter three main routes to enhance the performance of InGaAsN single junction and GaAs/InGaAsN tandem solar cells, by: i) increasing the nitrogen content, ii) optimizing the growth conditions and iii) increasing the thickness of the InGaAsN active layer.

The impact of 1 MeV electrons and 1 MeV protons on InGaAsN solar cells was addressed in **Chapter 5**. Three irradiation campaigns were conducted to assess the radiation hardness of i) $InGaAsN_{0.016}$ subcells towards 1 MeV electrons, ii) a GaAs/InGaAsN tandem solar cell and its component cells towards 1 MeV electrons and iii) $InGaAsN_{0.016}$ subcells towards 1 MeV protons. To our best knowledge, this is the first irradiation study conducted on InGaAsN solar cells integrated within a MJSC structure and the first study to report on the degradation of InGaAsN cells under proton irradiation. The impact of 1 MeV electron irradiation on $InGaAsN_{0.016}$ solar cells was detailed in a publication in the **IEEE Transaction on Nuclear Science** [2].

Because of their high NIEL value, 1 MeV protons were found to damage much more the $InGaAsN_{0.016}$ cells than 1 MeV electrons: the AM0 photocurrent decreased by ≈28 % after 10^{13} protons/cm^2 whereas it *only* decreased by ≈6 % after 10^{15} electrons/cm^2. In addition, the degradation rate of InGaAsN cells was shown to be highly dependent on their BOL properties: solar cells with lower growth defects concentration were found to be more sensitive to the introduction of irradiation-induced defects. Furthermore, lower degradation rates and even annealing behaviours were observed in samples irradiated at higher electronic flux, as illustrated by an enhancement in the PL signal of *as-grown* bulk layers as high as 156 %. Finally, we highlighted the importance of considering the degradation of the GaAs emitter when measuring the current-voltage characteristics under AM0 illumination, which is something that was not accounted for in previous reports from the literature [3, 4].

Perspectives

Optimization of the InGaAsN solar cells

We have seen in this thesis that the radiation hardness of an InGaAsN solar cell exhibits an anti-correlation with its BOL photovoltaic performance. Irradiation studies should then be performed on optimized solar cells delivering enough photocurrent under AM0>870 nm to satisfy the current-matching condition in a 3J or 4J architecture. To achieve higher photocurrents and higher open-circuit voltages, the epitaxial growth conditions should be optimized as the optoelectronic properties of InGaAsN were found to be extremely sensitive to the arsenic overpressure and the growth temperature. Introducing bismuth or antimony as surfactants during the growth of the InGaAsN layer could further decrease the nitrogen-related defects concentration [5, 6].

Moreover, the growth optimization should be conducted for dilute nitrides displaying a nitrogen content larger than 2.5 % (E_g<1 eV). Indeed, having a narrower bandgap energy allows to harvest more photons in the near infrared region, which can result in higher photocurrents. Two routes could then be followed:

- Optimization of the growth conditions coupled with an optimization of the post-growth annealing (RTP) recipe. This route was shown to be the most efficient way of achieving high quality InGaAsN solar cells.
- Optimization of the growth conditions without performing post-growth annealing. There are still doubts about the possibility of obtaining *as-grown* InGaAsN solar cells with photovoltaic performances as good as annealed cells. Yet, developing a RTP-free recipe appears to be a key requirement for the integration of the InGaAsN subcell in a 4J architecture. Indeed, the thermal load associated with the RTP is likely to severely degrade the already grown tunnel junction connecting the Ge and the InGaAsN subcells [7, 8, 9].

Either way, this optimization study requires to grow a large number of InGaAsN layers, with different growth temperatures and *As/III* ratios. At the end of this thesis, the *in-situ* curvature measurement setup has been *upgraded*: it can now communicate with the valve aperture of the nitrogen plasma cell which enables automatic growth of the InGaAsN layer. PL characterization would be the fastest way of determining the optimal growth conditions as it does not require additional technological process and as the photovoltaic performances of the InGaAsN solar cells were found to correlate with their PL intensity.

Further irradiation investigations

In order to rigorously quantify the impact of radiation on optimized InGaAsN solar cells (J_{sc}>15 mA/cm^2), irradiation campaigns should be conducted with one proton energy and two electron energies. Indeed, the displacement damage dose is not always found to vary linearly with the NIEL in the case of electron irradiation [10].

To study the defects introduction and defects annealing occurring in InGaAsN under irradiation, both *p*-type and *n*-type InGaAsN DLTS samples should be irradiated to observe hole and electron traps. Comparison of the defects electrical signature with *ab-initio* calculations could be a promising way of understanding the atomic nature of irradiation-induced defects in InGaAsN [11, 12].

Further investigation regarding the impact of the irradiation flux should be conducted. To discriminate thermal and non-thermal effects, three sets of InGaAsN solar cells, PL and DLTS samples could be irradiated with low electron flux, high electron flux with thermoregulation and high electron flux without thermoregulation.

Finally, TRPL and Hall measurements before and after irradiation could provide the minority carrier lifetime and the mobility values in InGaAsN. These values could then be used to model the degradation of InGaAsN solar cells using basic photovoltaic equations or simulation softwares such as SCAPS [13].

Bibliography

[1] M. Levillayer, A. Arnoult, I. Massiot, S. Duzellier, T. Nuns, C. Inguimbert, C. Aicardi, S. Parola, H. Carrere, A. Balocchi *et al.*, "As-grown InGaAsN subcells for multijunction solar cells by molecular beam epitaxy," *IEEE Journal of Photovoltaics*, vol. 11, no. 5, pp. 1271–1277, 2021.

[2] M. Levillayer, S. Duzellier, I. Massiot, A. Arnoult, T. Nuns, C. Inguimbert, C. Aicardi, S. Parola, F. Olivié, R. Monflier *et al.*, "Degradation study of InGaAsN PIN solar cell under 1 MeV electrons irradiation," *IEEE Transactions on Nuclear Science*, 2021.

[3] R. Campesato, A. Tukiainen, A. Aho, G. Gori, R. Isoaho, E. Greco, and M. Guina, "31% European InGaP/GaAs/InGaAs Solar Cells for Space Application," in *E3S web of conferences*, vol. 16. EDP Sciences, 2017, p. 03003.

[4] S. Kurtz, R. King, K. Edmondson, D. Friedman, and N. Karam, "1-MeV-electron irradiation of GaInAsN cells," in *Conference Record of the Twenty-Ninth IEEE Photovoltaic Specialists Conference*. IEEE, 2002, pp. 1006–1009.

[5] D. B. Jackrel, S. R. Bank, H. B. Yuen, M. A. Wistey, J. S. Harris Jr, A. J. Ptak, S. W. Johnston, D. J. Friedman, and S. R. Kurtz, "Dilute nitride GaInNAs and GaInNAsSb solar cells by molecular beam epitaxy," *Journal of Applied Physics*, vol. 101, no. 11, p. 114916, 2007.

[6] S. Tixier, M. Adamcyk, E. Young, J. Schmid, and T. Tiedje, "Surfactant enhanced growth of GaNAs and InGaNAs using bismuth," *Journal of crystal growth*, vol. 251, no. 1-4, pp. 449–454, 2003.

[7] P. Colter, B. Hagar, and S. Bedair, "Tunnel junctions for III-V multijunction solar cells review," *Crystals*, vol. 8, no. 12, p. 445, 2018.

[8] I. Rey-Stolle, I. García, E. Barrigón, J. Olea, D. Pastor, M. Ochoa, L. Barrutia, C. Algora, and W. Walukiewicz, "On the thermal degradation of tunnel diodes in multijunction solar cells," in *AIP Conference Proceedings*, vol. 1881, no. 1. AIP Publishing LLC, 2017, p. 040005.

[9] W. Dawidowski, B. Ściana, I. Zborowska-Lindert, M. Mikolášek, J. Kováč, and M. Tłaczała, "Tunnel junction limited performance of InGaAsN/GaAs tandem solar cell," *Solar Energy*, vol. 214, pp. 632–641, 2021.

[10] G. P. Summers, E. A. Burke, and M. A. Xapsos, "Displacement damage analogs to ionizing radiation effects," *Radiation measurements*, vol. 24, no. 1, pp. 1–8, 1995.

[11] P. Krispin, V. Gambin, J. Harris, and K. Ploog, "Nitrogen-related electron traps in Ga (As, N) layers (< 3% N)," *Journal of Applied Physics*, vol. 93, no. 10, pp. 6095–6099, 2003.

[12] S. Zhang and S.-H. Wei, "Nitrogen solubility and N-induced defect complexes in epitaxial GaAs: N," *Physica B: Condensed Matter*, vol. 308, pp. 839–842, 2001.

[13] M. Burgelman, P. Nollet, and S. Degrave, "Modelling polycrystalline semiconductor solar cells," *Thin solid films*, vol. 361, pp. 527–532, 2000.

Appendices

Appendix A

Investigation and mitigation of surface recombinations

"God made the bulk; the surface was invented by the devil." — Wolfgang Pauli

In a solar cell, photogenerated carriers need to be collected before recombination. Non-radiative recombinations (NRR) are the most detrimental to the photovoltaic properties because they do not give rise to photon recycling and lead to the heating of the device. Two types of NRR exist: bulk recombination – which was approached through DLTS characterization in Chapter 3 – and surface recombination. This latter kind arises from the total disruption of the crystal periodicity and the presence of dangling bonds at the surface.

Our solar cell structure presents two classes of surfaces: the (001) ones that correspond to the front side of the cell, and the vertical sidewalls appeared after the mesa etching. In this section, we show the influence of surface recombination through PL and dark current-voltage characterizations.

A.1 PL measurements

The photoluminescence characterization campaign presented in this section was realised with Ivan Flores, a fellow PhD student working on GaAs photonic crystal. We used a PL setup with a Nd-YAG laser emitting at 532 nm as the excitation source and an electron multiplying CCD camera. All of the measures were conducted at room temperature.

Impact of the AlGaAs window

To assess the impact of the field effect of the AlGaAs window repelling minority carriers in our solar cells, we have grown two 300 nm GaAs bulk layer samples. One was capped with a 40 nm $Al_{0.4}Ga_{0.6}As$ (just like in our cell architecture) whereas the other was not.

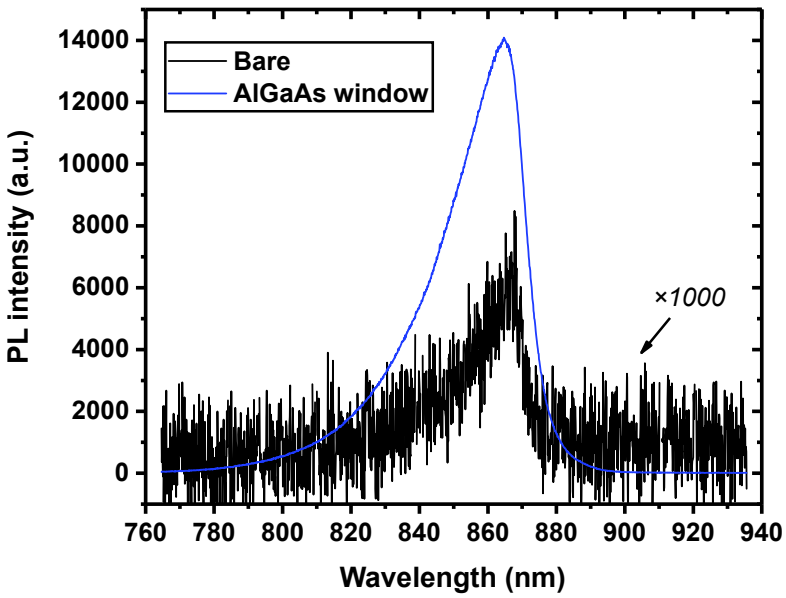

Figure A.1: PL spectra of GaAs samples with and without an AlGaAs window layer.

As we can see in Figure A.1, the PL signal of GaAs is hugely increased (×2000) when covered by an AlGaAs layer. This demonstrates the crucial role of the AlGaAs window layer in our solar cells, drastically reducing the NRR rate on the surface, also called surface recombination velocity (SRV). However, the AlGaAs capping only prevents recombination on the (001) frontside surface and does not reduce the recombination rate on the (100),(010),(110) and ($\bar{1}$10) mesa sidewalls.

Surface passivation

Passivation of the mesa sidewalls is necessary to reduce further the NRR rate. As a first study, we conducted PL measurements on bare GaAs samples before and after having passivated their front surface. We assumed a correlation between the passivation power on (001) surface and on vertical etch plans.

We know from the literature than compound with sulfur in the -2 oxidation state can passivate dangling bonds, through the formation of As-S-As ionic bonds and Ga-S covalent bonds [1]. This sulfide passivation occurs via HS^{-1} anions solvated by water or alcohol molecules [2]. Among various solvents, a study showed that using tert-butanol (C_4H_9OH) with Na_2S led to optimal and stable (001) GaAs surface passivation [3]. We thus decided to assess the passivation process described in this latter study: we added Na_2S powder into t-butanol until we reached the saturation point. This step was conducted under magnetic stirring and at ≈ 30 °C for the t-butanol to be liquid. After having been deoxidized with HCl 10 %, the GaAs samples were immersed into the Na_2S/t-butanol solution during 3 minutes. The samples were then rinsed, dried and measured within two days.

We can see in Figure A.2 that although the photoluminescence is enhanced with the Na_2S passivation (tenfold increase), the PL intensity decays over time.

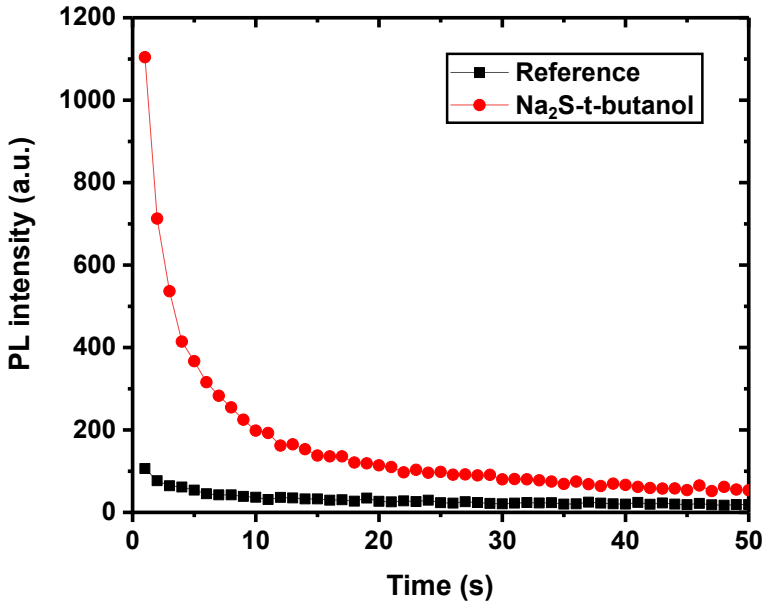

Figure A.2: Time evolution of the PL intensity at peak wavelength (≈ 865 nm) for bare and passivated GaAs.

This degradation of the PL signal indicates an instability of the sulfide passivating bonds (Ga-S and As-S-As) under excitation light. PL mapping showed that the deterioration of the passivation was limited to the laser excitation spot, confirming the photo-induced nature of the degradation.

We replicated the passivation procedure on a second sample and obtained similar results. Obviously, photodegradation of the passivating layer is incompatible with solar cell requirements and we believe depositing a GaN or CaF_2 overlayer to "encapsulate" the sulfide bonds might be a solution to this issue [4, 5]. Nitride passivation could also be used as a replacement for sulfide compounds, as notable passivation effect and extremely high stability were demonstrated with it [6]. However, chemical nitridation relies on hydrazine which is highly explosive, toxic and carcinogenic [7]. Passivation of the surface could also be achieved through physical nitridation with AlN_x atomic layer deposition [8].

A.2 Dark-IV measurements

The impact of surface recombination on the mesa sidewall can be evaluated by measuring the dark saturation current of cells of different shapes and sizes. Indeed, the n=2 term of the double diode equation can be separated into two contributions [9, 10]:

$$I_{02} = I_{02,B} + K_{02,P} \times P \Leftrightarrow J_{02} = J_{02,B} + K_{02,P} \times \frac{P}{A} \tag{A.1}$$

where P and A are the perimeter and area of the solar cell while $J_{02,B}$ and $K_{02,P}$ are the dark recombination current densities associated to bulk and perimeter recombination, respectively[1]. By plotting J_{02} as a function of the perimeter/area ratio, we can determine $K_{02,P}$. This latter parameter can be calculated for different shapes to analyse the influence of the sidewall orientation and can be used to evaluate the impact of surface passivation.

For our study, we fabricated GaAs solar cell diodes with six P/A ratios and three shapes, as described in Chapter 4. Same characterizations and analyzes were conducted on InGaAsN solar cells but we could not observe any significant trend of the J_{02} with the samples size and shape. This was found to be due to a recombination rate much higher in the bulk than on the perimeter.

To avoid the growth inhomogeneities described in Chapter 3, we only conducted dark *I-V* characterization on samples located near the centre of the wafer, as illustrated in Figure A.3. As shown in Table A.1, a large number of samples was analysed to access meaningful statistical data. Characterization and data analysis were performed by Moana Desbordes using a MPI TS2000 station for dark *I-V* measurements and using the *2/3-Diode Fit* freeware for diode modeling. All of our *I-V* results showed that the J_{01} term was completely negligible with respect to J_{02}.

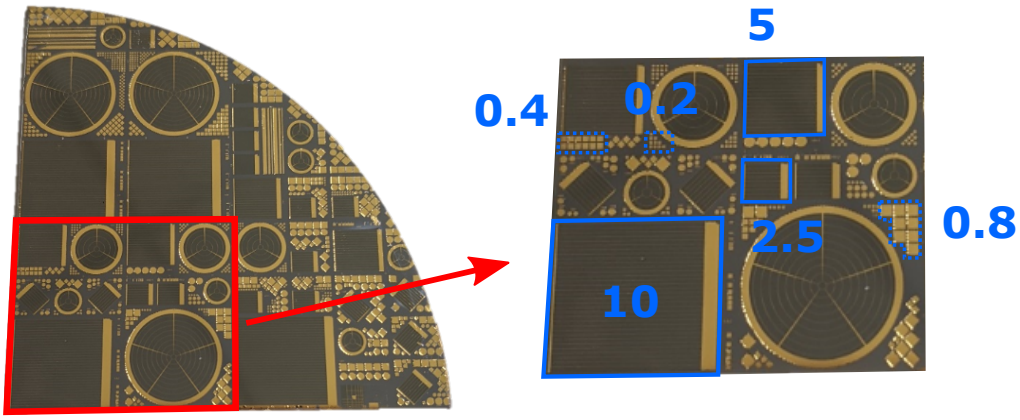

Figure A.3: Picture of a processed quarter wafer with the location of analysed samples. The zoomed-in picture on the right indicates the length of the square solar cells in *mm*.

Table A.1: Number of measured samples for each shape and P/A conditions

P/A ratio (cm^{-1})		4	8	16	50	100	200
Number of samples	□	1	2	2	36	18	10
	○	1	2	2	30	15	8
	◇	0	0	2	36	18	10

As depicted in Figure A.4, we extracted J_{02} from our measurements and plotted it for different perimeter over area ratios. As it can be seen with the J_{02} for

[1] $K_{02,P}$ is actually a *linear* dark recombination current density expressed in A/cm.

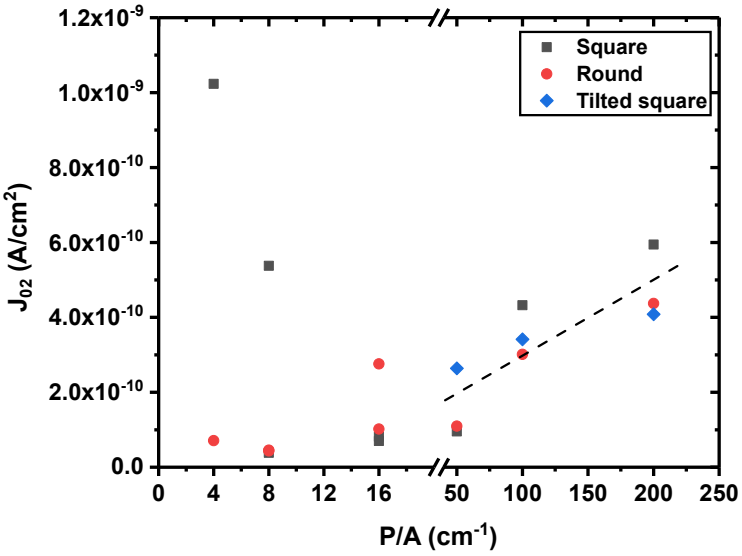

Figure A.4: Averaged J_{02} of samples with different shapes as a function of their P/A. The dashed line corresponds to the linear fitting of P/A=50, 100 and 200 devices.

P/A=4 and 8, we observed very high sample-to-sample variability arising from the diodes location. These differences probably originate from processing steps such as mesa etching where we cannot guarantee homogeneous spreading of the acidic solution through metal patterns. In addition, we could not observe any meaningful effect of the diode shape on the J_{02}. This indicates that the NRR is not significantly dependent on the crystallographic orientation of the mesa-etched sidewalls.

Because of their relatively low numbers leading to poor statistical data, we decided to exclude diodes with P/A equal to 4, 8 and 16 from our analysis. For P/A equal to 50, 100 and 200, we calculated mean J_{02} values and fitted this data with linear regression. We obtain $J_{02,B}$=9.56×10^{-11} A/cm^2 and $K_{02,P}$=2.02×10^{-12} A/cm, suggesting that the saturation current is dominated by perimeter recombination for P/A>47 ($J_{02,P}$= $K_{02,P} \times P/A > J_{02,B}$). The linear current density that we calculated is in great agreement with values reported by Espinet-González et al. ($K_{02,P}$=1.5×10^{-12} A/cm) [10] and by De Moulin et al. ($K_{02,P}$=1.2×10^{-12} A/cm) [11].

Assuming that the recombination rate is zero on the frontside (001) surface (because of the AlGaAs window), the surface recombination occurs exclusively on the mesa sidewalls. We can then calculate an *actual* recombination current density J_P dividing $I_{02,P}$ by the area of the mesa sidewalls A_{sw} where recombination can take place:

$$J_P = \frac{I_{02,P}}{A_{sw}} = \frac{K_{02,P} \times P}{h_{pn} \times P} = \frac{K_{02,P}}{h_{pn}} \tag{A.2}$$

A_{sw} was taken here as the product of the perimeter and h_{pn} the thickness of

the *pn* junction (region where both carrier types are present). In our GaAs solar cells, the combined thickness of the emitter and the base is 3.2 μm so we obtain J_P=6.32×10^{-9} A/cm^2. This current density is quite high, which indicates that the mesa-etched surfaces act as powerful recombination centres. A passivation of the dangling bonds present on the sidewalls appears essential to reduce the NRR plaguing small devices.

We assessed the passivating effect of trioctylphosphine sulfide (TOP:S), $SP(C_8H_{17})_3$, as an alternative to Na_2S compounds. This chemical is reported to enhance the PL signal of bare GaAs samples and to increase the power conversion efficiency of GaAs solar cells [12]. It relies on long aliphatic chains that prevent excessive etching of the passivated surface.

We synthesized TOP:S by dissolving sulfur powder into trioctylphosphine with equimolar quantities. For the dissolution process, the mixture was maintained at 50 °C and magnetically stirred for 24 hours. Small diodes with high P/A ratios (50, 100 and 200 cm^{-1}) were then immersed in TOP:S for 13 hours at room temperature. Afterwards, the samples were rinsed with xylene, IPA and DI water.

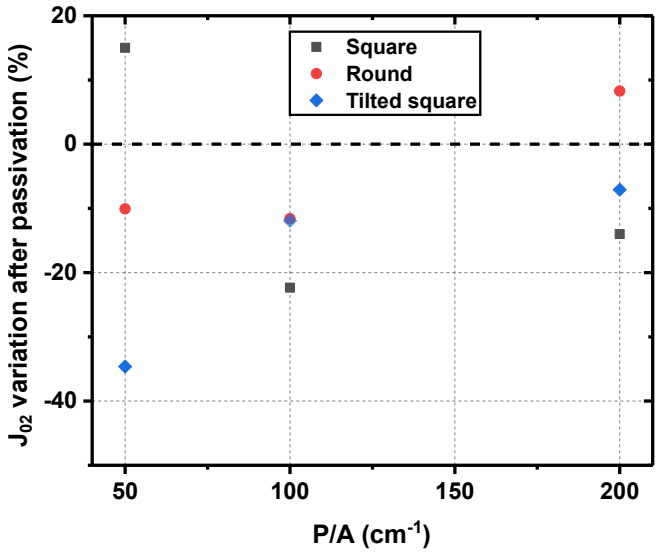

Figure A.5: Variation of J_{02} after TOP:S passivation

We could not observe any meaningful passivation effect for large samples (solar cells with P/A=4, 8 and 16), which can easily be explained by the preponderance of the bulk recombinations over the perimeter ones. Figure A.5 presents the relative variation of the J_{02} current density after TOP:S passivation, for P/A=50, 100 and 200 cm^{-1}. Although J_{02} increased a bit for two classes of samples, the majority of the diodes showed a decrease in J_{02} after the passivation step. The relatively low J_{02} reduction (compared to the 80 % reported by Sheldon et al. [12]) could result, as for Na_2S/t-butanol, from an unstable chemical passivation. Indeed, unlike the *I-V* measurements from [12] performed under TOP:S solution, our samples were put in contact with air and ambient light before being characterized. The TOP:S passivation step could then be beneficial to

the solar cell electrical properties provided that the passivating layer is stabilized. As it was said for Na_2S, this requires the development of a physical passivation procedure.

Bibliography

[1] M. V. Lebedev, "Passivation at semiconductor/electrolyte interface: Role of adsorbate solvation and reactivity in surface atomic and electronic structure modification of III–V semiconductor," *Applied surface science*, vol. 254, no. 24, pp. 8016–8022, 2008.

[2] ——, "Hardness and condensed softness of atoms in HS- ion solvated by amphiprotic solvents," *Chemical physics letters*, vol. 419, no. 1-3, pp. 96–100, 2006.

[3] V. N. Bessolov, E. V. Konenkova, and M. V. Lebedev, "Solvent effect on the properties of sulfur passivated GaAs," *Journal of Vacuum Science & Technology B: Microelectronics and Nanometer Structures Processing, Measurement, and Phenomena*, vol. 14, no. 4, pp. 2761–2766, 1996.

[4] A. Green and W. Spicer, "Do we need a new methodology for GaAs passivation?" *Journal of Vacuum Science & Technology A: Vacuum, Surfaces, and Films*, vol. 11, no. 4, pp. 1061–1069, 1993.

[5] M. Losurdo, P. Capezzuto, G. Bruno, G. Perna, and V. Capozzi, "N2–H2 remote plasma nitridation for GaAs surface passivation," *Applied physics letters*, vol. 81, no. 1, pp. 16–18, 2002.

[6] V. Berkovits, D. Paget, A. Karpenko, V. Ulin, and O. Tereshchenko, "Soft nitridation of GaAs (100) by hydrazine sulfide solutions: Effect on surface recombination and surface barrier," *Applied physics letters*, vol. 90, no. 2, p. 022104, 2007.

[7] INRS, "Hydrazine, hydrate d'hydrazine et solutions aqueuse," *Base de données FICHES TOXICOLOGIQUES INRS*, vol. 21, 2019.

[8] A. Chellu, E. Koivusalo, M. Raappana, S. Ranta, V. Polojärvi, A. Tukiainen, K. Lahtonen, J. Saari, M. Valden, H. Seppänen *et al.*, "GaAs surface passivation for InAs/GaAs quantum dot based nanophotonic devices," *Nanotechnology*, vol. 32, no. 13, p. 130001, 2021.

[9] H.-L. Chen, A. Cattoni, R. De Lépinau, A. W. Walker, O. Höhn, D. Lackner, G. Siefer, M. Faustini, N. Vandamme, J. Goffard *et al.*, "A 19.9%-efficient ultrathin solar cell based on a 205-nm-thick GaAs absorber and a silver nanostructured back mirror," *Nature Energy*, vol. 4, no. 9, pp. 761–767, 2019.

[10] P. Espinet-González, I. Rey-Stolle, M. Ochoa, C. Algora, I. García, and E. Barrigón, "Analysis of perimeter recombination in the subcells of GaInP/GaAs/Ge triple-junction solar cells," *Progress in Photovoltaics: Research and Applications*, vol. 23, no. 7, pp. 874–882, 2015.

[11] P. D. DeMoulin, S. P. Tobin, M. S. Lundstrom, M. Carpenter, and M. R. Melloch, "Influence of perimeter recombination on high-efficiency GaAs p/n heteroface solar cells," *IEEE electron device letters*, vol. 9, no. 8, pp. 368–370, 1988.

[12] M. T. Sheldon, C. N. Eisler, and H. A. Atwater, "GaAs passivation with trioctylphosphine sulfide for enhanced solar cell efficiency and durability," *Advanced Energy Materials*, vol. 2, no. 3, pp. 339–344, 2012.

Résumés des chapitres en français

Chapitre 1

Technologies photovoltaïques et dégradation en environnement spatial

1.1 Cellules solaires à haut rendement pour le spatial

L'effet photovoltaïque a été mis en évidence pour la première fois en 1839 par Edmond Becquerel [1]. Il consiste en l'apparition d'une tension aux bornes de deux matériaux juxtaposés sous excitation lumineuse.

Des jonctions *p-n* de silicium furent développées dans les années 50 afin de convertir l'énergie radiative solaire en énergie électrique [2]. Le silicium étant un semi-conducteur, il présente une énergie de bande interdite E_g séparant ses bandes de valence et de conduction. Un photon d'énergie supérieure à E_g rencontrant le semi-conducteur peut-être absorbé et permettre à un porteur de charge (électron ou trou) de traverser la bande interdite. Le porteur excité est alors dit "libre" et est capable de se déplacer au sein du matériau. Il peut également se recombiner en rencontrant un porteur du signe opposé et perdre l'énergie acquise lors de l'absorption du photon. Une jonction *pn* est en générale utilisée afin de séparer les porteurs photogénérés par effet de champ dans la zone de charge d'espace (ZCE). La Figure 1.1 illustre les différents mécanismes évoqués.

Une cellule solaire sous éclairement peut être décrite par la caractéristique électrique d'une diode à laquelle on ajoute un photocourant I_{ph}. En adoptant la convention de signe photovoltaïque ($I_{ph} > 0$) et en prenant en compte les résistances série R_s et parallèle R_{sh} de la cellule, on obtient la caractéristique courant-tension suivante :

$$I = I_{ph} - [I_0.(exp(\frac{q(V + IR_s)}{nkT}) - 1)] - \frac{V + IR_s}{R_{sh}} \tag{1.1}$$

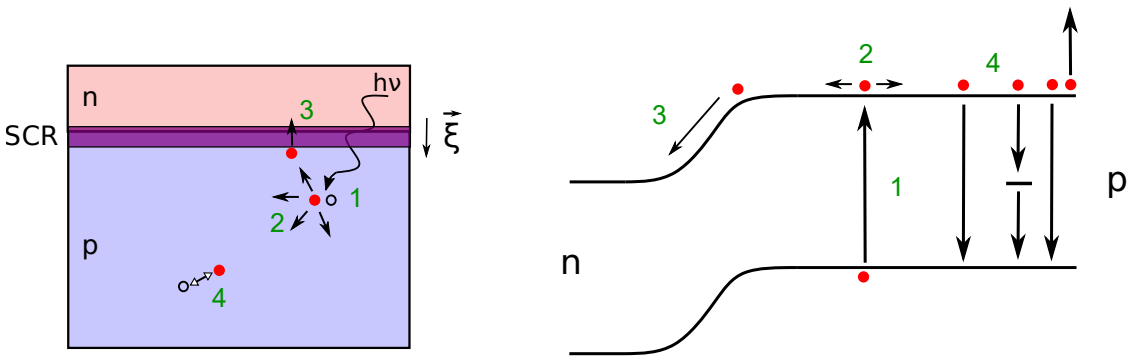

FIGURE 1.1 : Principaux mécanismes ayant lieu au sein d'une jonction *pn* sous éclairement. 1) photogénération de porteurs libres, 2) diffusion de l'électron libre, 3) collecte par dérive dans la ZCE, 4) Recombinaisons radiative, SRH (Shockley-Read-Hall) et Auger. On retrouve ces mêmes mécanismes pour les trous.

où I_0 et n sont respectivement le courant de saturation et le facteur d'idéalité de la cellule solaire. Tracer cette caractéristique dans le premier quadrant permet de mettre en évidence les principaux paramètres photovoltaïques : le courant de court-circuit J_{sc}, la tension de circuit-ouvert V_{oc} et le *fill-factor* FF (Figure 1.2). De plus, la courbe P-V renseigne la puissance maximale P_{max} que la cellule peut délivrer et son point de fonctionnement associé (V_{mp} ;I_{mp}).

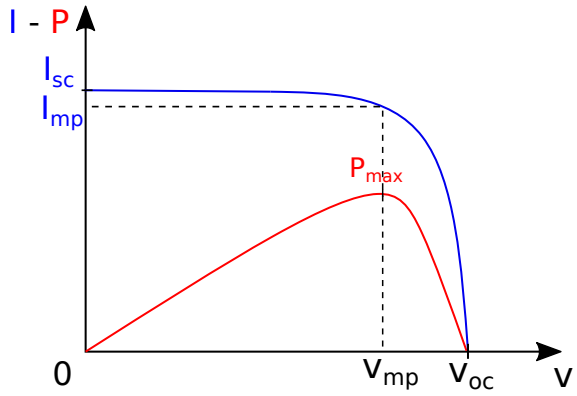

FIGURE 1.2 : Caractéristiques I-V et P-V d'une cellule solaire sous éclairement

Le rendement de la cellule est ensuite obtenu en divisant P_{max} par la puissance radiative incidente appelée *irradiance*. Les rendements typiques des technologies silicium cristallin (95 % du marché terrestre) sont légèrement supérieurs à 17 % [3] alors que les cellules solaires à multi-jonction (MJSC) utilisées dans l'espace offrent des rendements de 28-30 % [4].

Le développement du photovoltaïque a été porté par la course à l'espace entre les Etats-Unis et l'URSS. Dès 1958, les Américains lancent le satellite Vanguard 1 en orbite, équipé de six cellules solaires de silicium [5]. Les Soviétiques furent quant à eux les premiers à concevoir des cellules solaires à base d'arséniure de gallium GaAs, plus stables en température et plus résistantes aux radiations spa-

tiales [6].

Afin d'augmenter la puissance par unité de masse embarquée, des cellules tandems AlGaAs/GaAs [7] puis des triple-jonction GaInP/GaAs/Ge furent développées [8]. Ces structures à semi-conducteurs III-V permettent d'exploiter une gamme spectrale plus large et atteindre de plus hauts rendements. Une MJSC est un empilement de sous-cellules solaires d'énergie de bande interdite différente qui réduit les pertes par transmission et par thermalisation. Les sous-cellules sont en général connectées en série : les tensions s'additionnent alors que le courant qui les traverse est le même partout. Les hauts rendements que les MJSC affichent découlent donc des tensions élevées générées par ces architectures.

Il existe trois principales techniques pour réaliser des cellules solaires à multijonction. Premièrement, la structure peut-être épitaxiée par croissance monolithique en accord de maille sur son substrat. Le paramètre de maille des matériaux constituant les cellules doit alors être égal à celui du substrat. Cette méthode est fiable et adaptée aux contraintes industrielles, les MJSC fabriquées pour le spatial en sont issues. La deuxième technique consiste à faire croître séparément des sous-cellules pour ensuite les coller par *wafer-bonding*. Cette technologie permet d'associer des cellules solaires de paramètres de maille différents. Enfin, les MJSC peuvent être épitaxiées par croissance métamorphique inversée (IMM). Les cellules supérieures (*top-cells*) sont alors crues en premier et des tampons graduels de contrainte sont utilisés afin de s'affranchir du respect de l'accord de maille.

1.2 Impact de l'environnement radiatif spatial sur les cellules solaires

L'espace est un milieu traversé d'intenses radiations provenant de supernova (rayons cosmiques), du soleil (éruption et vent solaire) ou encore des ceintures de radiation de la Terre. Ces radiations spatiales sont en réalité des particules très énergétiques telles que des électrons, des protons ou des ions lourds.

Lorsque ces particules entrent en collision avec la matière, elles interagissent avec les atomes de deux manières. Elles peuvent tout d'abord interagir avec les nuages électroniques et ioniser des atomes. Bien que ces mécanismes puissent induire des charges internes et des erreurs logiques dans des transistors, ils n'engendrent pas de dégradation au sein de la cellule solaire.

Les particules incidentes peuvent également interagir avec le noyau et provoquer des déplacements atomiques dans le réseau cristallin. La dose de déplacement induite est appelée DDD et est associée à la création de défauts cristallins.

Les défauts créés peuvent être ponctuels (antisites, lacunes, interstitiels ...) ou se regrouper en structure plus grande (cascades de défauts, clusters, poches amorphes). Le désordre introduit vient alors rompre la périodicité du cristal, ce qui fait apparaitre des niveaux d'énergie dans la bande interdite du semi-

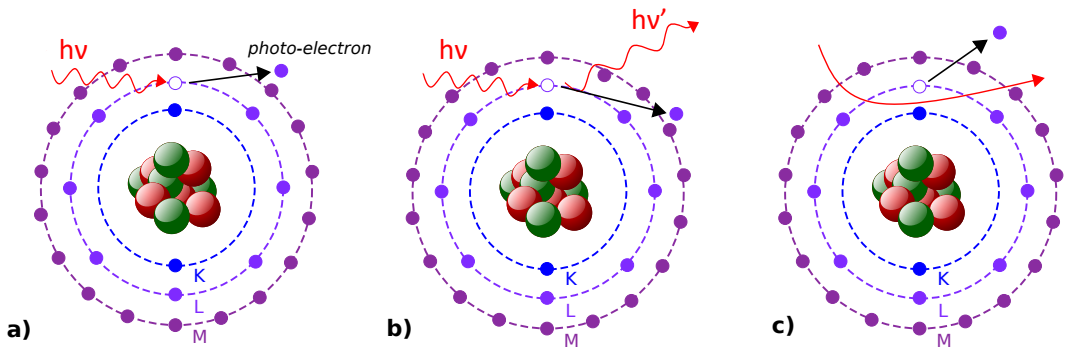

FIGURE 1.3 : Principales interactions particule/nuage électronique : a) Effet photoélectrique b) Effet Compton c) Interaction Coulombienne électronique.

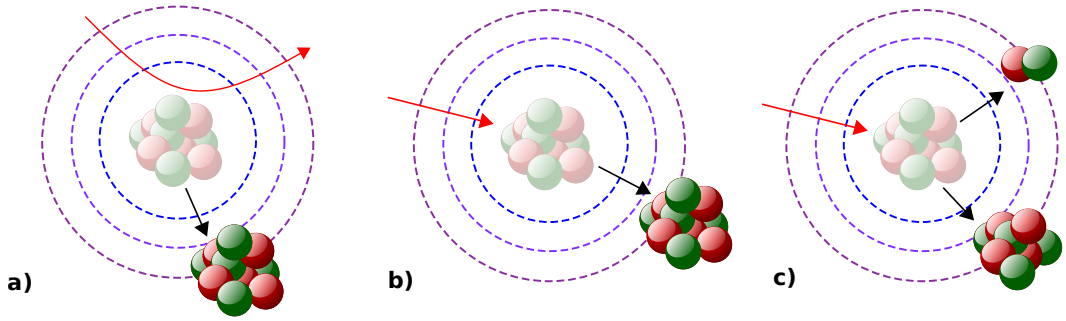

FIGURE 1.4 : Principales interactions particule/noyau atomique : a) Interaction Coulombienne nucléaire b) Interaction nucléaire élastique c) Interaction nucléaire inélastique (spallation).

conducteur. Les défauts se comportent par conséquent comme des centres de recombinaisons non-radiatives diminuant le temps de vie τ et la longueur de diffusion des porteurs minoritaires. Également, le courant de saturation I_0 augmente et la mobilité des porteurs μ diminue. Les paramètres photovoltaïques I_{sc} et V_{oc} des jonctions pn se dégradent alors car ils obéissent aux équations suivantes [9] :

$$J_{sc} = qG\left(\sqrt{\frac{kT}{q}\mu_n\tau_n} + \sqrt{\frac{kT}{q}\mu_p\tau_p}\right) \tag{1.2}$$

$$V_{oc} = \frac{kT}{q}\ln\left(\frac{I_{ph}}{I_0} + 1\right) \tag{1.3}$$

Il est alors nécessaire de pouvoir prédire la dégradation d'une cellule solaire en fonction de l'environnement spatial dans lequel elle évoluera. Pour se faire, il faut recourir à des tests d'irradiations généralement réalisés avec des accélérateurs de particules électrostatiques (Cockroft-Walton, Van de Graaff...). La dégradation peut être caractérisée pour différentes énergies de particules et normalisée par rapport à la dégradation engendrée par des électrons de 1 MeV et des pro-

tons de 10 MeV : c'est la méthode **JPL** [10]. Une autre approche consiste à calculer la dose de déplacement DDD induite pour chaque type de particule et chaque énergie pour ensuite déterminer empiriquement la relation :

$$RF(X) = 1 - C.log(1 + \frac{DDD}{D_x}) \tag{1.4}$$

où RF(X) est le *remaining factor* d'un paramètre photovoltaïque X. Cette méthode a été développée par le Naval Research Laboratory (NRL), elle est souvent privilégiée car son modèle demande moins de tests d'irradiation (tests souvent longs et coûteux).

Pour avoir un premier aperçu de la résistance aux radiations de cellules solaires, il est en général convenu d'irradier ces dernières avec des électrons de 1 MeV. Yamaguchi et al. ont ainsi proposé en 1995 une revue des taux de dégradation de différentes cellules sous bombardement électronique [11]. Les industriels doivent également qualifier la tenue aux radiations des cellules solaires développées pour application spatiale. La Figure 1.5 montre l'évolution de P_{max} pour des cellule 3J à haut rendement sous irradiation en électrons 1 MeV :

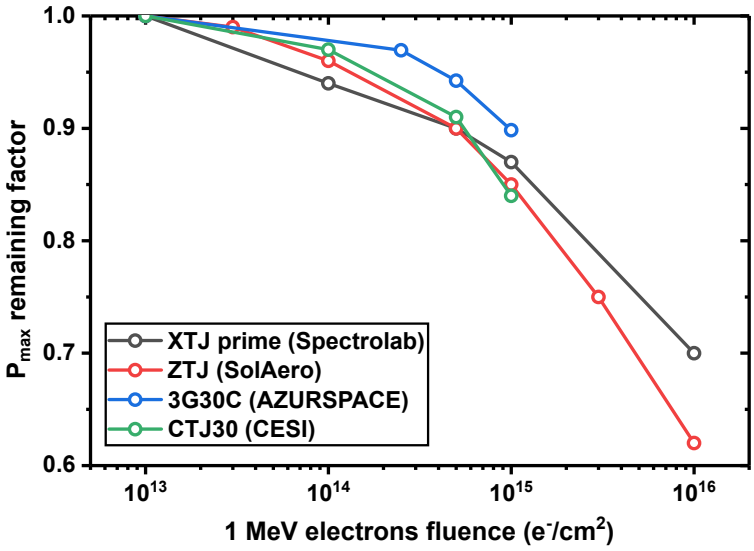

FIGURE 1.5 : Dégradation sous électrons 1 MeV de la puissance maximale fournie par 4 cellules 3J commerciales (les données proviennent de [12, 13, 14, 15]).

Analyser la dégradation globale de MJSC en environnement radiatif est indispensable pour estimer la durée de vie de toute mission spatiale. Toutefois, cette analyse globale masque en général des dégradations hétérogènes au sein des différentes sous-cellules qu'il est nécessaire d'étudier lors de la phase de conception de la structure. Déterminer quelle sous-cellule se dégrade la plus rapidement sous irradiation permet en effet d'adapter son épaisseur et son énergie de bande interdite. Ce faisant, la sous-cellule peut générer plus de photocourant et ne pas devenir courant-limitante au cours de la mission spatiale.

Références

[1] E. Becquerel, "Mémoires sur les effets électriques produits sous l'influence des rayons solaires," *Comptes rendus de l'académie des sciences*, vol. 9, p. 561, 1839.

[2] D. M. Chapin, C. S. Fuller, and G. L. Pearson, "A new silicon p-n junction photocell for converting solar radiation into electrical power," *Journal of Applied Physics*, vol. 25, no. 5, pp. 676–677, 1954.

[3] S. Philipps and W. Warmuth, "Photovoltaics Report 2019." Fraunhofer ISE, Tech. Rep. November, 2019.

[4] A. W. Bett, S. P. Philipps, S. S. Essig, S. Heckelmann, R. Kellenbenz, V. Klinger, M. Niemeyer, D. Lackner, and F. Dimroth, "Overview about technology perspectives for high efficiency solar cells for space and terrestrial applications," *28th European Photovoltaic Solar Energy Conference and Exhibition*, vol. 0, pp. 1–6, 2013.

[5] NASA, "Nasa space science data coordinated archive : Vanguard 1." [Online]. Available : https://nssdc.gsfc.nasa.gov/nmc/spacecraft/display.action?id=1958-002B

[6] G. Strobl, G. LaRoche, K.-D. Rasch, and G. Hey, "From Extraterrestrial to Terrestrial Applications," in *High-efficient low-cost photovoltaics : recent developments*. Springer, 2009, ch. 2, pp. 7–27.

[7] V. M. Andreev, V. R. Larionov, V. D. Rumyantsev, O. M. Fedorova, and S. S. Shamukhamedov, "pAlGaAs–pGaAs–nGaAs solar cells with efficiencies of 19% at AM0 and 24% at AM1.5," *Sov. Tech. Phys. Lett. (Engl. Transl.); (United States)*, vol. 9 :10, 1983.

[8] P. K. Chiang, J. H. Ermer, W. T. Nishikawa, D. D. Krut, D. E. Joslin, J. W. Eldredge, B. T. Cavicchi, and J. M. Olson, "Experimental results of GaInP2/GaAs/Ge triple junction cell development for space power systems," *Conference Record of the IEEE Photovoltaic Specialists Conference*, pp. 183–186, 1996.

[9] J. Gray, "The physics of the solar cells," in *Handbook of Photovoltaic Science and Engineering, Second Edition*. Wiley, 2011, ch. 3, p. 99.

[10] B. Anspaugh and R. Downing, "Radiation effects in silicon and gallium arsenide solar cells using isotropic and normally incident radiation," 1984.

[11] M. Yamaguchi, "Radiation resistance of compound semiconductor solar cells," *Journal of applied physics*, vol. 78, no. 3, pp. 1476–1480, 1995.

[12] Spectrolab, "Spectrolab datasheets," 2021. [Online]. Available : https://www.spectrolab.com/support.html#datasheets

[13] SolAero, "Ztj space solar cell," 2018. [Online]. Available : https://solaerotech.com/wp-content/uploads/2018/04/ZTJ-Datasheet-Updated-2018-v.1.pdf

[14] AZURSPACE, "Space solar cells," 2021. [Online]. Available : http://www.azurspace.com/index.php/en/products/products-space/space-solar-cells

[15] CESI, "Triple-Junction Solar Cell for Space Applications (CTJ30)." [Online]. Available : https://www.cesi.it/app/uploads/2020/03/Datasheet-CTJ30-1.pdf

Chapitre 2

L'InGaAsN à 1 eV pour intégration MJSC

"*Des nains sur des épaules de géants*" – Bernard de Chartres

2.1 L'épitaxie par jets moléculaire

Le terme épitaxie vient du grec *epi* qui signifie "dessus" et du suffixe *taxie* qui signifie "arrangement". L'épitaxie désigne donc une technique de croissance durant laquelle un matériau "croît" sur un substrat en prolongeant la maille cristalline de ce dernier. L'épitaxie d'une couche est donc possible si le paramètre de maille du matériau épitaxié est égal à celui du substrat : on parle de croissance en accord de maille. Dans le cas contraire (désaccord de maille), la couche est épitaxiée sous contrainte ce qui peut mener à la formation de dislocations lorsque l'on dépasse une épaisseur critique : on parle alors de croissance métamorphique.

Il existe différentes techniques de croissance selon l'origine des atomes incidents à la surface. En épitaxie par jets moléculaires (EJM), les espèces arrivent en régime balistique en traversant un ultravide. Les atomes proviennent en général de source solide appelée "cellule d'effusion" ou de source gazeuse dans le cas du carbone et de l'azote. Ces sources sont équipées de shutter et de valve permettant de contrôler précisément les flux atomiques et donc de maitriser le profil des couches épitaxiées, comme on peut le voir dans la Figure 2.1. La température du substrat est également soigneusement contrôlée en épitaxie car elle gouverne la mobilité des atomes adsorbés à la surface, leur arrangement cristallin ainsi que le taux de désorption des espèces. Afin de maitriser le régime de croissance, de nombreuses caractérisations *in-situ* peuvent être réalisées durant l'épitaxie, telles que la diffraction d'électrons de haute énergie en incidence rasante (RHEED) qui permet de déterminer l'arrangement atomique en surface.

Bien que n'offrant pas des rythmes de production industrielle aussi élevés que l'épitaxie en phase vapeur aux organométalliques (EPVOM), l'EJM dispose

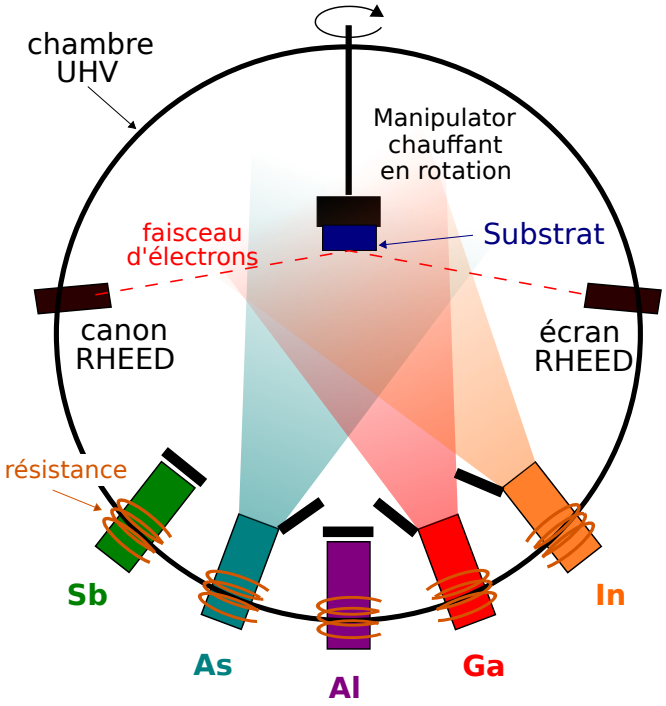

FIGURE 2.1 : Représentation schématique d'une croissance EJM avec cinq cellules d'effusion. Ici, les shutters Sb et Al sont fermés. Une couche d'InGaAs est donc épitaxiée.

d'un atout capital : de part son fonctionnement sous ultra-vide, l'EJM offre de très faibles niveaux de contamination et de dopage résiduel. Cet avantage couplé à un contrôle fin des profils de dopage et de composition font de l'EJM une technique privilégiée pour le développement de semi-conducteurs *III-V*.

2.2 Histoire des cellules solaires InGaAsN

Les nitrures dilués sont des alliages semi-conducteurs basés sur l'arséniure de gallium GaAs incorporant une faible fraction d'azote. En 1992, une équipe japonaise du NTT Lab rapporta un très important décalage vers le rouge (*redshift*) de l'énergie de bande interdite (gap) du GaAs après y avoir introduit moins de 1.5 % d'atomes d'azote [1]. Cette découverte fut reçue avec grand intérêt par la communauté laser car de nouveaux matériaux émettant dans l'infrarouge étaient alors activement recherchés. Une équipe de Hitachi proposa ainsi d'incorporer à la fois de l'indium et de l'azote dans le GaAs afin d'obtenir le quaternaire InGaAsN à faible énergie de gap et accordé en maille sur GaAs [2].

Parallèlement à cette découverte, des cellules solaires à multijonction étaient développées pour des applications spatiales et pour le photovoltaïque à concentration. La cellule à tri-jonction GaInP/GaAs/Ge fut ainsi démontrée en 1996 par Spectrolab [3]. Bien que présentant un rendement impressionnant de 25.7 % sous AM0, des calculs théoriques mirent en avant la sous-utilisation de l'infrarouge dans cette structure [4]. Le calcul des combinaisons d'énergie de bande interdite

idéale révéla le besoin de développer une sous-cellule à 1 eV accordable en maille sur GaAs. Cette sous-cellule pourrait remplacer la cellule de germanium (*bottom-cell*) ou bien être introduite au sein d'une quadri-jonction afin de mieux exploiter le proche infra-rouge. Des chercheurs américains au NREL décidèrent alors de développer des cellules solaires à 1 eV en se basant sur l'InGaAsN accordé en maille sur GaAs.

Les premières cellules à absorbeur InGaAsN présentaient de faibles rendements quantiques dûs aux courtes longueurs de diffusion des porteurs minoritaires. Il apparut très rapidement que ces courtes longueurs de diffusion résultaient de la présence de nombreux défauts cristallins provoqués par l'introduction d'azote dans le réseau. Des structures *pin* et *nip* furent donc développées pour s'affranchir de ce problème de diffusion en s'appuyant sur la collecte de porteurs libres par dérive (*drift*). Les croissances par EJM furent donc privilégiées car elles permirent d'atteindre des dopages résiduels faibles (<10^{16} cm^{-3}) et des photo-courants ≈ 15 mA.cm^{-2} en condition d'intégration [5]. L'optimisation des conditions de croissance (*e.g.* surpression d'arsenic, température de croissance) et du recuit thermique (RTP) fut également conduite afin de se prémunir des défauts cristallins. En 2012, Solar Junction annonça la fabrication d'une tri-jonction GaInP/GaAs/InGaAsNSb et décrocha le record mondial de rendement photovoltaïque : 43.5 % (sous concentration) [6].

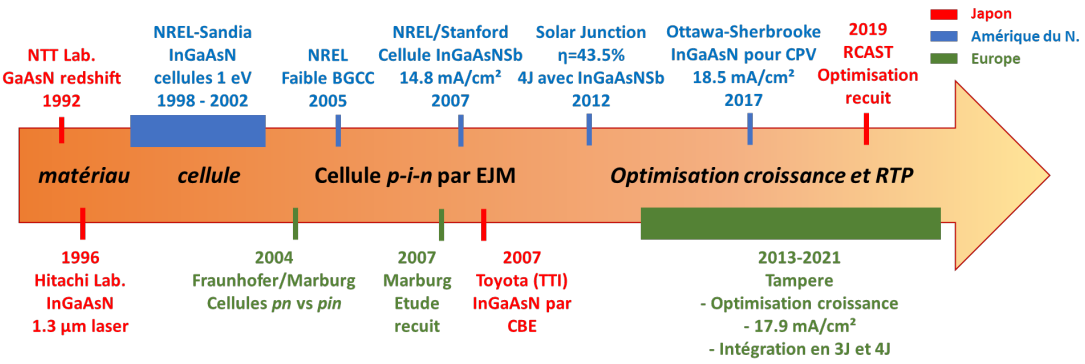

FIGURE 2.2 : Étapes clé dans le développement de cellules solaires InGaAsN pour intégration en MJSC.

2.3 Propriétés optoélectroniques de l'InGaAsN

Comme nous l'avons évoqué dans la section précédente, la principale singularité des nitrures dilués est le redshift qu'ils présentent pour de faibles teneurs en azote. Ce comportement se traduit par l'apparition d'un large paramètre de "bowing" b dans l'équation donnant l'énergie de bande interdite de l'alliage GaAsN :

$$E_g(GaAs_{1-x}N_x) = (1-x).E_g(GaAs) + x.E_g(GaN) - bx(1-x) \tag{2.1}$$

où x est la concentration atomique d'azote. De plus, il est nécessaire d'ajouter de l'indium au ternaire GaAsN afin de contrebalancer la contrainte en tension induite par l'azote et ainsi de rester accordé en maille sur GaAs. Sachant que l'énergie de bande interdite de l'InGaAs peut également se calculer à l'aide d'une relation de Vegard, on peut tracer l'évolution du gap de l'InGaAsN avec la concentration en azote (Figure 2.3).

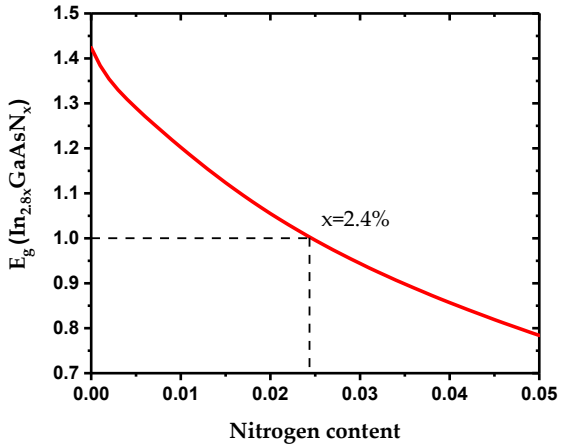

FIGURE 2.3 : Evolution de l'énergie de bande interdite de l'InGaAsN en fonction de la teneur en azote du quaternaire.

La diminution apparente de l'énergie de bande interdite est causée par l'introduction de défauts fortement localisés formant une bande résonant avec la bande de conduction de l'(In)GaAs. Le couplage de ces deux bandes par interactions dites "anticrossing" provoque la séparation de la bande de conduction de la matrice en deux sous-bandes [7]. L'énergie de bande interdite effective de l'alliage devient alors la transition entre la bande de valence et la branche inférieure de la bande de conduction, provoquant ainsi le redshift observé.

En plus de la réduction d'énergie de gap, les défauts présents dans l'(In)GaAsN peuvent introduire des niveaux d'énergie profonds dans la bande interdite car ils provoquent une rupture de la périodicité du cristal. A l'aide de caractérisations par spectroscopie et de calculs *ab-initio*, il a été démontré que les principaux défauts présents dans l'InGaAsN sont les doublets interstitiels $(N-X)_{As}$ [8, 9] et les lacunes de gallium [10, 11]. Ces deux défauts sont représentés en Figure 2.4.

Ces défauts sont plus particulièrement étudiés par caractérisations électriques afin d'évaluer leur impact sur le transport des porteurs de charge. La DLTS pour "deep level transient spectroscopy" est une technique couramment utilisée à cet escient car elle permet de mesurer la concentration en défauts N_t, leur position dans le gap E_A ainsi que leur section de capture efficace σ. Cette technique repose sur l'analyse de transitoire de capacité d'une jonction *pn* (ou Schottky) après un pulse de tension l'ayant placée hors-équilibre. A mesure que les porteurs injectés et piégés par les défauts durant le pulse vont se libérer, la zone de charge d'espace

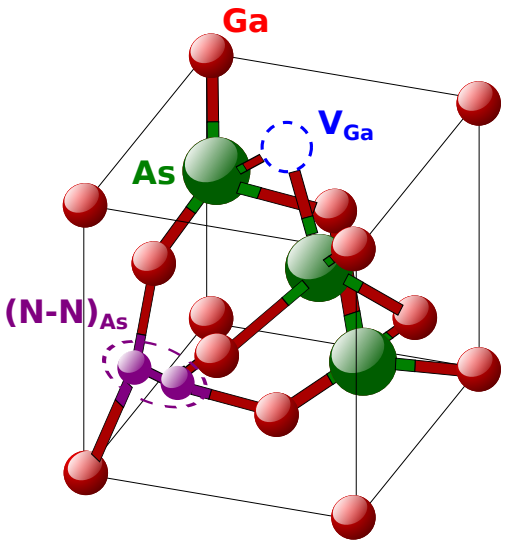

FIGURE 2.4 : Représentation atomique des deux défauts principaux dans l'InGaAsN : les doublets interstitiels (ici $(N\text{-}N)_{As}$) et les lacunes de gallium V_{Ga}. La structure zinc blende du GaAs est montrée ici sans atomes d'indium car ceux-ci ne représentent que quelques % des éléments *III* dans l'InGaAsN accordé en maille.

(ZCE) va revenir à son épaisseur et à sa capacité initiale. Le profil du transitoire de capacité dépend du taux d'émission du piège e qui dépend lui même de la température et de la nature du défaut.

$$e = A^* T^2 \sigma \exp(-\frac{E_A}{kT}) \tag{2.2}$$

où A^* est la constante de Richardson du matériau étudié. Le taux d'émission d'un piège est en général calculé en mesurant la différence de capacité ΔC entre deux instants t_1 et t_2. La mesure de ΔC à plusieurs températures donne alors un signal de DLTS représenté par la Figure 2.5.

De nombreuses publications ont rapporté la présence de défauts de croissance dans l'InGaAsN, observés par DLTS. Il apparait cependant que les propriétés électriques de ces défauts dépendent très largement des conditions de croissance et de la composition atomique des échantillons étudiés. Quoi qu'il en soit, les défauts observés sont préjudiciables au transport des porteurs de charge. D'une part le temps de vie des porteurs minoritaires est en général faible dans l'InGaAsN (typiquement quelques centaines de picosecondes [5, 12]), d'autre part la mobilité est elle aussi fortement réduite [13]. Les longueurs de diffusion des porteurs minoritaires sont donc globalement courtes dans les cellules solaires d'InGaAsN ce qui explique le développement d'architecture disposant de large ZCE (*pin* ou pn^-). Malgré des taux de contamination très faibles durant les croissances par EJM, il est apparu difficile d'obtenir des dopages résiduels inférieurs à 10^{15} cm^{-3} dans l'InGaAsN. En effet, le dopage résiduel des nitrures dilués est majoritairement *intrinsèque* : il émane de défauts accepteurs ou donneurs. Prévenir l'apparition de défauts cristallins peut alors mener à des longueurs de diffusion relati-

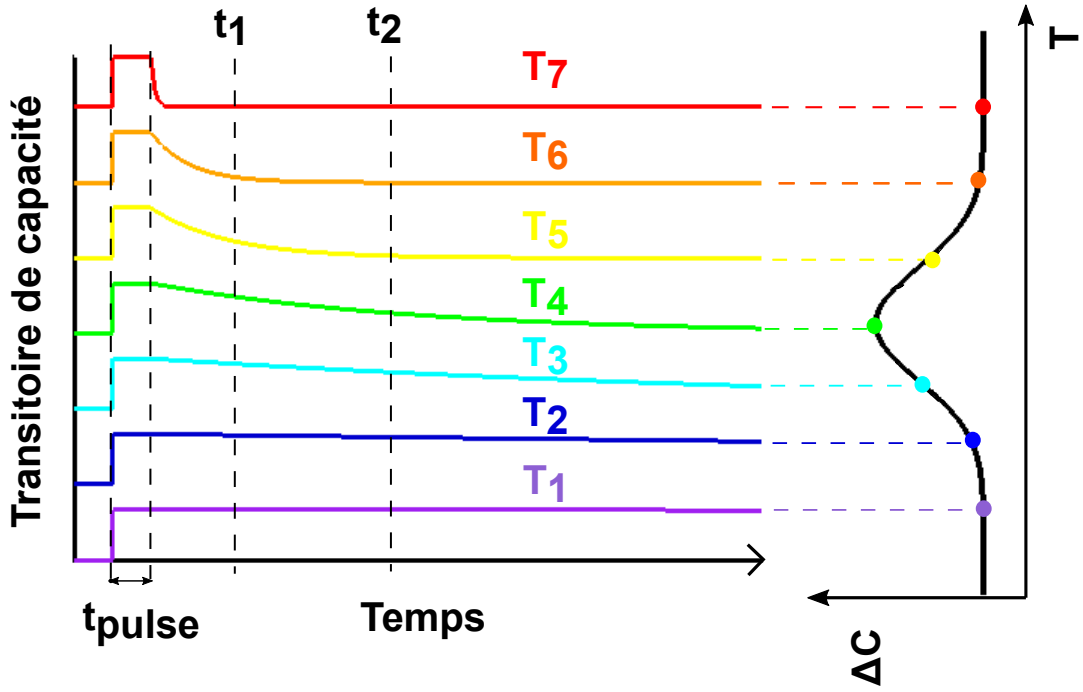

FIGURE 2.5 : Représentation schématique de transitoires de capacité pour différentes températures. Le signal DLTS est projeté à droite en fonction de la température.

vement bonnes ainsi qu'à de faibles dopages résiduels. Associé à l'optimisation des conditions de croissance, le recuit thermique est un moyen efficace pour obtenir de bonnes propriétés opto-électroniques. Ce dernier est toutefois accompagné d'un indésirable *blueshift* du gap de l'InGaAsN correspondant à la formation de liaisons In-N dans le réseau cristallin [14, 15].

Grâce aux optimisations structure/matériau réalisées pour des sous-cellules d'InGaAsN à 1 eV, des photocourants supérieurs à 15 mA/cm^2 furent obtenus sous éclairement AM0>870 nm. Certaines sous-cellules furent intégréees au sein de trijonction pour du photovoltaïque à concentration [6], d'autre furent utilisées dans des trijonctions pour application spatiale [16].

2.4 Dégradation de l'InGaAsN sous irradiation

A ce jour, deux analyses de dégradation de cellules solaires InGaAsN sous irradiation ont été rapportées [16, 17]. La première porte sur des cellules non-optimisées, épitaxiées par EPVOM. Elle met en évidence une très faible dégradation après 10^{15} e/cm^2 (électrons 1 MeV), comme le montre la Figure 2.6. Pour le même type de particule et la même fluence, la seconde étude rapporte une dégradation beaucoup plus conséquente du J_{sc} (≈ -30 %) et du V_{oc} (≈ -10 %). Cette importante dégradation s'explique probablement par des concentrations en défauts de croissance faibles en début de vie (BOL) relativement aux cellules étudiées par

Kurtz et al. Le temps de vie et la mobilité des porteurs sont alors plus sensibles aux défauts créés par l'irradiation dans ces structures optimisées.

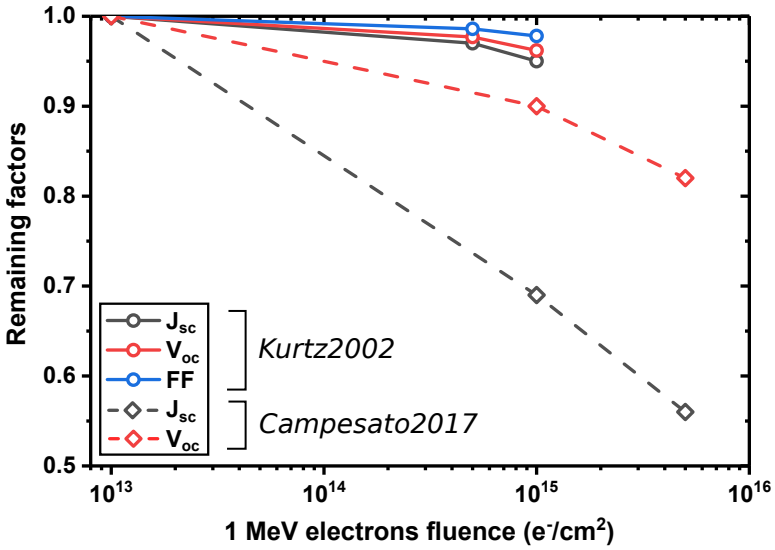

FIGURE 2.6 : Remaining factor des courants de court-circuit, tensions de circuit ouvert et facteurs de forme de cellules solaires InGaAsN irradiées aux électrons 1 MeV.

Parallèlement aux analyses de dégradation des cellules, la tenue à l'irradiation de l'InGaAsN a été étudiée par caractérisation matériau. Une étude DLTS a ainsi montré l'introduction de pièges (à électrons et à trous) dans l'InGaAsN irradié aux électrons 1 MeV [18]. D'autre part des mesures de photoluminescence ont mis en évidence des mécanismes de guérison de défauts de croissance sous irradiation en observant le signal PL augmenter après 10^{14} 7 MeV électrons/cm^2 [19].

Références

[1] M. Weyers, M. Sato, and H. Ando, "Red shift of photoluminescence and absorption in dilute GaAsN alloy layers," *Japanese Journal of Applied Physics*, vol. 31, no. 7A, p. L853, 1992.

[2] M. Kondow, K. Uomi, A. Niwa, T. Kitatani, S. Watahiki, and Y. Yazawa, "GaInNAs : A novel material for long-wavelength-range laser diodes with excellent high-temperature performance," *Japanese journal of applied physics*, vol. 35, no. 2S, p. 1273, 1996.

[3] P. K. Chiang, J. H. Ermer, W. T. Nishikawa, D. D. Krut, D. E. Joslin, J. W. Eldredge, B. T. Cavicchi, and J. M. Olson, "Experimental results of $GaInP_2$/GaAs/Ge triple junction cell development for space power systems," *Conference Record of the IEEE Photovoltaic Specialists Conference*, pp. 183–186, 1996.

[4] S. R. Kurtz, D. Myers, and J. M. Olson, "Projected performance of three-and four-junction devices using GaAs and GaInP," in *Conference Record of the Twenty Sixth IEEE Photovoltaic Specialists Conference-1997*. IEEE, 1997, pp. 875–878.

[5] D. B. Jackrel, S. R. Bank, H. B. Yuen, M. A. Wistey, J. S. Harris Jr, A. J. Ptak, S. W. Johnston, D. J. Friedman, and S. R. Kurtz, "Dilute nitride GaInNAs and GaInNAsSb solar cells by molecular beam epitaxy," *Journal of Applied Physics*, vol. 101, no. 11, p. 114916, 2007.

[6] D. Derkacs, R. Jones-Albertus, F. Suarez, and O. Fidaner, "Lattice-matched multijunction solar cells employing a 1 eV GaInNAsSb bottom cell," *Journal of Photonics for Energy*, vol. 2, no. 1, p. 021805, 2012.

[7] W. Shan, W. Walukiewicz, J. Ager III, E. Haller, J. Geisz, D. Friedman, J. Olson, and S. R. Kurtz, "Band anticrossing in GaInNAs alloys," *Physical Review Letters*, vol. 82, no. 6, p. 1221, 1999.

[8] W. Li, M. Pessa, T. Ahlgren, and J. Decker, "Origin of improved luminescence efficiency after annealing of Ga(In)NAs materials grown by molecular-beam epitaxy," *Applied Physics Letters*, vol. 79, no. 8, pp. 1094–1096, 2001.

[9] S. Zhang and S.-H. Wei, "Nitrogen solubility and N-induced defect complexes in epitaxial GaAs : N," *Physica B : Condensed Matter*, vol. 308, pp. 839–842, 2001.

[10] J. Toivonen, T. Hakkarainen, M. Sopanen, H. Lipsanen, J. Oila, and K. Saarinen, "Observation of defect complexes containing Ga vacancies in GaAsN," *Applied Physics Letters*, vol. 82, no. 1, pp. 40–42, 2003.

[11] A. Janotti, S.-H. Wei, S. Zhang, S. Kurtz, and C. Van de Walle, "Interactions between nitrogen, hydrogen, and gallium vacancies in $GaAs_{1-x}N_x$ alloys," *Physical Review B*, vol. 67, no. 16, p. 161201, 2003.

[12] A. Gubanov, V. Polojärvi, A. Aho, A. Tukiainen, N. V. Tkachenko, and M. Guina, "Dynamics of time-resolved photoluminescence in GaInNAs and GaNAsSb solar cells," *Nanoscale research letters*, vol. 9, no. 1, pp. 1–4, 2014.

[13] S. R. Kurtz, A. A. Allerman, C. H. Seager, R. M. Sieg, and E. D. Jones, "Minority carrier diffusion, defects, and localization in InGaAsN, with 2% nitrogen," *Applied Physics Letters*, vol. 77, no. 3, pp. 400–402, 2000.

[14] K. Volz, D. Lackner, I. Nemeth, B. Kunert, W. Stolz, C. Baur, F. Dimroth, and A. Bett, "Optimization of annealing conditions of (GaIn)(NAs) for solar cell applications," *Journal of Crystal Growth*, vol. 310, no. 7-9, pp. 2222–2228, 2008.

[15] K. Uno, M. Yamada, I. Tanaka, O. Ohtsuki, and T. Takizawa, "Thermal annealing effects and local atomic configurations in GaInNAs thin films," *Journal of crystal growth*, vol. 278, no. 1-4, pp. 214–218, 2005.

[16] R. Campesato, A. Tukiainen, A. Aho, G. Gori, R. Isoaho, E. Greco, and M. Guina, "31% European InGaP/GaAs/InGaAs Solar Cells for Space Application," in *E3S web of conferences*, vol. 16. EDP Sciences, 2017, p. 03003.

[17] S. Kurtz, R. King, K. Edmondson, D. Friedman, and N. Karam, "1-MeV-electron irradiation of GaInAsN cells," in *Conference Record of the Twenty-Ninth IEEE Photovoltaic Specialists Conference*. IEEE, 2002, pp. 1006–1009.

[18] A. Khan, S. R. Kurtz, S. Prasad, S. Johnston, and J. Gou, "Correlation of nitrogen related traps in InGaAsN with solar cell properties," *Applied physics letters*, vol. 90, no. 24, p. 243509, 2007.

[19] E. Pavelescu, R. Kudrawiec, N. Bălţăţeanu, S. Spânulescu, M. Dumitrescu, and M. Guina, "Enhancement in photoluminescence from 1 eV GaInNAs epilayers subject to 7 MeV electron irradiation," *Semiconductor science and technology*, vol. 28, no. 2, p. 025020, 2013.

Chapitre 3

Etude des conditions de croissance épitaxiale de l'InGaAsN

3.1 Croissance épitaxiale des couches d'InGaAsN

3.1.1 Matériel et méthode

Durant cette thèse, nous avons fait croître des couches d'InGaAsN par épitaxie par jets moléculaires au LAAS avec un bâti RIBER412. Dans notre système EJM, le carbone utilisé comme dopant *p* est introduit sous forme de CBr_4 et l'azote est fourni à travers une cellule RF plasma. Le reste des éléments utilisés provient de cellules d'effusion.

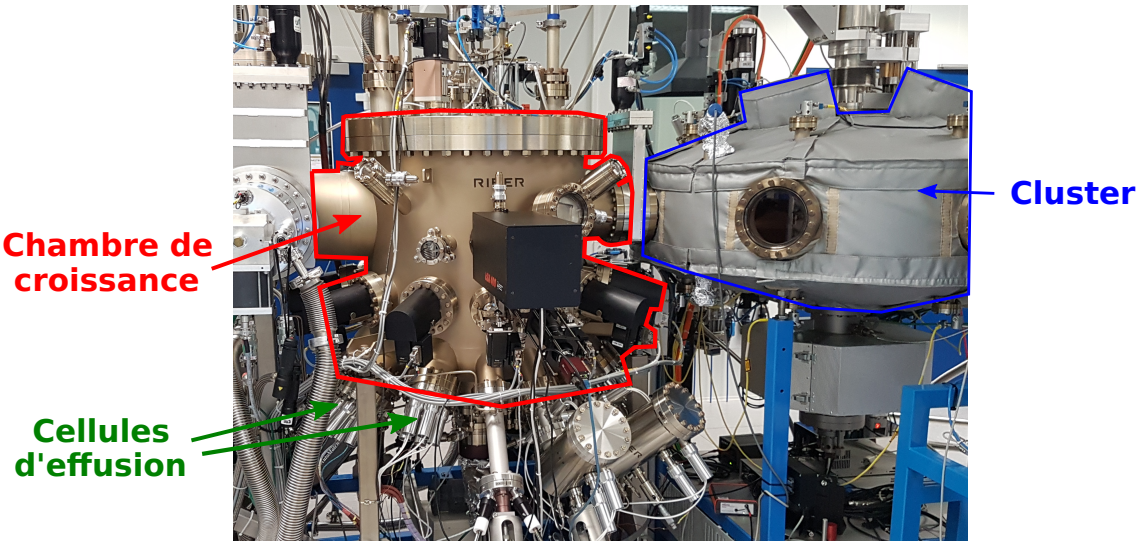

FIGURE 3.1 : Photo du bâti RIBER412 situé dans la salle blanche du LAAS-CNRS.

Afin de contrôler la croissance des nitrures dilués en temps réel, nous avons recours à des techniques de caractérisation *in-situ* telles que le RHEED et le suivi

de courbure. Cette dernière technique a été développée au LAAS, elle consiste à projeter une matrice de points sur la surface du wafer épitaxié et à analyser la distorsion que subit l'image après réflexion [1]. Comme le montre la Figure 3.2 a), une couche épitaxiée en accord de maille sur son substrat n'engendre aucune contrainte et ne provoque pas de déformation de la surface. Le faisceau de lumière est alors réfléchi sans subir de modification.

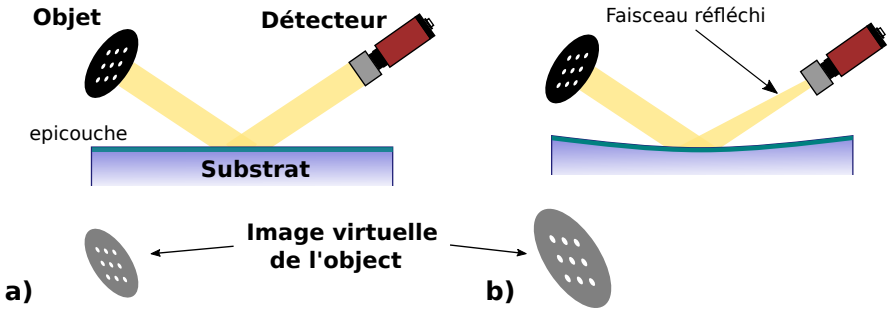

FIGURE 3.2 : Schéma du principe de fonctionnement du suivi de courbure *in-situ* pour a) une couche accordée en maille et b) une couche épitaxiée sous tension.

Cependant, la croissance d'InGaAsN ne se fait en accord de maille que lorsque le ratio entre le flux d'indium et le flux d'azote vaut ≈ 2.8. Une concentration en azote trop faible par rapport à l'indium mène à une contrainte en tension et à une déformation concave de la couche épitaxiée, comme le montre la Figure 3.2 b). Le faisceau est alors focalisé et la matrice de points image déformée. Cette distorsion est par la suite analysée afin de remonter au rayon de courbure de la couche et à la contrainte de croissance.

Au cours de cette thèse, nous avons épitaxié des structures cellule solaire et des couches épaisses (dites *bulk*) d'InGaAsN afin de réaliser des caractérisations matériau. Nous avons également fait croitre une cellule tandem GaAs/InGaAsN dont la structure est donnée en Figure 3.3.

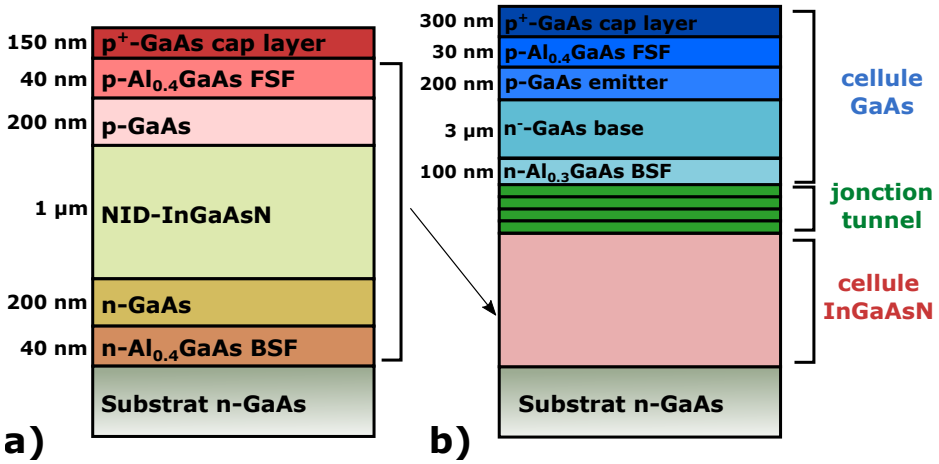

FIGURE 3.3 : a) Structure épitaxiale des cellules solaires InGaAsN. b) Structure épitaxiale d'une cellule tandem GaAs/InGaAsN intégrant une double hétéro-jonction tunnel.

TABLEAU 3.1 : Conditions de croissance des couches d'InGaAsN

Structure	Nom	N (%)	T_g (°C)	As/III	vit. croissance (μm/h)
Cellule solaire	A1	1.6	465	12 (+Bi)	0.3
	A2			12	
	A3		445	10	
	A4		485		
	A5	2.0	430	7.5	0.15
	A6	1.6	465	12	0.3
Couche bulk	B1	2	465	11	0.3
	B2		465	8	
	B3	2.3	430	7.5	0.15
	B4	1.2	465	12	0.3
Sous-cellule (tandem)	T1	2	430	7.5	0.15

Afin d'étudier l'impact des conditions de croissance sur les propriétés de l'InGaAsN, nous avons changé ces dernières d'un échantillon à l'autre, comme le montre le Tableau 3.1.

3.1.2 Défauts microscopiques de croissance

Durant notre dernière campagne d'épitaxie, nous avons remarqué une très importante densité de défauts ovales à l'issue de nos croissances de GaAs. Les défauts ovales sont des structures orientées dans la direction [110] ayant pour origine la croissance de plans secondaires provoquée par la contamination de la surface pendant ou avant la croissance (Figure 3.4 a) et b)). Certains auteurs mettent en cause une contamination au carbone lors de l'étape de préparation du substrat ou lors de son transfert dans le bâti [2, 3]. D'autres évoquent une contamination de particules de gallium (Ga ou Ga_2O) en provenance directe de leur cellule d'effusion [4, 5].

Comme nous pouvons le voir sur la Figure 3.4 c), nous avons identifié des gouttelettes de gallium présentes sur le bord du creuset de la cellule Ga6. Une lente procédure de nettoyage de ce creuset a été lancée et nous avons décidé d'utiliser la cellule d'effusion Ga11 pour compléter notre campagne de croissance. A l'aide de cette dernière, la densité de défauts ovales a pu être fortement diminuée, ce qui a confirmé Ga6 comme étant la source de contamination.

D'autre part, nous avons eu l'occasion de voir de très étranges défauts sur nos échantillons d'InGaAsN. Des caractérisations au microscope électronique à balayage (MEB) et au microscope à force atomique (AFM) ont permis d'observer des alignements de "*crevasses*" orientées dans la direction [110] (Figure 3.5).

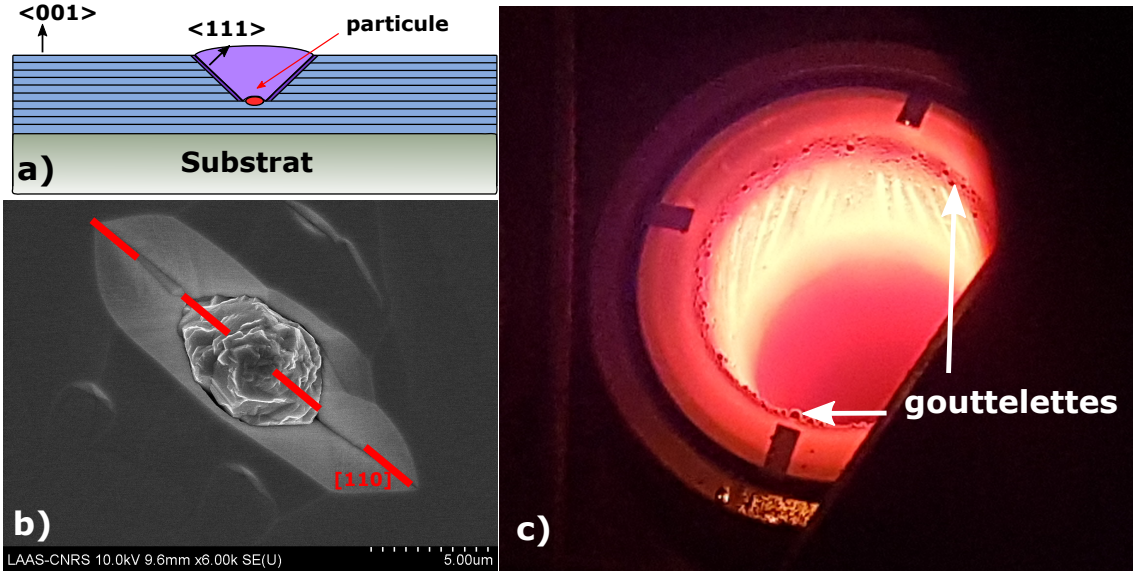

FIGURE 3.4 : a) Structure d'un défaut oval dans le GaAs, b) Image MEB d'un défaut ovale allongé dans la direction [110], c) Photo du creuset de la cellule Ga6 et de ces gouttelettes.

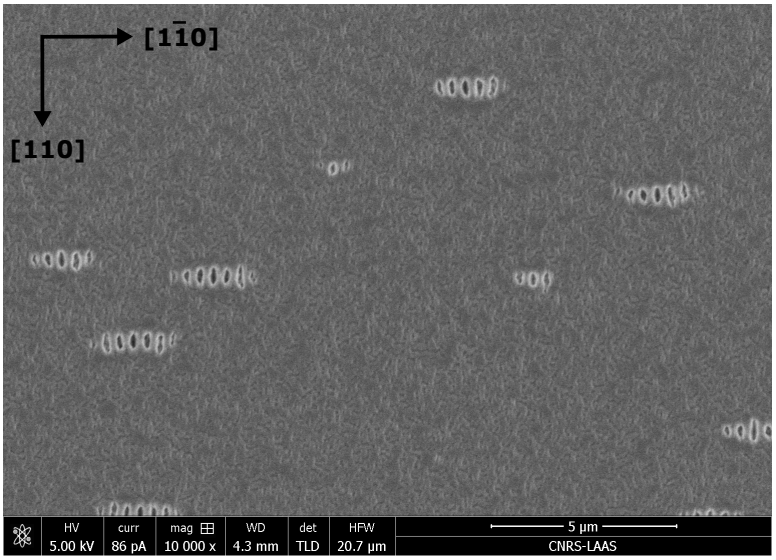

FIGURE 3.5 : Image MEB de défauts auto-répliqués dans l'InGaAsN.

Ces défauts apparaissent très majoritairement en nombre impair et une coupe transverse FIB (focused ion beam) a révélé dans ces arrangements une symétrie autour d'un premier défaut central. De plus, tous ces défauts sont espacés périodiquement et ont a leur base la même structure que le défaut originel. Nous avons pour cela décidé de les appeler "défauts auto-répliqués".

Notre hypothèse principale concernant la formation de ces défauts repose en premier lieu sur un évènement ponctuel de contamination ou d'apparition d'hétérogénéités en surface. Cependant, contrairement aux défauts ovales, ces défauts n'apparaissent que dans l'InGaAsN. Cela laisse à penser que le germe hétérogène

est causé par une ségrégation d'atomes d'azote ou un dommage engendré par une espèce énergétique provenant de la cellule plasma. Le caractère périodique de la réplication de ces défauts pourrait survenir de la création d'un champ de contrainte localement compensé par l'apparition d'un second défaut. Cette explication est toutefois largement spéculative. Des caractérisations de cathodoluminescence, de micro-photoluminescence ou d'EDX permettraient de vérifier l'état de contrainte local en dessous de l'échelle microscopique.

3.2 Impact des conditions de croissance sur les propriétés matériau de l'InGaAsN

3.2.1 Caractérisations structurelles

Comme nous l'avons dit dans la partie précédente, nous avons surveillé la croissance en temps réel avec l'outil de suivi de courbure. Connaissant la vitesse de croissance des nitrures dilués, l'historique de mesure peut se convertir en profil de courbure le long de la couche épitaxiée. Comme le montre la Figure 3.6, nous pouvons déduire de l'évolution de cette courbure une valeur de teneur en azote. Il apparait ainsi que les variations abruptes de contrainte dans A1 mènent à de larges oscillations dans sa composition en azote. Toutefois, la caractérisation aux rayons X de cette couche a montré que l'InGaAsN avait été globalement épitaxié en accord de maille sur son substrat.

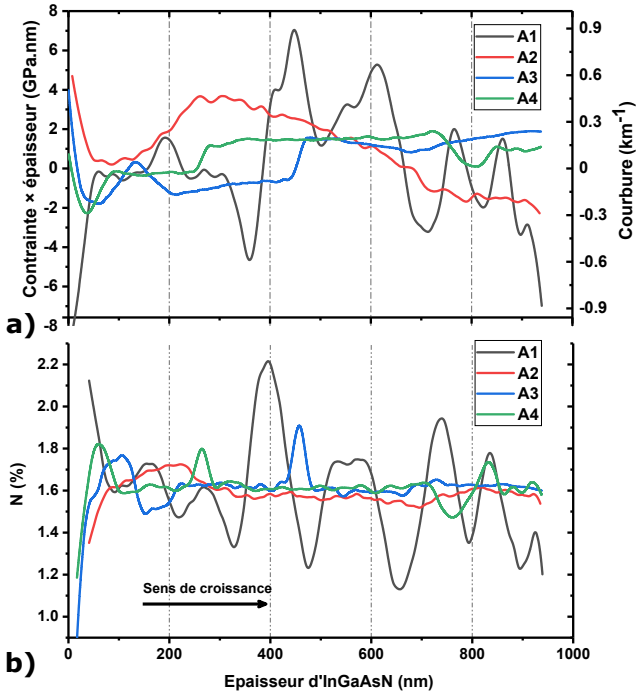

FIGURE 3.6 : a) Profil contrainte×épaisseur des absorbeurs InGaAsN des quatre cellules solaires A1, A2, A3 et A4. b) Profil de composition en azote déduit de a).

Des caractérisations par spectrométrie de masse des ions secondaires (SIMS) ont par ailleurs permis de vérifier les compositions des alliages épitaxiés. Un très bon accord est observé entre les teneurs en indium visées et mesurées mais nous constatons un décalage significatif pour l'azote, possiblement dû à l'incertitude de mesure SIMS. Les résultats SIMS ont par ailleurs mis en évidence des contaminations au carbone et à l'oxygène lors de la croissance.

3.2.2 Caractérisations optiques

Pour déterminer les propriétés optiques des couches épitaxiées, nous avons utilisé la technique de photoluminescence (PL). Les couches bulk ont été mesurées au LAAS avec un laser 488 nm et les absorbeurs des cellules solaires ont été analysés au LPCNO à l'aide d'un laser 950 nm.

La Figure 3.7 présente les spectres de photoluminescence des couches bulk B1 et B2, avant (as-grown) et après une étape de recuit de 30 secondes à 750 °C. Nous pouvons voir sur cette figure l'impact de la surpression d'arsenic : B1 et B2 ont été épitaxiés dans les mêmes conditions mais avec *As/III*=11 et *As/III*=8, respectivement. D'autre part, il apparait clairement sur cette figure que les recombinaisons radiatives sont promues par le recuit thermique. Cela indique que des centres de recombinaison non radiative issus de la croissance ont été guéris.

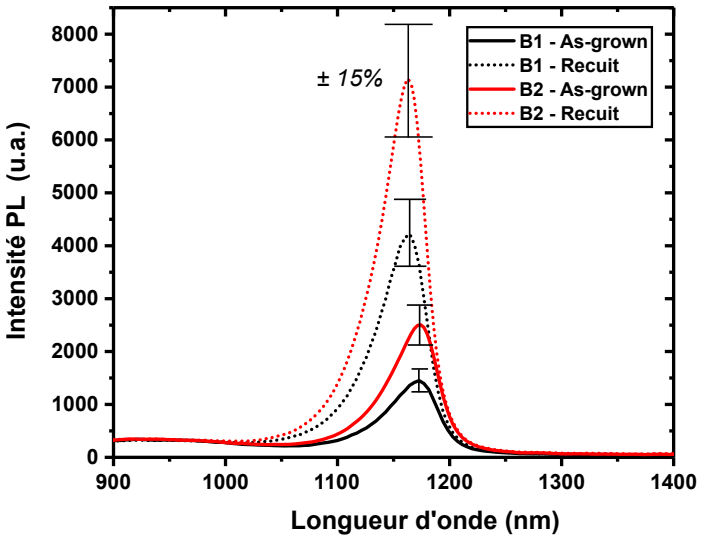

FIGURE 3.7 : Spectres PL de B1 et B2, mesurés à 300 K avant et après recuit.

Globalement, nous avons remarqué que l'intensité PL diminuait avec la concentration en azote, ce qui montre la prépondérance des défauts associés à cet atome. Une très forte sensibilité du signal PL à la surpression d'arsenic a également été observée dans les structures cellules solaires, pour lesquelles il est bénéfique de garder un ratio *As/III* supérieur à 10. Ce décalage de la surpression

en arsenic optimale comparé aux couches bulks s'explique par la différence de concentration en azote.

3.2.3 Caractérisations électriques

Puisque les cellules d'InGaAsN reposent sur la structure *pin*, il est capital de connaître le dopage de la couche non intentionnellement dopée (NID). Pour avoir accès à cette information, nous avons réalisé des mesures d'ECV (electrochemical capacitance-voltage) en collaboration avec le III-V Lab. La Figure 3.8 montre les niveaux de dopages *n* au sein de 5 cellules solaires.

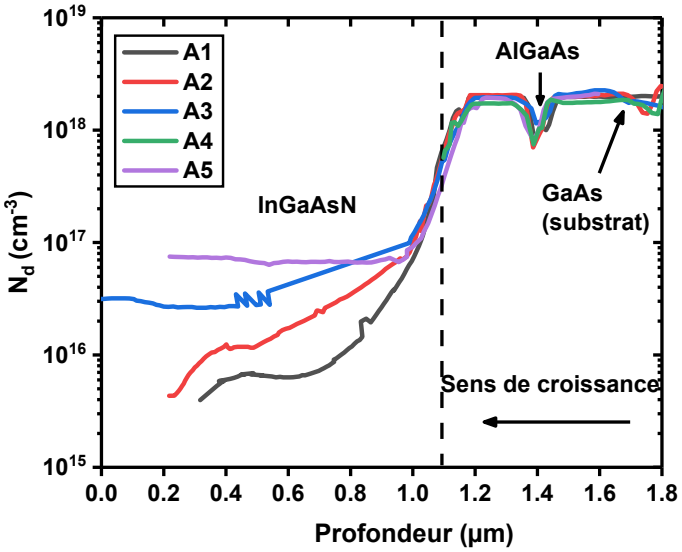

FIGURE 3.8 : Profil de dopage *n* des cellules solaires.

Il apparait à travers cette figure que le dopage résiduel (BGCC) est de type *n* pour toutes les cellules et que sa concentration dépend fortement des conditions de croissance. Le dopage résiduel de A4 se trouve en dessous de la limite de détection et nous mettons en évidence une anti-corrélation entre la température de croissance et le niveau de dopage NID. Des mesures d'ECV sur des couches bulks on par ailleurs montré une tendance du BGCC à augmenter avec la composition en azote.

La mesure du dopage résiduel renseigne sur des défauts donneurs ou accepteurs qui sont généralement superficiels. Nous avons donc caractérisé nos couches d'InGaAsN par DLTS afin d'obtenir des données complémentaires sur la présence de défauts profonds. La Figure 3.9 montre les spectres de DLTS des échantillons B1 et B2, avant et après recuit.

Nous pouvons tout d'abord remarquer que l'intensité DLTS, proportionnelle à la concentration en défauts, dépend très fortement du ratio *As/III*. La guérison de défauts de croissance par recuit thermique est par ailleurs clairement visible

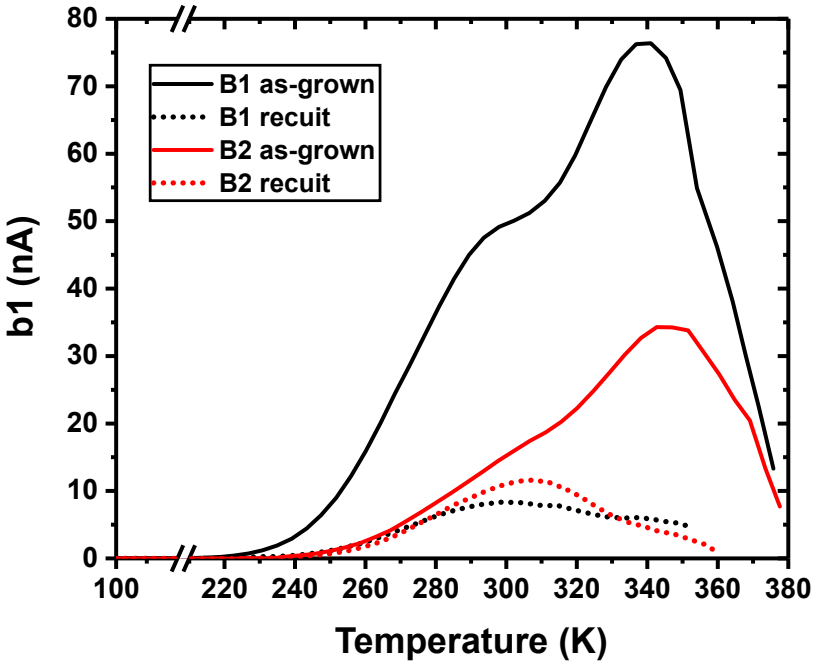

FIGURE 3.9 : Spectres DLTS de B1 et B2, avant et après recuit.

pour chacun de ces échantillons. Une déconvolution de ces spectres DLTS nous a permis de faire apparaître 2 pics pour lesquels nous avons pu tracer une régression $Ln(e_n/T^2)$ en fonction de 1000/T. Nous avons ainsi calculé une énergie d'activation environ égale à 0.6 eV pour E1 et 0.75 eV pour E2. Nous sommes donc en présence de défauts profonds de milieu de bande interdite qui constituent probablement d'important centres de recombinaisons non radiatives.

Références

[1] A. Arnoult and J. Colin, "Magnification inferred curvature for real-time curvature monitoring," *Scientific Reports*, vol. 11, no. 1, pp. 1–11, 2021.

[2] M. Bafleur, A. Munoz-Yague, and A. Rocher, "Microtwinning and growth defects in GaAs MBE layers," *Journal of Crystal Growth*, vol. 59, no. 3, pp. 531–538, 1982.

[3] S.-L. Weng, C. Webb, Y. Chai, and S. Bandy, "Particulates : An origin of GaAs oval defects grown by molecular beam epitaxy," *Applied physics letters*, vol. 47, no. 4, pp. 391–393, 1985.

[4] S.-L. Weng, "Ga2O3 : The origin of growth-induced oval defects in GaAs molecular beam epitaxy," *Applied physics letters*, vol. 49, no. 6, pp. 345–347, 1986.

[5] K. Takahashi, H. Kawada, S. Ueda, M. Furuse, and S. Shirayone, "The origins and elimination of oval defects in GaAs layers grown by molecular beam epitaxy," *Journal of Vacuum Science & Technology A : Vacuum, Surfaces, and Films*, vol. 9, no. 3, pp. 854–857, 1991.

Chapitre 4

Développement de cellules solaires InGaAsN pour intégration en MJSC

4.1 Procédé de fabrication

A l'issue de l'épitaxie des couches de la structure cellule solaire, nous réalisons des étapes de process technologique en salle blanche du LAAS-CNRS. Le process est réalisé sur des quarts de wafer 4 pouces.

Recuit post-croissance

Un recuit thermique des nitrures dilués est généralement effectué afin de guérir des défauts de croissance. Nous avons étudié l'impact d'un recuit de 750 °C de 30 secondes sous atmosphère N_2 à travers des mesures de rendement quantique présentées dans la prochaine section. Cependant, nous avons décidé de développer un procédé de fabrication ne reposant pas sur un recuit post-croissance et la majorité des cellules étudiées dans ce chapitre sont donc non-recuites, dites *as-grown*.

Métallisation avant Ti/Au

La première étape technologique réalisée en salle blanche du LAAS est le dépôt de la grille métallique en face avant de la cellule solaire. Nous avons eu recours à un procédé de photolithographie qui nous a permis de définir le négatif du motif de la grille, comme le montre la Figure 4.1 a). Un dépôt de titane (50 nm) suivi d'or (200 nm) est ensuite réalisé par évaporation thermique (Figure 4.1 b)). Enfin, la résine est dissolue dans de l'acétone dans un procédé appelé "lift-off", révélant en face avant la grille métallique (Figure 4.1 c)).

Le design de notre grille métallique repose sur deux *busbars* connectées par de fines lignes de métal appelées *fingers*. Ces fingers permettent la collection des porteurs dans la couche *window* mais absorbent une partie de la lumière incidente. Il y a donc un compromis entre collecte et absorption et nous avons opté pour un taux d'ombrage égal à 3,33 % pour les cellules caractérisées dans ce chapitre.

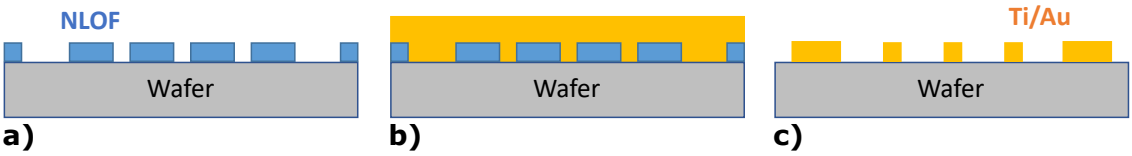

FIGURE 4.1 : Schéma des étapes de métallisation de la face avant a) après lithographie b) après évaporation thermique et dépôt de Ti/Au et c) après le retrait de la résine (lift-off).

Enfin, une étude de TLM (transfer length method) a montré une résistance spécifique de contact très faible (1.01×10^{-6} $\Omega.cm^2$) entre le cap layer p^+-GaAs et la métallisation Ti/Au.

Gravure des mésas

Afin d'isoler électriquement chaque diode et chaque cellule solaire du wafer, et dans le but de définir précisément l'aire de nos cellules, nous avons gravé des mésas entre chaque structure. Après avoir réalisé une étape de photolithographie permettant de protéger l'aire active de nos cellules solaires, nous avons immergé notre wafer dans une solution d'acide phosphorique. La résine est enfin retirée une fois les mésas gravés.

Gravure du cap layer

Le cap layer est une couche de GaAs très dopée permettant d'obtenir un contact ohmique de faible résistivité en face avant. Son fort dopage est cependant préjudiciable au fonctionnement de la cellule car il engendre de l'absorption porteur libre réduisant le nombre de photons atteignant l'absorbeur InGaAsN. Il est donc essentiel de retirer cette couche une fois la métallisation effectuée. Pour ce faire, nous utilisons une solution d'acide citrique offrant une haute sélectivité de gravure du GaAs par rapport à l'AlGaAs (window).

Métallisation arrière AuGeNi/Au

Contrairement à la face avant dont le contact ohmique est rendu possible grâce à une couche épitaxiée extrêmement dopée, le contact électrique du substrat modérément dopé ($n = 2 \times 10^{18}$ cm^{-3}) ne peut pas se faire avec Ti/Au. Afin d'éviter un contact Schottky typique d'une interface semi-conducteur/métal, nous déposons par pulvérisation cathodique un alliage AuGeNi. Lorsque cette métallisation est recuite, les atomes de germanium diffusent à la surface du GaAs et se comportent comme des donneurs, ce qui augmente le dopage n du semi-conducteur à l'interface et résulte en un contact ohmique.

Le recuit de cette métallisation est une étape délicate car la formation de phases AuGe et AuGa à l'interface peut dégrader la morphologie du contact. Nous avons donc conduit une campagne d'optimisation du recuit RTP (rapid thermal processing) en mesurant la caractéristique I-V sous obscurité d'échantillons recuits pendant 90 secondes à différentes températures. Comme nous pouvons le voir avec la Figure 4.2, nous obtenons la plus faible résistance de contact (inverse de la pente $I = f(U)$) pour un RTP de 350 °C. Nous avons donc choisi ces

paramètres de recuit (90 secondes à 350 °C) pour notre procédé de fabrication de cellules solaires.

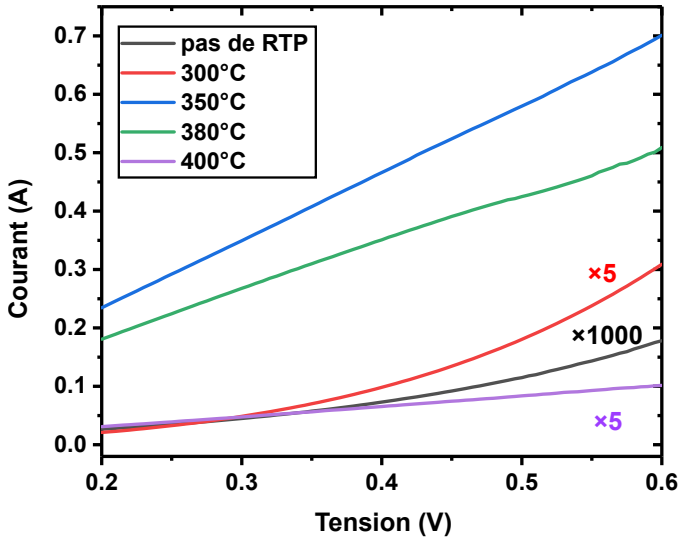

FIGURE 4.2 : Caractéristiques *I-V* des jonctions GaAs/AuGeNi recuites à différentes températures.

A l'issue de cette étape de métallisation arrière, la structure finale de la cellule solaire est obtenue, comme le montre la Figure 4.3.

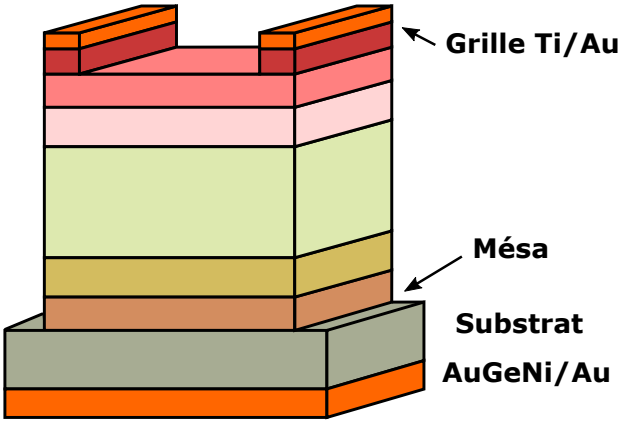

FIGURE 4.3 : Structure finale de la cellule solaire. Les dimensions ne sont pas à l'échelle.

Montage sur un porte-échantillon

Afin de faciliter les campagnes de caractérisation et d'irradiation, le quart de wafer est clivé et les cellules solaires d'1 cm^2 sont récupérées. Ces cellules sont alors collées sur des porte-échantillons d'AlN dont les dimensions sont données en Figure 4.4 a). Les pads en or présents sur ce porte-échantillon permettent le report des contacts après une étape de wire-bonding (Figure 4.4 b)).

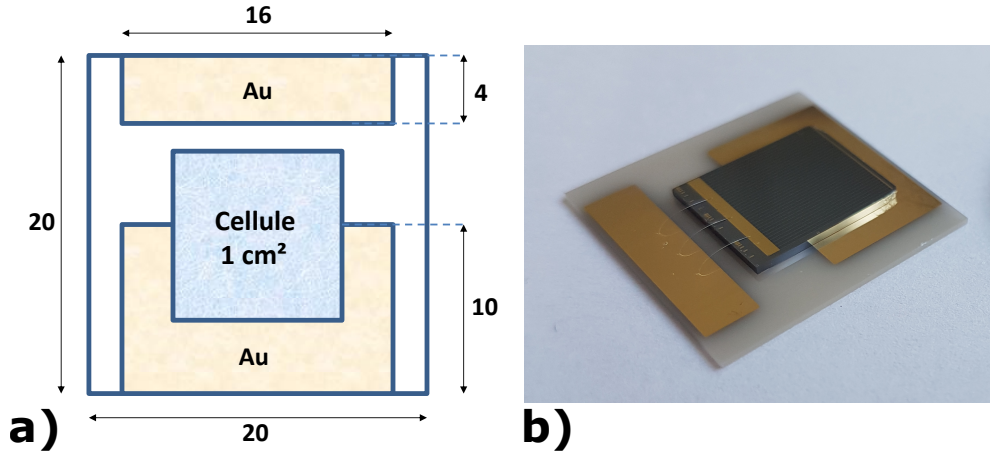

FIGURE 4.4 : a) Dimensions (en *mm*) du porte-échantillon d'AlN b) Photo d'une cellule solaire montée sur son porte-échantillon et dont les contacts sont reportés par wire-bonding.

4.2 Caractérisation des cellules solaires

4.2.1 Réponse spectrale

Le rendement quantique externe (EQE) est définie, pour une longueur d'onde donnée, comme le rapport entre le nombre de porteurs collectés par une cellule solaire en condition de court-circuit (V=0 V) et le nombre de photons incidents. Nous avons mesuré l'EQE de nos cellules solaires ainsi que leur réflectance afin d'obtenir leur rendement quantique *interne* (IQE).

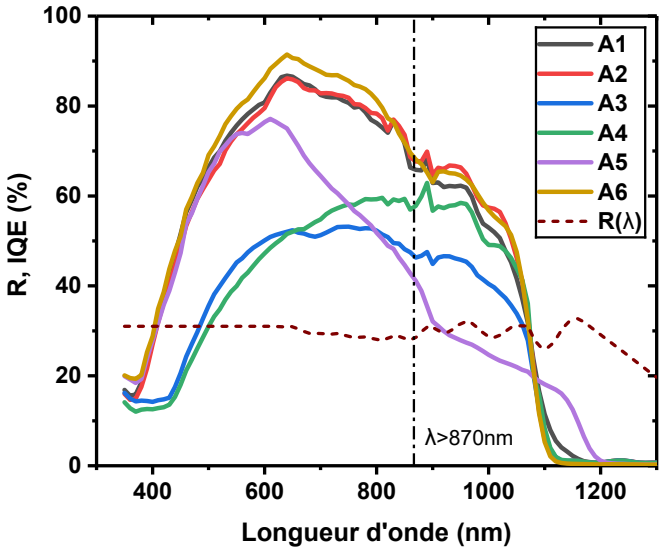

FIGURE 4.5 : Spectres de rendement quantique interne des cellules solaires InGaAsN et réflectance spectrale associée.

Comme le montre la Figure 4.5, les cellules A1, A2 et A6, épitaxiées avec une

plus haute surpression d'arsenic, offrent une meilleure réponse spectrale. Nous remarquons également un rendement quantique faible pour la cellule A5, dont la teneur en azote est plus importante. Cette observation est en adéquation avec les mesures PL et DLTS réalisées dans le chapitre précédent montrant une corrélation entre la densité de défauts et la concentration en azote.

D'autre part, nous observons une différence importante d'IQE entre les gammes spectrales λ<870 nm et λ>870 nm. Cette disparité s'explique par l'absorption de photons d'énergie supérieure à 1.42 eV (≡ 870 nm) dans l'émetteur de GaAs qui contribue à la collecte totale de la structure. Pour λ>870 nm, le rendement quantique n'est lié qu'à la collecte dans l'absorbeur InGaAsN. Dans cette gamme, la cellule A4 dispose d'un important rendement quantique comparée à la cellule A3, épitaxiée avec le même ratio *As/III*. Cette différence provient de la large zone de charge d'espace (ZCE) de A4 qui lui permet de collecter les porteurs photogénérés loin de la jonction p-GaAs/n^--InGaAsN.

Les spectres de rendement quantique externe sont également utilisés pour déterminer la densité courant de court-circuit J_{sc} que peut fournir une cellule sous un éclairement donné. Pour ce faire, nous intégrons la réponse spectrale SR des cellules en s'appuyant sur les deux équations suivantes :

$$SR(\lambda) = EQE(\lambda) \times \frac{\lambda q}{hc} \tag{4.1}$$

$$J_{sc} = \int_{\lambda_1}^{\lambda_g} SR(\lambda) \times H_0(\lambda)\, d\lambda \tag{4.2}$$

où H_0 correspond à l'irradiance spectrale, λ_1 à la limite basse du spectre et λ_g à la longueur d'onde de coupure de la cellule solaire. Les valeurs de J_{sc} calculées avec ces EQE sont reprises et récapitulées dans la Section *Mesure courant-tension sous éclairement*.

Nous avons également étudié l'effet du recuit thermique sur les rendements quantiques de nos cellules. La Figure 4.6 montre l'effet antinomique du RTP sur les cellules A3 et A4.

Des mesures ECV ont montré que les améliorations et dégradations respectives des échantillons A3 et A4 s'expliquent par de larges variations du dopage résiduel. Le BGCC de la cellule A3 est en effet divisé par 6 après recuit, ce qui élargit sa zone de dépletion et améliore la collection de porteurs. En revanche, le dopage résiduel de A4 est approximativement multiplié par 10 après RTP, ce qui explique la chute considérable de son IQE.

Enfin, nous avons mesuré le rendement quantique des cellules tandem GaAs/InGaAsN. Lors de la mesure d'une des sous-cellules, il est nécessaire de biaiser optiquement la seconde de telle sorte à ce qu'elle ne soit pas courant-limitante. Nous utilisons pour cela un système de biais optique constitué d'une lampe Xenon associée à des filtres passe-haut et passe-bas. Un condensateur est

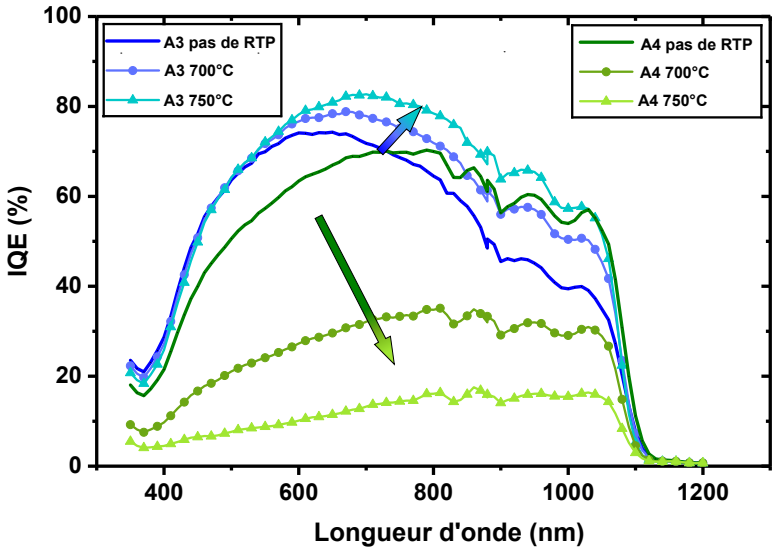

FIGURE 4.6 : Impact du recuit thermique sur les spectres d'IQE de A3 et A4.

également connecté en série à la cellule tandem afin de contrebalancer la polarisation induite par la sous-cellule biaisée.

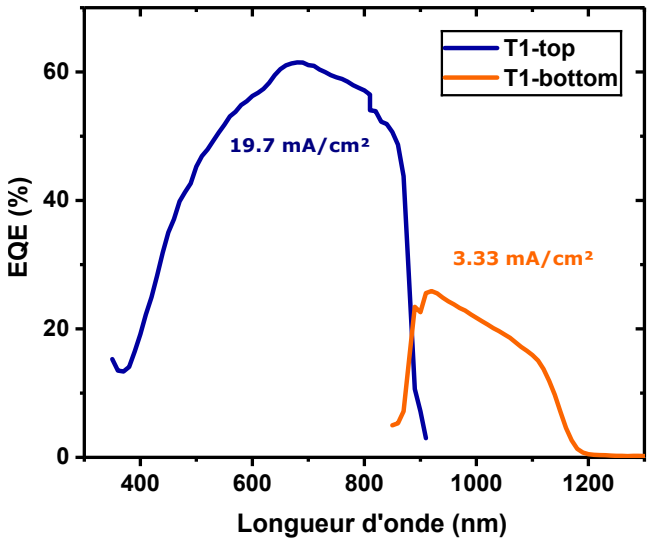

FIGURE 4.7 : Rendement quantique externe des sous-cellules de la tandem.

Nous pouvons voir dans la Figure 4.7 une différence de rendement quantique considérable entre la top cell (GaAs) et la bottom cell (InGaAsN) de la tandem T1. Les densités de courant de court-circuit présentées sur la figure indiquent un très large désaccord de courant qui souligne une architecture et un matériau non-optimisés. En effet, l'épaisseur de la top cell de GaAs pourrait-être réduite de manière à transmettre une partie de la lumière visible (<870 nm) à la sous-cellule InGaAsN. Par ailleurs, la croissance de l'$InGaAsN_{0.02}$ de la bottom cell n'est pas optimisée et cette dernière affiche un faible rendement quantique, similaire à la cellule A5. Il apparait alors nécessaire d'identifier les paramètres de croissance

menant à un faible BGCC et une longue durée de vie des porteurs minoritaires dans l'InGaAsN$_{0.02}$.

4.2.2 Mesure courant-tension sous obscurité

Nous avons étudié les caractéristiques courant-tension obtenues sous obscurité afin de déterminer les propriétés de diode de nos cellules solaires (Figure 4.8). Les résistances série (R_s) et parallèle (R_{sh}, appelée résistance de shunt) ont été calculées en prenant l'inverse des pentes des caractéristiques à $V = V_{oc}$ et $V = 0$, respectivement. Les valeurs de ces résistances ainsi que des densités de courant de saturation sont données en Table 4.1.

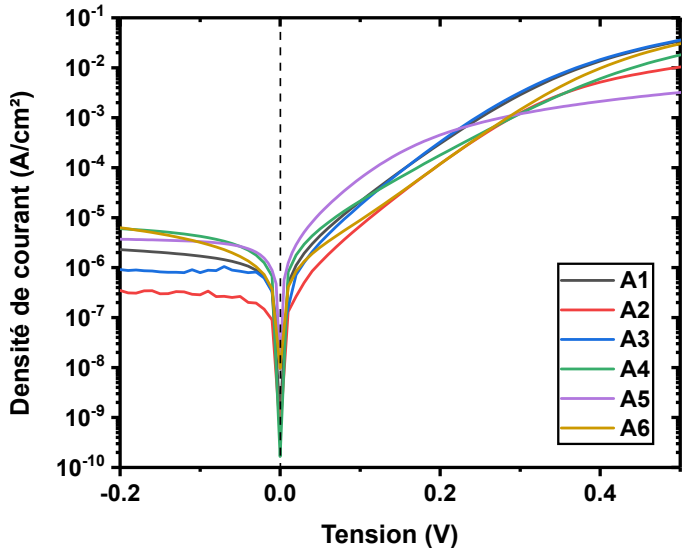

FIGURE 4.8 : Caractéristiques *I-V* sous obscurité des cellules solaires d'InGaAsN mesurées à température ambiante. Les courants inverses sont donnés en valeurs absolues.

TABLEAU 4.1 : Propriétés de diode des six cellules solaires InGaAsN

	A1	A2	A3	A4	A5	A6
$R_{sh}(\Omega/cm^2)$	22500	93400	29800	13100	9400	25400
$R_s(\Omega/cm^2)$	10.9	22.1	15.0	24.5	122	9.1
$J_0(\mu A/cm^2)$	1.2	0.32	0.78	2.2	5.1	0.7

Nous remarquons une faible résistance de shunt et une résistance série très importante pour A5. Ces valeurs de R_{sh} et R_s sont observées dans toutes les cellules solaires issues du wafer A5. Le procédé de fabrication technologique étant identique pour toutes les cellules solaires, ces résistances parasites ne peuvent provenir que de l'absorbeur InGaAsN de concentration en azote supérieure aux autres composants. Le courant de saturation dans A5 est par ailleurs plus élevé que dans les autres échantillons, ce qui indique un taux de recombinaison plus important.

4.2.3 Mesure courant-tension sous éclairement

La Figure 4.9 présente les caractéristiques courant-tension des cellules solaires InGaAsN obtenues sous AM0>870 nm. Cette illumination correspond à la partie du spectre transmise à la sous-cellule d'InGaAsN en condition d'intégration MJSC.

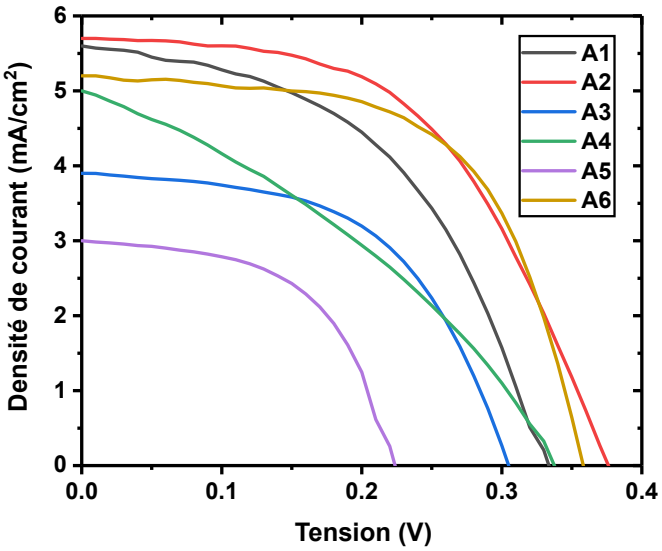

FIGURE 4.9 : Caractéristiques *J-V* des six cellules solaires InGaAsN mesurées sous éclairement AM0>870 nm.

Tout comme le rendement quantique, nous observons de meilleurs couples courant-tension pour les cellules épitaxiées avec *As/III*=12. En particulier, A2 peut photogénèrer jusqu'à 5.75 mA/cm^2 en condition d'intégration et sans couche anti-reflet (ARC). Comme indiqué en Table 4.2, A2 est également l'échantillon présentant la plus haute tension de circuit-ouvert (0.375 V).

Le faible *FF* de la cellule A4 s'explique par son régime de collecte par effet de champ, dépendant fortement de l'épaisseur de la zone de dépletion. A mesure que la tension aux bornes de la cellule augmente, la ZCE rétrécit, ce qui fait chuter la densité de courant. Les mesures *J-V* réalisées sous obscurité démontrent par ailleurs que le faible *FF* n'est pas dû à du shunt dans la cellule.

TABLEAU 4.2 : Propriétés des six cellules solaires InGaAsN sous éclairement AM0>870 nm.

	A1	**A2**	**A3**	**A4**	**A5**	**A6**
$J_{sc}(A/cm^2)$	5.59	5.75	3.86	5.02	2.96	5.21
$V_{oc}(V)$	0.335	0.375	0.305	0.340	0.225	0.355
$FF(\%)$	48.3	52.6	54.1	34.6	58.9	60.4

Enfin, nous remarquons que la cellule A5, de concentration en azote supé-

rieure aux autres échantillons, offre de plus faibles valeurs de J_{sc} et de V_{oc}, ce qui témoigne d'un taux de recombinaison plus élevé. La Figure 4.10 présente les courbes *J-V* des cellules tandem et GaAs obtenues sous AM0 et de la cellule A5 obtenue sous AM0>870 nm.

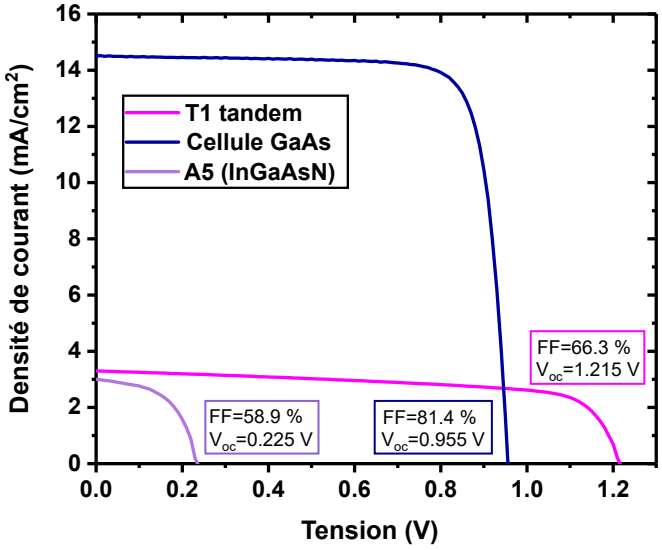

FIGURE 4.10 : Caractéristiques *J-V* de la cellule tandem T1 ainsi que des cellules monojonction GaAs et InGaAsN. Les réponses *J-V* sont obtenues sous éclairement AM0 pour T1 et la cellule GaAs et sous AM0>870 nm pour la cellule InGaAsN A5.

Nous retrouvons sur cette figure le désaccord de courant pénalisant la cellule tandem. En outre, la caractéristique *J-V* de cette dernière présente une large valeur de tension de circuit ouvert approximativement égal à la somme des V_{oc} des deux sous-cellules connectées en série.

4.3 Conclusion

Les mesures *I-V* ainsi que les spectres de rendement quantiques montrent que les performances des cellules solaires d'InGaAsN sont majoritairement conditionnées par deux paramètres : le dopage résiduel et le taux de recombinaison. Les cellules épitaxiées avec un ratio *As/III* égal à 12 présentent de relativement faibles BGCC et de plus hautes intensités de photoluminescence ce qui explique leur meilleures caractéristiques *I-V*.

La cellule A2 peut photogénérer jusqu'à 5.75 mA/cm^2 en condition d'intégration et pourrait atteindre un J_{sc} égal à 7.96 mA/cm^2 avec un ARC parfait. Cette valeur ne permettant pas l'accord de courant au sein d'une MJSC ($\approx$ 15 mA/cm^2), nous identifions 3 points à développer afin d'augmenter le photocourant de nos cellules :

- **Augmenter la composition en azote et indium** de l'alliage InGaAsN afin

de réduire son énergie de bande interdite et augmenter la longueur d'onde de coupure.

- Continuer l'**optimisation des conditions de croissance** de l'InGaAsN et plus spécifiquement pour N>2 %.
- Augmenter l'épaisseur de la couche active d'InGaAsN afin de limiter les pertes par transmission.

Chapitre 5

Étude de dégradation sous irradiation de cellules solaires InGaAsN

5.1 Matériel et méthode

Afin d'étudier la dégradation des cellules solaires InGaAsN développées au cours de cette thèse, nous avons utilisé deux accélérateurs de particules de type Van de Graaff. Les cellules ont été irradiées à l'ONERA dans l'enceinte MIRAGE, avec des électrons et des protons de 1 MeV. La Figure 5.1 a) montre quatre cellules solaires de 1 cm^2 ainsi que des échantillons de type couches bulk, fixés sur la platine d'irradiation. Cette platine de cuivre est ensuite montée dans l'enceinte MIRAGE comme illustré en Figure 5.1 b).

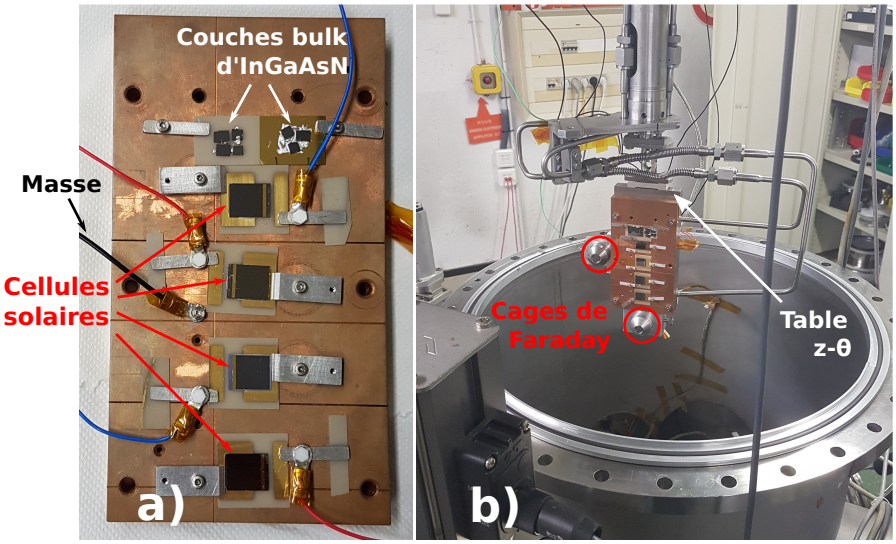

FIGURE 5.1 : a) Photo des échantillons fixés sur une platine de cuivre, b) Photo de la platine de cuivre introduite dans l'enceinte d'irradiation MIRAGE.

L'enceinte MIRAGE permet également des mesures *in-situ* de courant-tension sous éclairement AM0 et une thermorégulation de la platine de cuivre. Nous

avons eu recours à ces fonctionnalités lors de la deuxième et de la troisième campagne d'irradiation.

5.2 Analyse de dégradation de cellules InGaAsN sous électrons 1 MeV

La résistance des cellules solaires $InGaAsN_{0.016}$ aux électrons 1 MeV a été évaluée en irradiant des échantillons épitaxiés avec différentes conditions de croissance, provenant des wafers A1, A2, A3 et A4. Trois cellules solaires d'InGaAsN (A1a, A2a et A4a) ainsi qu'une cellule témoin GaAs (G1) ont tout d'abord été irradiées sous fluence cumulative, avec mesure *I-V ex-situ*. La dégradation de leur caractéristique *J-V* obtenue sous éclairement AM0 est présentée en Figure 5.2.

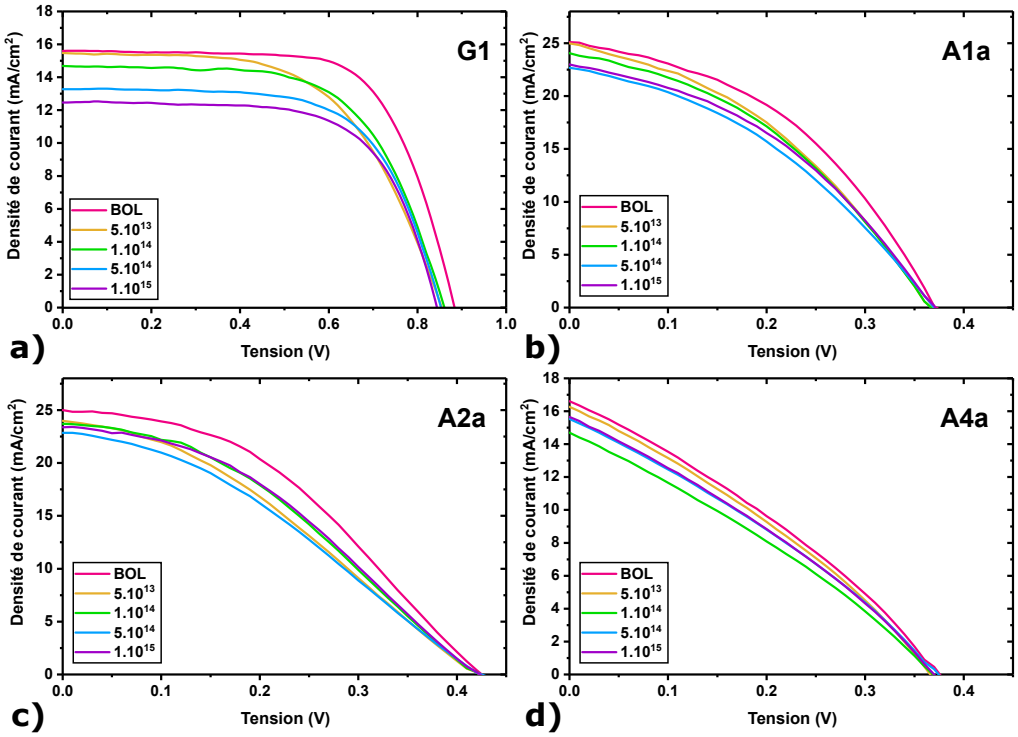

FIGURE 5.2 : Évolution des caractéristiques *J-V* mesurées sous illumination AM0 pour différentes fluences (e^-/cm^2), pour les échantillons G1, A1a, A2a et A4a.

La cellule de GaAs G1 affiche une dégradation monotone de sa courbe *J-V* et une chute de photocourant de 20.1 % après 10^{15} e^-/cm^2. Ce résultat est en accord avec les données trouvées dans la littérature [1, 2, 3]. D'un autre côté, il apparait que les cellules d'InGaAsN ne se détériorent que très peu sous irradiation électronique. De plus, la dégradation de leur photocourant n'est pas monotone et nous observons même une légère augmentation de ce paramètre lors de la dernière étape d'irradiation. Ce phénomène est illustré en Figure 5.3 à travers l'évolution des J_{sc} obtenus sous éclairement représentatif des conditions d'intégration (AM0>870 nm).

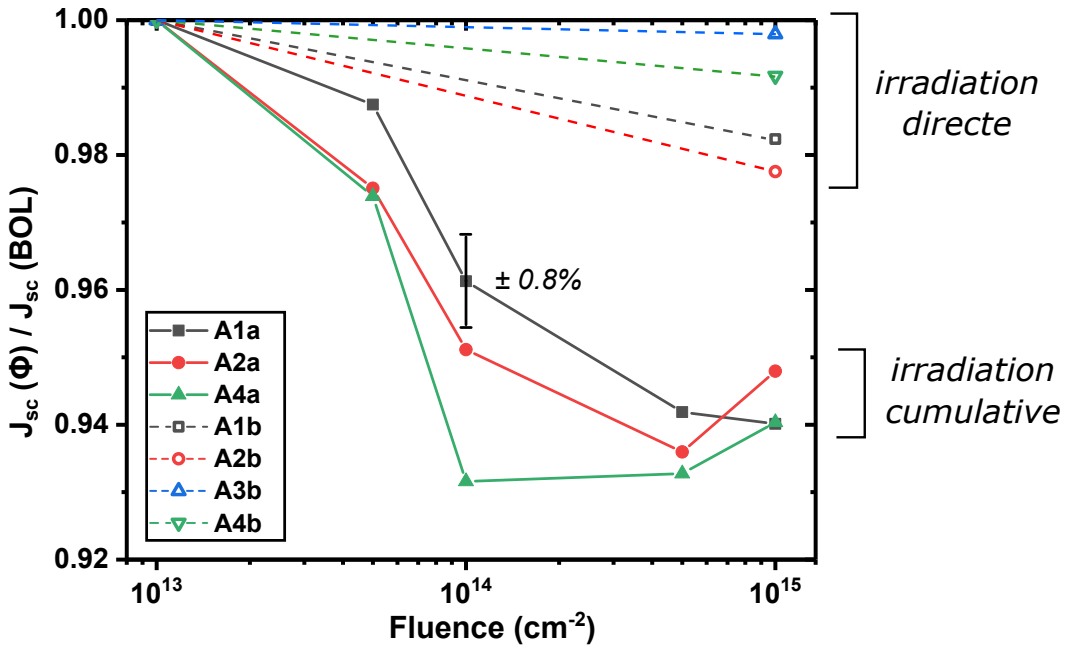

FIGURE 5.3 : Évolution du photocourant obtenu sous AM0>870 nm et normalisé par rapport à sa valeur BOL (beginning of life), en fonction de la fluence en électrons 1 MeV.

La Figure 5.3 présente également les données de dégradation correspondant à quatre cellules d'InGaAsN (A1b, A2b, A3b et A4b) directement irradiées à 10^{15} e^-/cm^2. Ces dernières cellules affichent un taux de dégradation significativement inférieur aux cellules irradiées par fluences successives. Nous attribuons cette différence au flux d'irradiation supérieur dans le cas de l'irradiation directe et de la dernière fluence étape de l'irradiation cumulative.

Les mesures de température réalisées durant la deuxième campagne d'irradiation ont révélé un échauffement des échantillons irradiés sous haut flux électronique. Puisque la diffusion atomique augmente avec la température, l'échauffement des échantillons favorise la recombinaison des défauts d'irradiation et de croissance. De plus, la diffusion atomique est facilitée par la présence de lacunes introduites sous irradiation [4], et la concentration en lacunes (hors-équilibre) dépend du courant d'irradiation. Il est donc cohérent que le taux de dégradation soit plus faible pour des cellules irradiées à plus haut flux électronique.

Par ailleurs, des phénomènes de guérison (*annealing*) des propriétés optoélectroniques ont été observés à travers des mesures de photoluminescence réalisées avant et après irradiation directe à 10^{15} e^-/cm^2 sur des couches bulk d'InGaAsN correspondant aux wafers B1 et B2. La Figure 5.4 montre en effet une amélioration de l'intensité PL des échantillons non recuits après irradiation, ce qui implique une guérison de centres de recombinaisons non radiatives.

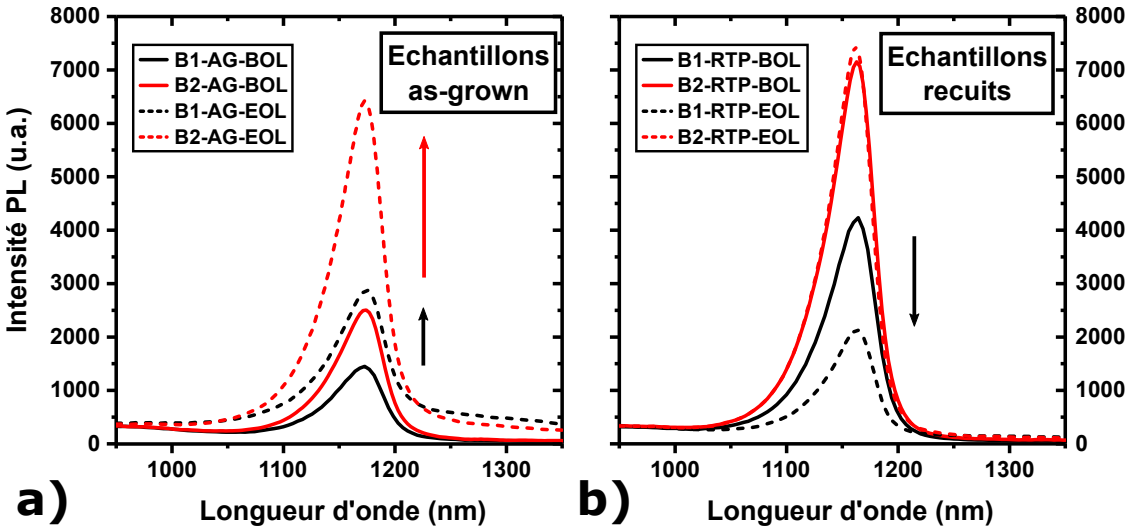

FIGURE 5.4 : Spectres de photoluminescence avant et après irradiation aux électrons 1 MeV (10^{15}/cm^2) pour des échantillons a) *as-grown* et b) recuits.

5.3 Analyse de dégradation de cellules tandem GaAs/InGaAsN sous électrons 1 MeV

Afin d'évaluer l'impact des électrons 1 MeV sur des sous-cellules d'InGaAsN intégrées au sein de MJSC, nous avons irradié une cellule tandem GaAs/InGaAsN ainsi que des cellules à mono-jonction représentatives des sous-cellules la composant. La Figure 5.5 montre la dégradation de la caractéristique *J-V* de la cellule tandem T1, de cellules d'InGaAsN as-grown et recuite (A5-AG et A5-RTP), et d'une cellule de GaAs (G2).

De manière similaire à la première campagne, nous observons une plus faible dégradation des cellules InGaAsN comparées à la cellule de GaAs. Ceci est dû à la différence de propriétés optoélectroniques des cellules avant irradiation : les cellules d'InGaAsN affichent de relativement hautes concentrations en défauts de croissance, ce qui les rend moins sensibles à l'introduction de défauts d'irradiation. Nous observons par ailleurs que les cellules d'InGaAsN irradiées lors de cette deuxième campagne se dégradent moins que leurs homologues de la première campagne. Cela s'explique par leur plus forte teneur en azote et par conséquent leur plus forte densité en défauts cristallins (voir Chapitre 3).

La dégradation de la cellule tandem T1 peut se décomposer en deux éléments principaux :

- La chute de sa tension de circuit ouvert correspond à l'augmentation du taux de recombinaison dans la top-cell de GaAs. Cette augmentation provoque une diminution du V_{oc} de la cellule de GaAs ce qui provoque une chute du V_{oc} global de la structure, puisque les sous-cellules sont connectées en série.

- La diminution du photocourant de la tandem correspond à une légère dégradation de la cellule courant-limitante, *i.e.* de la botom cell d'InGaAsN. Nous observons par ailleurs une dégradation similaire de photocourant pour les cellules A5-AG et A5-RTP, mesurées sous AM0>870 nm.

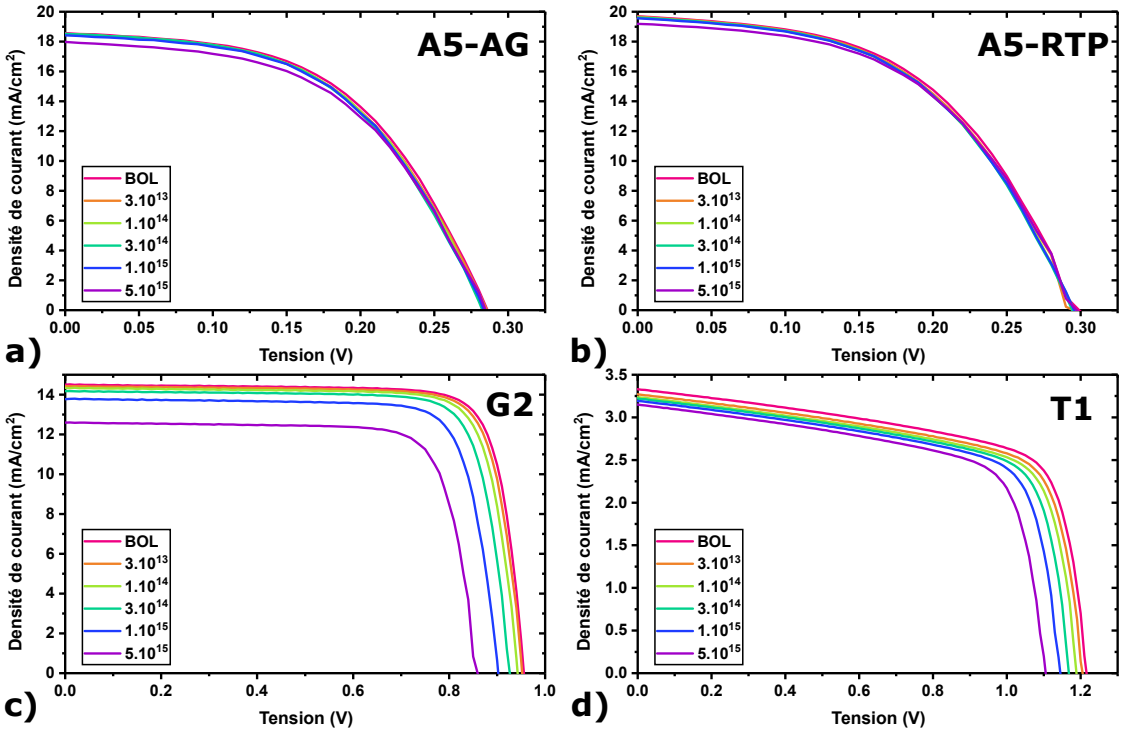

FIGURE 5.5 : Évolution des caractéristiques *J-V* mesurées sous illumination AM0 pour différentes fluences (e^-/cm^2), pour les échantillons A5-AG, A5-RTP, G2 et T1.

L'impact de l'irradiation aux électrons 1 MeV ainsi que la réduction du photocourant délivré par la cellule tandem peuvent se visualiser à travers la dégradation des spectres de rendement quantique des sous-cellules, comme le montre la Figure 5.6. Nous observons sur cette figure que la réponse spectrale est beaucoup plus dégradée dans la top-cell que dans la bottom-cell. Cette plus forte dégradation de l'EQE de la top-cell n'est cependant pas préjudiciable à la cellule tandem puisque la sous-cellule d'InGaAsN reste très largement la cellule courant-limitante après irradiation.

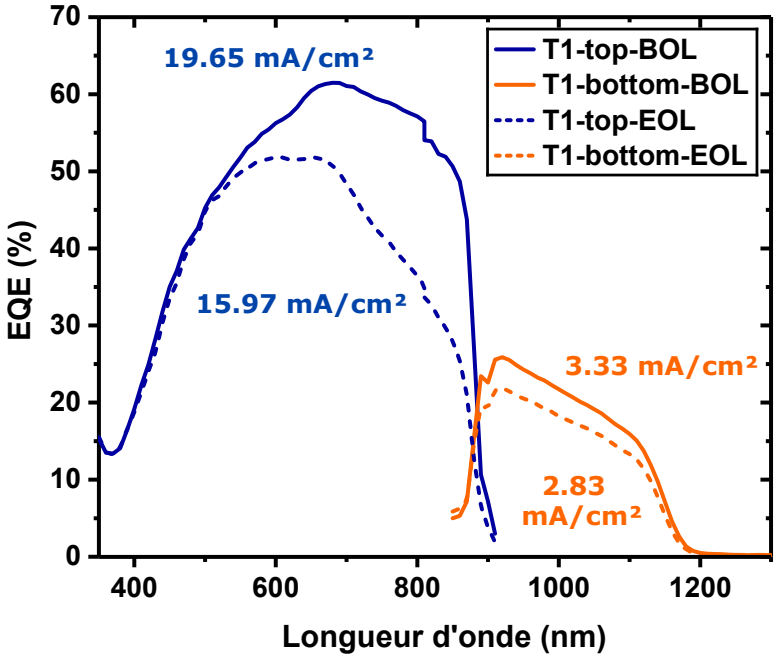

FIGURE 5.6 : Spectres d'EQE des sous-cellules de la tandem T1, avant et après une irradiation de 5×10^{15} e^-/cm^2.

5.4 Analyse de dégradation de cellules InGaAsN sous protons 1 MeV

Une dernière campagne d'irradiation a été menée avec des protons d'1 MeV sur quatre cellules solaires d'InGaAsN provenant du wafer A6. Ces échantillons disposent d'une teneur en azote équivalente aux cellules irradiées aux électrons lors de la première campagne. La Figure 5.7 présente la dégradation des caractéristiques *J-V* des cellules A6, obtenues sous AM0 à différentes fluences. Nous observons une remarquable homogénéité dans le taux de dégradation des quatre cellules et notons une dégradation importante des trois paramètres photovoltaïques (J_{sc}, V_{oc} et FF) après 10^{13} p^+/cm^2.

Des mesures courant-tension sous obscurité montrent une corrélation entre la dégradation de la tension de circuit ouvert et l'augmentation du courant de saturation. Concernant la diminution du fill factor, il est possible qu'elle soit liée à l'introduction de défauts électriquement chargés dans l'absorbeur d'InGaAsN [5].

La dégradation considérable du courant de court-circuit des cellules A6 après irradiation s'explique par une importante réduction du rendement quantique aux faibles longueurs d'ondes, comme l'illustre la Figure 5.8 a). La disparité de dégradation du spectre d'EQE entre λ<870 nm et λ>870 nm suggère par ailleurs que la diminution du rendement quantique résulte majoritairement de la dégradation de l'émetteur de GaAs. En effet, la Figure 5.8 b) montre que l'émetteur de 200 nm

absorbe une large partie des photons de longueur d'onde inférieure à 870 nm. L'absorbance de l'émetteur est calculée ici avec la formule de Beer-Lambert, présentée sur la Figure 5.8 b), pour laquelle α est le coefficient d'absorption du GaAs tiré de [6] et t est l'épaisseur de l'émetteur égale à 200 nm.

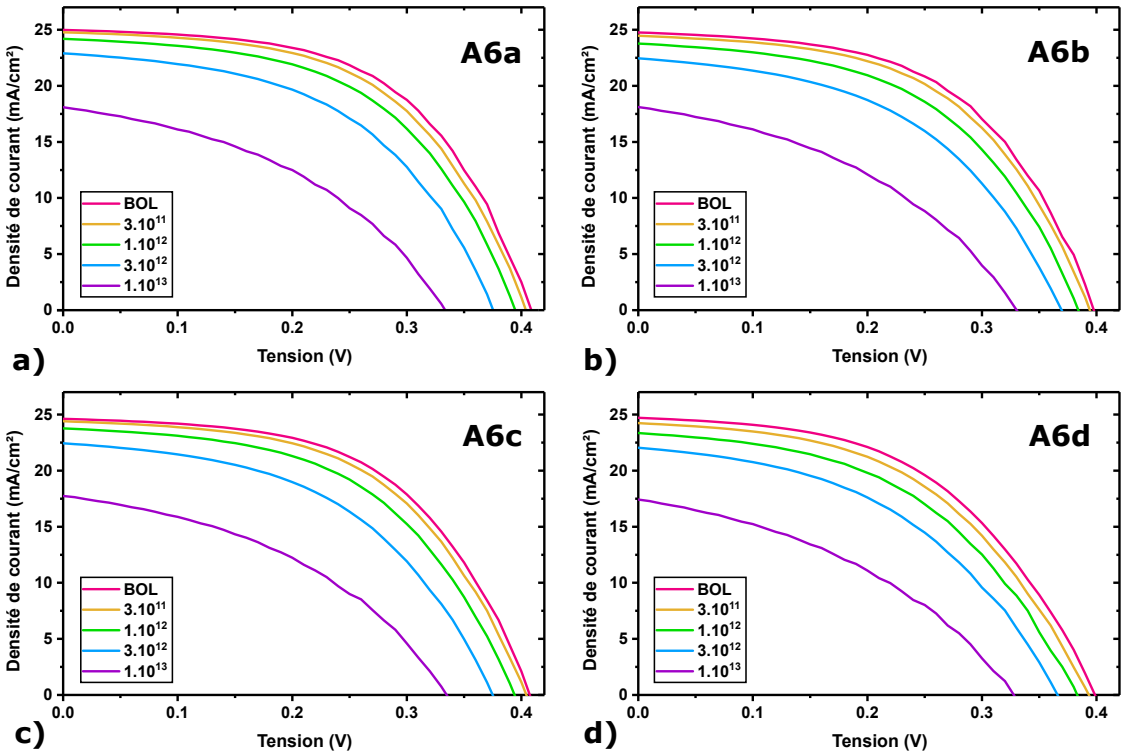

FIGURE 5.7 : Évolution des caractéristiques *J-V* des cellules A6 mesurées sous illumination AM0 pour différentes fluences (p^+/cm^2).

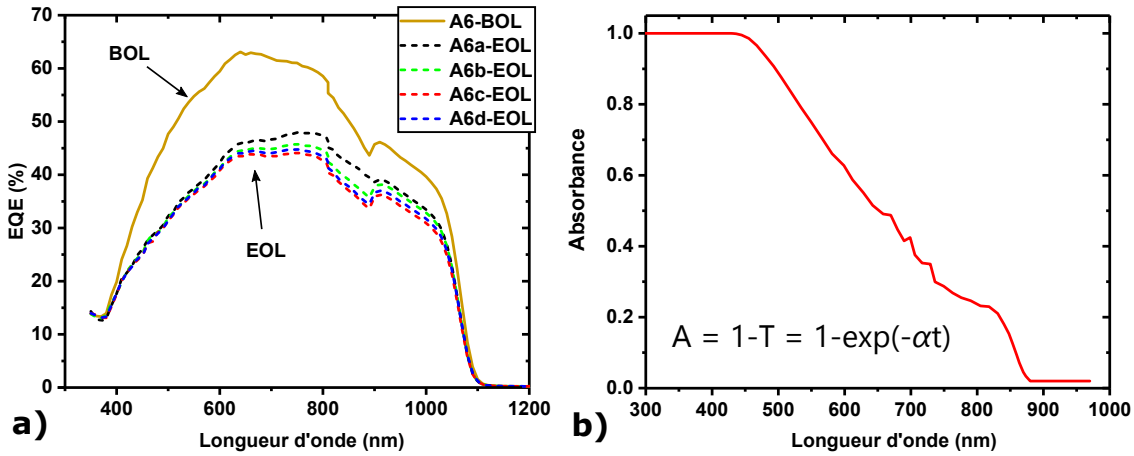

FIGURE 5.8 : a) Spectres d'EQE des cellules A6 avant et après irradiation aux protons 1 MeV (10^{13} p^+/cm^2) b) Spectre d'absorbance de l'émetteur de 200 nm de GaAs.

5.5 Analyse croisée de l'impact des électrons et protons 1 MeV

Les campagnes d'irradiation présentées dans ce chapitre montrent une dégradation beaucoup plus importante des cellules d'InGaAsN soumises à l'irradiation protonique. Ceci s'explique par le grand pouvoir d'arrêt nucléaire des protons 1 MeV dans l'InGaAsN. Afin de pouvoir comparer l'effet de différentes particules ou l'effet de particules de différentes énergies, la dégradation des cellules est en générale tracée en fonction de la dose de déplacement (DDD). Cette dose est obtenue en multipliant la fluence d'irradiation par le NIEL de la particule (voir Chapitre 1). La Figure 5.9 présente les dégradations de photocourant des cellules d'InGaAsN irradiées lors des trois campagnes, en fonction de leur DDD correspondante.

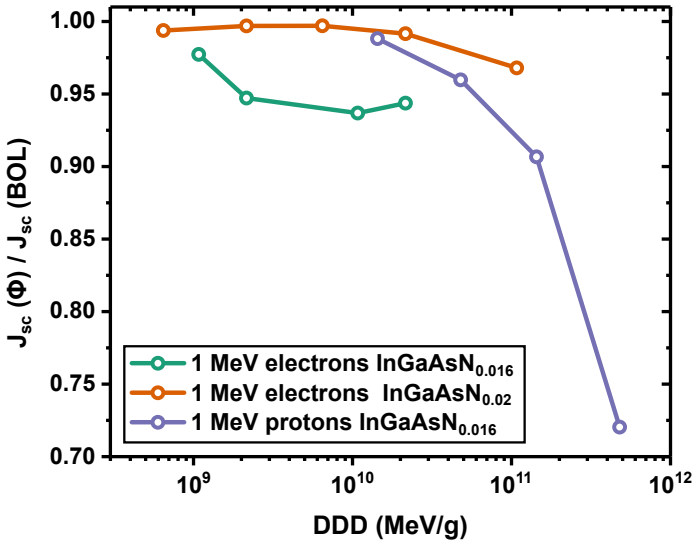

FIGURE 5.9 : Évolution des photocourants obtenus sous AM0 et normalisés par rapport à leur valeur BOL, en fonction de la DDD.

Nous voyons à travers cette figure qu'à DDD équivalente, les protons d'1 MeV ne dégradent pas plus les cellules d'InGaAsN. Le décalage de dégradation observable entre les deux courbes correspondant aux cellules irradiées aux électrons provient de la différence de composition en azote, comme nous l'avons expliqué précédemment.

Références

[1] J. H. Warner, S. R. Messenger, R. J. Walters, G. P. Summers, J. R. Lorentzen, D. M. Wilt, and M. A. Smith, "Correlation of electron radiation induced-damage in GaAs solar cells," *IEEE Transactions on nuclear science*, vol. 53, no. 4, pp. 1988–1994, 2006.

[2] B. Danilchenko, A. Budnyk, L. Shpinar, D. Poplavskyy, S. Zelensky, K. Barnham, and N. Ekins-Daukes, "1 MeV electron irradiation influence on GaAs solar cell performance," *Solar energy materials and solar cells*, vol. 92, no. 11, pp. 1336–1340, 2008.

[3] B. E. Anspaugh *et al.*, *GaAs solar cell radiation handbook*. National Aeronautics and Space Administration, Jet Propulsion Laboratory, 1996, vol. 7.

[4] G. J. Dienes and A. Damask, "Radiation enhanced diffusion in solids," *Journal of Applied Physics*, vol. 29, no. 12, pp. 1713–1721, 1958.

[5] S. Park, J. C. Bourgoin, H. Sim, C. Baur, V. Khorenko, O. Cavani, J. Bourcois, S. Picard, and B. Boizot, "Space degradation of 3J solar cells : I—Proton irradiation," *Progress in Photovoltaics : Research and Applications*, vol. 26, no. 10, pp. 778–788, 2018.

[6] E. D. Palik, *Handbook of optical constants of solids*. Academic press, 1998, vol. 2.